2021

Elucidating the Contribution of the BAF A12T Mutation to Cellular Mechanisms of Premature Aging

Maya Fadia Marwan El-Sabban
Medical University of South Carolina

Elucidating the Contribution of the BAF A12T Mutation to Cellular Mechanisms of Premature Aging

By

Maya Fadia Marwan El-Sabban

A dissertation submitted to the faculty of the Medical University of South Carolina in partial fulfillment of the requirements for the degree of Doctor of Philosophy in the College of Graduate Studies

Molecular Cell Biology and Pathobiology Program

Department of Biochemistry and Molecular Biology

2021

Approved by:

Chairman, Advisory Committee — Paula Traktman, PhD

Robin Muise Helmricks, PhD

C. Amanda LaRue, PhD

Denis Guttridge, PhD

W. Dave Hill, PhD

Acknowledgements

To Mama and Baba: The shoes you've left me to fill are massive- two accomplished faculty members who have discussed scientific discovery at the dining room table my whole life. From a young age you encouraged me to be curious and ask about the world around me. By buying me a microscope as a gift, taking me to seminars about cloning, and spending weekends in the lab, it was the natural progression of things for me to pursue a higher degree in the biological sciences… fated by who my parents are. You are to thank for providing me with the tools to persevere and persist during a struggle, and to question everything.

To Rami: My genetic half, and my whole soul. Your free spirit and your ability to live life to its fullest is always a fresh breath of air when I need it. Thank you for encouraging me to be the best version of myself.

To Paula: I was lucky to have you as my mentor, someone who reflected back to me the stern look of my father when I didn't critically analyze data, and the encouragement of my mother who reminded me the only way to succeed was to get up and try again. You molded me, the unshapen ball of curiosity and enthusiasm, into a true scientist, committed to rigor and thoughtfulness, and taught me the drive to follow my passion.

Traktman Siblings: The lab has been my home for the past years, and in being so, you have become my family. We partook in discussions over beer about signaling pathways, heated debates about how to design experiments, and asked questions that left me thinking about the microscopic world of the cell late into the night. Of course, one cannot discount the importance of also having a good laugh over inexplicable results and throwing lab dance parties and singalongs at the bench while working through the day. It

has been my joy to be part of the Traktman lab lineage and to have gained scientific siblings along the way.

To Josh: The time I spent in the lab sometimes took away time spent with family and friends. An unfortunate but necessary sacrifice in the achievement of a doctorate. The only way to overcome the feeling of missing out is to have a support system that encourages you to keep going, day by day. You have never made me feel guilty for not being home, have never asked me to skive off with you, nor have you ever complained about the meals or weekends I have missed. You have absolutely been my scaffolding throughout and while you may not enjoy hearing about the cell, you always listen. By balancing the demands of the degree and becoming parents to our niece, Thai, we have grown both individually and together and we will continue to do so. **Thai:** Never stop learning and seeking knowledge.

To my friends:

"In the sweetness of friendship let there be laughter, and sharing of pleasures. For in the dew of little things the heart finds its morning and is refreshed" –Gibran Khalil Gibran

MAYA EL-SABBAN. Elucidating the contribution of the BAF A12T mutation to cellular mechanisms of premature aging. (Under the direction of PAULA TRAKTMAN)

Abstract

The nuclear envelope is a dynamic structure and organizing hub for cell structure and function. The underlying nuclear lamina is composed of a thick network of intermediate filaments, Lamin A/C and B, and inner nuclear membrane-associated proteins such as Lap2, Emerin and Man1. BAF, a central organizing protein, is a small, dimeric, essential protein that binds to dsDNA, proteins of the inner nuclear membrane and Lamin A. Cells with perturbations of the nuclear lamina display dysmorphic nuclei which have the potential to lead to altered gene expression, increased DNA damage events, and premature cellular senescence. In this study, we address a single amino acid substitution from Alanine 12 to Threonine (A12T) in BAF that gives rise to a nuclear morphology defect. At the clinical level, patients who inherit a homozygous BAF A12T mutation have a rare premature aging syndrome called Nestor Guillermo Progeria Syndrome (NGPS) with symptoms such as osteolysis, adipolysis and craniofacial defects that present at approximately two years of age and progress rapidly, ultimately shortening patient lifespan significantly. Tissues of mesenchymal origin appear to be most severely impacted in this disease, leading to the hypothesis that mesenchymal stem cells are preferentially affected. To address the cellular and organismal pathology of NGPS, we used CRISPR/Cas9 technology to establish BAF^{A12T}/BAF^{A12T} human induced pluripotent stem cells (hiPSCs). A12T BAF iPSCs appeared normal, however when differentiated to induced mesenchymal stem cells (iMSCs), A12T BAF cells exhibited a marked increase in cellular senescence and an elevated cellular stress response. The mechanism of A12T BAF's contribution of this cell-type specific pathology was not well understood. Our data

indicate that A12T BAF ‘s binding to Lamin A is greatly diminished, thereby weakening the Lamin A network of the nuclear lamina and the structural integrity of the nuclear envelope. Mechanosensitive iMSCs are unable to withstand this weakened network and the nuclei appear to rupture, thereby causing cellular stress and ultimately, senescence. Our results indicate that the A12T BAF mutation is necessary but not sufficient to cause premature cellular aging. All cell types expressing BAF^{A12T}/BAF^{A12T} have dysmorphic nuclei, however cells derived from BAF^{A12T}/BAF^{A12T} mice are viable and primary dermal fibroblasts are not senescent, nor do they demonstrate elevated levels of DNA damage. Furthermore, A12T BAF mice do not have shortened lifespans nor do they have defects in mesenchymal derived tissue. These data highlight the nuances of this mutation’s effect both at the cellular and organismal level and elucidates a new role for BAF at the nuclear envelope as a key player in cell mechanosensitivity and the network of the nucleoskeleton and cytoskeleton.

Table of Contents

Table of Figures

Chapter 1: Introduction

As early as the first microscopic observations in the 18th century, the nucleus was described as a central feature of the eukaryotic cell. Over 100 years later, Robert Brown coined the term *nucleus* in 1831 and suggested that the nucleus played a key role in the fertilization and development in plant cells (Brown, 1833). The late 1800's saw a spike in the study of the nucleus and its role in the heredity and development. By the early 1900s there were extensive studies and observations about the discrete entities within the cell, including the nucleus, and in 1964 Gall described the nuclear envelope using electron microscopy. This final observation established the division between the nucleus and the cytoplasm (Gall, 1964; Wilson, 1900). As time continues to press on, studies continue to uncover the complexities of this organelle, revealing the intricate relationships between chromatin, the nuclear envelope, the nuclear lamina and the nuclear substructures.

Overview of the Nucleus and its Substructures

The nucleus is one of the defining feature of eukaryotic cells. It encloses and sequesters the entire genome and is delimited by two concentric lipid bilayers that are punctuated by nuclear pores, which facilitate selective transport between the nucleus and cytoplasm. The nucleus is the site of the major metabolic activities of the cell including DNA replication and repair, gene transcription, RNA processing and ribosome maturation and assembly. The limited nuclear space must contain within it: DNA, RNA, histones, non-histone proteins, regulatory and processing enzymes, stable elements of the nuclear envelope and nuclear pores, structural proteins, and the nuclear lamina. Spatio-temporal regulation of this crowded nucleus is managed through the non-stochastic 3-D architecture of chromatin into distinct territories determined by the association of chromatin domains with other nuclear structures such as the nuclear envelope (Dekker & van Steensel, 2013).

DNA Organization in the Nucleus

The majority of the nuclear volume is occupied by genetic material packaged into high-order DNA-histone complexes called chromatin (Wolffe, 1998). The building blocks of chromatin are discrete entities called nucleosomes, which consist of 160-200bp stretches of DNA wrapped around an octamer of histones folded into a condensed structure (Felsenfeld & McGhee, 1986; Kornberg & Lorch, 1999). Compacted chromatin is transcriptionally repressed and chromatin is remodeled during replication and transcription (Adams & Workman, 1993; Alexiadis, Varga-Weisz, Bonte, Becker, & Gruss, 1998; Beato & Eisfeld, 1997; Kornberg & Lorch, 1991).

Histones:

Core histones are the main components of the nucleosome and are comprised of histones H2A, H2B, H3 and H4. Core histones are regulated through post translational modifications such as acetylation, methylation and phosphorylation which influence the accessibility and remodeling of chromatin (Davie & Chadee, 1998; Wu, Panusz, Hatch, & Bonner, 1986). The post translational modifications of histones are carried out by histone modifiers, which are organized into subfamilies such as histone acetyltransferases (HATs) and histone deacetylases (HDACs), histone methyltransferases (HMTs) and histone demethylases (HDMs) and protein kinases. (Gilbert, Gilchrist, & Bickmore, 2004). The function of the nucleosome is not only to act as a structural component but also as a modulator of gene expression. Precise positioning across genes allows differential access to transcription factors and are repositioned by chromatin remodeling complexes (Längst & Becker, 2001; Simpson, 1991). Linker histones H1, H5 and H1° are located outside of the nucleosome and are responsible for the condensation and the stabilization of the chromatin fiber (Pruss, Hayes, & Wolffe, 1995; Thoma & Koller, 1977). Histone acetylation

is correlated with transcriptional activity, while methylation is correlated with transcriptional repression (Hebbes, Thorne, & Crane-Robinson, 1988)

Chromatin Compaction:

Interphase nuclei have two distinct chromatin organizations: heterochromatin and euchromatin. Heterochromatin is highly condensed and euchromatin adopts an open conformation. Heterochromatin is further subcategorized into: i) constitutive heterochromatin, which is comprised of tandem repeats that remain condensed throughout the cell cycle, ii) facultative heterochromatin, which changes throughout development and as a result of signaling and is therefore regulated in a temporal manner and iii) senescence associated heterochromatin foci (SAHF) which accumulate throughout the genome as cells undergo cellular aging (Gilbert et al., 2004). Interphase chromatin is organized spatially into territories. Territories are discrete entities delimited by the interchromatin domains (ICD) and their structured organization influences gene expression (Cremer & Cremer, 2001; Leitch, 2000). Chromosomes return to the configuration in which they were found preceding anaphase, which is fixed during cell cycle and can be arranged into similar patterns among similar species or cell type (Leitch, 2000). These data highlight the non-random positioning of chromatin within the nucleus.

Lamina Associated Chromatin:

An important substrate for the tethering of chromatin to specific localizations in the nucleus is the nuclear envelope (Chubb, Boyle, Perry, & Bickmore, 2002; Heun, Laroche, Shimada, Furrer, & Gasser, 2001). The regulation of transcription through chromatin conformation is facilitated by long range interactions which form intrachromosomal loops and contacts. The development of chromosome conformation capture allowed the identification of subdomains within chromatin that associate spatio-temporally (Dekker,

Rippe, Dekker, & Kleckner, 2002). These interacting domains are called topology associated domains, or TADs. Discrete TAD organization is subdivided into two major compartments: the “A” compartment which correlates with proteins and histone modifications that are involved with active transcription; and the “B” compartment which correlates with repression of gene transcription (Dixon et al., 2012). Within the “B” type compartment is a subset of TADs which associate with the nuclear envelope and the underlying nuclear lamina, called lamina-associated domains (LADs) (Guelen et al., 2008; Pickersgill et al., 2006).

The nucleolus:

The nucleolus is a nuclear body that forms around rRNA enriched gene loci called “nucleolar organizer regions” (NORs). The function of the nucleolus is the synthesis of rRNA and processing and assembly of the ribosomal subunits which are then exported from the nucleolus to the cytoplasm to carry out their function of mRNA translation. The nucleolus is divided into three subcategories: the fibrillary center, the dense fibrillary component and the granular component. Each step of rRNA synthesis and maturation occurs in a discrete nucleolar structure (Lamond & Sleeman, 2003).

Figure 1-1

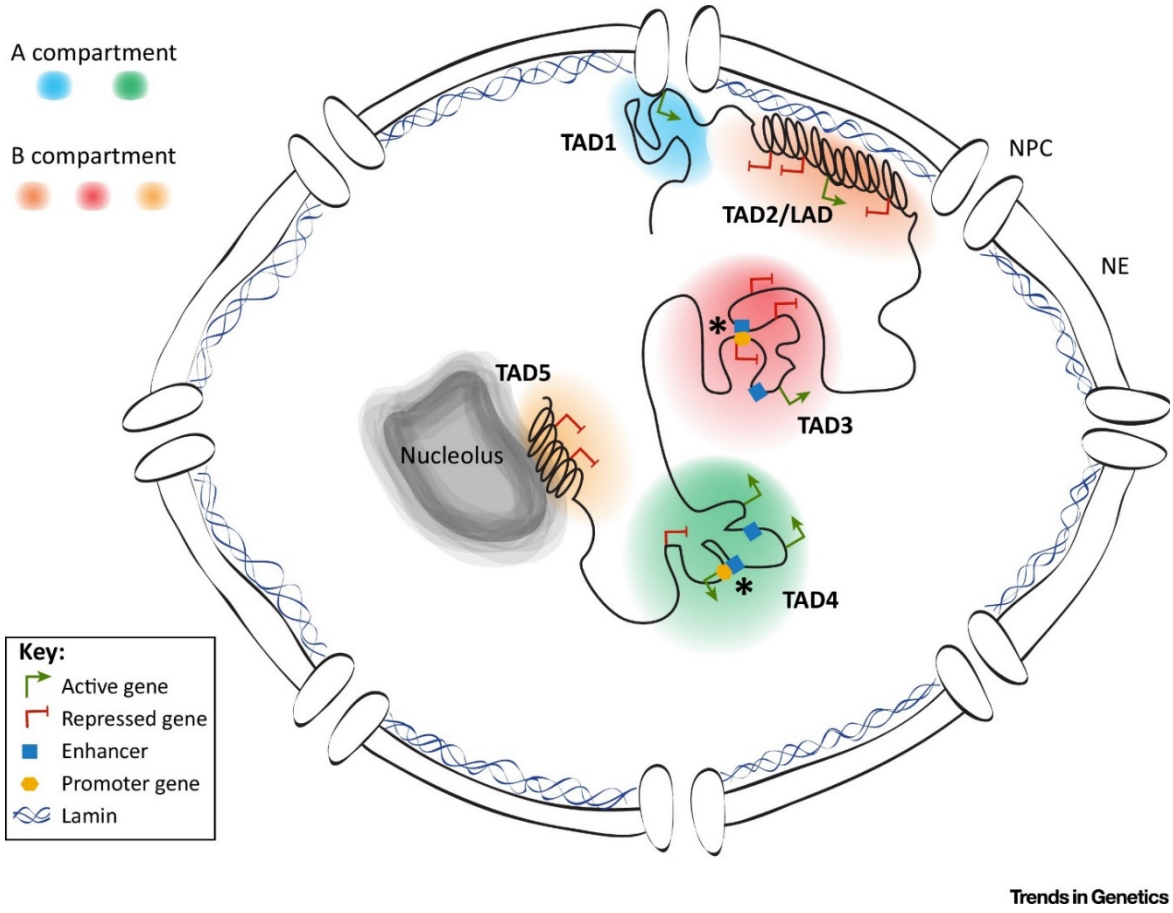

Figure 1-1. The 3-D Organization of Chromatin in the Nucleus. Taken from (Gonzalez-Sandoval & Gasser, 2016). Chromatin is highly organized within the cell, and chromosome territories are conserved throughout the lifespan of the cell and across cell type and species. Long rage chromatin interactions facilitate chromatin organization within the nucleus. Topology associated domains are classified as transcriptionally active or repressed (Compartment A or B respectively) and TADs associated with the nuclear lamina, termed Lamina Associated Domains, LADs are generally associated with transcriptional repression.

The Nuclear Envelope and Nuclear Lamina

The nuclear envelope (NE) is a dynamic structure that determines the overall shape, size, and integrity of the nucleus. The NE is comprised of two lipid bilayers giving rise to an outer nuclear membrane (ONM) and inner nuclear membrane (INM). The ONM is continuous with the endoplasmic reticulum which allows for direct insertion of NE proteins and the translocation of proteins into the perinuclear space; the INM contains within it a population of stable membrane proteins that interact with chromatin and the nuclear lamina (Schirmer, Florens, Guan, Yates, & Gerace, 2003; Schirmer & Gerace, 2005). The INM acts as the scaffolding for the intermediate filaments of the nucleoskeleton which, in turn, provide critical stability, elasticity, rigidity, and organization to the structure of the nucleus.

The INM and ONM fuse at the sites of nuclear pore complexes (NPC) which are involved in the selective trafficking between the nucleus and cytoplasm. Pore density and distribution varies greatly between different cell and tissue types and across development. The membrane delimiting each pore is highly curved and studded with specific pore proteins called Poms which facilitate the anchoring of nucleoporins (Nups), thus generating a series of interactions contributing to the formation of the complex structure of the NPC (Rout et al., 2000). High resolution structures for the Nups and their interaction partners reveal a 9mm aqueous central channel that allows for the diffusion of small molecules (<40kDa). Large proteins, RNA and other macromolecules are transported across the membrane using facilitated transport

The NE further contains of the nuclear lamina (NL). The NL is comprised primarily of type V intermediate filament proteins, termed lamins, which form a meshwork of filamentous structures. They feature a central α-helical rod that is flanked by non-helical

head and tail domains organized in an Ig-like-β -fold that contains a nuclear localization sequence, see Figure 1-3 (Brian Burke & Stewart, 2013). There are two major families of lamins: Lamin A/C and Lamins B1 and B2. Lamin A and Lamin C are isoforms of the LMNA gene that arise due to alternative splicing and that are only expressed in differentiated cells. Lamins B1 and B2 are encoded by the LMNB1 and LMNB2 genes respectively, and one or the other are expressed in all cells throughout development and differentiation (Thomas Dechat et al., 2008). Lamin A and Lamins B1 and B2 contain a C-terminal CaaX motif (Cys, aliphatic residue, aliphatic residue, and X, usually a Met), that defines the site of farnesylation and carboxymethylation (Beck, Hosick, & Sinensky, 1990; Kitten & Nigg, 1991). Newly synthesized lamins are targeted to the nuclear envelope through farnesylation and are associated with the INM. Once incorporated, Lamin A undergoes proteolytic cleavage by ZMPSTE24 after Tyr646 to remove 15 amino acids from the C-terminus to give rise to mature Lamin A, whereas B-type Lamins remain farnesylated at the INM (Pendás et al., 2002). The proper expression and processing of both A-type and B-type lamins are critical to cell function and will be discussed in more detail later. Lamins are integral to the organization of chromatin at the nuclear periphery. Analysis of NE and NL-associated DNA indicates that for the most part, transcriptionally silent chromatin is concentrated at the nuclear periphery, and genes move towards or away from the NP based on repression or expression respectively, providing a mechanism for the spatial control of DNA replication and transcription.

Resident proteins of the INM and underlying NL contribute to the regulation of nuclear functions. A family of INM proteins that contain a 40 amino acid bi-helix motif, LAP-2, Emerin, Man1 domain (LEM-D), share the ability to bind lamins and BAF at the NP. LEM-D proteins interact with a diverse array of substrates, implicating them in

mechanotransduction, cellular and nuclear architecture, transcriptional regulation and chromatin tethering (Barton, Soshnev, & Geyer, 2015). LEM-D proteins represent the most studied subset of INM proteins and contribute to the organization of chromatin within the nucleus by tethering genomic regions to the NP through direct interactions or through their interactions with BAF and Lamin. LEM-D proteins also play a role in gene regulation through histone mark regulation by interacting with histone deacetylases, or by direct association with transcription factors (Barton et al., 2015). The mammalian genome encodes 7 LEM-D proteins: LAP2α, Emerin, MAN1, LEM2, LMD1, Ankle1 and Ankle2 most of which contain transmembrane domains that tether them to the INM (Brachner & Foisner, 2014).

Lamina associated peptide (LAP) 2α arises from the LAP2 gene which gives rise to 6 LAP2 isoforms. The LAP isoforms share the first 187 N-terminal residues that contain within them the LEM domain and a LEM-like motif which allows for direct DNA binding. LAP2α differs from other LAP2 isoforms in that it is not stably anchored into the INM at its C-terminal tail, whereas LAP2β, for example contains a C-terminal transmembrane domain. LAP2α is distributed within the nucleoplasm and binds Lamin A, chromatin and pRb (Gesson, Vidak, & Foisner, 2014). LAP2α's association with the cell cycle regulator pRb is suggestive of a role in cell cycle regulation. LAP2α preferentially interacts with hypophosphorylated pRb and anchors it in the nucleus, thereby inhibiting the expression of E2F target genes and inhibiting cell proliferation (Dorner et al., 2006). LAP2α is highly dynamic and localizes throughout the nucleoplasm during interphase. During NEBD and prophase, it disperses into the cytoplasm, and during late anaphase and telophase it interacts with sub-telomeric regions and TRF1, a member of the Sheltrin complex (T. Dechat et al., 2004). Furthermore, LAP2α plays a role in DNA repair pathways through its

association with DNA repair machinery, such as the Werner helicase (WRN) and Ku86, in the context of non-homologous end joining (NHEJ), and with PARP to generate a docking site for DNA damage repair proteins (Gagné et al., 2012; Lachapelle et al., 2011).

Emerin is an integral membrane protein that localizes to the INM and directly binds BAF and lamins. Emerin is encoded by the EMD gene, which was identified during the genetic mapping of Emery-Drifuss muscular dystrophy (EDMD) (Emery & Dreifuss, 1966). EDMD is characterized by the progressive wasting of skeletal muscle and dilated cardiomyopathy, which results in cardiac arrest (Dalton, Goldman, & Sampson, 2015). The identification of Emerin as a nuclear membrane protein gave rise to the new category of diseases termed laminopathies that are involved in the binding to and regulation of the nuclear lamins (B. Burke & Stewart, 2006; Méndez-López & Worman, 2012).

Figure 1-2

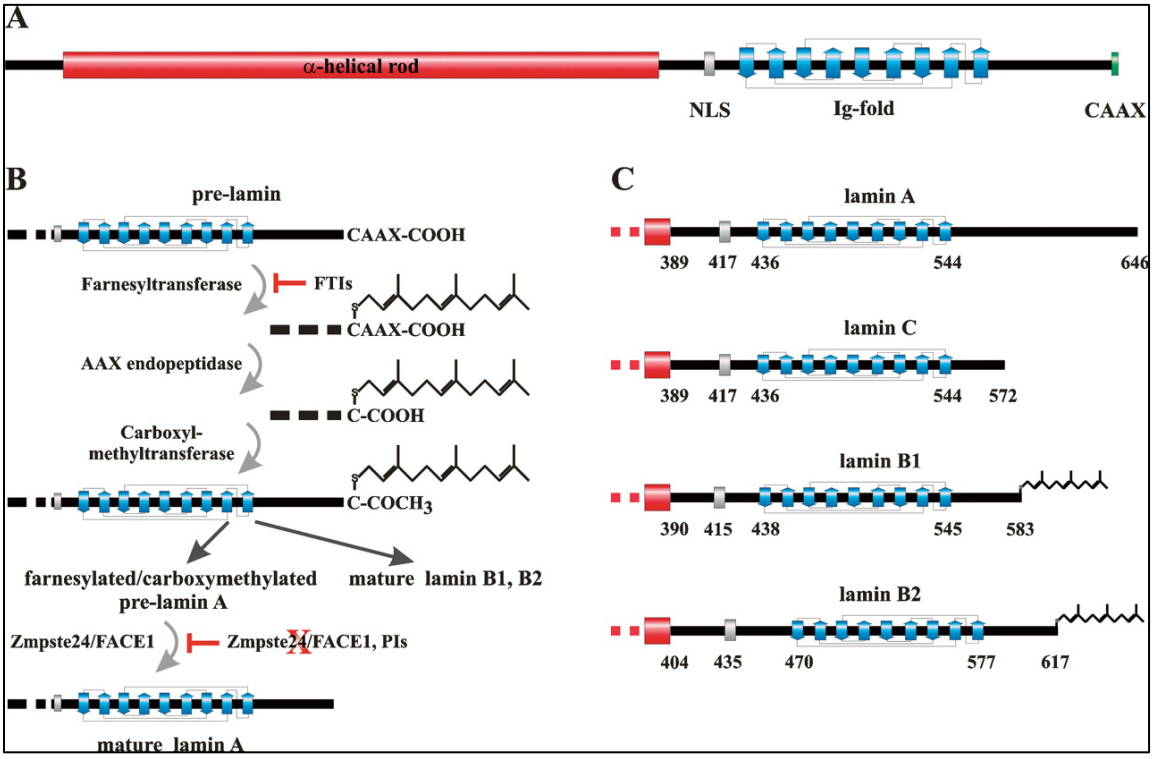

Figure 1-2. Structure and processing of Lamin A, C and B1/2. Taken from (Thomas Dechat et al., 2008). (A) Conserved structure between LMNA and LMNB1/2. Lamins are type V intermediate filaments which contain an α-helical rod, nuclear localization signal (NLS), an Ig-fold domain and a C-terminal CAAX domain. (B) The processing of pre-Lamin involves farnesylation, trimming and carboyxymethylation, as shown. Lamins B1 and B2 remain farnesylated in their mature form, whereas pre-Lamin A is cleaved internally by Zmptse24 to give rise to non-farnesylated, mature Lamin A. (C) Comparison of the nuclear lamins structure at the C-terminus.

The Nucleoskeleton and Mechanotransduction

The shape of the nucleus is regulated by the mechanical properties of the NE and NL, but also by the attachments it makes to the cytoskeleton. Cellular and extracellular mechanical forces are transduced at the cell periphery into signaling cascades that directly affect cell function. Mechanical changes at the cell periphery can arise as a result of changes to the extracellular matrix (ECM), changes in cell-cell junctions, or sheer and mechanical forces. Membrane-bound mechanosensitive proteins, such as integrins and cadherins, induce the reorganization of actin filaments, triggering downstream signaling pathways (Bouzid et al., 2019). The nucleus and cytoskeleton are coupled through a complex termed the *Li*nker of *N*ucleoskeleton to the *C*ytoskeleton, or LINC complex.

The LINC complex is composed of two protein families that span the nuclear envelope: Nesprin and SUN proteins. Nesprins are found at the nuclear envelope and contain a variable N-terminal domain, a C-terminal transmembrane KASH domain and a rod domain composed of a series of spectrin repeats (Lombardi & Lammerding, 2011). Nesprin binds actin at the N-terminus and SUN proteins in the preinuclear space at the C-terminus. A SUN monomer is made up of Unc-84 and Sad1 homology domains and assembles in a homotrimer (Malone, Fixsen, Horvitz, & Han, 1999). SUN interacts with Lamin A at its nucleoplasm domain thereby linking the perinuclear space and the nucleoplasm. The tethering of actin to Nesprin, Nesprin to SUN, and SUN to Lamin A, therefore, connects the cellular periphery to the nucleus and integrates the forces of the cytoskeleton and the nucleus. Cells require the LINC complex for migration and to establish nuclear structure, function, shape and position (Lombardi & Lammerding, 2011). Changes in nuclear shape affect gene expression and protein synthesis, and lamins are upregulated and reorganized in response to mechanical stress (Lammerding et al., 2005).

Nuclear shape is dependent on the rigidity of the underlying extracellular substrate: the nucleus assumes a spherical shape on soft surfaces due to smaller actomyosin tension and becomes flattened and ellipsoid on rigid substrates where the extracellular forces on the cell are greater (Lovett, Shekhar, Nickerson, Roux, & Lele, 2013). Lamin A levels are proportional to substrate rigidity, implicating Lamin A as a stabilizer for the nucleus under mechanical stress (Swift et al., 2013).

The coupling of the nucleus with the surrounding cytoskeleton indirectly connects the nucleus with the extracellular matrix and the surrounding cells. Mechanical deformations within the tissue are transduced along the cytoskeleton to the nucleus and influence nuclear function and gene expression. The interphase nucleus is a rigid, but deformable structure and is 2-10 fold stiffer than the remainder of the surrounding cell (Caille, Thoumine, Tardy, & Meister, 2002). The nuclear lamina and chromatin impart the nuclear stiffness and cells deficient in Lamin A/C are softer and more fragile (Lammerding et al., 2006). The interior of the nucleus can be characterized as being an aqueous, compressible viscoelastic material that increases in stiffness when compressed (Dahl, Engler, Pajerowski, & Discher, 2005). During cellular migration, the movement of the nucleus is coordinated with the motile cytoskeleton, which results in complex changes in both position and shape. Through the LINC complex, the nuclear lamina absorbs the mechanical stresses and tensile forces acting on the nucleus (Broers et al., 2005). As mentioned previously, the vast majority of the volume of the nucleus is comprised of genetic material. An increase in the proportion of heterochromatin restricts chromatin mobility and stiffens the nucleus (Pajerowski, Dahl, Zhong, Sammak, & Discher, 2007). The nuclear lamins also contribute to the rigidity of the nuclear interior and provide structure and organization between the nuclear interior and periphery (Broers et al., 2005).

Figure 1-3

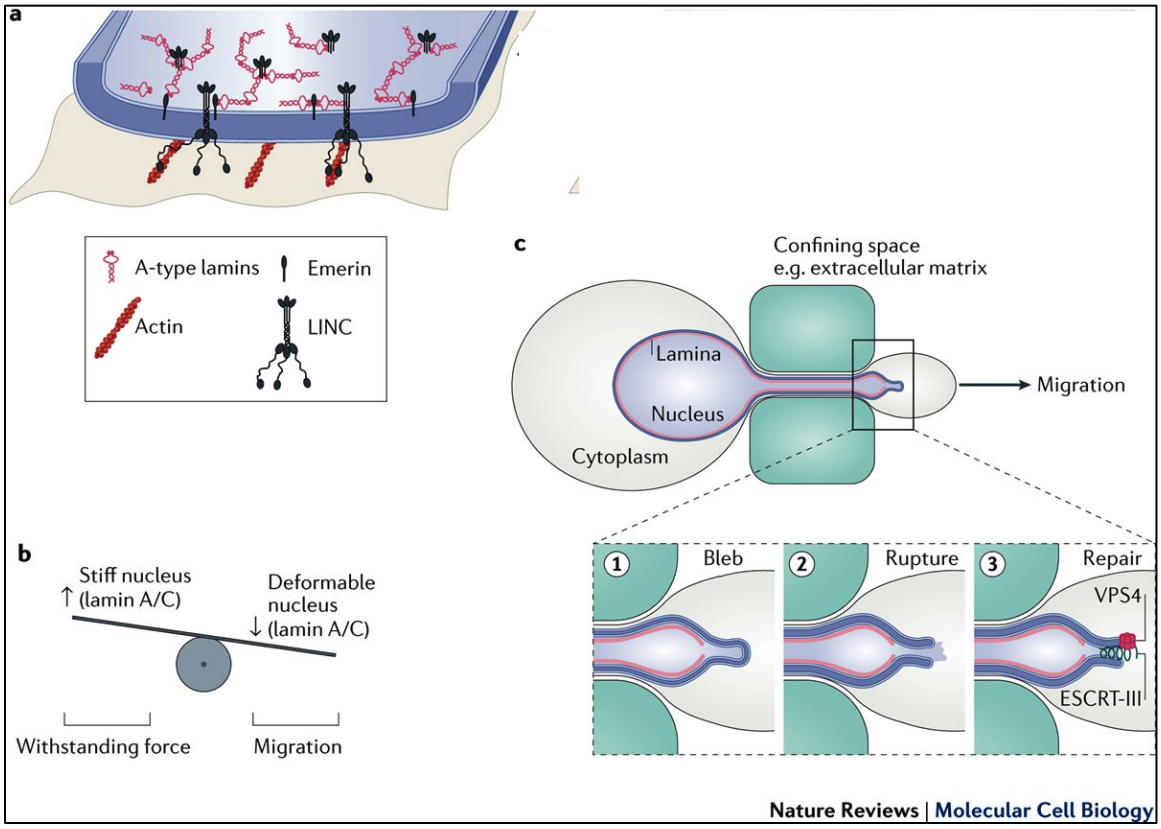

Figure 1-3. Nuclear deformations as a result of mechanical stress. Adapted from (Ungricht & Kutay, 2017). The NE responds to force stiffening of the nuclear lamina which results in the transduction of the signal from the cytoskeleton to the LINC complex, and in turn the nucleoskeleton. (B) The balance between nuclear rigidity and flexibility is crucial for cells to withstand mechanical forces on the nucleus. (C). Cells deform their nuclei to migrate, or mechanosensitive cells under mechanical strain, can results in the loss of the NE integrity and subsequent NE rupture and chromatin herniation. BAF is a component of the nuclear rupture repair complex and acts by binding dsDNA at the site of rupture and recruiting LEM-D proteins of the INM through the ESCRT-III machinery.

Structure and Function of BAF

The Discovery of BAF

The integration of viral DNA, synthesized by reverse transcription, into the host genome is essential for the retrovirus life cycle. Integration is carried out by a nucleoprotein complex which directs viral DNA to integrate into the host chromosome rather than undergoing self-destructive, self-integration. Viral nucleoprotein complexes isolated from Moloney Murine Leukemia Virus (MoMLV) featured a host cellular component that inhibited auto-integration (M. S. Lee & Craigie, 1994). Analysis of this host component revealed a single protein that was termed Barrier to Autointegration Factor, or BAF. Sequencing revealed an 89 amino acid protein highly conserved across species (Figure 1-4)

Structure Resolution of BAF

In 1998, the structure of BAF was solved by nuclear magnetic resonance (NMR), which revealed that BAF is a globular shaped protein composed of 5 helices and a small helical turn. The core is tightly packed and composed of hydrophobic residues. BAF forms a stable dimer in solution with Gly 47 of each monomer in helix 3 forming the dimeric axis (Cai et al., 1998). Importantly, helices 4 and 5 of BAF were thought to constitute a helix-turn-helix (HTH) motif, where the small turn between helix 4 and helix 5 is three residues in length beginning with a Gly, typical to HTH domains that recognize DNA. The N-terminus of helix 5, the DNA recognition helix of the HTH, appeared to readily fit into the major groove of DNA, aligning the residues along the DNA and orienting residues of helix 1 to position along the phosphate backbone. These DNA-interacting residues comprise a patch of positively charged residues on the surface of the protein and are highly conserved between human, mouse and zebrafish. These NMR data were mostly validated by x-ray

crystallography, confirming and refining the structure solution. The high-resolution structure however, replaced the theory of an HTH domain facilitating DNA binding with evidence of a helix-hairpin-helix (HhH), sequence-independent, DNA binding motif. An HhH motif is defined as containing two helices connected by a reverse turn. DNA binding occurs via hydrogen bonds formed between two adjacent phosphate groups of the DNA backbone with the residues of the reverse turn and second helix of the HhH (Umland, Wei, Craigie, & Davies, 2000). The dimerization of BAF at the third helix using the Gly47 notch frees the HhH on either side of the dimer to bind distinct DNA strands, foreshadowing BAF's ability to cross-bridge DNA for the first time. Using 21-mer oligonucleotides, BAF was observed to form discrete complexes with DNA and, extending the study of the role of BAF from viral integration, revealing BAF's extremely high affinity to dsDNA (Harris & Engelman, 2000; R. Zheng et al., 2000). See Figure 1-4.

Figure 1-4

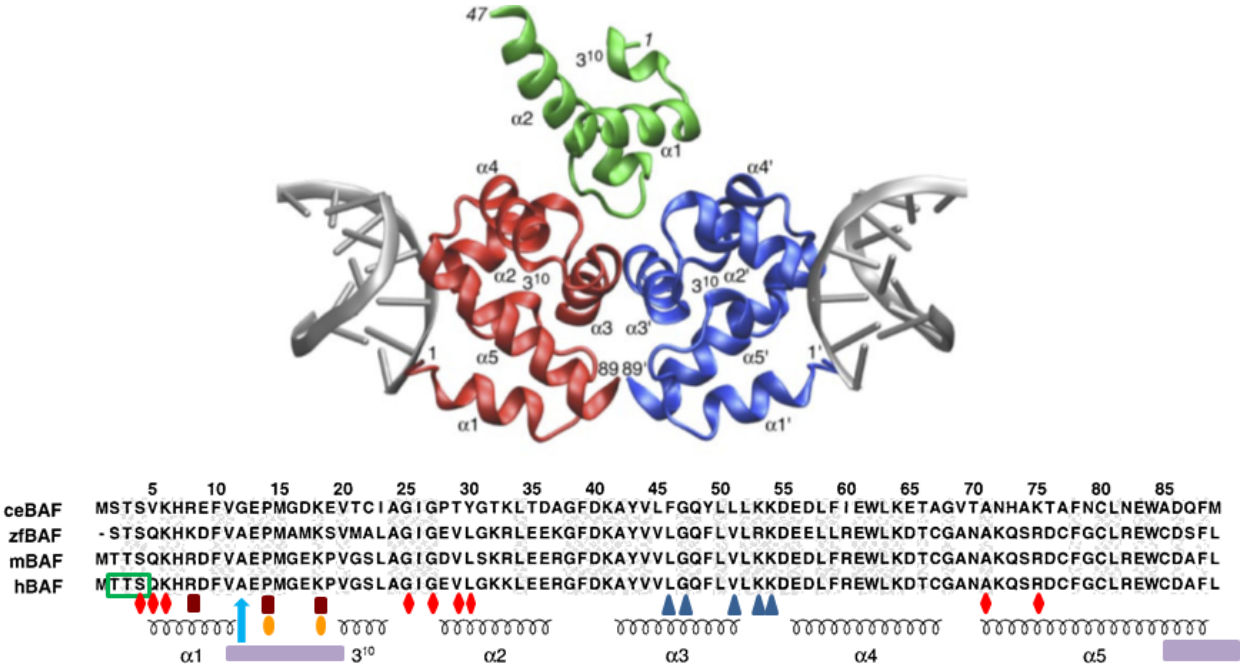

Figure 1-4. BAF's structure and Binding Surfaces. (A) The structure of the BAF dimer (Red= BAF monomer 1 Blue=BAF monomer 2) creates a binding surface for the interaction with LEM-D proteins (Green=LEM domain). Each BAF monomer binds dsDNA in a sequence independent manner. BAF A12T mutation occurs on the binding surface on the opposite pole of the LEM-D binding site (Pink Oval = surface of A12T mutation) (B) Sequence alignment reveals that BAF is highly conserved among species. Important resides are highlighted: Green box=sites of phosphorylation, red diamonds=interactions with dsDNA, cyan arrow=site of A12T mutation, maroon boxes and yellow ovals= residues that affect histone binding and chromatin compaction blue triangles= LEM-D binding, purple rectangles= Lamin A IgFold binding

BAF Protein Partners

In 1999, a yeast two-hybrid assay was performed to identify binding partners of Lap2. An 89 aa protein that localized to the nucleus was retrieved as a top hit; further analysis revealed that the Lap2-binding protein was indeed BAF. The binding site for BAF corresponded to the chromosome-binding site of Lap2. These data suggested, for the first time, that BAF might play a role as an organizer of DNA within the nucleus. By interacting with both DNA and proteins within the INM, it was postulated that BAF might serve to tether DNA to the INM (Furukawa, 1999). Building on this, NMR analyses elucidated the complex formed between BAF, DNA and Lap2's LEM domain, a domain shared, as discussed previously, with other components of the INM. A study in 2001 analyzed the contribution of the Emerin-BAF binding complex to chromosome dynamics during mitosis and the reassembly of the nuclear envelope. BAF was implicated in the assembly of the lamina and nuclear envelope at the end of mitosis, including the recruitment of INM components to the newly forming nucleus (T. Haraguchi et al., 2001).

BAF has been shown to interact with pre-Lamin A and Progerin and influence chromatin organization in the nucleus (Loi et al., 2016). Pre-Lamin accumulation affects chromatin organization through HeK9me3 clustering. Furthermore, BAF was found to regulate the distribution of Lamin A during nuclear envelope assembly implying its direct interaction with it (Tokuko Haraguchi et al., 2008).

There is evidence that BAF interacts directly with transcriptional regulators to influence gene expression, such as Crx to repress target gene activation (X. Wang et al., 2002), LAP2ζ to repress LAP2β-mediated transcriptional repression (Shaklai et al., 2008), and Sox2 to regulate stem cell fate in mouse embryonic stem cells (Mallanna et al., 2010). Furthermore, BAF is thought to regulate gene expression epigenetically. Mapping of LAD

sequences revealed that Lamins B1&2, Lamin A and BAF all interacted with the same genomic regions at the NP forming a structural complex that modulates LAD positioning (Kind & van Steensel, 2014). Furthermore, BAF interacts with a variety of histones including H4 and the nucleosome core histones (De Oca, Lee, & Wilson, 2005; Rocío Montes de Oca, Andreassen, & Wilson, 2011). BAF inhibits HAT-mediated acetylation of H3 and H4, consistent with its ability to bind H3 by sterically inhibiting access of chromatin regulators to the nucleosome (Rocío Montes de Oca et al., 2011). Furthermore, 3 specific post translational modifications (PTMs) increase in the presence of BAF overexpression: H3K4me2, H3K9me3 and H3K79me2. Paradoxically, H3K4me2 is associated with active chromatin and H3K9me3 with transcriptional silencing. It is unclear how BAF influences these PTMs and the downstream effects on gene expression (Rocío Montes de Oca et al., 2011)

Moreover, BAF was found to bind to regulators of the DNA damage response. PARP1 was found to bind to BAF and may implicate BAF in the repression of transcription during the DDR. Additionally, BAF binds to damage-specific DNA binding protein (DDB2) and CUL4A in a UV dependent manner. BAF is bound to DDB2 before the onset of DNA damage. Once DNA damage is induced, BAF is released from DDB2 and binds CUL4A until the damage process is complete (R. Montes de Oca, Shoemaker, Gucek, Cole, & Wilson, 2009).

BAF's interactions with LEM-D proteins, dsDNA and the nuclear lamina, transcription factors, histones and other binding partners such as DNA damage effectors highlights BAF's role as a nuclear organizing hub that bridges a myriad of components of the nucleus together. A summary of BAF function and interactions is represented in Figure 1-5.

Figure 1-5

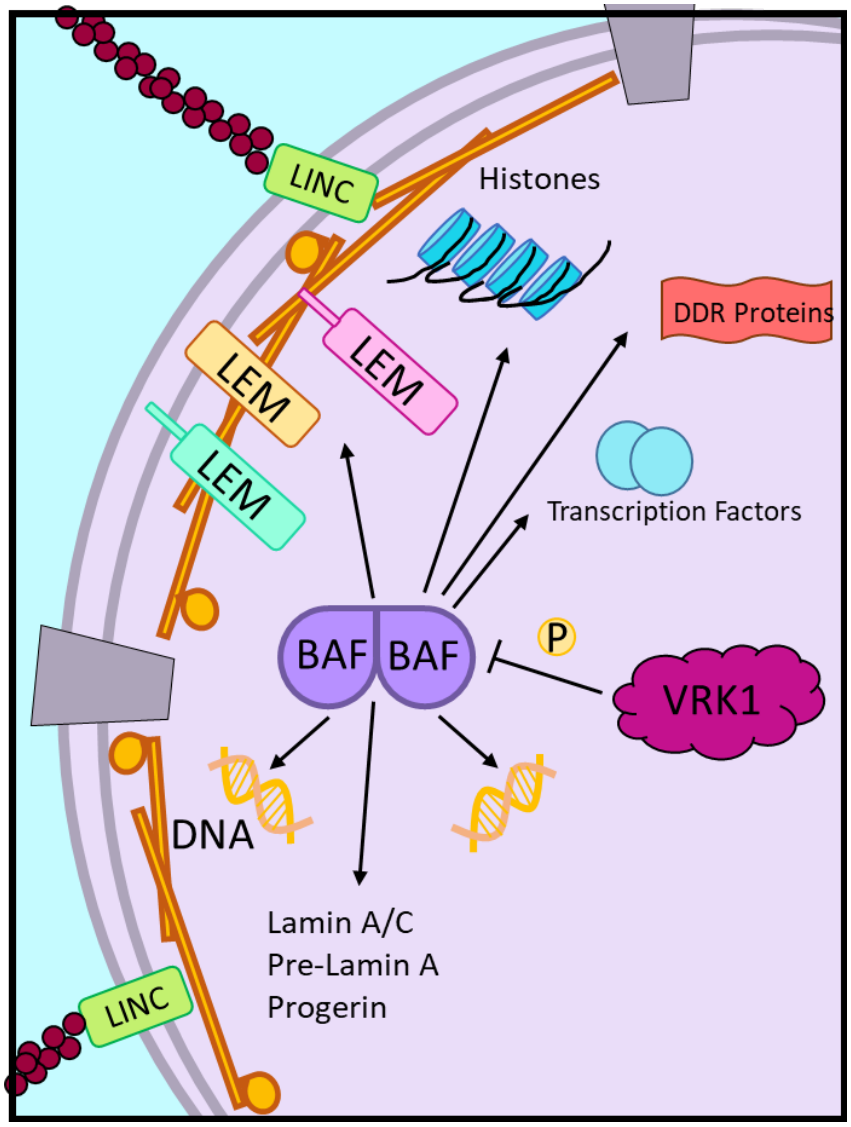

Figure 1-5. The Known Interactions of BAF. The BAF dimer is able to bind dsDNA in a sequence independent manner, proteins of the INM that contain a LEM domain and the Ig Fold of Lamin A. Furthermore, it has been show to play a role in the regulation of transcription factors, histones and effectors of the DNA damage response pathway. BAF is phosphorylated by VRK1 which regulates its interactions with its binding partners.

BAF/VRK1 Signaling Axis and Mitosis

Our lab showed that BAF is phosphorylated preferentially on Serine 4 by Vaccinia Related Kinase 1 (VRK1) which regulates its interactions and localization within the cell (Bengtsson & Wilson, 2006; R.J. Nichols, M.S. Wiebe, & P. Traktman, 2006). Threonine 2 and 3 are weaker sites of phosphorylation. BAF is primarily localized at the INM but there is also a cytoplasmic pool (Tokuko Haraguchi et al., 2007). BAF's localization and binding affinity to LEM-D proteins and DNA is reliant on its phosphorylation status: pBAF increases the cytosolic fraction, and decreases BAF's affinity to its interacting partners (R.J. Nichols et al., 2006). In particular, the interaction between BAF and dsDNA is nearly abrogated by phosphorylation.

The NE undergoes disassembly (NEBD) at the onset of mitosis. During NEBD, nuclear integrity and compartmentalization is completely lost. NEBD marks the transition from prophase to prometaphase and results in the retraction of the NE from chromatin, NPC disassembly, and the mixing of the contents of the nucleoplasm and cytoplasm. The components of the NE during this reorganization are released into the mitotic cytoplasm and endoplasmic reticulum, either as individual proteins or stable subcomplexes (Hetzer, Walther, & Mattaj, 2005; L. Yang, Guan, & Gerace, 1997). NEBD is regulated at multiple levels by phosphorylation of NE- associated proteins, NPC proteins, lamins and other INM proteins at the onset of mitosis (Anderson & Hetzer, 2008a). Cdk1/Cyclin B phosphorylates lamins directly to trigger lamina depolymerization, Nup phosphorylation initiates NPC disassembly, and other important phosphorylation events provide the temporal signal for NEBD. Phosphorylation-mediated disruption of protein-protein interactions at the NE leads to bulk disassociation (Buendia, Courvalin, & Collas, 2001; Dephoure et al., 2008). BAF is hyperphosphorylated, by VRK1 at the onset of mitosis,

which abrogates BAF binding to dsDNA and diminishes its interaction with the LEM-D proteins, thereby releasing the chromatin from the nuclear lamina during mitosis (Bengtsson & Wilson, 2006; T. P. Molitor & Traktman, 2014; R.J. Nichols et al., 2006). Chromosomes aligned on the metaphase plate are membrane free and the proteins of the NE reside in the mitotic ER, the precursor membrane of the interphase NE. At the end of mitosis, BAF is dephosphorylated by PP4, and PP2A phosphatases, which reestablishes its binding affinity to the LEM-D proteins of the INM to recruit membranes to chromosomes through its interactions with dsDNA and the LEM domain-containing proteins (Asencio et al., 2012; Gorjanacz, 2012; Gorjanacz et al., 2007). NE reformation and reconstitution occurs by chromosomes binding to and targeting ER tubules and immobilizing them on the chromosome surface which flattens and seals into a closed NE (Anderson & Hetzer, 2008b). The formation of flat membrane sheets on chromatin is initiated by the recruitment of DNA-binding INM proteins or INM proteins containing a LEM domain bound to BAF (Anderson & Hetzer, 2008b; Puhka, Vihinen, Joensuu, & Jokitalo, 2007; Samwer et al., 2017). Depletion of BAF causes defects in chromatin segregation during mitosis and subsequent nuclear envelope assembly (Furukawa et al., 2003; Gorjanacz et al., 2007), and the expression of BAF is required for the reformation of a single nucleus at the end of mitosis (Samwer et al., 2017).

BAF and Nuclear Rupture

Ruptures in interphase nuclei can occur as a result of migration through confined spaces, weakening of the NE due to changes at the NP and mechanical strain and tension (N. Y. Chen et al., 2018; Denais et al., 2016; Hatch & Hetzer, 2016). Repetitive nuclear rupture causes loss of cellular compartmentalization and is a feature of laminopathies (De Vos et al., 2011). Following NE rupture there are cellular consequences such as DNA

damage, innate immune signaling, and mechanisms to functionally repair the rupture. BAF's predominantly non-phosphorylated pool of cytosolic BAF localizes to sites of nuclear rupture to bind herniated dsDNA and recruits LEM-D with their associated membranes proteins to functionally repair the NE (Halfmann et al., 2019; Young, Gunn, & Hatch, 2020).

Overview of Cellular Aging and Progerias

The Hallmarks of Aging

Aging is characterized by the loss of physiologic integrity over time. The isolation of longevity mutants in *C. elegans* by Klass in 1983 launched the study of genes contributing to organismal aging (Klass, 1983). The study of the molecular basis of cellular aging has become a widely studied field and has helped inform different areas of research such as cancer biology and metabolism. There are nine hallmarks of aging that fill the criteria of: i) manifesting during normal aging ii) aggravation accelerates aging iii) amelioration retards the aging process and increases lifespan (both cellular and organismal) (Lopez-Otin, Blasco, Partridge, Serrano, & Kroemer, 2013)

Genomic Instability:

The Disposable Soma model introduced the idea that aging is a consequence of the investiture of energy required only to maintain the soma only long enough to reproduce, and that the damage to cellular components is a consequence of this process (Kirkwood & Holliday, 1979). DNA damage accumulates throughout the lifespan of a cell and is likely one of the most critical contributors to the aging process (Moskalev et al., 2013). The insults to DNA through exogenous damage, and endogenous stresses such as replication errors, result in DNA lesions that require DNA repair. Insults to DNA repair mechanisms cause premature aging syndromes, such as mutations in ATM, PARP-1,

Ku86, DNA-PKcs, XPF, WRN and BLM (Espejel et al., 2004; H.-W. Lee et al., 1998; Lombard et al., 2000).

Telomere Attrition:

Telomeric regions in the genome are highly susceptible to deterioration with each round of replication, due to the inability of DNA polymerase to prime synthesis at the end of linear DNA. Therefore, maintenance of telomere length during cellular DNA replication relies on a specialized polymerase called telomerase (Blackburn, Greider, & Szostak, 2006). After birth, most somatic cells do not express telomerase, which causes the progressive loss of telomeric sequences and eventually culminates in the inability of the cell to replicate any further (Blackburn et al., 2006; Hayflick & Moorhead, 1961). Inducing the expression of telomerase rescues cells from senescence and imparts cellular immortality (Bodnar et al., 1998). Cells deficient in telomerase or components of the telomeric complex results in cellular senescence and organismal aging (Armanios et al., 2009).

Epigenetic Modifications:

Histone modifications can modulate gene expression through the methylation of longevity-associated genes (Greer et al., 2010). Specifically, sirtuins, a family of histone deacetylases, have been studied extensively because Sir2 overexpression increases the lifespan of yeas, flies and worms (Guarente, 2011). In mammals Sirt1, Sirt3 and Sirt6 overexpression results in genomic stability and enhanced metabolic efficiency (Nogueiras et al., 2012). Furthermore, DNA becomes hypermethylated with age and the patterns of physiologic aging-driven hypermethylation of the genome is mirrored in premature aging syndromes (Maegawa et al., 2010). Chromosome modifying proteins such as HP1α or

members of the Polycomb or NuRD complexes all contribute to overall epigenetic modifications that influence cellular aging (Pegoraro et al., 2009; Pollina & Brunet, 2011).

Loss of Proteostasis:

Impaired protein homeostasis is linked to aging. Endogenous and exogenous insults to the cell leads to impaired protein folding during protein synthesis. The detection of unfolded proteins is usually met either with refolding by heat-shock proteins or targeted degradation through ubiquitin-mediated proteasomal or lysosomal pathways. Cells that fail to clear unfolded proteins accumulate unfolded protein aggregates, with resultant proteotoxicity (Powers, Morimoto, Dillin, Kelly, & Balch, 2009).

Deregulated Nutrient Sensing:

The IGF-1 pathway has been famously linked to aging through the identification of *C. elegans* longevity mutants, and is one of the most conserved age-controlling pathway between multiple species (Klass, 1983). Inhibition of IGF-1 signaling through caloric restriction upregulates FoXO1, a tumor suppressor gene that mediates the observed longevity effects (Yamaza et al., 2010). mTOR kinase downregulation also increases longevity and mimics the effects of caloric restriction (Johnson, Rabinovitch, & Kaeberlein, 2013). The contributions of these two pathways indicate that reduced anabolic activity mediates longevity.

Mitochondrial Dysfunction:

The free radical theory states that progressive aging results in the production of reactive oxygen species (ROS) which leads to mitochondrial damage and global cellular stress (Harman, 1965). Reduced mitochondrial biogenesis can occur as a result of telomere attrition or p53 signaling but also occurs during physiologic aging (Bernardes de

Jesus et al., 2012). Furthermore, the SIRT genes discussed above also modulate mitochondrial biogenesis and can control the rate of ROS production by regulating the antioxidant enzyme manganese superoxide (Qiu, Brown, Hirschey, Verdin, & Chen, 2010). Furthermore, the accumulation of mtDNA damage, the oxidation of mitochondrial proteins or the destabilization of the electron transport change may all result in a decrease in the proportion of healthy mitochondria and in turn contribute to cellular aging (K. Wang & Klionsky, 2011).

Cellular Senescence:

Cellular senescence is the stable arrest of the cell cycle that is coupled with phenotypic changes (Campisi, 2013). Senescence was first described by Hayflick while culturing human fibroblasts, who noticed the inability of cells to progress past a certain number of passages, termed the Hayflick number (Hayflick & Moorhead, 1961). Senescence Associated β-Galactosidase is used to diagnose cellular senescence. Senescent cells have an altered secretome, referred to as the senescence associated secretory phenotype (SASP), which is a pro-inflammatory paracrine signaling pathway that contributes to cellular aging and senescence (Campisi, 2013).

The accumulation of DNA damage and cellular stress responses results in the induction of the $p16^{INK4a}$/Rb and $p19^{ARF}$/p53 pathways, which leads to cellular senescence and contributes to physiologic aging (Baker et al., 2011). It is argued that cellular senescence is a compensatory mechanism in response to the accumulation of damage, and that senescence increases as cells exhaust their replicative capacity (Varela et al., 2005).

Stem Cell Exhaustion:

The loss of regenerative potential is an obvious characteristic of physiologic aging. Functional attrition of stem cells from nearly every adult stem cell reservoir is exhibited as aging progresses (Lopez-Otin et al., 2013). The accumulation of cellular damage, telomere shortening and induction of cell cycle inhibitory proteins such as p16 or p53 contribute to the reduced self-renewal capacity of hematopoietic stem cells (HSCs) (Janzen et al., 2006; Rossi et al., 2007). Stem cell exhaustion is likely the integrative consequence of many age-related insults and is likely the definitive cellular defect that underlies tissue and organismal aging.

Altered Intercellular Communication:

Alterations in intercellular communication modulate aging at a level beyond the individual cell. Pro-inflammatory intercellular communication arises from inflammatory tissue damage, chronic pathogen infection, dysfunctional immune signaling and the activation of SASP, and age-associated inflammation reinforces the aging program (Lopez-Otin et al., 2013; Salminen, Kaarniranta, & Kauppinen, 2012). The activation of SASP causes a bystander effect in which senescent cells induce senescence in neighboring cells through gap-junction mediating signaling, for example (Nelson et al., 2012).

Conclusions:

The nine hallmarks of aging are divided into three subcategories: primary, antagonistic and integrative. Primary hallmarks are unequivocally deleterious to the cell, as is the case for DNA damage, telomere attrition, epigenetic alterations and defective proteostasis. Conversely, antagonistic hallmarks are dependent on intensity: at low levels they may be benign, but at high levels they impart damage to the cell. Examples of

antagonistic hallmarks include senescence, ROS accumulation and elevated nutrient sensing and metabolism. Lastly, integrative hallmarks such as stem cell exhaustion and altered intercellular communication integrate some of the primary or antagonistic hallmarks and in turn affect cellular and tissue homeostasis. Primary hallmarks are thought to be the initiating hallmarks, which in turn lead to the antagonistic hallmarks, eventually culminating in the integrative hallmarks that give rise to organismal aging (Lopez-Otin et al., 2013). The hallmarks of aging are summarized in Figure 1-6.

Figure 1-6

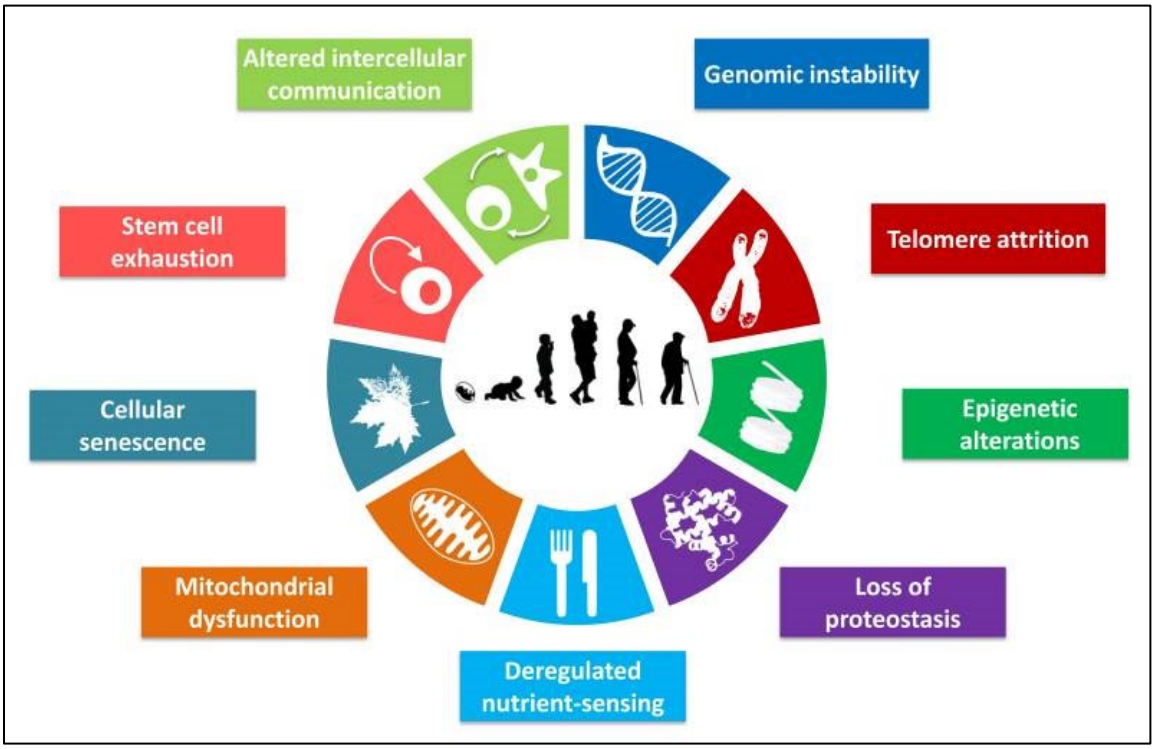

Figure 1-6. The Hallmarks of Aging. Taken from (Lopez-Otin et al., 2013). The nine hallmarks of aging include: Genomic instability, telomere attrition, epigenetic alterations, loss of proteostasis, deregulated nutrient-sensing, mitochondrial dysfunction, cellular senescence, stem cell exhaustion and altered intercellular communication.

The Aging Nucleus & Nuclear Envelopathies and Premature Aging Syndromes

They study of premature aging syndromes have been instrumental in elucidating the molecular mechanisms behind physiologic aging. Moreover, the examination of cellular aging is impossible without addressing the inextricable relationship between cellular aging and nuclear structure and integrity.

Hutchinson Guilford Progeria Syndrome (HGPS)

The organization within the nucleus non-stochastic, and highly regulated into functional neighborhoods of chromatin, subcompartments such as the nucleolus, and the nuclear lamina. As described previously, the nuclear lamina is thought to act as the shield that protects the genome from mechanical stress and as a regulator of chromatin organization and gene expression. In 2003, the Collins and Levy labs identified mutations in LMNA as the genetic cause for a premature aging syndrome termed Hutchinson-Gilford progeria syndrome (HGPS) (Annachiara De Sandre-Giovannoli et al., 2003; Eriksson et al., 2003). HGPS patients undergo normal embryonic development and appear normal at birth and during infancy; however during childhood they begin to exhibit severe degenerative symptoms such as failure to thrive, lipoatrophy, skeletal defects, osteolysis, and alopecia. HGPS patients also suffer cardiovascular defects that lead to heart attack and stroke, the ultimate cause of their extremely short lifespan. HGPS arises from the Mendelian inheritance of a spontaneous C$\rightarrow$T transition at position1824 of the LMNA gene. Replacement of a single base produces a silent mutation which does not alter the amino acid sequence (G608G). However, the mutation reveals a cryptic splice site within LMNA; utilization of this splice site leads to an internal deletion of 50aa within the protein. This deletion spans the Zmptse24 cleavage site. The resultant protein, termed Progerin, therefore contains a 50 aa deletion and is permanently farnesylated at its C-terminus.

HGPS is inherited as a heterozygous trait; Progerin exerts a dominant, negative effect even in the presence of WT Lamin A (A. De Sandre-Giovannoli et al., 2003). Cells derived from HGPS patients display irregular nuclear morphology, designating HGPS as a laminopathy (Eriksson et al., 2003).

The expression of Progerin render cells more susceptible to damage by physical stress because WT cells respond are thought to respond to mechanical stress by redistributing Lamin A (Zhang et al., 2011). Progerin is found exclusively at the periphery of the nucleus, unlike Lamin A. Moreover, HGPS nuclei exhibit a loss of LAD-associated heterochromatin, a loss of overall repressive histone modifications and changes at the level of chromatin-modifying complexes such as NuRD (Scaffidi & Misteli, 2005; Vidak & Foisner, 2016). Progerin expression also affects genome stability by negatively affecting DNA damage repair pathways. HGPS cells exhibit the accumulation of double strand breaks as a result of impaired recruitment of DNA repair machinery such as 53BP1 and Rad50/51. The accumulation and persistence of DNA damage leads to the induction of p53 and promotes senescence (Brachner & Foisner, 2014).

HGPS preferentially targets tissue of mesenchymal origin, and evidence from the literature indicates that the regulation and function of mesenchymal stem cells (MSCs) are affected by Progerin expression (Gotzmann & Foisner, 2006). Low levels of Progerin are observed during normal cellular aging, however, MSCs derived from HGPS patients accumulate significant amounts of Progerin with passaging *in vitro,* and their self-renewal and differentiation capacity are impaired (Wenzel et al., 2012).

Therapeutic treatment of HGPS was initially focused on repairing the mutant protein with farnesyltransferase inhibitors, which improved some disease parameters such as weight gain and bone structure (Cau et al., 2014; Gordon et al., 2012). Other

approaches have included treatment with Rapamycin, an inhibitor of mTOR, which relieves lobulated nuclei and clears DNA damage (Cao et al., 2011), Sulforaphane, an antioxidant which enhances protein clearing and reverses some of the hallmarks of HGPS (Gabriel, Roedl, Gordon, & Djabali, 2015), and Retinoids which showed promise by decreasing Progerin levels (Kubben, Brimacombe, Donegan, Li, & Misteli, 2016).

Nestor Guillermo Progeria Syndrome (NGPS)

The homozygous inheritance of a single amino acid substitution from Alanine12 to Threonine in BAF was identified as the cause of a novel progeria disease known as Nestor-Guillermo Progeria Syndrome (NGPS) (R. Cabanillas et al., 2011). NGPS patients share clinical features similar to those exhibited by HPGS patients, but lack cardiovascular disease (R. Cabanillas et al., 2011). The clinical manifestations of NGPS do not begin until approximately two years of age, when patients exhibit skin atrophy, general lipoatrophy and severe osteoporosis with marked osteolysis (Puente et al., 2011). Craniofacial abnormalities result from the atrophy of the facial subcutaneous fat and osteolysis of the maxilla and mandible and incomplete closure of the cranial sutures. Diverging from HGPS, NGPS patients retain eyebrows and eyelashes and, importantly do not exhibit cardiac dysfunction, ischemia, atherosclerosis or metabolic syndromes (R. Cabanillas et al., 2011; H. G. Fisher, N. Patni, & A. E. Scheuerle, 2020; Puente et al., 2011). The index patient suffered of severe secondary pulmonary hypertension and subsequent heart failure as a result of severe scoliosis (R. Cabanillas et al., 2011). Fibroblasts from NGPS patients exhibit aberrant nuclear morphology which can was rescued by exogenous expression of wild type BAF (R. Cabanillas et al., 2011; N. Paquet et al., 2014). A third NGPS patient was recently identified in the US (Heather G. Fisher, Nivedita Patni, & Angela E. Scheuerle, 2020)The literature has suggested that the A12T mutation in BAF does not

affect interactions with LEM-D proteins or histone H3 (N. Paquet et al., 2014). Interestingly, alanine12 is in close proximity to the BAF residues which have been previously shown to affect in vitro chromatin condensation and histone binding (De Oca et al., 2005), suggesting the possibility that A12T-expressing cells might exhibit defects in chromatin condensation and histone binding, which could have negative consequence for gene expression and eventual cellular dysfunction.

The ternary complex of BAF, a LEM-D domain and the IgF of Lamin A has shed significant light the implications of the BAF A12T mutation. This report was the first to demonstrate a direct interaction between BAF and the IgF of Lamin A and showed that alanine12 is buried within the BAF: Lamin A interface. Moreover, this interface not only contains alanine12, but contains several residues on the BAF-binding IgF surface of Lamin A that are mutated in atypical progeria syndromes (Samson et al., 2018) (Figure 4-7 A).

Figure 1-7

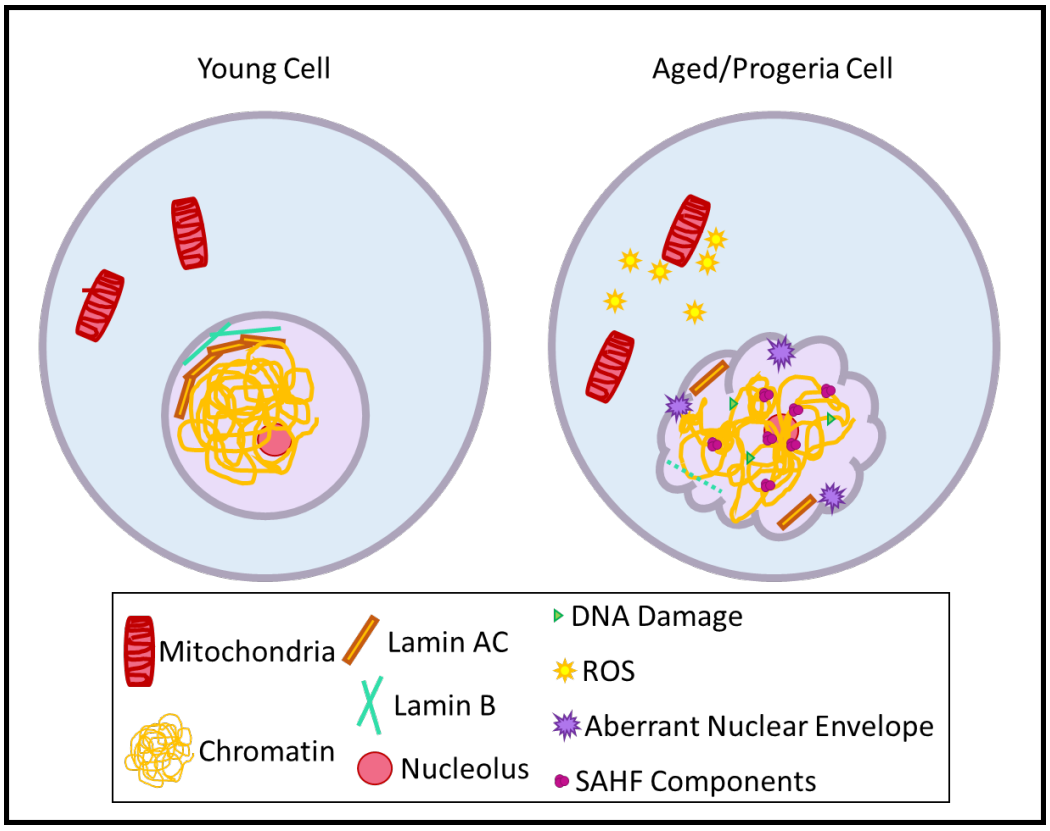

Figure 1-7. The Structure of the Nucleus and Aging. Cells that have undergone physiologic aging or pathologic aging through the expression of progeria-associated mutant proteins both undergo structural changes at the level of the nuclear envelope. The integrity of the nuclear lamina is lost over time and nuclei develop dysmorphic nuclear envelopes. Furthermore, these changes are met with the accumulation of DNA damage, overall changes in the compaction of chromatin (including the formation of SAHF), and the accumulation of stress responses like ROS accumulation and p53 signaling.

Biochemical Characterization of BAF A12T

Dr. Aye Mon of the Traktman lab performed in depth biochemical comparison of WT BAF and A12T BAF. To begin with, she established a model system in MCF10a cells by expressing shRNA resistant 3XF-BAF or 3XF-A12T (discussed in Chapter 3) and then depleting endogenous BAF. This approach established a close-to homozygous expression system. In so doing, she observed that 3XF-A12T expressing cells exhibited aberrant nuclear morphology, an observation that was also reproduced in this study. She determined that 83% of 3XF-BAFexpressing cells exhibited normal nuclear morphology whereas only 53% of 3XF-A12T-BAF-expressing cells had normal nuclear envelopes (data not shown).

The first published study of the biochemical properties of A12T BAF noted that cells derived from NGPS patients had lower steady state levels of BAF as analyzed by immunoblot analysis (Puente et al., 2011). Based on this finding, the authors posited that the stability of A12T was diminished and that this contributed to the molecular mechanism behind the disease state. Using the model described above, Dr. Mon metabolically labeled cells with ^{35}S-methionine and performed pulse chase experiments to analyze the half-life of the protein. BAF is an extremely stable protein with a half-life of 35h; importantly, the introduction of A12T did not alter the half-life (Fig 1-9 A).

The functional unit of BAF is a homodimer, through which it is able to associate with its binding partners. The next question that was asked was whether A12T is able to dimerize to the same efficiency of WT BAF. Recombinant BAF was purified and its dimerization state analyzed using a size exclusion column: BAF dimers elute at approximately 20 kDA, whereas monomers eluate at approximate 10 kDA. Analysis of the

gel filtration fractions that corresponded to these molecular masses indicated that the A12T mutation does not affect dimerization (Fig 1-9-B).

BAF is rapidly and efficiently phosphorylated by VRK1 at Serine 4 and more slowly at Threonine 2& 3 (R. J. Nichols, M. S. Wiebe, & P. Traktman, 2006). In vitro kinase assays performed with recombinant WT or A12 BAF and purified VRK1 indicated that A12T does not prevent the phosphorylation of BAF. In fact, A12T BAF appeared to be phosphorylated more rapidly than WT BA (Fig 1-9-C). This result was intriguing, and led us to question of whether threonine12 generated a novel phosphorylation site. To address this question, T2, T3 and S4 were mutated to Alanine to generate a BAF phospho-null mutant or a BAF A12T phospho-null mutant (R.J. Nichols et al., 2006). In vitro kinase assays indicated that neither of these mutants were phosphorylated by VRK1, thereby showing that the introduction of threonine as a result of the A12T mutation did not result in a novel phosphorylation site. It is possible that the A12T mutation leads to a slight alteration in the folding of the BAF protein that makes ser4 more accessible to VRK1.

The BAF homodimer binds dsDNA on either side with high affinity, and cross bridges DNA into higher order structures. Paquet et al. found that A12T bound to dsDNA with a lower affinity than WT BAF (Nicolas Paquet et al., 2014), as assessed by electrophoretic mobility shift assays (EMSAs). Dr. Mon performed similar assays using ^{32}P-radiolabeled dsDNA oligonucleotide probes and purified recombinant WT or A12T BAF dimers. In these experiments, BAF and A12T had comparable DNA binding activity *in vitro* (Fig 1-9 D). Interestingly, a very recent 2021 paper (Marcelot et al., 2021) assessed DNA binding in another manner, and their work demonstrated that the dsDNA binding activity of WT and A12T BAF are indistinguishable.

Cumulatively, these data indicate that the previously known biochemical functions of BAF were unperturbed by the introduction of the A12T mutation. Therefore, this study aimed to elucidate the molecular impact of the A12T mutation on BAF function in the context of the nuclear envelope, and the overarching effects that these effects would have at the level of the cell and the organism.

Figure 1-8

A

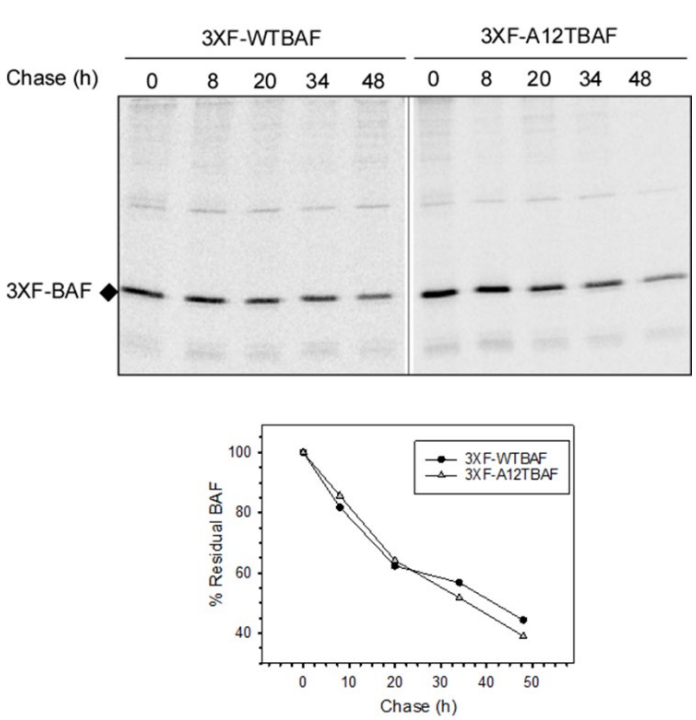
3XF-WTBAF
3XF-A12TBAF
Chase (h)
0 8 20 34 48 0 8 20 34 48
3XF-BAF
3XF-WTBAF
3XF-A12TBAF
% Residual BAF
Chase (h)

B

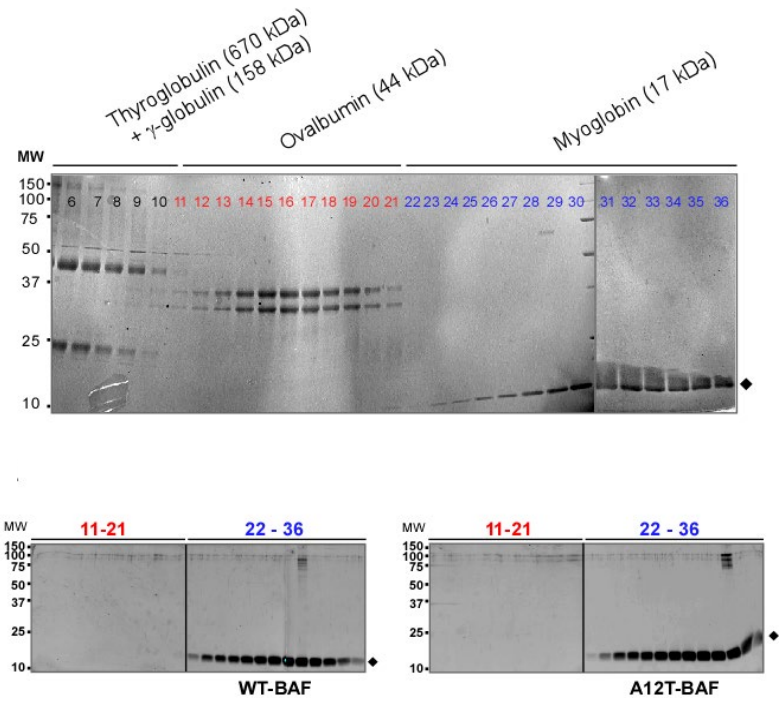
Thyroglobulin (670 kDa)
+ γ-globulin (158 kDa)
Ovalbumin (44 kDa)
Myoglobin (17 kDa)
MW
150
100
75
50
37
25
10
6 7 8 9 10 11 12 13 14 15 16 17 18 19 20 21 22 23 24 25 26 27 28 29 30 31 32 33 34 35 36
MW
11-21
22 - 36
WT-BAF
MW
11-21
22 - 36
A12T-BAF

C

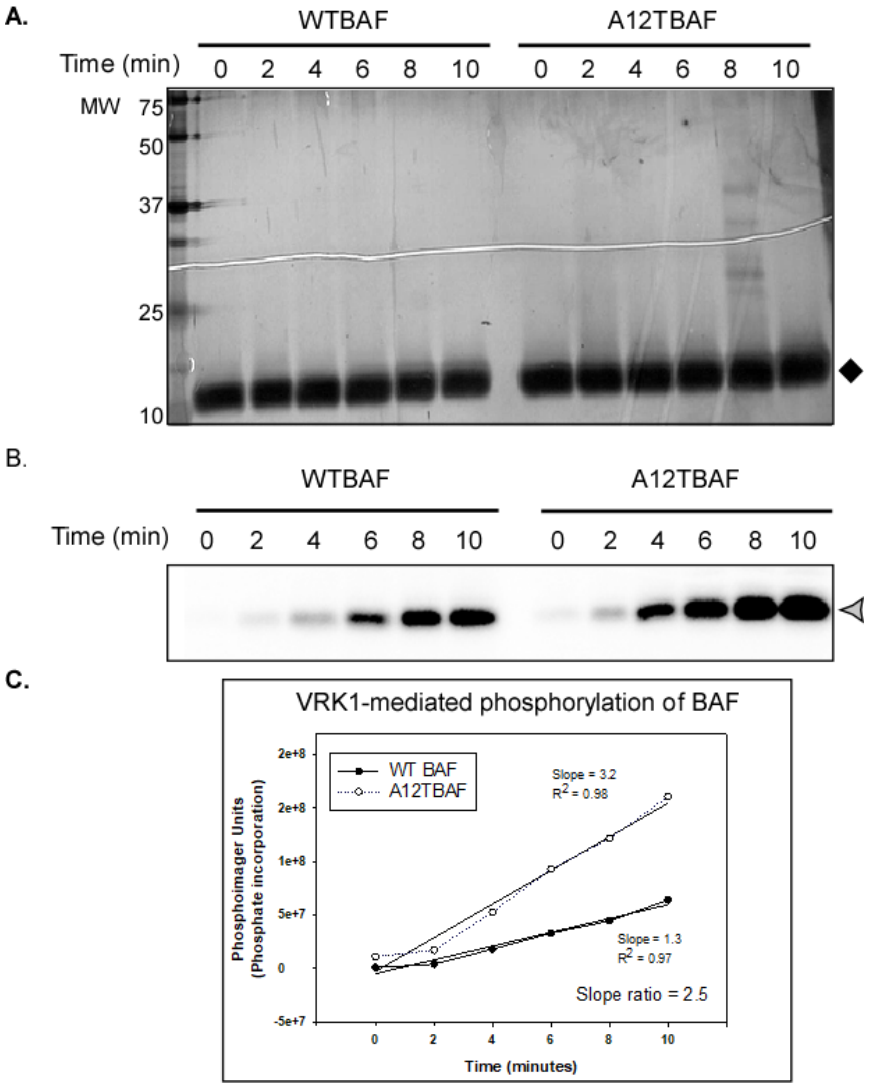
A.
WTBAF
A12TBAF
Time (min)
0 2 4 6 8 10 0 2 4 6 8 10
MW
75
50
37
25
10
B.
WTBAF
A12TBAF
Time (min)
0 2 4 6 8 10 0 2 4 6 8 10
C.
VRK1-mediated phosphorylation of BAF
WT BAF
A12TBAF
Slope = 3.2
R2 = 0.98
Slope = 1.3
R2 = 0.97
Slope ratio = 2.5
Phosphoimager Units
(Phosphate incorporation)
2e+8
2e+8
1e+8
5e+7
0
-5e+7
0 2 4 6 8 10
Time (minutes)

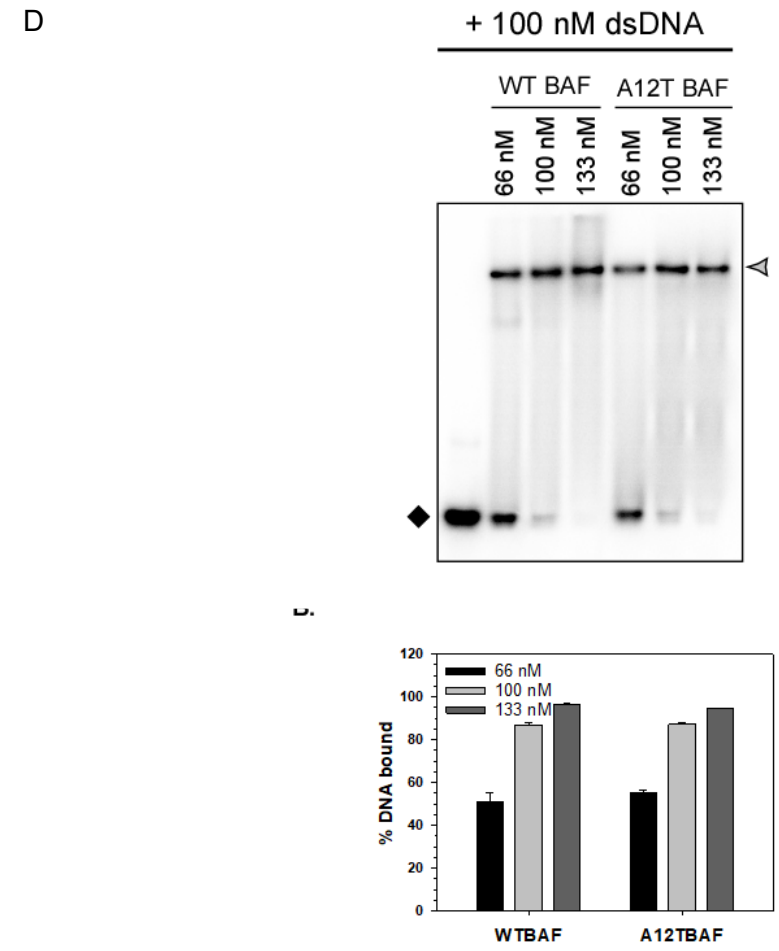

Figure 1-9. The Biochemical Characterization of BAF A12T. Aye Mon 2018-Unpublished. (A) Assessment of the stability of WT and BAF A12T. (Top) MCF10a cells that stably express 3XF-WTBAF and 3XF-A12TBAF were pulsed with ^{35}S-met containing DMEM medium for 2 h. Cells were washed and chased with DMEM complete media for 8 to 48 h. The 3XF-BAF proteins (WT and A12T) were retrieved by immunoprecipitation and analyzed by SDS-PAGE \ and phosphorimager analysis. Black diamond indicates the residual BAF protein during the chase. Bottom: Data were plotted; the half-lives of the two proteins were indistinguishable (n = 3). (B) Dimerization of BAF is not perturbed by the A12T mutation. The elution profile of gel filtration standards is shown. Lanes 6 -10 correspond to the protein standards of thyroglobulin and bovine γ-globulin with the

molecular weights of 670 kDa and 158 kDa respectively; Lanes 11 – 21 correspond to the ovalbumin protein standard with the molecular weight of 44 kDa; Lanes 22 – 36 correspond to the myoglobin protein standard with the molecular weight of 17 kDa. Black diamond indicates the myoglobin with 17 kDa (bottom left and right) Size exclusion chromatography of WT BAF dimers (bottom left) and A12T BAF dimers (bottom right). Black diamonds indicate WTBAF and A12TBAF dimers. WTBAF and A12TBAF dimers have the molecular weight of approximately 20 kDa, and were resolved from the size exclusion column in the same fractions as the myoglobin standard (17 kDa). (C) VRK1 phosphorylates BAF A12T at least as well as WT BAF, and threonine 12 is not a new site of phosphorylation. VRK1 kinase (10 nM) was incubated with WT or A12T BAF dimers (1.5 μM) in the presence of [γ-32P] ATP for 0-10 min at room temperature. Reaction products were resolved by SDS-PAGE and analyzed by silver staining (top) and autoradiography (middle panel). In top panel, black diamond indicates the equal input of BAF dimeric protein. On autoradiography, gray triangle indicates the phosphorylated BAF proteins. Bottom panel: phosphorylated products were quantified and plotted; linear regression analysis was performed to determine the slopes of WTBAF and A12TBAF. The slope ratio $\frac{A12TBAF\ slope}{WTBAF\ slope}$ indicates the difference in the rate of phosphorylation of WTBAF and A12TBAF by VRK1. (n = 3) (D) BAF A12T and WT BAF exhibit comparable DNA binding. Top: EMSA was performed using 100 nM of a 21-mer dsDNA probe and purified recombinant WT and A12T BAF dimers at 66 nM, 100 nM, and 133 nM. Reaction products were resolved on 4-10% acrylamide gel; a representative gel is shown. Black diamond represents the free dsDNA probes, and gray triangle indicates dsDNA bound to BAF. Quantitation of BAF binding to dsDNA. Calculation was performed using the formula $(\frac{bound}{bound+free} \times 100)$, in which bound means dsDNA + BAF, and free means dsDNA.

Chapter 2: Materials and Methods

Cell Culture Methods

All cells were cultured at 37°C in the presence of 5% CO2.

Harvest and Culture of Primary Mouse Dermal Fibroblasts

48-well dishes for culture were prepared by coating with 0.1% Gelatin solution (Life Technologies #S006100) and incubating for 30-60min at room temperature. After incubation, the remaining gelatin was aspirated and replaced with 250uL of warm mPEF medium described in Table 2-1. Plates were left in the incubator while explants were harvested in the mouse facility. In order to harvest ear punches, each mouse was restrained in one hand and was placed inside the tissue culture hood. The ears, head and face were sterilized using 70% ethanol. After the ear was sufficiently dry from the ethanol, an ear puncher was used to generate a 1mm circular punch. Each individual punch was placed in 500uL of ice cold mPEF medium on ice. Instruments were heat sterilized and appropriately cooled between each mouse. After the harvesting was complete, the ear punches were brought back to the tissue culture room on ice. The collection medium was carefully aspirated and each punch was placed forcefully using sharp, sterile, forceps on the gelatin at the bottom of the well, ensuring that the forceps were heat sterilized and appropriately cooled between each ear punch

The 48-well dish was placed in the incubator and monitored daily. 100uL of fresh media was added to each well every three to four days to compensate for evaporation. After approximately two weeks, the volume of media was increased to 500uL/well and the medium was carefully changed every three to four days without disturbing the ear punch.

Once fibroblasts were confluent in each well, they were detached using 0.05% Trypsin Ethylenediaminetatracetic acid (EDTA) (Life Technologies #15400054). They were passaged at a 1:2 ratio until cells were comfortably doubling every 24-48 hours. The subsequent passaging dishes did not need to be coated with gelatin. Once at least $5x10^7$ cells were obtained, at least three vials were frozen in 10% Dimethylsulfoxside (DMSO) with complete medium at a density of $1x10^6$ cells/vial. Fibroblasts were kept relatively confluent and passaged at a ratio of 1:3 to 1:5.

Stem Cell Culture

Culture of Induced Pluripotent Stem Cells

Induced pluripotent stem cells were cultured on human embryonic stem cell (hESC) qualified Matrigel (Corning #8774552). Culture dishes are prepared by diluting the Matrigel in DMEM/F12 (Life Technologies #1330057) at the appropriate ratio specified by the manufacturer based on lot number. Dishes were then left to incubate one hour at room temperature and stored for up to one week at 4°C. Coated dishes were then warmed for one hour at 37°C before use. iPSCs were subcultured at a ratio of no less than 1:5 and the medium was changed daily (see Table 2-1). iPSCs were subcultured by aspirating media, washing twice with PBS, and adding Versene (Life Technologies #15040066), formulated with 0.48mM EDTA in PBS, in order to gently lift the iPSCs in the absence of proteases. Cells were then allowed to gently lift for 2-3 minutes at room temperature, the Versene was aspirated and fresh media was added to the culture dish. Cells were gently scraped in the fresh media using a cell scraper and, without dissociating the intact colonies, transferred to a new Matrigel coated dish containing fresh medium.

Differentiation and Culture of Induced Pluripotent Stem Cells to Induced Mesenchymal Stem Cells

In order to differentiate iPSCs into induced mesenchymal stem cells (iMSCs), iPSCs were plated on Matrigel coated dishes at a confluence of approximately 25%. Cells were cultured in iPSC media for three to five days before switching the media to iMSC media (see Table 2-1). Media was changed every three days for a total of 21 days. After the 21st day, cells were passaged on to dishes coated with 0.1% gelatin (Attachment Factor, Life Technologies #S006100) using 0.25% Trypsin EDTA (Life Technologies #15400054), a concentration five-fold higher than generally used in cell subculturing. The cells were subcultured at a ratio of 1:4 on gelatin for a total of three passages, each passage using 0.25% Trypsin to lift the cells. On the fourth passage after gelatin, cells were plated on uncoated tissue culture dishes, deemed passage zero. Subsequent passaging of the cells occurred using 0.025% Trypsin EDTA and cells were always subcultured at a ratio of 1:4. The success of this protocol is measured by the ability of the cells to continue to proliferate on uncoated culture dishes.

Differentiation of Induced Mesenchymal Stem Cells to Lineage Cells

In order to determine whether the iMSCs are functional, they must be differentiated into lineage cells such as osteoblasts and pre-adipocytes. To do this, iMSCs were plated in 24-well dishes at a density of $1x10^4$ cells/cm^2. Cells are cultured for three days in MSC media, and then switched to either StemPro Osteogenesis Differentiation Medium (Life Technologies #A1007201) or StemPro Adipogenesis Differentiation Medium (Life Technologies #A1007001). The medium was changed every three days for a total of 28 days. Every seven days, cells were assessed for lineage staining: Alizarin Red (abcam

#146374) for osteoblasts, and Oil Red O (Simga Aldrich #O0625) for pre-adipocytes (protocol outlined below). Pre-adipocytes and osteoblasts were not subcultured.

Table 2-1 Table of Cell Culture Media

Cell Line	Cell Line Description	Base Media	Supplements	Source
mPEF	Primary Mouse Dermal Fibroblast	DMEM (Sigma Aldrich #D5796) containing 4,500 mg/L glucose, 4mM L-Glutamine and $NaHCO_3$ (no Sodium Pyruvate, no HEPES)	20% Fetal Bovine Serum	Derived from mouse ears in house
h-iPSC	Human Induced Pluripotent Stem Cells	mTesR1 defined medium containing zbFGF	Zebrafish derived	Bought from Applied Stem Cell
iMSC	Induced Mesenchymal Stem Cells	DMEM containing (Sigma Aldrich #D5546) containing 1,000 mg/L glucose, $NaHCO_3$, and sodium pyruvate (no L-Glutamine)	10% Fetal Bovine Serum, 2mM L-Glutamine (added fresh).	Differentiated in house from iPSCs
hASC	Human Adipose Derived Mesenchymal Stem Cells	DMEM containing (Sigma Aldrich #D5546) containing 1,000 mg/L glucose, $NaHCO_3$, and sodium pyruvate (no L-Glutamine)	10% Fetal Bovine Serum, 2mM L-Glutamine (added fresh).	Bought from LaCell
Hek293T	Human Embryonic Kidney Cells Expressing T-Antigen	DMEM (Sigma Aldrich #D5796) containing 4,500 mg/L glucose, 4mM L-Glutamine and $NaHCO_3$ (no Sodium Pyruvate, no HEPES)	10% Fetal Bovine Serum	Bought from American Type Culture Collection (ATCC)
MCF-10a	Human Mammary Epithelial Cells	DMEM-F:12 (Life Technologies # 11330057) containing 2.5mM L-Glutamine and 15mM HEPES	5% Horse Serum, 500ng/mL hydrocortisone, 100ng/mL Cholera Toxin, 10ug/mL human insulin and 20ng/mL epidermal growth factor (EGF)	Bought from ATCC

Established Cell Lines

Previously established cell lines were cultured in media according to Table 2-1. Cells that were genetically manipulated to generate stable cell lines were cultured in the presence of antibiotic selection that corresponded to the gene of interest, see Table 2-2.

Molecular Biology Methods

Generation of lentiviral particles for transduction of shRNA

A variant of the pHAGE lentiviral from containing a multiple cloning site (MCS) was used to generate replication-deficient viral particles for stable transduction of cDNA. pHAGE-PURO^{R}-MCS (pPM), as described in Molitor & Traktman 2014 (T. P. Molitor & Traktman, 2014). pPM was used to generate replication deficient lentivirus for shRNA mediated depletion of target proteins were generated by transfecting HEK293T cells with 2ug of helper plasmids pRRE and pRSV-REV, 4ug of pVSVG and 12ug of the target shRNA plasmid of interest using Lipofectamine 2000 transfection reagent (Life Technologies #11668019). 24h after transfection, the medium was replaced with a lentiviral harvest media containing: DMEM (Sigma Aldrich #5546), 10% Fetal Bovine Serum (FBS), 0.5% bovine serum albumin (BSA), 10mM HEPES (4-(2-hydroxyethyl)-1-piperazineethanesulfonic acid) and 2.5mM sodium butyrate. Following a 24h incubation in harvest medium, the supernatant containing lentiviral particles was filtered using a 45um filter and then treated with 8ug/mL of polybrene. Target cells were transduced with 1mL of viral particles for 8-10h at 37°C, then media was replaced with the appropriate standard media. After approximately 48h, cells were placed under selection appropriate to the transfer plasmid at a concentration of 7.5ug/mL. Assays performed on these cell lines were performed after selection and within 30 days post infection.

Table 2-2 Table of Generated Cell Lines

Cell Line	Expression Outcome	Expression System	Genomic Insertion	Promoter	Antibiotic Selection
MCF-10a pHM	Empty Vector	Lentiviral Transduction	Multiple Random	CMV	Hygromycin
MCF-10a 3XF-VRK1	3XF-VRK1	Lentiviral Transduction	Multiple Random	CMV	Hygromycin
MCF-10a 3XF-VRK1 D177A	3XF-VRK1 D177A	Lentiviral Transduction	Multiple Random	CMV	Hygromycin
MCF-10a Scrm	Scramble Control	Lentiviral Transduction	Multiple Random	Pol II	Puromycin
MCF-10a shVRK1 (L1)	Silenced VRK1	Lentiviral Transduction	Multiple Random	Pol II	Puromycin
MCF-10a shVRK1 (KK2)	Silenced VRK1	Lentiviral Transduction	Multiple Random	Pol II	Puromycin
MCF-10a WT BAF	3XF-BAF	Lentiviral Transduction	Multiple Random	CMV	Hygromycin
MCF-10a BAF A12T	3XF-BAF A12T	Lentiviral Transduction	Multiple Random	CMV	Hygromycin
MCF-10a BAF_shBAF	3XF-BAF (sh Resistant) _ Silenced endogenous BAF	Lentiviral Transduction	Multiple Random	CMV & Pol II	Hygromycin & Puromycin
MCF-10a A12T_shBAF	3XF-BAF A12T (sh Resistant) _ Silenced endogenous BAF	Lentiviral Transduction	Multiple Random	CMV & Pol II	Hygromycin & Puromycin
MCF-10a BAF_shBAF _ H2B GFP	3XF-BAF (sh Resistant) _ Silenced endogenous BAF_ GFP H2B histones	Lentiviral Transduction	Multiple Random	CMV & Pol II	Hygromycin, Puromycin & Zeocin
MCF-10a BAF A12T_shBAF _ H2B GFP	3XF-BAF A12T (sh Resistant) _ Silenced endogenous BAF_ GFP H2B histones	Lentiviral Transduction	Multiple Random	CMV & Pol II	Hygromycin, Puromycin & Zeocin

Generation of lentiviral particles for stable expression of transgenes

To generate lentiviral particles for expression of transgenes, 0.5ug of helper plasmids pREV, pGAG/Pol, and pTAT, 1ug of VSVG and 12ug of a hygromycin-resistance cassette, pHAGE-HYG^{R}-MCS (pHM) (T. P. Molitor & Traktman, 2014) containing the target gene of interest was used to transfect HEK293T cells at approximately 70% confluence. The harvest of viral particles was performed as described above. Stable cell lines were placed under selection using hygromycin at a concentration of 50ug/mL.

Transient Transfection

Cells were subjected to transient transfection using Lipofectamine 2000 (Life Technologies #11668019) according to the manufacturer's instructions. Plasmids that were introduced to cells using transient transfection can be found in Table x.

Biochemical Methods

Purification of pGEX-Lamin A proteins

pGEX-Lamin A Ig fold constructs were generously gifted to us by the Zinn Justin Lab (Institut de Biologie Intégrative de la Cellule, University of Paris) (Samson et al., 2018). BL21-DE3 cells expressing pGEX-Lamin A IG fold (WT, R453C or R527H) were grown to an OD_{550} of 0.5-0.7. in Luria-Bertani (LB) medium supplemented with 100ug/mL of ampicillin at 37°C. Cultures were induced by the addition of Isopropyl-b-D-1-thiogalactopyranoside (IPTG) to a final concentration of 1mM for three hours at 37°C. Cells were harvested by centrifugation at 4,000xg for 30 minutes. Cells were suspended in PBS containing: 1ug/mL Leupeptin, 1ug/mL Pepstatin and 0.2mM PMSF and subjected to sonication 15 times per sample. After sonication, Triton-X 100 was added to a final concentration of 1% and gently mixed and incubated on ice for 30 minutes. Lysates were then clarified by centrifugation at 10,000xg for 20 minutes at 4°C. The resulting

supernatant contained the soluble fraction of the pGEX-Lamin fusion proteins. *In Vitro* Lamin-A and BAF binding assays were performed on the crude soluble lysate achieved in this step.

Visualization of Proteins by Silver Staining of SDS-PAGE

In order to visualize and quantify protein content after induction or purification of recombinant proteins, silver staining was performed on SDS-PAGE resolved protein samples. BSA was serially diluted to 50ng, 100ng, 200ng, 400ng and 800ng, and utilized as a protein standard for comparison. The gels were dehydrated by soaking in methanol then incubated with 10uM DTT and stained with 0.1% (w/v) Silver Nitrate solution (Sigma Aldrich #209139). Gels were placed in developer solution containing 6% sodium carbonate (w/v) until protein bands were detectable. The developing reaction was quenched by the addition of citric acid. Cells were then fixed using a solution of 50% methanol and 10% acetic acid and then dried between two pieces of cellophane.

Co-Immunoprecipitation of GST-Lamin A with BAF

In order to assess the interaction of BAF with the Ig Fold of Lamin A, *in vitro* co-immunoprecipitation was performed. Crude GST-Lamin A (WT, R453C or R527H) lysates were incubated with Glutathione sepharose beads (GE Healthcare #52-2303-00 AK) for two hours at 4°C with end over end rotation in PBS containing the protease inhibitors described above. Samples were washed twice and then 2ug of purified BAF WT or BAF A12T were added to the samples. Samples were re-incubated for two hours at 4°C with end over end rotation. Samples were boiled in sample buffer containing: 1% SDS, 1% b-Mercaptoethanol, 50mM Tris (pH 6.8), 6.5% glycerol, and bromophenol blue. Eluate was subjected to SDS-PAGE alongside inputs, and samples were either subjected to silver

staining or transferred on to nitrocellulose membrane and subjected to immunoblot analysis to detect GST or BAF.

Cell Biology Methods

Growth curve assay and doubling time

Cells were detached from their dishes using 0.05% Trypsin EDTA and collected in an equal amount of complete medium, then spun at 673xg for 5 minutes at room temperature. The trypsin-containing media was then aspirated and the cells were flicked to dissociate the pellet and resuspended into a single cell suspension in 1-2mL of complete media. An aliquot of cells was taken and diluted 1:1 with 5% Trypan Blue. The number of live cells in each of the outer quadrants of a hematocytometer were counted and the average cell number per quadrant was taken. This number was multiplied by the dilution factor of Trypan blue and the number of cells per mL was determined. Equal densities of cells were plated in a 24-well plate in technical triplicate for each desired time point. Cells were then counted using the same method described above at each desired time point. The number of cells was plotted against the time elapsed, generating a growth curve. To assess the apparent doubling time, cells were plated at equal densities and counted 48h after plating. To determine the number of doublings, the equation $2^x=n_{final}/n_{initial}$, where *x* equals the number of doublings and n equals the number of cells. The apparent doubling time is then determined by h/x where h equals the number of hours after seeding and x is the number of doublings calculated in the previous formula.

MTT Assay and Cell Titer Glo Assay

In order to generate a growth curve based on the metabolic activity of cells, an MTT assay, a colorimetric assay based on the formation of insoluble formazan in viable cells, was used. Cells were plated at a density of 5×10^3 cells per well of a 96-well dish

and incubated for a desired period of time (usually 0, 24, 48, 72 and 96 hours). At each desired time point, tetrazolium dye MTT 3-(4,5-dimethylthiazol-2-yl)-2,5,diphenyltetrazolium bromide (MTT) was added to a final concentration of 250ug/mL per well, and incubation continued for three additional hours at 37°C. After three hours, the plate was removed and 100uL of Stop Solution containing 20% Sodium dodecyl sulfate (SDS) and 50% dimethylformamide (DMF) in dH2O was added to each well and the plate was rocked at room temperature for one hour. After one hour, the plate was read on a multi-well spectrophotometer at 570nm. The absorbance was plotted against the elapsed time to generate a growth curve.

An alternative method to assess cell viability is the use of Cell Titer Glo (Promega #G9241). Cell Titer Glo is a luminescent assay that measures ATP. The mono-oxygenation of luciferin by luciferase in the presence of Mg^{2+}, molecular oxygen and ATP, which is contributed by viable cells, results in a luminescent signal that is measured on a spectrophotometer. Cells were plated at a density of 5×10^3 cells per well of a black walled, clear bottom, 96-well dish and incubated for a desired period of time (usually 0, 24, 48, 72 and 96 hours). Cell Titer Glo reagent was added to each well and incubated for 10 minutes at room temperature. Luminescence was measured on a multi-well spectrophotometer and was plotted against the elapsed time to generate a growth curve.

Preparation of Cell Lysates and Immunoblotting

Medium was aspirated from dishes and cells were washed twice with ice cold 1xPBS, then lysed directly in the dish using “phospho-lysis buffer” (PLB) containing: 0.01M NaPO4 (pH7.4), 0.1M NaCl, 1% Triton X-100, 2% SDS and 0.5% Deoxycholate supplemented with protease and phosphatase inhibitors at a concentration of 1ug/mL of Pepstatin, 1ug/mL of Leupeptin, 1mM PMSF, 1mM NaF, 5nM Calyculin A and 25 U/mL of

Benzonase (Sigma Aldrich #E1014). Cells were scraped in the lysis buffer and transferred to 1.5mL tubes and incubated on ice for 30 minutes. Lysates were cleared by spinning at 600xg at 4°C for 15 minutes. The supernatant was collected into a fresh tube. Protein concentration was quantified using a Thermo Pierce BCA assay (#PI23227). 25-50ug of protein was resolved by SDS-PAGE at 1W/cm between electrodes and then transferred onto nitrocellulose membranes. Antibodies used in this study are described in Table 2-1. Immunoblots were developed using Super Signal West Pico Chemiluminescence Substrate (Thermo Pierce #PI34578) and developed on a FluorChem HD2 Imaging Platform from Protein Simple. To quantify signal, densitometry was performed using the protein simple quantification software (Alpha View).

Table 2-3- Table of Antibodies

Antibody	Manufacturer	Product Number	Host	Reactivity	IF -Dilution	WB - Dilution
53BP1 (H-300)	Santa Cruz Biotechnology	sc-22760	Rabbit	Human, Mouse	1:200	--
APO-B (LDL20/17)	MabTech	3715-3-250	Mouse	Human	--	1:500
ATR	Santa Cruz Biotechnology	sc-515173	Mouse	Human, Mouse	--	1:200
BAF (A-11)	Santa Cruz Biotechnology		Mouse	Human	--	1:1000
BAF	Abcam	ab129184	Rabbit	Human	1:200	1:1000
Calnexin	Enzo Life Sciences	ADI-SPA-860-F	Rabbit	Human, Mouse	--	1:1000
Chk-1	Santa Cruz Biotechnology	sc-8408	Mouse	Human, Mouse	--	1:1000
E-Cadherin	BD Biosciences	610181	Rabbit	Human, Mouse	1:250	1:500
Emerin (FL-254)	Santa Cruz Biotechnology	15378	Rabbit	Human, Mouse	1:100	1:1000
Fibrillarin	Novus Biologics	NB300-269	Mouse	Human, Mouse	1:50	1:500
Flag (M2)	Sigma Aldrich	F1804	Mouse	--	1:200	1:2000
GAPDH (EPR6256)	Abcam	ab128915	Rabbit	Human	--	1:1000
GFP (EPR14104)	Abcam	ab183734	Rabbit	--	1:200	1:1000
GST						
H2B						
H3K9me3	Abcam	ab8898	Rabbit	Human, Mouse	1:200	1:1000
HNF4a (H-1)	Santa Cruz Biotechnology	sc-374229	Mouse	Human, Mouse	--	1:500
Ku70			Mouse	Human, Mouse	--	1:200
Lamin A/C (2E8.2)	Millipore	7538	Mouse	Human, Mouse	1:200	1:1000

Antibody	Manufacturer	Product Number	Host	Reactivity	IF -Dilution	WB - Dilution
Lamin B1	Abcam	ab16048	Rabbit	Human, Mouse	1:200	1:1000
Nucleolin (D4C70)	Cell Signaling Technologies	14574S	Rabbit	Human, Mouse	1:100	1:1000
p53 (DO-1)	Santa Cruz Biotechnology	sc-126	Mouse	Human, Mouse	1:200	1:1000
p65 (D14E12)	Cell Signaling Technologies	8242S	Rabbit	Human, Mouse	1:100	1:1000
PARP (46D11)	Cell Signaling Technologies	9532S	Rabbit	Human, Mouse	--	1:1000
p-Chk1	Cell Signaling Technologies	2348S	Mouse	Human, Mouse	--	1:1000
p-p53 (Thr-18)	Santa Cruz Biotechnology	16716R	Rabbit	Human	--	1:1000
p-p65 (Ser-536)	Cell Signaling Technologies	3031S	Rabbit	Human, Mouse	--	1:1000
RPA			Mouse	Human, Mouse	--	1:1000
V5	Invitrogen	R960-25	Mouse	--	1:100	1:1000
Vimentin	Abcam	ab92547	Rabbit	Human, Mouse	1:200	1:1000
VRK1	Sigma Aldrich	HPA017929	Rabbit	Human, Mouse	--	1:1000
γH2AX (Ser-139)	Cell Signaling Technologies	2577S	Rabbit	Human, Mouse	--	1:1000
γH2AX	Millipore	05636	Mouse	Human	1:200	1:1000

Co-Immunoprecipitation of Flag-Tagged Proteins

Cells were harvested by lysing directly in the dish using “flag-lysis buffer” containing: 150mM NaCl, 25mM Tris pH 7.4, 50mM EDTA, 0.1% Triton X-100, 0.01% NP40 and 0.1% Tween. Protease and phosphatase inhibitors were supplemented in the lysis buffer at a concentration of 1ug/mL of Pepstatin, 1ug/mL of Leupeptin, 1mM PMSF, 1mM NaF, 5nM Calyculin A and 25 U/mL of Benzonase (Sigma Aldrich #E1014). Cells were incubated with magnetic Flag-conjugated beads (Sigma Aldrich #M8823) according to the manufacturer’s instructions. Lysates were incubated with beads for four hours at 4°C with end over end rotation. Elution was performed by boiling samples for 10 minutes in sample buffer containing: 1% SDS, 1% b-Mercaptoethanol, 50mM Tris (pH 6.8), 6.5% glycerol, and bromophenol blue. Eluant was subjected to SDS-PAGE alongside inputs, transferred on to nitrocellulose membrane and immunoblots against Flag and the protein of interest were performed according to the specifications in Table 2-3.

Immunofluorescence

Cells were plated at equal densities on either four- or eight-well chamber slides (NUNC Inc. #154526 or #154534 respectively) or 35mm (20mm imaging area) glass bottom culture dishes (Mattek Corporation #NC9650104) either in the presence or absence of a substrate coating of gelatin or Matrigel described above. If no substrate was present, a Poly L-Lysine (Simga Aldrich #P8920) layer was coated on the glass. Cells were treated as desired and then fixed for 15 minutes with 4% paraformaldehyde in PBS (Electron Microscopy Sciences #15710) in dH_2O on ice. Following PBS washes, cells were permeabilized with 0.2% Triton-X 100 for five minutes on ice or, using “Hetzer Buffer” containing: 0.1% Triton-X 100, 0.02% SDS and 10mg/mL of bovine serum albumin (BSA), for 30 minutes at room temperature. The latter was only used when nucleolar structures

were under investigation. Samples were then incubated for one hour at room temperature with antibodies in 3% BSA (w/v), (or Hetzer buffer when appropriate) at concentrations outlined in Table 2-3. Cells were then washed and incubated for one hour at room temperature with secondary antibodies conjugated to Alexa Fluor 488 or 596 (Life Technologies, 488: #A11034, 594: #A11037), or, when visualizing actin, phalloidin conjugated to rhodamine (Life Technologies #A12381) was used. DNA was visualized by staining with 4',6'-diamidino-2-phenylindole (DAPI). Cells were then imaged on a Nikon Eclipse Ti microscope.

Analysis of Nuclear Morphology

In order to define nuclear morphology, cells were analyzed by immunofluorescence as described above. Specifically, Lamin A/C was used to visualize the nuclear envelope and DAPI to visualize the nucleus. Based on previously published scoring methodologies (T. P. Molitor & Traktman, 2014) in each population of cells, the nuclear envelope morphology was ascribed a score from one to six. Normal nuclei= 1, invaginated= 2, highly invaginated= 3, pinched off= 4, blebbed= 5 and multi-nucleated= 6.

Live Imaging for Nuclear Rupture

Flow Cytometry to Assess Mesenchymal Stem Cell Surface Markers

Mesenchymal stem cell surface marker expression was assessed by flow cytometry using an MSC Phenotyping Kit (Miltenyi Biotec #130-125-285). Samples were fixed using 4% paraformaldehyde (Electron Microscopy Sciences #15710) at room temperature for 15 minutes. Cells were washed with PBS and then resuspended in "FACS Buffer" containing 0.5% BSA and 2mM EDTA in PBS, and the phenotyping cocktail provided by the kit. The phenotyping cocktail contains positive surface markers: anti-CD73 conjugated to allophycocyanin (APC), anti-CD105 conjugated to phycoerythrin (PE), anti-CD 90

conjugated to fluorescein isothiocyanate (FITC); and negative surface markers: anti-CD 34, anti- CD45, anti-CD20, anti- CD14 all conjugated to PerCP-Cy5.5. Cells were incubated with the phenotyping cocktail for 15 minutes at 4°C. Cells were analyzed on a BD Fortessa X-20 Analytical Flow Cytometer. 10,000 events for each sample were collected, and only live, individual cells were gated on. Samples were analyzed using the FACSDiva software (BD Biosciences).

Metabolic Labeling of Cells to Assess Protein Synthesis

Cells were plated at a density of $1.5x10^5$ cells in a 35mm culture dish. 48 hours later, cells were washed with methionine free media, and then labeled with 100uCi/mL of 35S-methionine (Perkin Elmer #NEG709A500UC) for 45 minutes. As a control, cells were pre-treated with cycloheximide for 20 minutes at a concentration of 50ug/mL. Cells were harvested by scraping in ice cold PBS and lysed in lysis buffer containing 1% SDS, 1% b-Mercaptoethanol, 50mM Tris (pH 6.8), 6.5% glycerol, bromophenol blue and 2.5U of Benzonase. Samples were incubated on ice for 30 minutes and then boiled for 5 minutes. 10% (for autoradiography) and 50% (for western blotting) of each sample was loaded and run on a 7%-17% SDS-PAGE. For autoradiography: the gel was fixed in a solution of 50% Methanol, 10% Acetic Acid and 40% dH2O, then dried between two sheets of cellophane. The dried gel was then exposed on a phosphor-screen overnight and exposed on a Typhoon for quantification. For western blotting: the gel was transferred overnight on to a nitrocellulose membrane at 4°C at 35V then subjected to western blotting.

Senescence Associated b-Galactosidase Staining

Senescence associated b-galactosidase was used in order to detect β-galactosidase activity at a pH of 6, a characteristic of senescent cells. This was done by examining the hydrolysis of 5-bromo-4-chloro-3-indolyl-b-d-galactopyranoside (BCIG or

X-gal) by β-galactosidase yielding an insoluble blue byproduct visible to the naked eye and by microscopy. A b-galactosidase staining kit from Cell Signaling Technology (Cell Signaling Technology # 9860) was used. Cells were plated on four-chamber microscopy slides (NUNC Inc. #154526) or 35mm (20mm imaging area) glass bottom petri dishes (Mattek Corporation #NC9650104). Growth media was removed from the dishes and cells were washed with PBS then fixed in situ using a proprietary fixative solution provided in the components of the kit. Next, cells were washed and then overlayed with a β-galactosidase staining solution containing proprietary buffers and 10mg/mL of X-gal. Cells were incubated at 37°C overnight and then imaged by phase microscopy. Quantification of β-Galactosidase staining was performed by generating a scoring mechanism where 0= absence of blue staining in the cell, 1= partial blue staining of the perinuclear area of the cell and 2= complete blue staining of the perinuclear area and cytoplasm of the cell. Senescence was reported as the number of cells falling into one of the three categories described above divided by the total number of cells per condition.

Detection of Reactive Oxygen Species

The accumulation of reactive oxygen species (ROS) generates an oxidative environment within the cell. 2',7'-Dichlorofluorescin diacetate (DCFDA), a non-fluorescent probe, is permeable across the plasma membrane. In the presence of oxidative conditions, DCFDA is de-esterified and becomes highly fluorescent and trapped within the cell. Cells were plated in 96-well tissue culture dishes. Cells were washed with serum free media prior to the addition of DCFDA (Sigma #D6883). A solution of 2.5uM of DCFDA in serum free media was added to the cells and incubated for 30 minutes at 37°C. Cells were then washed and then analyzed for fluorescence intensity at 488nm on a

spectrophotometric plate reader. As a positive control, cells were treated with 10uM hydrogen peroxide (H_2O_2) for 30 minutes prior to the addition of DCFDA.

Comet Assay

Cells were plated at an equal density in 60mm dishes and incubated for 48h. Cells were then treated with 50uM Etoposide for one hour. Samples were collected by scraping gently in 1mL PBS and then counted on a hematocytometer and diluted to $1x10^5$ cells/mL. Comet assays were performed according to the Comet Assay Kit from TREVIGEN (2350-050-K). Briefly, cells were combined with low-melt agarose and spread on a microscope slide by using the side of a pipet tip. Slides were then gently immersed in the provided lysis solution overnight in the dark. The next day slides were then aligned equidistant from electrodes and subjected to electrophoresis at a voltage of 1 volt/cm (between electrodes) at 4°C. The DNA was then ethanol precipitated *in situ,* then dried and stained with DAPI. Slides were imaged at 10X magnification and comet moment was quantified by measuring the vector length from the center of the comet head to the end of the comet tail.

Assessment of Lineage Differentiation Using Histologic Stains

In order to assess efficiency of lineage differentiation from mesenchymal stem cells to osteoblasts and pre-adipocytes histologic stains against a specific cell types were used. All samples were fixed in situ using 4% paraformaldehyde (Electron Microscopy Sciences #15710) for 15 minutes at room temperature. Samples were plated in duplicate in order to be stained with Crystal Violet as a positive stain for all cells, and to be used to calculate the percentage of cells that stain positive for the lineage specific markers. For osteoblasts, Alizarin Red (abcam #146374) was used at a concentration of 40mM. Pre-adipocytes were stained with Oil Red O (Simga Aldrich #O0625) at 0.5% in methanol. All samples were stained for 30 minutes at room temperature and then washed with dH_2O and imaged on a

light microscope. Following microscopy, samples were solubilized for quantitative analysis. Samples stained with Crystal Violet were solubilized with 100% methanol, samples stained with Alizarin Red were solubilized with 10% Cetylpyridinium chloride (CPC) and samples stained with Oil Red O were solubilized with 100% Isopropanol. Solubilized samples were then transferred to a clear-bottom 96-well dish in triplicate and read on a spectrophotometer at 590mm absorption for Crystal Violet, 570mm absorption for Oil Red O and 540mm absorption for Alizarin Red.

ATAC-Seq

ATAC-Seq is a method for mapping chromatin accessibility throughout the genome. ATAC-Seq employs the use of hyperactive transposases that insert adapter sequences into accessible areas of the genome; the presence of these integrated adapters can then be assessed by sequence analysis (Buenrostro, Wu, Chang, & Greenleaf, 2015). Cell pellets prepared from in duplicate for ATAC-Seq analysis at Active Motif. Three analyses were used to assess differences in the accessibility of chromatin in these cells. The preliminary analysis was performed by using a genome browser and manually identifying peaks that exhibited at least a two-fold difference between the samples. Secondly, we examined whether there were observable differences in chromatin accessibility specifically at any of the following regions: distal intergenic, intronic, exonic, 3'UTR, 5'UTR, or any promoters ranging from <1kb to 5kb. These analyses were performed on raw sequencing files. Following this, we filtered our reads and used Partek Flow Software to call peaks that specifically align at transcription start sites.

Electron microscopy.

Confluent 60mm dishes of confluent cells were washed with Sorensen's buffer containing: 133mM Na_2HPO_4, 133mM KH_2PO_4 pH7.2, and fixed in situ with 1%

glutaraldehyde in Sorensen's buffer for 30min at room temperature. Cells were collected by centrifugation at 800 x g for 7min and fresh fixative was added. Cells were then processed for conventional electron microscopy and embedded in Embed 810 resin (Electron Microscopy Sciences, Hatfield, PA). Thin sections were examined on a JEOL JEM-1010 microscope and images were taken using a Hamamatsu camera.

Mouse Methods

All animal procedures were performed in accordance with the protocols approved by the Medical University of South Carolina Institutional Animal Care and Use Committee (IACUC).

Generating BANF1 A12T/+ mice

To generate a BANF1 A12T/+ mice, Applied Stem Cell generated an allele which replaced a single codon in the second exon of the BANF1 gene. The codon encoding Alanine 12, GCA, was replaced using CRISPR/Cas9 technology, and the resultant codon, ACC, gave rise to a Threonine at position 12, thereby generating an A12T mutation in the BAF protein.

Applied Stem Cell generated a six-mouse colony comprising three heterozygous (A12T/+) females and three heterozygous males. Subsequent colony expansion was performed in-house.

Genotyping BANF1 A12T Mice

In the WT BANF1 allele, the codon for the 12th amino acid, alanine, is GCA. To generate the A12T amino acid substitution in our mice, the codon was changed from GCA to ACC. This codon substitution generates two *de novo* restriction enzyme sites. The BANF1 WT coding sequence contains two HPY 188III and one TSP 45I restriction enzyme sites whereas the mutant allele generates a novel HPY 188III and TSP 45I restriction

enzyme proximal to the mutation. We utilized the introduction of this unique restriction enzyme site in order to genotype the mice.

Tail clips were obtained from mice at weaning by restraining the mouse in one hand, introducing an ear tag, and using a fresh razor, cutting 1mm from the tip of the tail, caudal to the end of the tail vein. Tail clips were maintained in 1.5mL tubes on ice until all clips were complete.

Tail clips were subjected to an alkaline DNA extraction by incubating them in of Alkaline Lysis Buffer containing: 25mM NaOH and 0.25mM EDTA in dH_2O for 45 minutes at 100°C. Extracted DNA was subjected to polymerase chain reaction (PCR) to amplify exon two of the BANF1 coding sequence. Forward and reverse primers were designed against the flanking regions of Exon 2. Once PCR was complete, restriction enzyme digestion was performed on the PCR products. HPY 188III (NEB #R0622) and TSP 45I (NEB #R0583) were individually incubated with the amplified BANF1 Exon 2 PCR product for 2h according to the manufacturer's instructions. Undigested and digested DNA were electophoretically resolved using a 20% polyacrylamide gel cast in TBE at 250V. Bands were subsequently visualized by staining with SYBR Gold (Life Technologies #S11494). Genotypes were analyzed based on the banding patterns described in Figure 5-2.

X-Ray Imaging and Analysis of Mouse Skeleton

Mice were subjected to anesthesia using 20% Isoflurane by nose cone inhalation. Mice were then laid on their left lateral side inside the imaging chamber of a Faxitron LX-60 Cabinet X-Ray System. Mice were subjected to 40 kV of energy or 40 seconds and then x-rays were developed. Mice were revived from anesthesia spontaneously under a warming lamp. Skeletal measurements were taken based on anatomical landmarks. Measurements taken include: length of nasal bone, distance between nasomaxillary point

to superior incisor point, mandible length, menton to mandibular condyle, cranial length, occipital bone to coronal suture, coronal suture to tip of nasal bone, body length (from nose to anus), femur length, tibia length, humerus length, the height and width of the fifth lumbosacral vertebra, the distance between the top of the fourth lumbosacral vertebra to the bottom of the sixth lumbosacral vertebra, and the kyphosis index which is measured by taking the distance between the bottom of the sixth cervical vertebra to the bottom of the sixth lumbosacral vertebra (line AB) and the distance from the highest point in the curvature of the spine down to line AB, generating line CD. The ratio of line AB to line CD is deemed the kyphosis index. Figure x depicts the measurements made for each x-ray taken.

Full Body Mouse Necropsy and Histologic Analysis

In order to perform histopathologic studies on the mice, full body necropsies were performed by euthanizing mice using CO_2 inhalation followed by secondary cervical dislocation. All organs were harvested and maintained in 10% neutral buffered formalin (Sigma Aldrich #HT501128). Samples were then submitted to the Division of Laboratory Animal Resources, Veterinary Pathology Services at the Medical University of South Carolina. Briefly, samples were subjected to either Hematoxylin & Eosin staining or Masson's Trichrome staining in order visualize microscopic substructures.

Chapter 3: The Effect of BAF and BAF A12T Overexpression in Mammary Epithelial Cells

Introduction

As discussed extensively in Chapter 1, the nuclear envelope is a highly-organized structure which provides a barrier between the cytoplasm and the nucleus while still allowing for highly regulated communication between the two cellular compartments (Hetzer, 2010). BAF acts as a bridge between the nuclear lamina and chromatin and creates an interface between the two. In addition to regulating nuclear structure, BAF is involved in the disassembly and reassembly of the nuclear envelope in mitosis. It is also *thought* to play a unique role in gene expression in two ways: the first is through transcriptional regulation, and the second through epigenetic organization of chromatin. At the transcriptional level, BAF has been shown to associate with multiple transcription factors, pointing at a potential for regulating gene expression. At the epigenetic level, BAF has been shown to bind histones and chromatin, thereby modifying overall chromatin organization. Although BAF binds dsDNA in a sequence independent manner, it also binds histones H3 and H1.1, and affects accessibility to chromatin through these interactions (T. Chandra et al., 2015; R. Montes de Oca, Lee, & Wilson, 2005; Ronglang Zheng et al., 2000). **These findings indicated to us that BAF has the capacity to influence chromatin organization and epigenetic regulation of gene expression.**

Rationale

BAF is an essential protein that bridges the nuclear lamina and chromatin and regulates nuclear structure. Phosphorylation of BAF by VKR1 regulates its interactions with dsDNA, and LEM-D proteins and alters its subcellular localization (R.J. Nichols et al., 2006). Molitor and Traktman demonstrated in 2014 that the depletion of VRK1 resulted in

nuclear dysmorphia in MCF-10a cells and decreased the fraction of mobile BAF (T. P. Molitor & Traktman, 2014). Molitor and Traktman also published that the depletion of VRK1 slowed the doubling time of breast cancer cells and reduced the instances of distal metastases in a breast cancer model (T.P. Molitor & Traktman, 2013). Moreover, the homozygous inheritance of a missense mutation in BAF from Alanine 12 to Threonine results in a premature aging syndrome termed NGPS; patient-derived cells exhibit aberrant nuclear envelope structure, thereby designating it as a laminopathy (Puente et al., 2011). We hypothesized that the hypophosphorylation of BAF contributed to the nuclear envelope defect observed in VRK1-depleted cells and that the discovery of the A12T mutation could further inform the model generated by Molitor and Traktman and help elucidate the molecular mechanisms underlying these observations.

The BAF A12T mutation is not predicted to alter in the overall secondary structure of the protein: A12 is not localized in the dimerization interface of BAF, and dimerization is not disrupted *in vitro* (Nicolas Paquet et al., 2014). Furthermore, A12T mutation did not compromise binding to known protein partners such as Emerin, Lamin and histone H3 protein, however purified protein exhibited decreases DNA binding (Nicolas Paquet et al., 2014). Before the publication of the paper identifying the binding interface between BAF and Lamin A, the surface was thought as being important in chromatin condensation and histone binding (R. Montes de Oca et al., 2005; Samson et al., 2018; Segura-Totten, Kowalski, Craigie, & Wilson, 2002). We posited that the mutation had implications in chromatin structure and organization. Knowing that BAF may be involved in the regulation of higher order chromatin organization, we **hypothesized that the spatial organization of the nucleus would be disrupted and that there might be an overall loss of heterochromatin**. We further hypothesize that the **loss of higher order structure in the**

nucleus would cause a shift in gene expression profiles, which is a contributing factor the development of the disease phenotype.

Chromatin conformation is tightly orchestrated spatially and temporally within the nucleus (Harr, Gonzalez-Sandoval, & Gasser, 2016). In an extensive review (Harr et al., 2016), a compilation of the histone associated proteins of the nuclear envelope revealed the extent to which the INM proteins participated in the coordination of chromatin organization through histone modifications. Although BAF has been fairly well characterized, the role it plays in higher order chromatin organization has not yet been well parsed out in interphase nuclei. Given what is known about tissue-specific chromatin organization, we aimed to characterize the role of WT BAF and BAF A12T on higher order chromatin structure. Chromatin can be classified in two compartments, open, euchromatin, and closed, heterochromatin. **Whether the overall chromatin organization in NGPS is altered has yet to be seen and characterizing the structural differences of chromatin in BAF A12T cells will provide insight into the contribution of higher order chromatin organization to the disease phenotype.**

Results

Generating a Stable Mammary Epithelial Cell Line That Constitutively Expresses 3XF-BAF or 3XF-BAF A12T Depleted for Endogenous BAF

The clinical manifestation of NGPS results from the homozygous inheritance of the BAF A12T allele (Puente et al., 2011). To examine the impact of the BAF A12T mutation in a close-to homozygous setting, we generated MCF-10a cells that constitutively overexpress 3XF-BAF or 3XF-BAF A12T through a lentiviral transduction system, while also introducing shRNA that targets endogenous BAF. Control cells were transduced with a corresponding empty lentiviral vector. In order to silence endogenous BAF but not the

BAF introduced by the lentiviral expression system, the 3XF-BAF and 3XF-BAF A12T constructs had mutations introduced into the shRNA recognition sites in the 3' untranslated region (UTR). Lentiviral mediated transduction of MCF-10a cells with both expression vectors resulted in modest overexpression of 3XF-BAF to an average of two-fold the levels of endogenous BAF while in turn depleting the levels of endogenous BAF.

Figure 3-1.

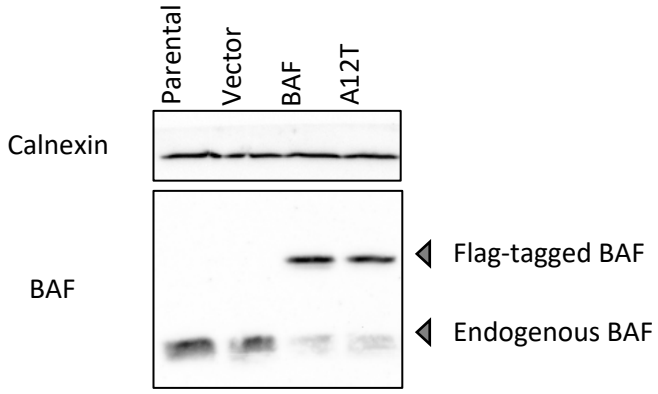

Figure 3-1. Generating a Stable Mammary Epithelial Cell Line That Constitutively Expresses 3XF-BAF or 3XF-BAF A12T Depleted for Endogenous BAF. The first lane represents parental MCF-10a cells, unmodified by lentiviral transduction, the vector control lane represents MCF-10a cells transduced with an empty pHM vector that does not encode for any mammalian protein, the remaining two lanes represent MCF-10a cells transduced with lentiviruses encoding shRNA resistant 3XF-BAF or 3XF-A12T in order to introduce exogenous BAF protein. Endogenous BAF was then depleted using lentiviral mediated-transduction of shBAF targeting the endogenous (but not exogenous) protein. This model achieves near homozygous expression of either WT BAF or A12T, allowing the study of the effects of this recessive mutation in this model.

The Expression of Wild Type 3XF-BAF or 3XF-BAF A12T Does Not Alter the Doubling Time or Growth of Cells Compared to Vector Control

When MCF10a cells are depleted of VRK1, the kinase responsible for phosphorylating BAF, the apparent doubling time increases (T.P. Molitor & Traktman, 2013). In order to ask the question whether MCF-10a cells expressing 3XF-BAF or 3XF-BAF A12T in a close-to homozygous background also have an altered doubling time, we performed four different assessments: analysis of apparent doubling time, growth by counting cells on a hemocytometer, MTT assay and Cell Titer Glo assay. In all cases, proliferation between vector control cells and cells overexpressing 3XF-BAF or 3XF-BAF A12T showed no significant difference. Statistical significance was determined by performing a student's t-test for the assessment of apparent doubling time and non-linear regression and multiple t-tests for the growth curves.

Figure 3-2

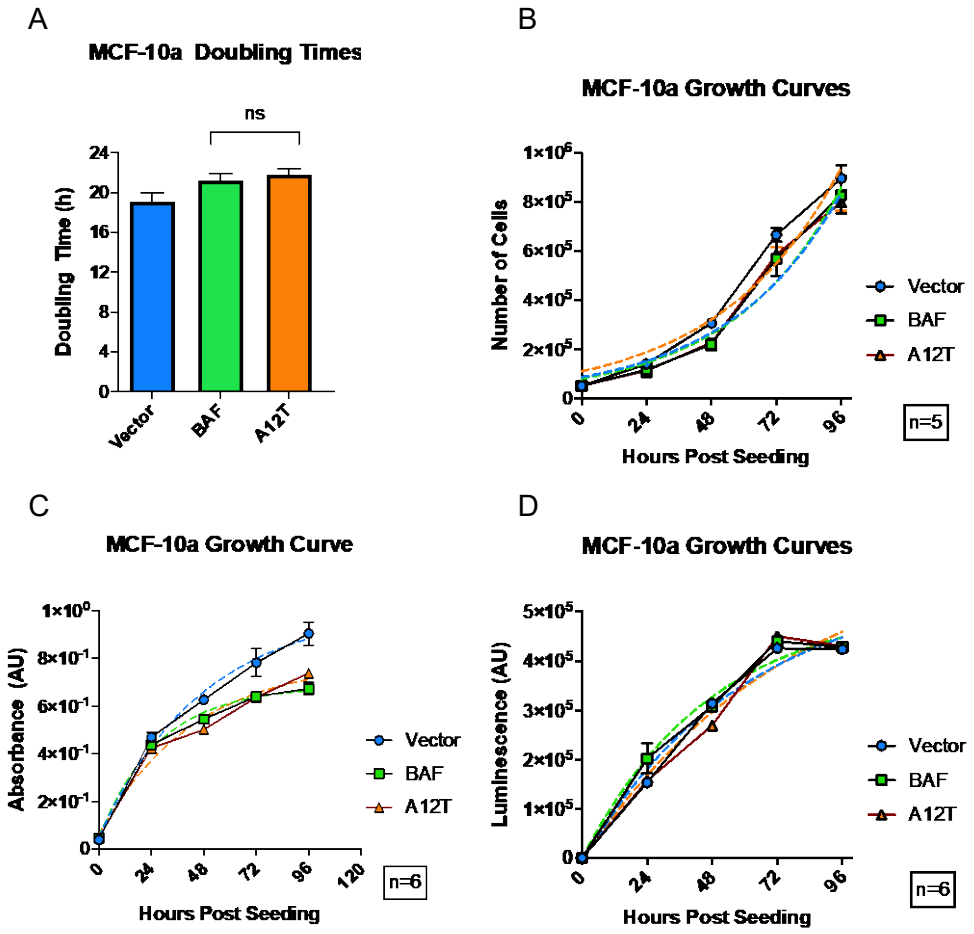
A
MCF-10a Doubling Times
ns
Doubling Time (h)
24
20
16
12
8
4
0
Vector
BAF
A12T
B
MCF-10a Growth Curves
Number of Cells
1x10^6
8x10^5
6x10^5
4x10^5
2x10^5
0
0
24
48
72
96
Hours Post Seeding
Vector
BAF
A12T
n=5
C
MCF-10a Growth Curve
Absorbance (AU)
1x10^0
8x10^-1
6x10^-1
4x10^-1
2x10^-1
0
0
24
48
72
96
120
Hours Post Seeding
Vector
BAF
A12T
n=6
D
MCF-10a Growth Curves
Luminescence (AU)
5x10^5
4x10^5
3x10^5
2x10^5
1x10^5
0
0
24
48
72
96
Hours Post Seeding
Vector
BAF
A12T
n=6

Figure 3-2. Assessment of Proliferation in 3XF-BAF or 3XF-A12T Expressing Cells. (A) Apparent doubling time of vector control cells is approximately 18h, whereas cells expressing either 3XF-BAF or 3XF-A12T have a doubling time of approximately 20h, an apparent doubling time of 2h greater than vector control, but not different between the homozygous expression of WT 3XF-BAF and 3XF-A12T as described in Chapter 2. (B) Cells were seeded at equal densities and counted every day for 4 days by staining with Trypan Blue and counting live cells. This was repeated in 5 independent experiments and cell number was plotted against time to generate a growth curve. (C) Cells were plated at equal densities and then subjected to MTT analysis across 4 days as described in Chapter 2. This represents 6 independent experiments. 570nm absorbance was measured on a spectrophotometer and plotted against time to generate a growth curve. There was no significant difference between the rate of proliferation of 3XF-BAF expressing cells and 3XF-A12T expressing cells. (D) Cells were plated at equal densities and then subjected to Cell Titer Glo analysis as described in Chapter 2. This represents 6 independent experiments. Luminescence was measured by spectrophotometer and plotted against time to generate a growth curve. Statistical analysis revealed no significant difference between the growth curves of cells expressing 3XF-BAF or 3XF-A12T.

The Homozygous Expression of 3XF-BAF A12T Results in Aberrant Nuclear Morphology

Cells derived from patients afflicted with NGPS display a clear change in nuclear morphology that is characteristic of all premature aging syndromes arising from mutations in the components of the nuclear periphery. Expression of 3XF-BAF A12T results in the deformation of the shape of the nucleus. Cells were stained using a Lamin A antibody and were assessed by fluorescence microscopy as described above. Approximately 50% of the cells expressing 3XF-BAF A12T display some amount of nuclear envelopathy. Furthermore, using the scoring scheme described in Moltior & Traktman 2014 (T. P. Molitor & Traktman, 2014) the distribution of the severity of the nuclear dysmorphia was analyzed. Whereas vector control cells and cells overexpressing 3XF-BAF WT displayed normal nuclei at a frequency of 83% and 79% respectively, only 51% of cells expressing 3XF-BAF A12T displayed a normal nuclear morphology. 35% of 3XF-BAF A12T expressing cells had nuclei that were assigned a score of 2 and 8% were assigned a score of 3.

Figure 3-3

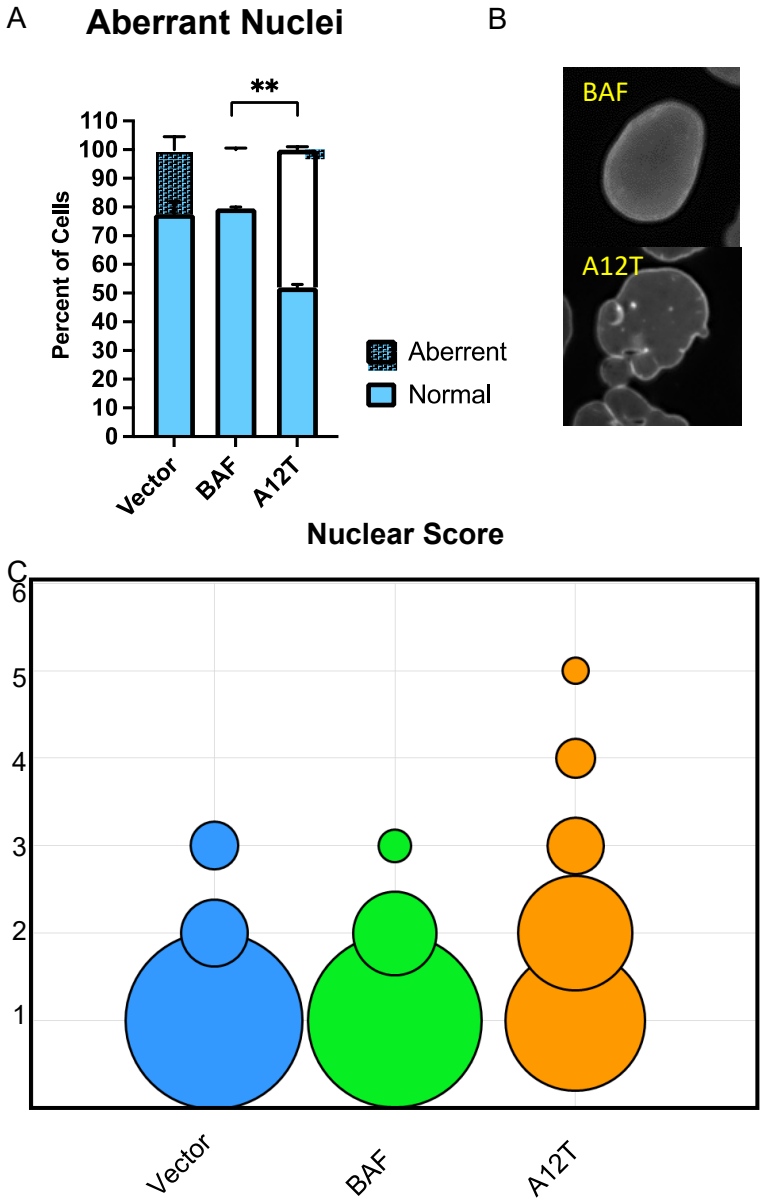
A
Aberrant Nuclei
**
Percent of Cells
110
100
90
80
70
60
50
40
30
20
10
0
Vector
BAF
A12T
Aberrent
Normal
B
BAF
A12T
Nuclear Score
C
6
5
4
3
2
1
Vector
BAF
A12T

Figure 3-3. Homozygous Expression of 3XF-A12T Results in Aberrant Nuclear Morphology. (A) Cells were analyzed by immunofluorescence of Lamin A to for nuclear morphology abnormalities. Normal nuclei were defined by a score of 1 based on the scale defined in Molitor & Traktman 2014, and aberrant nuclei were defined by a score >1. 50% of the cells expressing 3XF-A12T exhibited dysmorphic nuclei. (B) Cells expressing 3XF-BAF appear to have well rounded, smooth nuclei when analyzed by immunofluorescence of Lamin A; meanwhile, cells expressing 3XF-A12T exhibit dysmorphic nuclei that contain invaginations, blebs and in some cases multinuclei. (C) Using the scoring scheme defined in Molitor and Traktman 2014, cell nuclei were assigned a score of 1-6, with 1 defined as smooth round nuclei, and 6 as multinucleated and blebbed. Vector expressing cells and 3XF-BAF expressing cells both exhibited approximately 80% normal nuclei, whereas cells expressing 3XF-A12T had a majority of their nuclei with a score of 2 or greater.

The Homozygous Expression of 3XF-BAF A12T Does Not Alter the Steady State Levels of Proteins of the Nucleus

BAF interacts with many different binding partners within the nucleus, including the nuclear lamins and proteins with a conserved LEM domain. We used immunoblotting and band analysis, in order to ask whether the steady state levels of components of the nuclear periphery were altered during 3XF-BAF A12T expression. The proteins of the nuclear lamina, together with BAF, organize the nuclear periphery to provide structure and modulate the functions of the nucleus. Any alterations in the steady state levels of these proteins could point at a loss of interaction or organization at the nuclear periphery and may be a contributing factor to the formation of dysmorphic nuclei in the presences of a homozygous expression of 3XF-A12T. Using immunoblotting and immunofluorescence, we assayed steady state levels and distribution of Emerin, Lamin A/C and Lamin B, and found that they were unchanged in the presence of homozygous 3XF-BAF A12T.

Additionally, cells that exhibit premature aging phenotypes have an increased amount of heterochromatin and as such, an increase in the amount of tri-methylated histone 3 at lysine 9 (H3K9me3). H3K9me3 is found at sites of physiologic heterochromatin but also is a component of senescence associated heterochromatin foci (SAHF) in the context of cellular aging (Romero-Bueno, de la Cruz Ruiz, Artal-Sanz, Askjaer, & Dobrzynska, 2019). While senescent cells can exhibit dynamic signaling changes such as the upregulation of senescence associated secretory phenotype (SASP) components, once SAHFs have been formed, the heterochromatic structures are largely static and organized into repressive layers that are spatially distinct from transcriptionally active chromatin (Tamir Chandra & Narita, 2013). The use of H3K9me3 for analysis by immunofluorescence to analyze distribution and by immunoblotting to assess steady state

levels are, therefore, straightforward methodologies to ask whether SAHF are being formed in association with cellular senescence. Steady state levels of H3K9me3 were unaltered in the presence of homozygous expression of 3XF-A12T, and the distribution of H3K9me3 foci was undistinguishable between cells expression 3XF-BAF and 3XF-A12T.

Figure 3-4

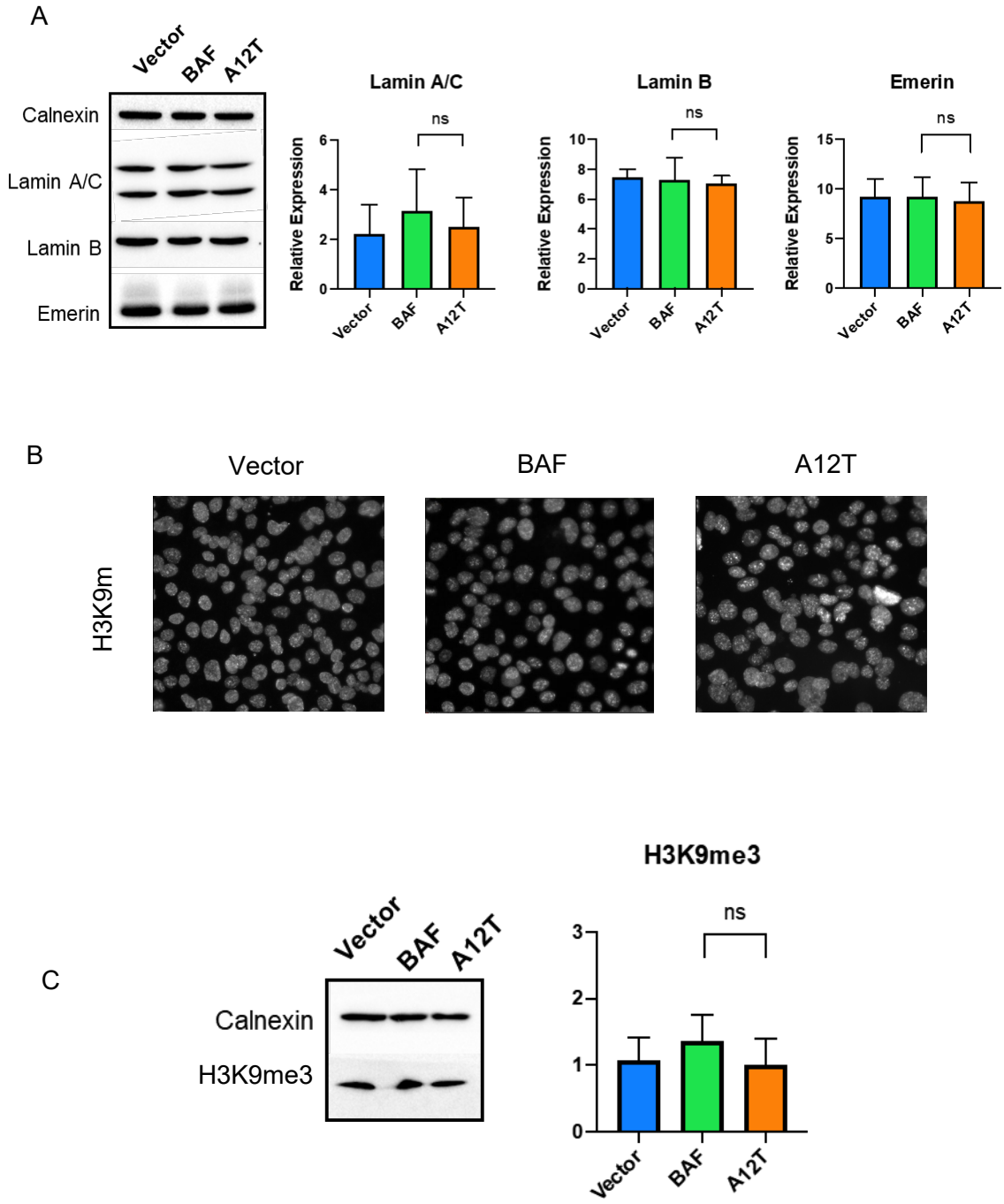
A
Vector
BAF
A12T
Calnexin
Lamin A/C
Lamin B
Emerin
Lamin A/C
Lamin B
Emerin
Relative Expression
ns
B
Vector
BAF
A12T
H3K9m
C
H3K9me3
Calnexin
H3K9me3

Figure 3-4. Nuclear Protein Expression and Distribution Is Unaltered by The Expression of 3XF-A12T. (A) Steady state levels of Lamin A/C, Lamin B and Emerin were analyzed by immunoblotting. Band analysis and quantification revealed no significant differences between the steady state levels of these NP proteins in 3XF-BAF expressing cells compared to 3XF-A12T expressing cells. This experiment is representative of 4 independent experiments. Statistical analysis was done by individual student's T-tests between conditions (B) Immunofluorescence for H3K9me3 was performed to compare the distribution of heterochromatin foci in cells expressing 3XF-BAF or 3XF-A12T. The number of foci and fluorescence intensity were no different between cells expressing 3XF-BAF and 3XF-A12T indicating no changes in the formation of SAHF. (C) Immunoblot analysis of the steady state levels of H3K9me3 further indicate that the expression of 3XF-A12T does not result in the accumulation of H3K9me3 in the nucleus. Band analysis and Student's T-tests were used to determine no significant differences between samples.

The Homozygous Expression of 3XF-BAF A12T Results in Minor Alterations in the Nucleus

The nucleolus is a nuclear substructure in which the transcription of ribosomal RNA (rRNA) occurs. The nucleolus is a dynamic structure that responds to cellular signaling, stress, and metabolism.(Boulon, Westman, Hutten, Boisvert, & Lamond, 2010). Previous studies have shown that in normal cells, nucleolar size and function are tightly regulated by the Lamin A meshwork, whereas in the context of HGPS, the Lamin A meshwork is lost and in turn nucleolar expansion and rRNA production increases. These phenomena result in an increase in nascent protein synthesis. (Buchwalter & Hetzer, 2017). Furthermore, nucleolar size inversely correlates with longevity. Tiku et al. demonstrated that *C. elegans* longevity mutants have reduced ribosome biogenesis, smaller nucleoli, and decreased protein synthesis (Tiku et al., 2017). Owing to the idea that nucleolar size can indicate changes in rRNA synthesis and in turn nascent protein synthesis, we asked whether steady state levels of a nucleolar marker, nucleolin, were altered and whether nucleolar number or size were altered in the context of 3XF-A12T homozygous expression. Measuring these nucleolar parameters was performed by fluorescence microscopy. Nucleoli were visualized by immunostaining for nucleolin, and DAPI was used to counterstain the DNA. The area of the nuclei and nucleoli were measured based on DAPI staining and nucleolin staining respectively and the area and the number of nucleoli were quantified.

Whereas cells expressing 3XF-BAF A12T had a slightly increased nuclear area, the nucleolar area was decreased, and the number of nucleoli was not altered. These data suggest that the area occupied by the nucleoli within the nucleus is significantly smaller in cells expressing 3XF-BAF A12T as compared to cells with wild type BAF expression. The

decreased occupancy of the nucleolus within the 3XF-A12T nucleus could imply variations in the amount of rRNA production and overall nascent protein synthesis. The inversion of the phenotype, however, is intriguing. While HGPS cells exhibit nucleolar expansion, the homozygous expression of 3XF-A12T leads to a decrease in nucleolar area and nuclear occupancy. Whether these slight variations have a biological influence on the behavior of the cells would be determined by the overall protein turnover as assessed by metabolic labeling and analysis of nascent protein synthesis.

Figure 3-5

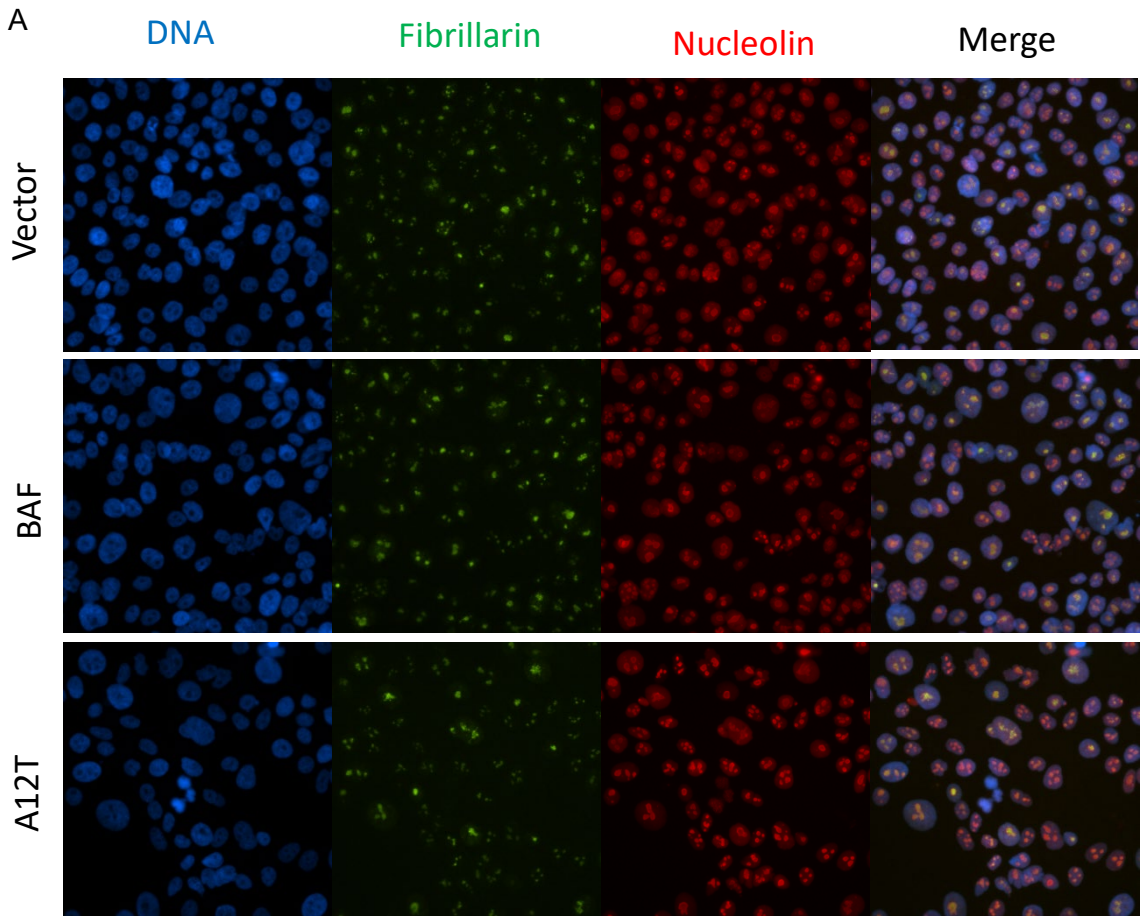
A
DNA
Fibrillarin
Nucleolin
Merge
Vector
BAF
A12T

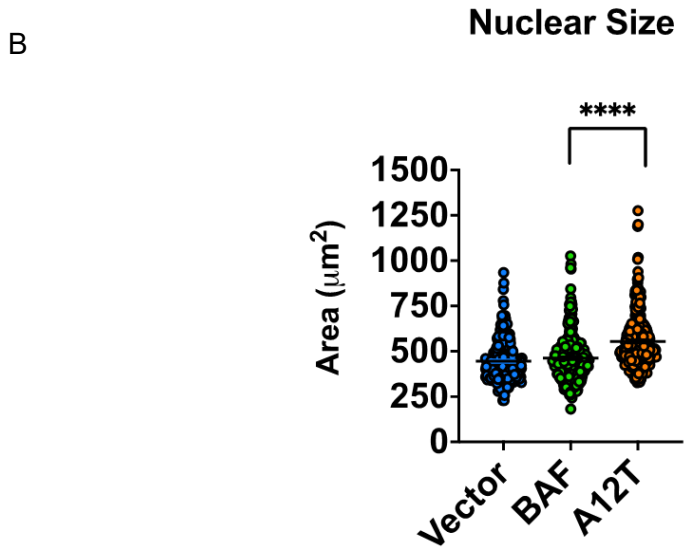
B
Nuclear Size
****
Area (μm²)
1500
1250
1000
750
500
250
0
Vector
BAF
A12T

C

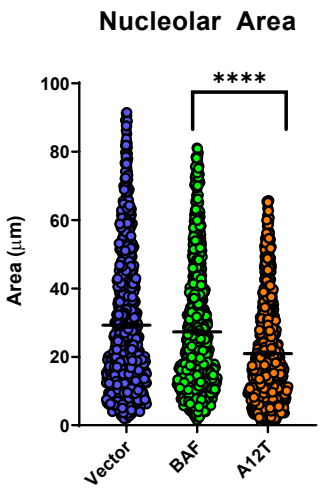
Nucleolar Area
****
Area (μm)
100
80
60
40
20
0
Vector
BAF
A12T

D

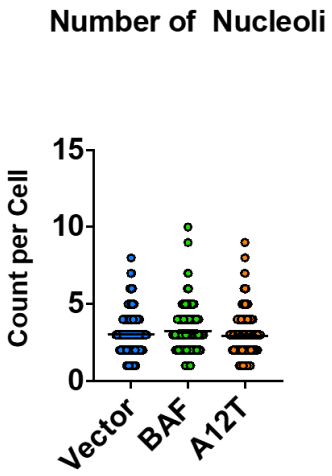
Number of Nucleoli
Count per Cell
15
10
5
0
Vector
BAF
A12T

E

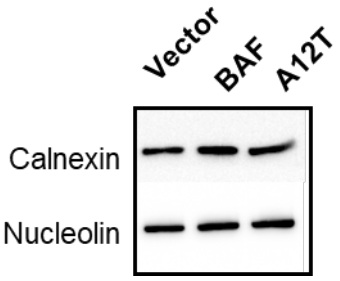
Vector
BAF
A12T
Calnexin
Nucleolin

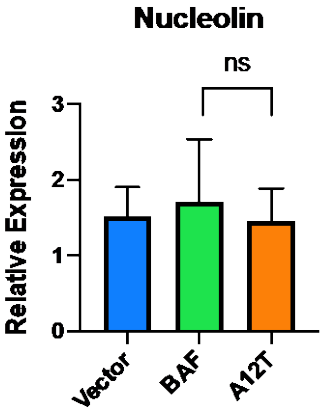
Nucleolin
ns
Relative Expression
3
2
1
0
Vector
BAF
A12T

Figure 3-5. Assessment of Nucleoli in 3XF-BAF and 3XF-A12T Expressing Cells. (A) Cells were immunostained with antibodies directed against Fibrillarin, a marker of the fibrillar component of the nucleolus and Nucleolin, a nucleolar marker, and counterstained with DAPI (for DNA). Representative images are shown; 3 independent experiments were performed and approximately 10 fields/experiment were analyzed. (B) Nuclear size was analyzed by taking the total area of positive DAPI staining per cell; approximately 500 cells from 3 independent experiments were analyzed. Statistical significance was determined by multiple Student's T-tests. The average area of vector and 3XF-BAF expressing cells is approximately $500um^2$, whereas the average nuclear area of 3XF-A12T-expressing cells is approximately $600um^2$. (C) Nucleolar area was determined by measuring the total area of Nucleolin staining that is delimited by a strong outer ring, and that colocalizes with Fibrillarin staining. The nucleolar area is the measurement of each nucleolus in the cell, not the average nucleolar area per cell. Approximately 1000 nucleoli were analyzed from 3 independent experiments and statistical significance was determined by multiple Students T-tests. The average nucleolar area of 3XF-BAF expressing cells and vector control cells is $30um^2$, whereas the average nucleolar area of 3XF-A12T expressing cells is $20um^2$. (D) The number of nucleoli per cell was counted by indexing any structures that contained were delimited by a strong outer ring of Nucleolin and that co-localized with Fibrillarin. The number of nucleoli per cell was taken by analyzing 50 nuclei from 3 independent experiments. There are approximately 3 nucleoli per cell in all conditions. In all measurements, the mean and standard error of the mean were plotted. (E) Immunoblot analysis of the steady state levels of Nucleolin reveal no alterations between any of the conditions. Band analysis reveals no significant differences in the relative expression levels of Nucleolin.

Nascent Protein Synthesis Was Unaltered in Cells Expressing 3XF-BAF A12T

Based on the observation that the nucleolar area was significantly smaller in cells expressing 3XF-BAF A12T, we asked whether the rate of nascent protein synthesis was altered. One of the nine hallmarks of aging is the loss of proteostasis, with a concomitant increase in nascent protein synthesis (Buchwalter & Hetzer, 2017; Lopez-Otin et al., 2013). To ask whether there were alterations in protein synthesis in cells expressing 3XF-BAF A12T, we performed metabolic labeling using ^{35}S-methionine/cysteine. Protein synthesis remained unaltered in cells expressing 3XF-BAF A12T as compared to cells expressing wild type BAF. Therefore, even though we observed differences in nucleolar occupancy in the nucleus, this did not correlate to changes in protein synthesis.

Figure 3-6

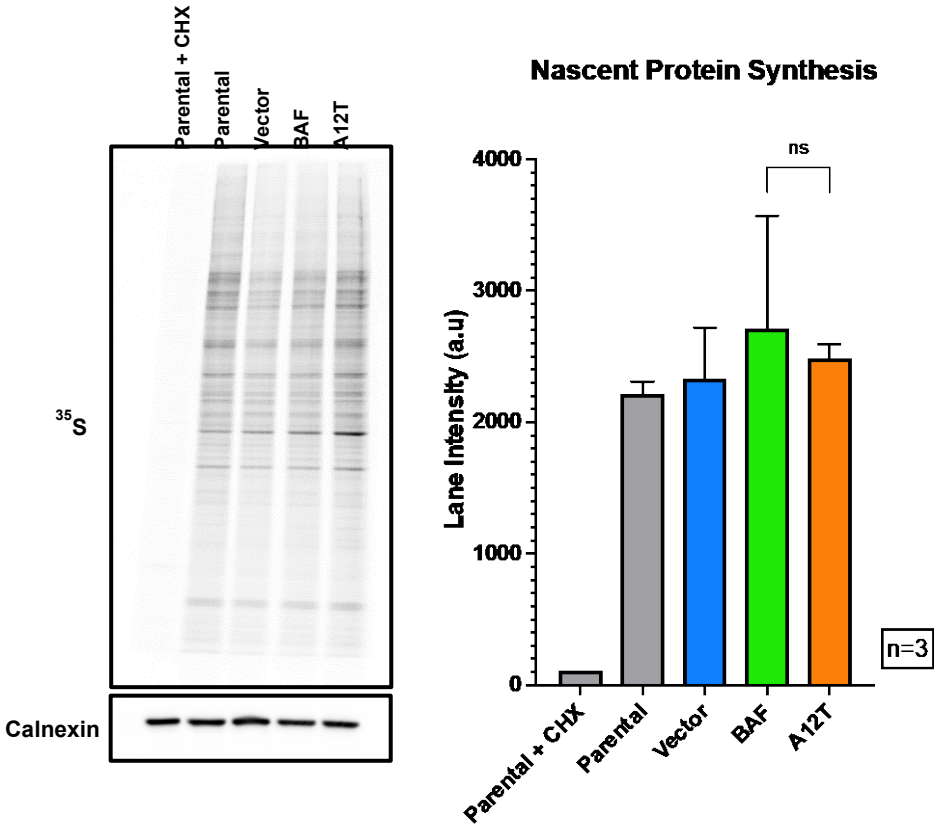

Figure 3-6. Nascent Protein Synthesis is Unaltered in Cells Expressing 3XF-A12T. The production of nascent proteins was analyzed by pulsing the cells with ^{35}S-methionine/cysteine. Samples were resolved by SDS-PAGE and subjected to phosphorimager analysis (left). Protein synthesis was unaltered in cells expressing 3XF-A12T compared to 3XF-BAF or vector control. These data are representative of 3 independent experiments. Band analysis was performed, and statistical analysis was based on multiple student T-tests.

Cells Expressing 3XF-BAF A12T Exhibited an Increase in the Accumulation of DNA Double Strand Breaks, but Do Not Accumulate Reactive Oxygen Species as a Measure of Cellular Stress

The accumulation of DNA damage is one of the hallmarks of aging (Lopez-Otin et al., 2013). The accumulation of dsDNA breaks results in genomic instability and in some cases, a subsequent arrest in cell proliferation (Efeyan & Serrano, 2007). To measure DNA damage, we assessed the levels of RPA, p53 and gamma-H2AX steady state levels in cells expressing 3XF-BAF A12T as compared to those expressing wild type 3XF-BAF or vector controls. As a positive control, cells were treated with the DNA damaging agent Etoposide at a concentration of 100μM for one hour. Interestingly, cells expressing 3XF-BAF A12T exhibited an increase in the steady state levels of gamma-H2AX in the absence of any exogenous DNA damaging agents, whereas the steady state levels of RPA and p53 remained unaltered. These results were intriguing, since the constitutive phosphorylation-mediated activation of histone H2AX normally leads to the activation of the DNA damage response pathway, and to the resolution of dsDNA breaks or cell cycle arrest (Itahana, Dimri, & Campisi, 2001; Jakob et al., 2011). However, as indicated by figure 3-2, proliferation was unaltered in these cells, indicating an ability for these cells to bypass the presumed accumulation of DNA damage. To further assess whether the activation of H2AX was truly a result of the accumulation of dsDNA breaks, we performed a comet assay. Single cell DNA electrophoresis indicated that there was, in fact, an increase in the number of DNA double strand breaks per cell in cells expressing 3XF-BAF A12T, as indicated by the vector length of the comet tails generated by resolved dsDNA on slides coated with agarose and then stained with DAPI. The presence of “basal” DNA damage in 3XF-A12T cells is clear, what remains unclear is the biological significance. The cells do not exhibit slowed proliferation, nor do they have increased levels of p53.

To assess whether the genotoxic stress present in these cells results in the accumulation of other stress responses, we next asked whether there was an accumulation of reactive oxygen species. We posited that cells may accumulate reactive oxygen species as a result of cellular stress. Furthermore, one of the nine hallmarks of aging is mitochondrial dysfunction (Lopez-Otin et al., 2013). The accumulation of genomic stress and reactive oxygen species is also a phenomenon observed in prematurely aged cells. In order to measure whether cells accumulated reactive oxygen species, they were treated with DCFDA. ROS lead to the esterification of the substrate DCFDA, which can be measured by the emission of light at 488nm. As a positive control, cells were treated with hydrogen peroxide for one hour prior to the assay. Cells expressing 3XF-BAF A12T did not have a noticeable accumulation of ROS as compared to cells expressing 3XF-BAF WT, and both conditions had a negligible accumulation of ROS as compared to cells treated with H_2O_2. Therefore, even though genomic instability was present in these cells, the accumulation of ROS and eventual mitochondrial dysfunction was not observed.

Figure 3-7

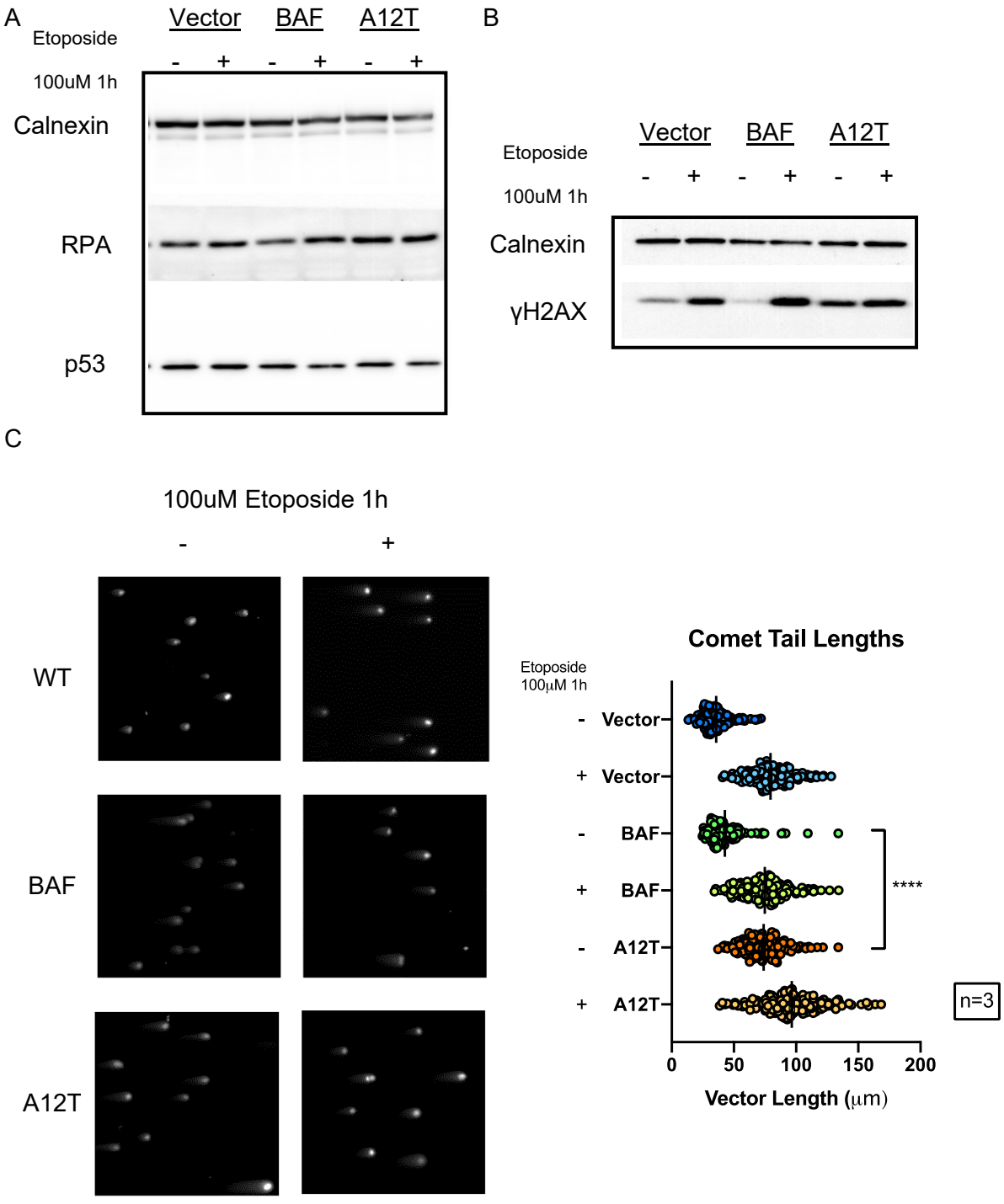
A
Etoposide
100uM 1h
Vector
BAF
A12T
- + - + - +
Calnexin
RPA
p53
B
Etoposide
100uM 1h
Vector
BAF
A12T
- + - + - +
Calnexin
γH2AX
C
100uM Etoposide 1h
- +
WT
BAF
A12T
Comet Tail Lengths
Etoposide
100μM 1h
- Vector
+ Vector
- BAF
+ BAF
- A12T
+ A12T
****
n=3
0 50 100 150 200
Vector Length (μm)

Figure 3-7. DNA Damage Analysis of Cells Expressing 3XF-A12T. (A) Immunoblot analysis of DNA damage response proteins RPA and p53 in the presence and absence of 100uM Etoposide for 1h. Steady state levels of RPA and p53 were not different between cells expressing 3XF-BAF or 3XF-A12T, nor were there differences in the response to exogenous DNA damage (increased levels). (B) Immunoblot analysis of γH2AX in the presence and absence of 100uM Etoposide was performed. The steady state level in the absence of exogenous DNA damage is 2-fold higher in cells expressing 3XF-A12T BAF in comparison to cells expressing 3XF-BAF or Vector control cells. The level of γH2AX increases approximately 2-fold in the presence of etoposide in control cells, whereas it appears that there is no further induction of this damage response in 3XF-A12T expressing cells. (C) A comet assay was performed on cells expressing 3XF-BAF or 3XF-A12T in the absence and presence of 100uM Etoposide. Single cell electrophoresis was followed by DAPI staining to visualize DNA. Vector tail lengths were measured and plotted. This image is representative of approximately 25 fields per experiment, 3 independent experiments. Quantification was performed on approximately 500 cells, and multiple Students T-tests were used for statistical analysis. In each cell line the vector length of each comet tail increased in the presence of Etoposide, however the comet tail vector length was significantly greater in cells expressing 3XF-A12T in the absence of Etoposide compared to cells expressing 3XF-BAF.

Figure 3-8

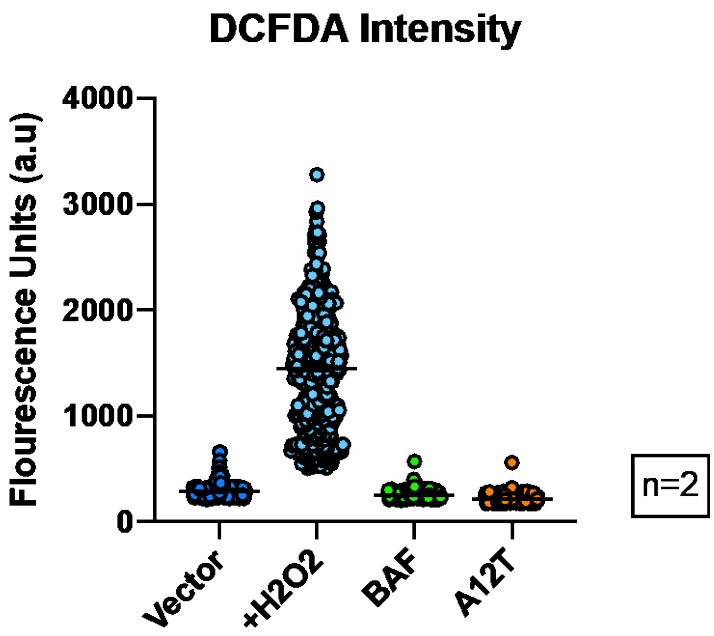

Figure 3-8. DCFDA Analysis of ROS. Cells were treated with DCFDA in order to measure the accumulation of reactive oxygen species in the cells. Vector control cells were treated with H_2O_2 as a positive control prior to DCFDA treatment. Vector control cells, 3XF-BAF and 3XF-A12T cells alike had a fluorescence intensity of about 300 A.U. whereas H_2O_2 treated cells had a fluorescence intensity of greater than 1500 A.U., a massive increase compared to the rest of the cells.

ATAC-Seq Analysis Reveals No Overall Alterations in Gene Accessibility in Cells Expressing BAF A12T

ATAC-Seq is a method for mapping chromatin accessibility throughout the genome. ATAC-Seq employs the use of hyperactive transposases that insert adapter sequences into accessible areas of the genome; the presence of these integrated adapters can then be assessed by sequence analysis (Buenrostro et al., 2015). Proteins of the nuclear periphery participate directly in chromatin organization, and in the context of HGPS, the expression of Progerin results in differences in gene accessibility and altered gene expression. BAF, which directly binds to dsDNA, acts as an organizational hub at the nuclear periphery. We therefore posited that chromatin conformation might be altered in cells expressing BAF A12T, and that such changes might result in altered gene accessibility. As a first test of this hypothesis, cells were subjected to ATAC-Seq. Cell pellets prepared from our vector control, 3XF-BAF wild type or 3XF-BAF A12T cell lines were submitted in duplicate for ATAC-Seq analysis. After ATAC-Seq was performed (see Chapter 2 for details) three analyses were used to assess differences in the accessibility of chromatin in these cells. The preliminary analysis was performed by using a genome browser and manually identifying peaks that exhibited at least a two-fold difference between the samples. At the time of this preliminary analysis, we did not ask whether these peaks fell within exonic, intronic, genic, intergenic, proximal or distal promoter regions or other regulatory regions within the genome. Our preliminary analysis indicated that there were no overall differences in the accessibility the genome. In order to ask whether differences might be revealed with a more precise analysis, we examined whether there were observable differences in chromatin accessibility based on specifically annotated chromatin regions. When organized into these categories, we were unable to observe gross alterations in chromatin accessibility at any of the following regions: distal

intergenic, intronic, exonic, 3'UTR, 5'UTR, or any promoters ranging from <1kb to 5kb. Knowing that these categories did not necessarily encompass all the important regions for gene accessibility and expression, we further asked whether there might be alterations in accessibility specifically at transcription start sites. Mapping these regions and peak annotations revealed no gross alterations in the accessibility of chromatin at transcription start sites overall. Taken together, these data, ranging from broad analysis down to detailed annotation, indicate no changes in the accessibility of chromatin based on the homozygous expression of BAF A12T in mammary epithelial cells.

Figure 3-9

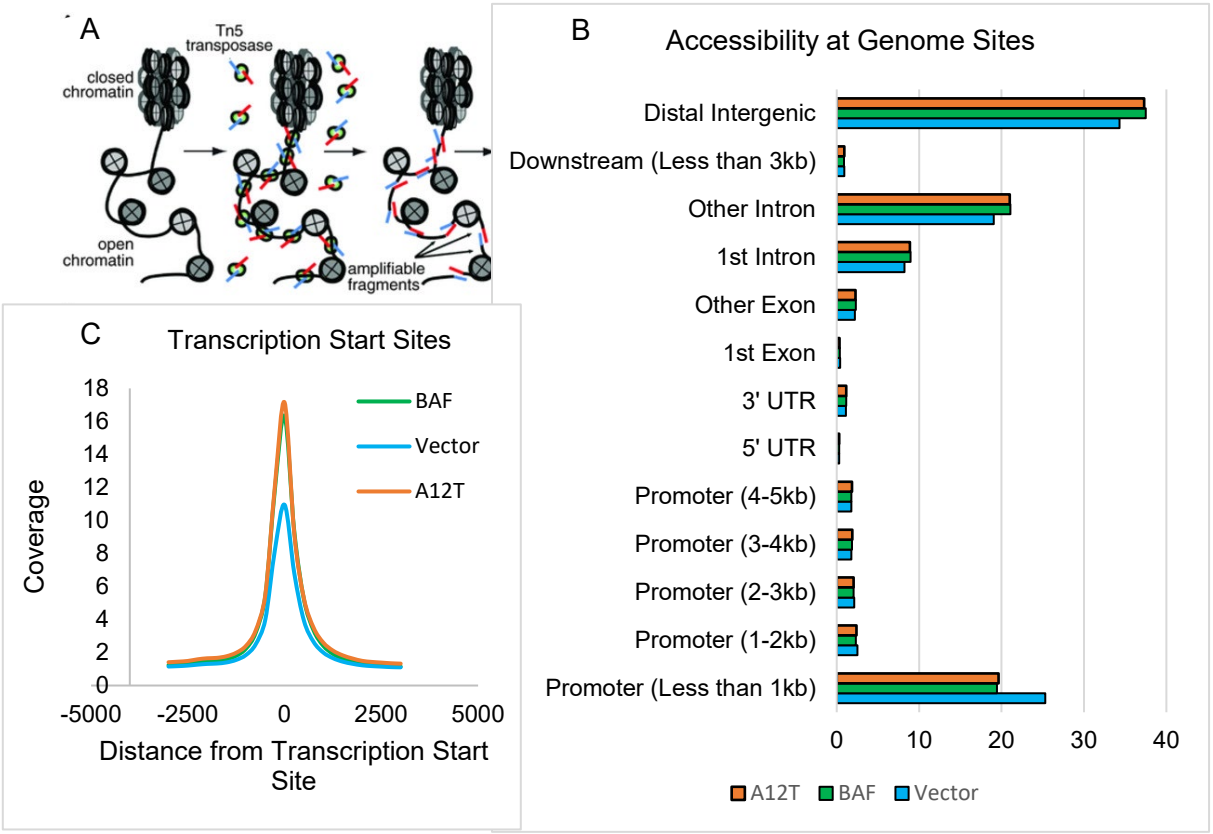

Figure 3-9. ATAC Seq Analysis on 3XF-BAF and 3XF-A12T Expressing Cells. (A) Schematic of ATAC Seq methodology taken from (Buenrostro et al., 2015) depicting transposes attacking accessible areas of the genome that insert adapter sequences in open chromatin that are then amplified and sequenced. (B) Analysis of peaks of open and accessible chromatin organized by their genome designation. There are no differences between the accessibility of chromatin in cells expressing 3XF-BAF or 3XF-A12T regardless of their location in the genome. (C) Analysis of accessibility at the average of all transcription start sites. Vector control cells had a lower accessibility at transcription start sites in comparison to 3XF-BAF or 3XF-A12T expressing cells, however there is no marked difference between the accessibility at transcription start sites between 3XF-BAF and 3XF-A12T expressing cells.

Overall Heterochromatin and Euchromatin Distribution is Unaltered in Cells Expressing BAF A12T

Another measure of overall chromatin organization and compaction is the ratio of heterochromatin to euchromatin within the cell and the amount of heterochromatin at the nuclear periphery. Chromatin that is associated with the lamina is often times compacted into foci of heterochromatin that are directly bound to Lamin A or to other components of the nuclear periphery; these are called Lamina Associated Domains (LADs). While cells expressing 3XF-BAF and 3XF-A12T did not exhibit variations in the levels and distribution of H3K9me3, nor were there observable differences in overall chromatin accessibility, the use of electron microscopy offers a unique and direct visualization of the chromatin within the nucleus. MCF-10a cells expressing Vector control, 3XF-BAF, or 3XF-BAF A12T were subjected to glutaraldehyde fixation and processed for electron microscopy. The area of the nucleus was analyzed at 2,000x magnification and the respective areas of heterochromatin and euchromatin were measured. The ratio of heterochromatin to euchromatin was calculated, revealing that the overall distribution of heterochromatin to euchromatin was largely unchanged in cells expressing 3XF-A12T compared to vector control. The heterochromatin at the nuclear periphery is associated with lamina associated domains, which, as discussed above, are generally sites of silenced genes tethered to the nuclear lamina. The thickness of heterochromatin was measured, and the average thickness of the heterochromatin at the NP was 0.002 um (+/- 0.001). There were no significant differences in the overall thickness of the heterochromatin at the nuclear periphery indicating no gross changes in the quantity of lamina associated domains in cells expressing homozygous 3XF-A12T.

Figure 3-10

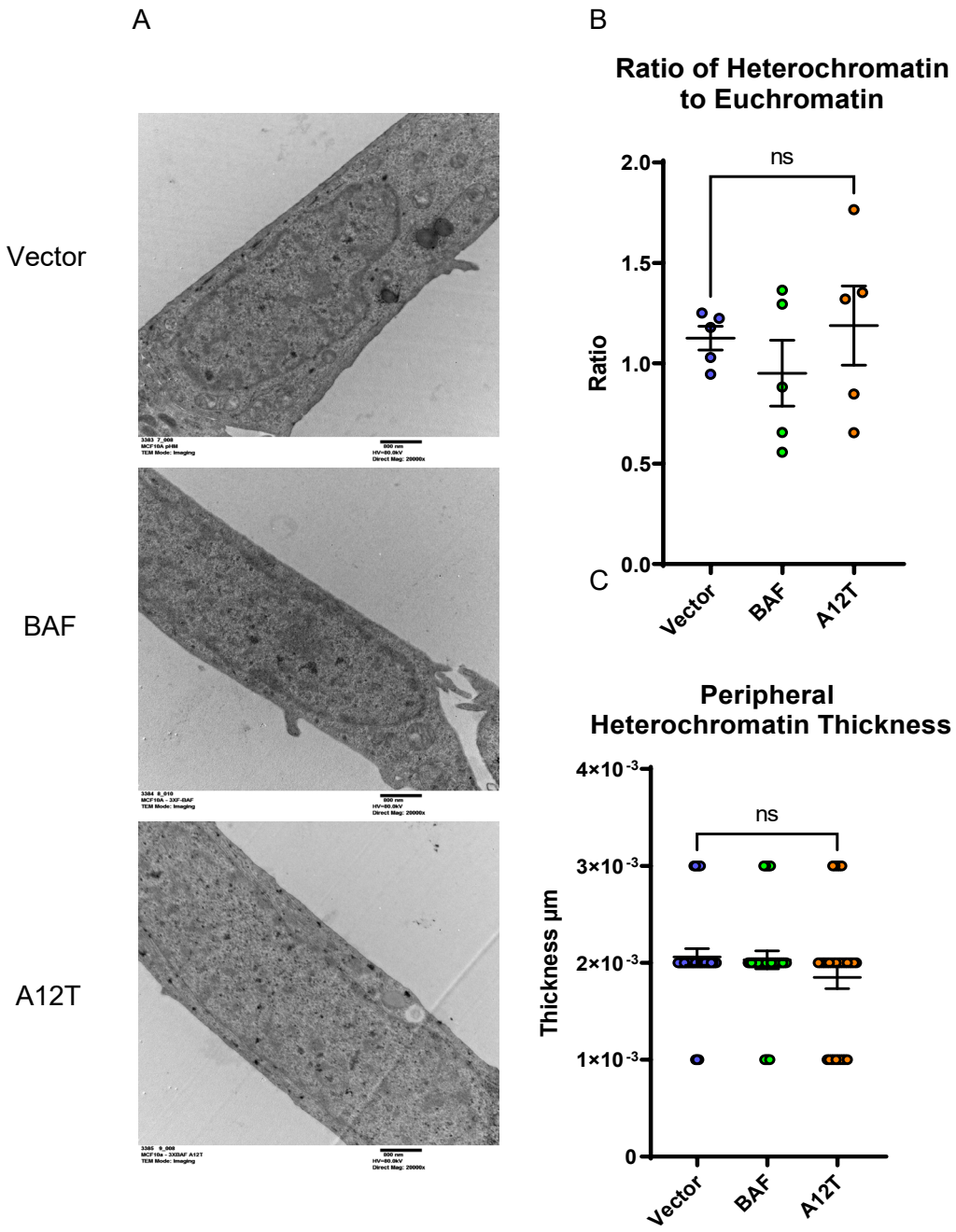
A
B
Vector
BAF
A12T
Ratio of Heterochromatin to Euchromatin
ns
2.0
1.5
1.0
0.5
0.0
Ratio
Vector
BAF
A12T
C
Peripheral Heterochromatin Thickness
ns
4×10-3
3×10-3
2×10-3
1×10-3
0
Thickness µm
Vector
BAF
A12T

Figure 3-10. Electron Microscope Analysis of 3XF-BAF and 3XF-A12T Expressing Cells. (A) Cells pellets were processed for transmission electron microscopy; images were taken at a magnification of 2,000x. Approximately 5 fields per condition were analyzed. (B) The ratio of heterochromatin to euchromatin was analyzed by taking the overall nuclear area, and using automated measurement of heterochromatin area vs euchromatin area based on the pixel density. (C) Peripheral heterochromatin was measured by measuring the vector length between the edge of the nucleus and the end of any peripheral heterochromatin. Student's T-tests were performed to determine statistical significance.

Discussion

Here, we have demonstrated that the expression of BAF A12T causes a nuclear envelopathy in MCF10a cells. Since the BAF A12T allele is associated with a premature aging syndrome, our goal was to determine if this envelopathy was correlated with agreed-upon hallmarks of cellular aging. As described in detail in Chapter 1, the hallmarks of aging are: genomic instability, telomere attrition, epigenetic alterations, loss of proteostasis, deregulated nutrient signaling, mitochondrial dysfunction, cellular senescence, stem cell exhaustion and altered intercellular communication (Lopez-Otin et al., 2013). We asked about epigenetic alterations and the alteration of nuclear substructures and found that there were no significant changes in the steady state levels of the nuclear periphery proteins, histone modifications, or the substructures of the nucleus. We did find a decreased area occupied by the nucleoli; however, this was not met with any changes in *de novo* protein synthesis, indicating that there were no gross alterations in protein synthesis. We addressed the question of cellular senescence and exhaustion by asking whether the growth curves or doubling times were altered in BAF A12T expressing cells and found no variation in cell proliferation. We asked whether there was genomic instability in these cells by examining the cells for double strand break accumulation. While we did see an increase in the accumulation of double strand breaks, the remaining data indicate that these double strand breaks did not result in an increase in cellular stress responses. We addressed the question of mitochondrial dysfunction by examining the accumulation of ROS and found that cells did not accumulate ROS nor did they accumulate other cellular stress responses.

Furthermore, we asked whether premature aging in this model might manifest with gross alterations at the level of euchromatin and heterochromatin organization. By using

two high resolution methodologies: electron microscopy and ATAC-Seq, we were unable to distinguish changes in overall nuclear organization.

All these data together highlight that while the homozygous expression of BAF A12T causes a human premature aging disease, the expression of BAF A12T in an epithelial cell line does not recapitulate the hallmarks of cellular premature aging. It also highlights that while BAF A12T causes a nuclear envelopathy, nuclear envelopathies are not sufficient to result in a model of cellular aging and dysfunction. While on the surface this may appear to be a limitation, we find that a model of nuclear envelopathies lacking a premature aging phenotype actually presents itself as a powerful tool for the understanding of nuclear envelope dynamics without the downstream sequalae that arise from cellular stress responses.

We posited that, since the BAF A12T-associated progeria primarily affects tissues of mesenchymal origin, the use of a mammary epithelial cell line might not recapitulate some of the cellular features of the disease. Furthermore, the model of lentiviral transduction to overexpress shRNA resistant 3XF-BAF or 3XF-A12T followed by the depletion of endogenous BAF is a somewhat complex approach to modeling a homozygous expression system. Therefore, we sought to address these limitations by generating a CRISPR/Cas9 mouse model that introduces A12T into the endogenous BAF locus. Generating a mouse model allows for the examination of different tissue to ask about cell type specificity, and the impact of the disease at the organismal level. Importantly, primary cells derived from these mice may also provide valuable insight into the etiology of the disease phenotype.

Chapter 4: The Characterization of a Novel NGPS Mouse Model

Introduction

Background on Murine Models of Progeria

Aging at the cellular level is defined by nine hallmarks (outlined in Chapter 1). At the organismal level, aging is characterized by the loss of function of physiologic systems over time, and the inability to maintain homeostasis (Blair, 1990). Clearly, the accumulation of cellular aging culminates in organismal aging and the sites of age-related pathologies are also the sites of the accumulation of senescent cells (Jeyapalan & Sedivy, 2008). Several studies have identified genes in which mutations arise that either accelerate or delay the effects of aging, indicating a genetic component to this physiologic phenomenon (Liao & Kennedy, 2014).

Mouse models for accelerated aging, or progeroid models, are not defined solely by a shortened life span, but rather must encompass the accumulation of age-associated pathologies. As of 2014, nine categories of genes whose alteration result in premature aging and/or shortened life span were established: Lamin A processing, the somatotropic axis, DNA repair, DNA replication, oxidative stress, sirtuins, hormones, genes involved in inflammation, and tumor suppressor genes. The existing mouse models for premature aging syndromes arising from nuclear envelopathies (see Chapter 1) all fall under the category of Lamin A processing mutations, thereby mirroring human HGPS (Liao & Kennedy, 2014). Patients with HGPS exhibit accelerated aging that involves the degeneration of tissues of mesenchymal origin including osteolysis and joint contracture, musculoskeletal disorders, severe craniofacial deformities, lipodystrophy, alopecia, thinning skin. Interestingly, HGPS patients also exhibit cardiovascular defects which ultimately results in heart attack or stroke and death, with the lifespan of HGPS patients

averaging merely 13 years (Tsiligiri, Fekos, Theodoridou, & Lavdaniti, 2014). A range of murine models of LMNA derived mutations have been generated in order to study the mechanisms of disease progression and to generate novel therapies. As detailed in Chapter 1, HGPS arises from a mutation in Lamin A resulting in a mutant protein termed Progerin. Progerin is unable to undergo cleavage by the endopeptidase ZMPTSE24, resulting in Progerin's permanent farnesylation and accumulation at the NE (Goldman et al., 2004). Mice with mutations in, LMNA or the deletion of ZMPTSE24 both recapitulate the phenotypes observed in HGPS in humans including failure to thrive, loss of adipose tissue, craniofacial defects, musculoskeletal abnormalities, nuclear envelopathies, and premature death as a result of dilated cardiomyopathy (Navarro et al., 2004; Pendás et al., 2002). Interestingly, while HGPS is associated with a heterozygous mutation in LMNA, specifically LMNA G608G/+, in order to recapitulate the progeria syndrome in mice, the paralogous LMNA G609G mutation is best modeled using a homozygous LMNA G609G/G609G model of inheritance, highlighting an important difference between human manifestation of HGPS and the murine model (Fernando G. Osorio et al., 2011).

Werner's syndrome is a progeria syndrome arising from mutations in the WRN gene (Oshima, Martin, & Hisama, 1993), which encodes a protein involved in DNA repair. The *Werner's* helicase contributes to the resolution of double strand breaks through homologous recombination and non-homologous end joining (NHEJ) (Thompson & Schild, 2002). To recapitulate this premature aging syndrome using a mouse model, Lombard et al. generated a WRN knockout mouse; however the WRN -/- mouse does not exhibit the features or clinical phenotypes of premature aging (Lombard et al., 2000). However, when WRN -/- mice were crossed with mice deficient for Terc, a component of the telomerase complex, the mice began to develop key premature aging phenotypes at

the organismal level, such as alopecia and osteoporosis, and at the cellular level such as replicative senescence and accumulation of genotoxic stress (Chang et al., 2004). This model is highlighted because it required a “double hit” model to capture the premature aging syndrome in mice, whereas the human disease results from a “single hit”.

There are key differences between the clinical manifestation of human progeria syndromes and the parallel mouse models aiming to recapitulate these diseases. These differences highlight the complexity of developing a mouse model in order to study a disease state at the organismal level.

The Study of Progeroid Primary Cells

Organismal aging is the culmination of cellular aging and replicative senescence (Campisi, 1998). The use of primary cells is therefore a useful methodology for the study of premature aging at the molecular and cellular levels. The first studies of HGPS patient-derived dermal fibroblasts revealed a reduced capacity for proliferation due to a steady decline of the fraction of proliferating cells over time with each passage (Kill, Faragher, Lawrence, & Shall, 1994; Martin, Sprague, & Epstein, 1970). The presence of abnormal nuclei is characteristic of cells expressing mutant Lamin A, and the discovery of these dysmorphic nuclei pointed at the molecular etiology of the disease phenotype (Annachiara De Sandre-Giovannoli et al., 2003; Eriksson et al., 2003). Further, another study indicated that the fraction of cells with dysmorphic nuclei increases with both cellular and organismal age (Bridger & Kill, 2004). Together these data helped inform the subsequent studies that revealed the molecular pathways of cellular aging, especially those arising from insults to the nuclear envelope. Furthermore, the study of fibroblasts from elderly patients compared to HGPS-derived fibroblasts has been an excellent method of comparison between

physiologic and pathologic aging (Cao, Capell, Erdos, Djabali, & Collins, 2007; Scaffidi & Misteli, 2006).

While the study of patient-derived cells has been valuable in the analysis of premature aging syndromes, especially in the context of treatment prospects, the use of reprogrammed patient cells has been an important tool in analyzing the differences between normal cellular aging and premature cellular aging as well (Carrero et al., 2016). Induced pluripotent stem cells (iPSCs) derived from patient fibroblasts have provided a mechanism to understand the process of differentiation and the upstream mechanisms leading to cells prone to premature aging phenotypes. For example, in the case of Werner's syndrome (WS), patient-derived fibroblasts that were reprogrammed to iPSCs had telomere length elongation, and restoration of cellular function, whereas when they were differentiated to mesenchymal stem cells they exhibited the hallmarks of premature aging once again (Cheung et al., 2014; Shimamoto et al., 2014).

In parallel to patient derived cells, primary cells derived from mouse models have also been valuable for the study of premature aging syndromes at the cellular level. The study of cells derived from ZMPTSE24 null mice established that the accumulation of Progerin damages the nuclear envelope, a critical and central feature of HGPS (Varela et al., 2005). Analysis of these cells also revealed other pathways involved in the pathologic aging phenotype including upregulation of p53 signaling, stem cell dysfunction and DNA repair defects (Liu et al., 2005; Fernando G. Osorio et al., 2011; Varela et al., 2005).

Measuring Aging in Mice

Premature aging syndromes arising from components of the nuclear lamina manifest at the cellular level with nuclear morphology defects, as outlined in Chapter 1. However, based on this study and others (T. P. Molitor & Traktman, 2014) a nuclear

envelopathy is not sufficient to generate a premature aging phenotype. Therefore, the measurement of premature aging in mice must rely on the accumulation of tissue degeneration and organ system dysfunction. Previous models of mouse aging syndromes, both arising as a result of LMNA mutations or other etiologies, use an array of measurements to assess the progression of premature aging.

Clearly, as defined by shortened lifespans, published characterizations of premature aging syndrome report survival. For example, the LMNA G609/G609 murine model of HGPS has an average lifespan of 125 days, approximately four months, compared to 242 days, approximately 8 months in LMNA G609G/+ mice and the 24 month life span of a healthy mouse (Flurkey, Currer, & Harrison, 2007; Fernando G. Osorio et al., 2011). Consistent with human phenotypes, mice expressing progeria-inducing genetic mutations exhibit reduced growth rates and significantly lower weights compared to their wild type counterparts (Navarro et al., 2004; F. G. Osorio et al., 2011; Pendás et al., 2002; Santiago-Fernández et al., 2019).

As mentioned previously, premature aging syndromes specifically target the degeneration of tissues of mesenchymal origin. Importantly, these include the bones, cartilage, muscle and adipose tissue. Skeletal aging specifically is defined by the progressive loss of function in the bone and articular cartilage. The most common clinical manifestations include osteoporosis and osteoarthritis (Hambright, Niedernhofer, Huard, & Robbins, 2019). Osteoporosis is characterized by reduced bone mass resulting from a loss in the balance between bone formation and resorption resulting in increased porosity, trabecular erosion and an increased incidence in fractures (Demontiero, Vidal, & Duque, 2012). The many murine models of HGPS all exhibit skeletal aging features including osteoporosis, kyphosis, and spontaneous fractures resulting in craniofacial defects due to

inappropriate healing (Bergo et al., 2002; Kuro-o et al., 1997; Pendás et al., 2002). X-ray analysis of the entire skeleton elucidates overall skeletal defects such as kyphosis, and fractures whereas micro-computed tomography (uCT) is used to assess bone density and volume, trabeculae number and other high-resolution analyses (Shazeeb et al., 2018). On the histological level, murine progeria syndromes arising from a LMNA processing mutation, and cells exhibit a classic nuclear envelopathy as expected, but also exhibit an increase in nuclear stress and cellular senescence markers, and defects at the microscopic level in structures of the skin, muscle, bone, cartilage and the aortic arch.

Nestor Guillermo Progeria Syndrome: Clinical Manifestation

As previously described above, the discovery of the BAF A12T mutation in patients provided insight into BAF's role in aging. The clinical manifestations closely mirror those of HGPS with one marked difference: patients expressing BAF A12T do not suffer from the cardiovascular defects that results in the premature death of HGPS patients. As addressed before, the clinical manifestations of NGPS do not begin until approximately two years of age. Patients present with failure to thrive, skin atrophy, general lipoatrophy and severe osteoporosis with marked osteolysis (Puente et al., 2011). Craniofacial abnormalities result from the atrophy of the facial subcutaneous fat and osteolysis of the maxilla and mandible and incomplete closure of the cranial sutures, see figure 4-1. Diverging from HGPS, NGPS patients retain eyebrows and eyelashes and, importantly do not exhibit cardiac dysfunction, ischemia, atherosclerosis or metabolic syndromes (R. Cabanillas et al., 2011; H. G. Fisher et al., 2020; Puente et al., 2011). The index patient suffered of severe secondary pulmonary hypertension and subsequent heart failure as a result of severe scoliosis (R. Cabanillas et al., 2011).

Rationale

Patients with NGPS had progressive and dramatic skeletal degeneration. Studies of murine models have been used to elucidate fundamental mechanisms of disease progression in a tissue-specific, systems-based approach. Based on the ability to replicate progeria syndromes in mice, albeit with some limitations and shortcomings, we aimed to generate the first murine model of NGPS to assess a number of parameters.

Figure 4-1

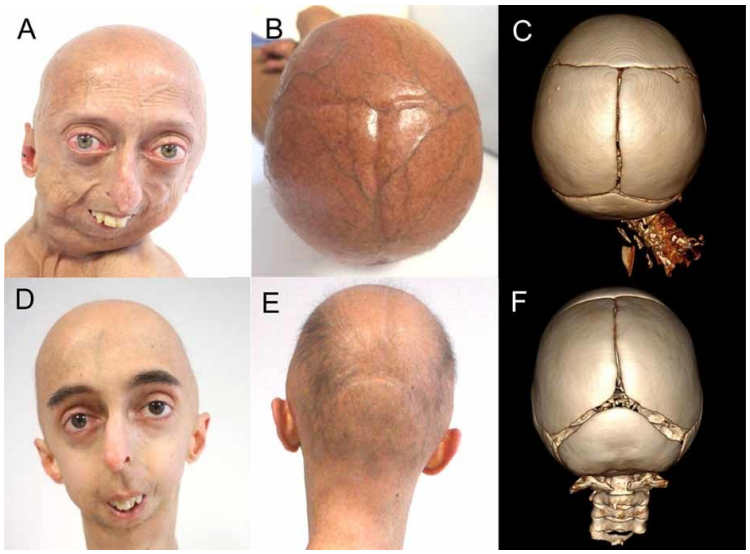

Figure 4-1. Craniofacial Defects in Patients with NGPS. Adapted from R. Cabanillas et al. 2011 (Rubén Cabanillas et al., 2011). Depicted in photographs and computed tomography reconstructions, patients with the homozygous inheritance of BAF A12T have severe craniofacial defects: the skull retains open cranial sutures, the facial bones undergo osteolysis with complete mandibular resorption, and they exhibit a marked loss of subcutaneous adipose tissue.

Results

The Generation of a BANF A12T/+ Mouse Colony and Genotyping BANF1 Mice

To generate a BANF1 A12T/+ mice, Applied Stem Cell generated an allele which inserted the NGPS associated mutation into the second exon of the BANF1 gene, see Figure 4-2. Applied Stem Cell generated a six-mouse colony comprised of three heterozygous (A12T/+) females and three heterozygous males in a C57/B6 background. Subsequent colony expansion was performed in-house by mating heterozygous sires and dams. The colony was subsequently inbred and maintained over 6 generations and resulted in approximately 330 mice. Genotyping was performed at weaning.

In the WT BANF1 allele, the codon for the 12th amino acid, alanine, is GCA. To generate the A12T amino acid substitution in our mice, the codon encoding Alanine 12 was changed from GCA to ACC. This codon substitution generates two *de novo* restriction enzyme sites. The BANF1 WT coding sequence contains two HPY 188III and one TSP 45I restriction enzyme sites, whereas the mutant allele generates a novel HPY 188III and a novel TSP 45I restriction enzyme proximal to the mutation (Figure 4-3 C). We took advantage of the introduction of this unique restriction enzyme site in order to genotype the mice. Genotyping PCR amplified exon two of the BANF1 coding sequence followed by restriction enzyme digestion of the PCR products using HPY 188III and TSP 45I. Undigested and digested DNA were resolved on a 20% polyacrylamide gel. Genotypes were analyzed based on the banding patterns described in Figure 4-3 A, B.

Figure 4-2

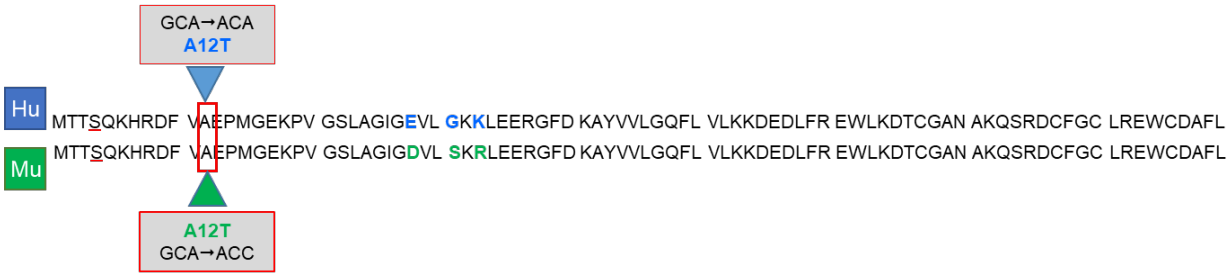

Figure 4-2. Alignment of human BAF and mouse BAF protein sequences. BAF is highly conserved between human and murine BAF sequences. Only 3 of the 89aa differ (blue and green). *Ser*4, the predominant phosphorylation site is underlined in red. A12 (red box) is mutated to a Threonine with a single codon change.

Figure 4-3

A

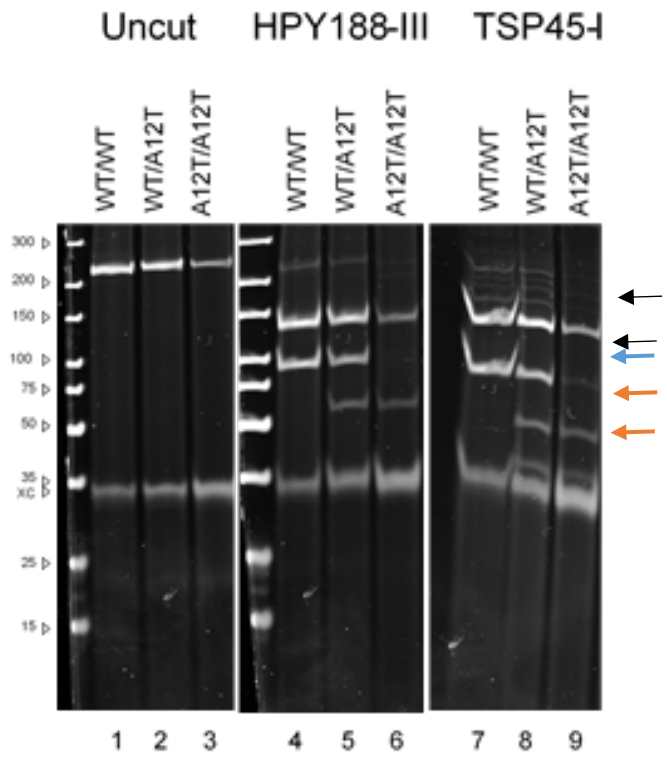

B

Banding Pattern Based on Genotype Using Restriction Enzyme Digest		
Restriction Enzyme	**Product Size (bp)**	**Corresponding Genotype**
Uncut	222	--
HPY 188III	132 and 90	*Wild Type (+/+)*
	132, 57 and 33	*Homozygous Mutant (A12T/A12T)*
	132, 90, 57 and 33	*Heterozygous (A12T/+)*
TSP 45I	140 and 82	*Wild Type (+/+)*
	140, 49 and 33	*Homozygous Mutant (A12T/A12T)*
	140, 82, 49 and 33	*Heterozygous (A12T/+)*

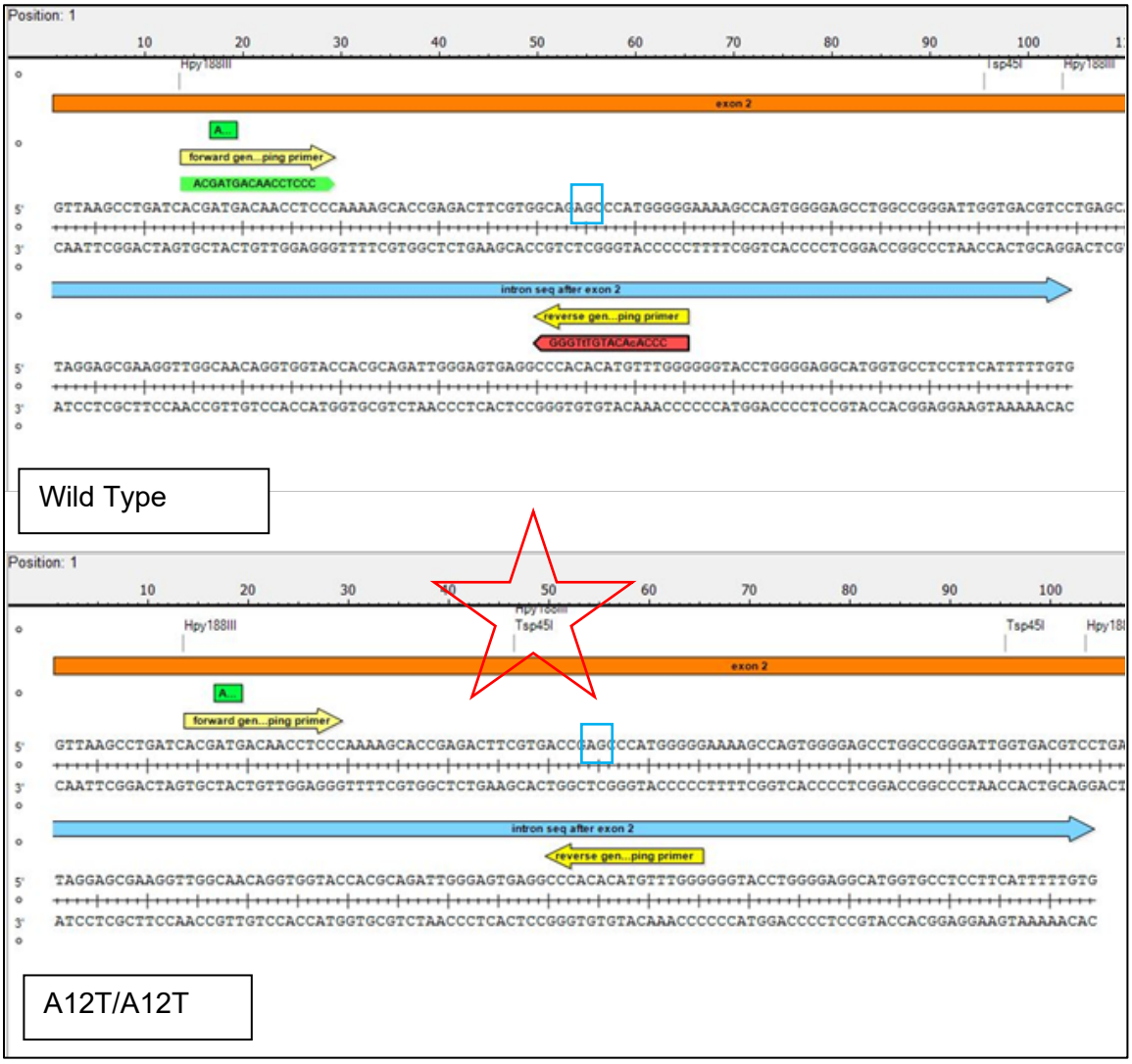
Position: 1
10 20 30 40 50 60 70 80 90 100
Hpy188III
Tsp45I
Hpy188III
exon 2
A...
forward gen...ping primer
ACGATGACAACCTCCC
5' GTTAAGCCTGATCACGATGACAACCTCCCAAAAGCACCGAGACTTCGTGGCAGAGCCCATGGGGGAAAAGCCAGTGGGGAGCCTGGCCGGGATTGGTGACGTCCTGAGC
3' CAATTCGGACTAGTGCTACTGTTGGAGGGTTTTCGTGGCTCTGAAGCACCGTCTCGGGTACCCCCTTTTCGGTCACCCCTCGGACCGGCCCTAACCACTGCAGGACTCG
intron seq after exon 2
reverse gen...ping primer
GGGTttGTACAcACCC
5' TAGGAGCGAAGGTTGGCAACAGGTGGTACCACGCAGATTGGGAGTGAGGCCCACACATGTTTGGGGGGTACCTGGGGAGGCATGGTGCCTCCTTCATTTTTGTG
3' ATCCTCGCTTCCAACCGTTGTCCACCATGGTGCGTCTAACCCTCACTCCGGGGTGTGTACAAACCCCCCATGGACCCCTCCGTACCACGGAGGAAGTAAAAACAC
Wild Type
Position: 1
10 20 30 40 50 60 70 80 90 100
Hpy188III
Tsp45I
Tsp45I
exon 2
A...
forward gen...ping primer
5' GTTAAGCCTGATCACGATGACAACCTCCCAAAAGCACCGAGACTTCGTGACCGAGCCCATGGGGGAAAAGCCAGTGGGGAGCCTGGCCGGGATTGGTGACGTCCTGA
3' CAATTCGGACTAGTGCTACTGTTGGAGGGTTTTCGTGGCTCTGAAGCACTGGCTCGGGTACCCCCTTTTCGGTCACCCCTCGGACCGGCCCTAACCACTGCAGGACT
intron seq after exon 2
reverse gen...ping primer
5' TAGGAGCGAAGGTTGGCAACAGGTGGTACCACGCAGATTGGGAGTGAGGCCCACACATGTTTGGGGGGTACCTGGGGAGGCATGGTGCCTCCTTCATTTTTGTG
3' ATCCTCGCTTCCAACCGTTGTCCACCATGGTGCGTCTAACCCTCACTCCGGGGTGTGTACAAACCCCCCATGGACCCCTCCGTACCACGGAGGAAGTAAAAACAC
A12T/A12T

Figure 4-3. Genotyping BAF A12T Mice. The BANF1 WT coding sequence contains two HPY 188III and one TSP 45I restriction enzyme sites. The BANF1 A12T mutant allele generates a novel HPY 188-III and TSP 45-I restriction enzyme site that digests six base-pairs downstream of the mutation. (A) DNA electrophoresis of uncut or restriction enzyme digested samples reveal a unique banding pattern based on mouse genotype. Lanes 4 and 7 indicate a WT genotype based on the appearance of 2 distinct bands at 132bp and 90bp in HPY188-III digested and at 140bp mutant allele, giving rise to new bands of 33bp and 57bp in the presence of HPY 188-III and bands of 49bp and 33bp in the presence of TSP45-I. The heterozygous mice have the appearance of all the bands due to the existence of one WT allele and one A12T allele. (B) Table describing the banding patterns based on genotype (C) Primer target for PCR amplification of exon 2 of BAF. The amplified PCR product in the WT allele contains pre-existing HPY188-III and TSP 45-I restriction enzyme digest sites. However, in the mutant allele, GCA (blue box top) is mutated to ACC (blue box bottom) to give rise to the A12T mutation which generates a *de novo* restriction enzyme site for both HPY 188-III and TSP45-I (red star).

Distribution of Phenotype and Analysis of Fertility

We first sought to characterize the distribution of males and females, and to determine whether the distribution of the mutation followed Mendelian patterns of inheritance. Matings were maintained between heterozygous mice, and the distribution of male and female mice was evenly distributed at an approximate ratio of 1:1 (Figure 4-4 A). Furthermore, the distribution of wild type, heterozygous and homozygous mutant mice was distributed at approximately 25:50:25 as predicted by Mendelian patterns of inheritance. Next, we test-mated homozygous mutant males and females by mating A12T/A12T males with WT females or A12T/A12T females with WT males followed by crossing A12T/A12T females with A12T/A12T males, in order to ask whether they were fertile. Data from our lab have shown that VRK1 hypomorphic mice are infertile as a result of the progressive loss of spermatogonia in the testes and defects in oocyte maturation (Wiebe, Nichols, Molitor, Lindgren, & Traktman, 2010) and (Traktman unpublished). Therefore, it was an important question to ask whether a mutation in VRK1's target, BAF, also resulted in defects in fertility. We assessed 15 litters per group, and we found that heterozygous and homozygous females both produced an average litter size of approximately 5 mice per litter as compared to an average of 7 pups per litter in their wild type counterparts (Figure 4-4 B). Pups from all groups grew and weaned appropriately and there was no increase in the pre-weaning mortality of heterozygous or homozygous mutant pups. Therefore, there were no detectable defects in fertility as a result of A12T expression, and A12T/+ and A12T/A12T distribution is based on classic genetic ratios.

To the best of our ability, we counted the number of pups born at day p=0-1 and then matched the number of pups at weaning. This information indicated to us that there was no death previous to weaning, however the loss of any pups before detection of

parturition could be a confounding factor since mothers scavenge dead pups. Taken together, these data indicate that heterozygous and homozygous A12T mice do not have defects in fertility and that there is no early loss of pups at a young age.

Figure 4-4

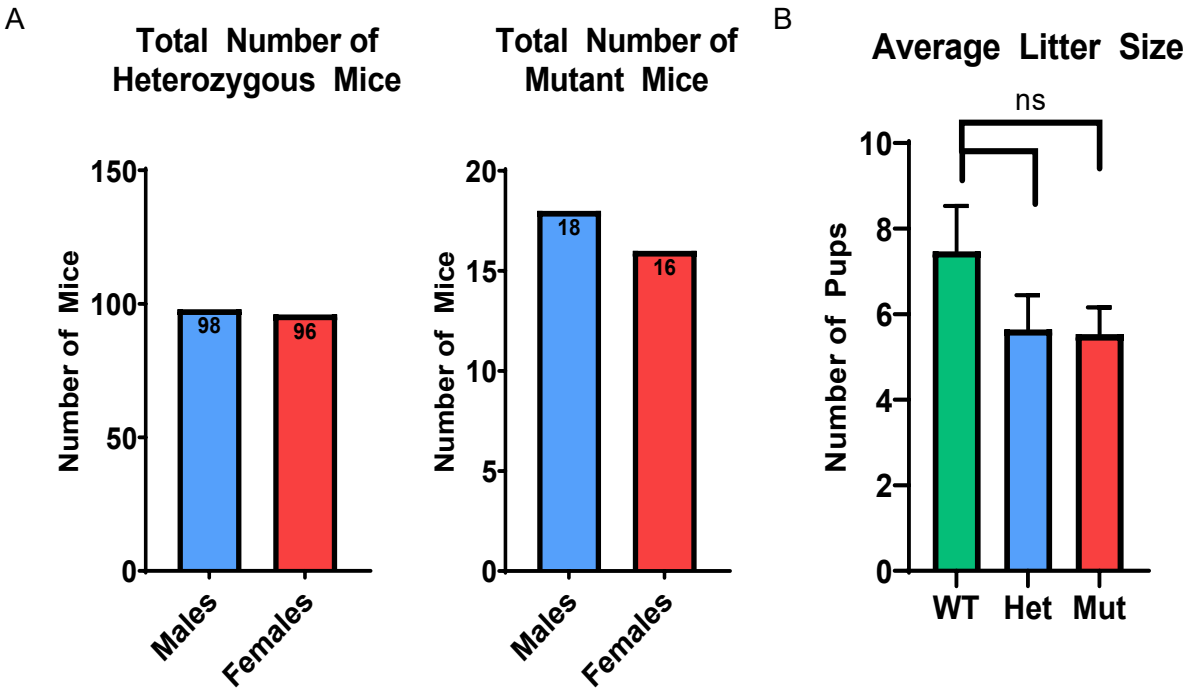

Figure 4-4. Distribution of Genotype and Analysis of Litter Size. (A) The distribution of genotypes among BANF1 mouse colony. There was a similar distribution of heterozygous and homozygous mice among males and females alike. (B) Average litter size between Dam genotypes were not statistically different (p=0.1871 n=15 litters each)

Characterization of Lifespan and Growth

The average lifespan for C57/B6 mice 18-22 months, or 540 to 660 days. In HGPS mice, LMNA G609G/+ and G609/G609 mice have dramatically shorter lifespans of approximately 250 days and 100 days respectively (Fernando G. Osorio et al., 2011; Villa-Bellosta et al., 2013). The lifespan of A12T/A12T mice is equal in length to wild type mice (Figure 5-5 A). We allowed the lifespan study to continue for 670 days before euthanizing the mice for endpoint analysis. Necropsy of the mice revealed no gross anatomical differences or gross abnormalities in either WT or A12T/A12T mice.

HGPS mice exhibit failure to thrive and exhibit body weights approximately 1/3 of their wild type counterparts (Zaghini et al., 2020). Therefore, we next measured the body weight of mice consistently between 3 and 12 weeks of age (Figure 4-6 A). No significant difference was observed in the growth rate between wild type and mutant mice. Furthermore, body weight was re-measured at 9 months of age and no significant difference was observed between wild type and mutant mice see Figure 4-6 A. During necropsy at end point analysis at 9 months of age, weights of heart, spleen, kidneys, liver, and lungs were all measured. No statistical significance was observed in organ weight, including liver weight, between wild type and mutant mice. Further, when liver weights were normalized to body weights, the differences between the groups was even smaller. These data suggest that there is no growth defect between in A12T/A12T mice and that they thrive comparably to wild type controls (Figure 4-6 B).

Figure 4-5

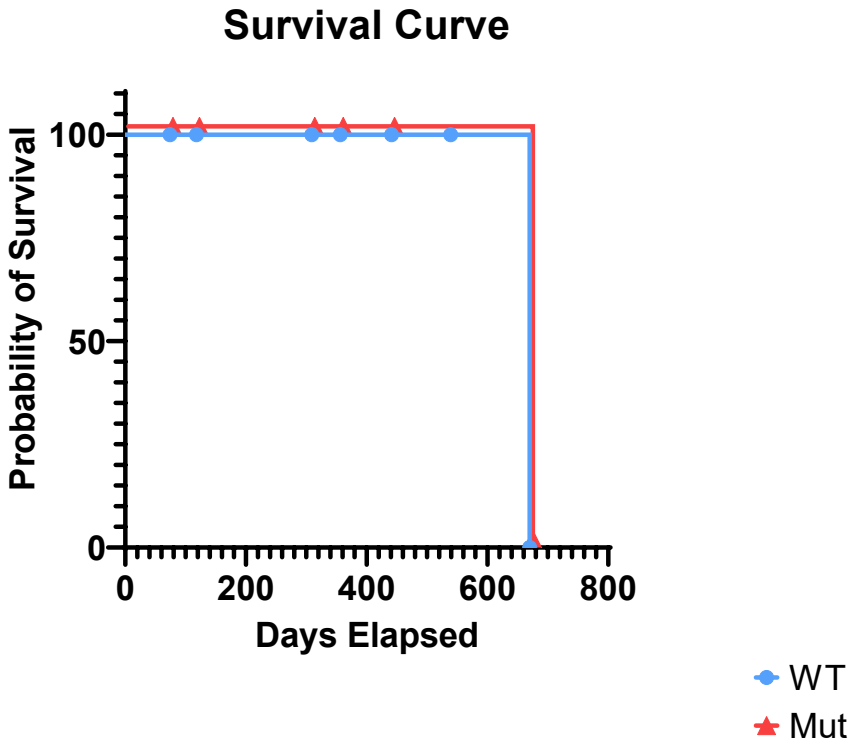

Figure 4-5. Survival Curve of BAF A12T Mice. Litter mates were maintained in a survival study across 670 days. The end point of this study was 22 months of age. The mice were then euthanized for further analysis. The p value between the survival curves is >0.9999.

Figure 4-6

A

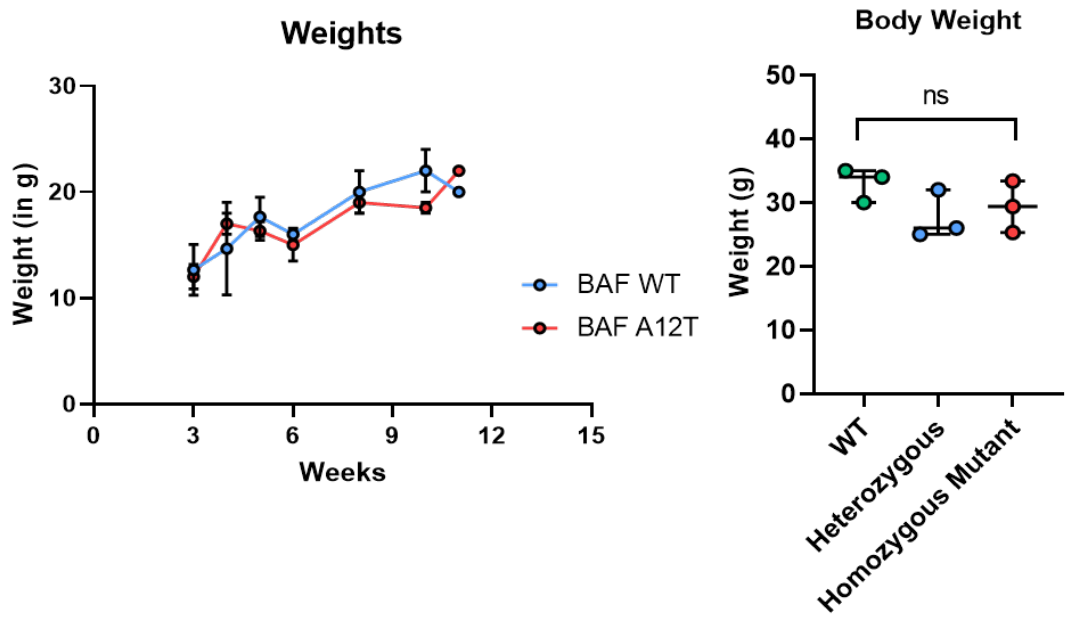
Weights
Weight (in g)
30
20
10
0
0
3
6
9
12
15
Weeks
BAF WT
BAF A12T
Body Weight
Weight (g)
50
40
30
20
10
0
ns
WT
Heterozygous
Homozygous Mutant

B

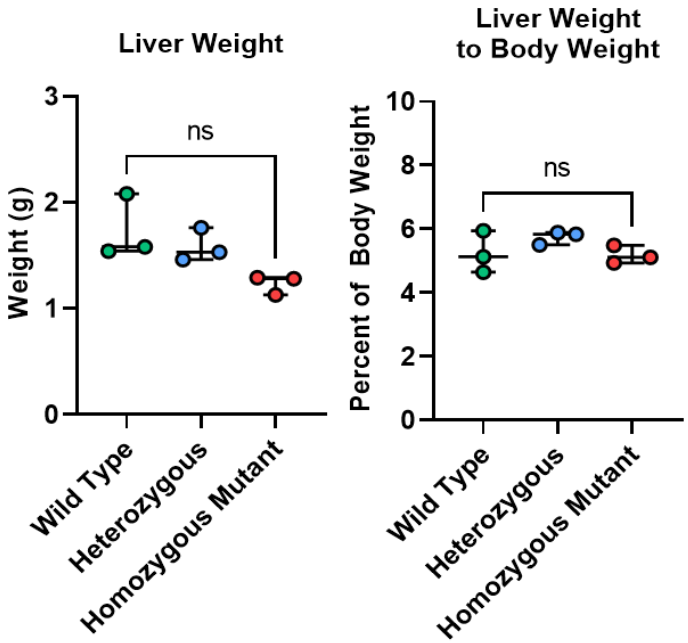
Liver Weight
Weight (g)
3
2
1
0
ns
Wild Type
Heterozygous
Homozygous Mutant
Liver Weight
to Body Weight
Percent of Body Weight
10
8
6
4
2
0
ns
Wild Type
Heterozygous
Homozygous Mutant

Figure 4-6. Analysis of BAF A12T Mice Growth. (A) Mouse body weight was measured over time from 3 weeks of age to 12 weeks of age (left panel) n=6 per group. No significant difference was observed in the growth rate between wild type and mutant mice (p=0.572). Body weight between mice was taken at 9mo of age and no significant difference was observed between wild type and mutant mice (right panel) n=3 per group. (B) Liver weights were taken at 9mo of age after end point euthanasia. No statistical significance was observed between wild type and mutant mice. Further, when liver weights were normalized to body weights, the differences between the groups was even smaller. We did not observe a difference in the weights of other organs including heart, spleen, kidney, and lungs.

Radiographic Analysis of BANF A12T/A12T Mice

Mice that exhibit premature aging syndromes such as HGPS exhibit severe skeletal defects such as osteoporosis, craniofacial defects, and severe kyphosis (F. G. Osorio et al., 2011; Zaghini et al., 2020). In order to ask whether the mice expressing A12T/A12T developed craniofacial or skeletal defects we used radiographic analysis to measure different skeletal parameters. At 9 months of age, mice were anesthetized using isoflurane and laid on their left lateral side inside the imaging chamber of a Faxitron LX-60 Cabinet X-Ray System. Skeletal measurements were taken based on anatomical landmarks. Measurements taken include: length of nasal bone, distance between nasomaxillary point to superior incisor point, mandible length, menton to mandibular condyle, cranial length, occipital bone to coronal suture, coronal suture to tip of nasal bone (Figure 4-8), and body length (from nose to anus), femur length, tibia length, humerus length, the height and width of the fifth lumbosacral vertebra, the distance between the top of the fourth lumbosacral vertebra to the bottom of the sixth lumbosacral vertebra, and the kyphosis index (Figure 4-7) which is measured by taking the distance between the bottom of the sixth cervical vertebra to the bottom of the sixth lumbosacral vertebra (line AB) and the distance from the highest point in the curvature of the spine down to line AB, generating line CD. The ratio of line AB to line CD is deemed the kyphosis index. There were no obvious defects in the living animals and the radiographic analysis revealed no significant differences between the measurements of the skeleton indicating that there were no underlying skeletal defects.

Figure 4-7

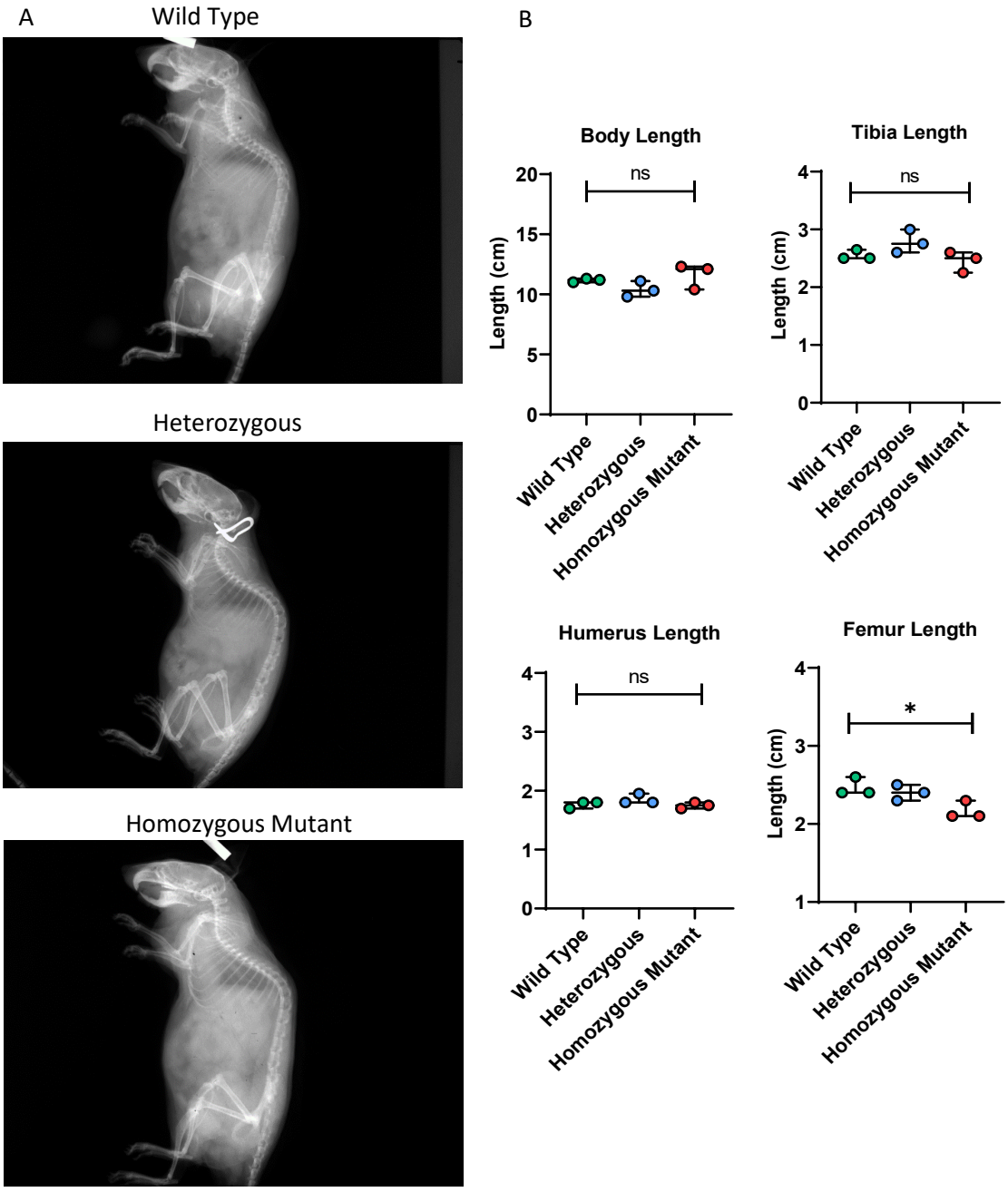
A
Wild Type
Heterozygous
Homozygous Mutant
B
Body Length
Tibia Length
Humerus Length
Femur Length
Length (cm)
ns
*
Wild Type
Heterozygous
Homozygous Mutant

C

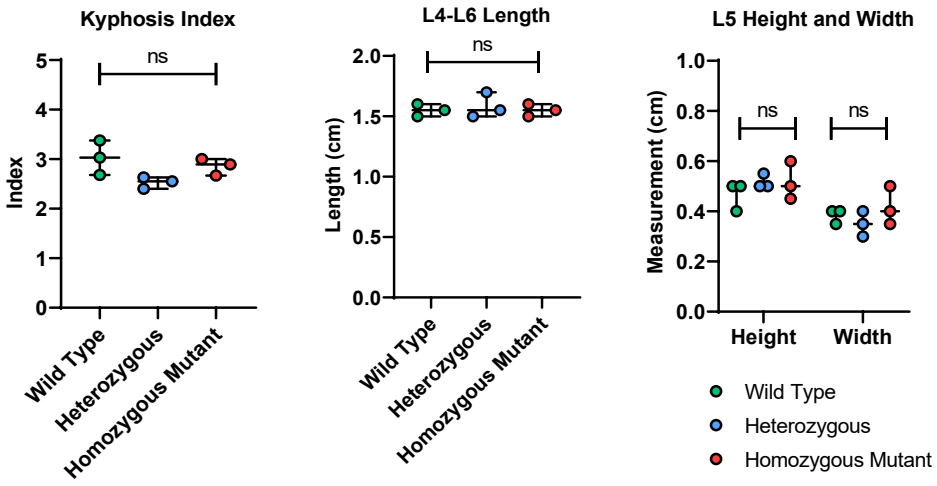

Figure 4-7. Radiographic Analysis of the Skeleton. (A) Full body x-ray imaging was performed on 9mo old mice (n=3 per group) by irradiating at 60kV for 60 seconds. (B) Body length, tibia, humerus, femur and cranial lengths were all measured. No significant differences were observed between wild type and mutant mice except femur length (p=0.0335). (C) The kyphosis index is measured by taking the distance from the C7 vertebra to the wing of the ilium (line AB); and the distance from the point of maximum curvature of the spine to the intersection of line AB (line CD); The kyphosis index (KI) is the ratio of line AB to line CD: (KI=AB/CD). No significant difference in the KI was found between wild type and mutant mice. Other spinal measurements such as the distance from L4-L6 and the height and width of L5 were assessed and no differences in these measures were observed.

Figure 4-8

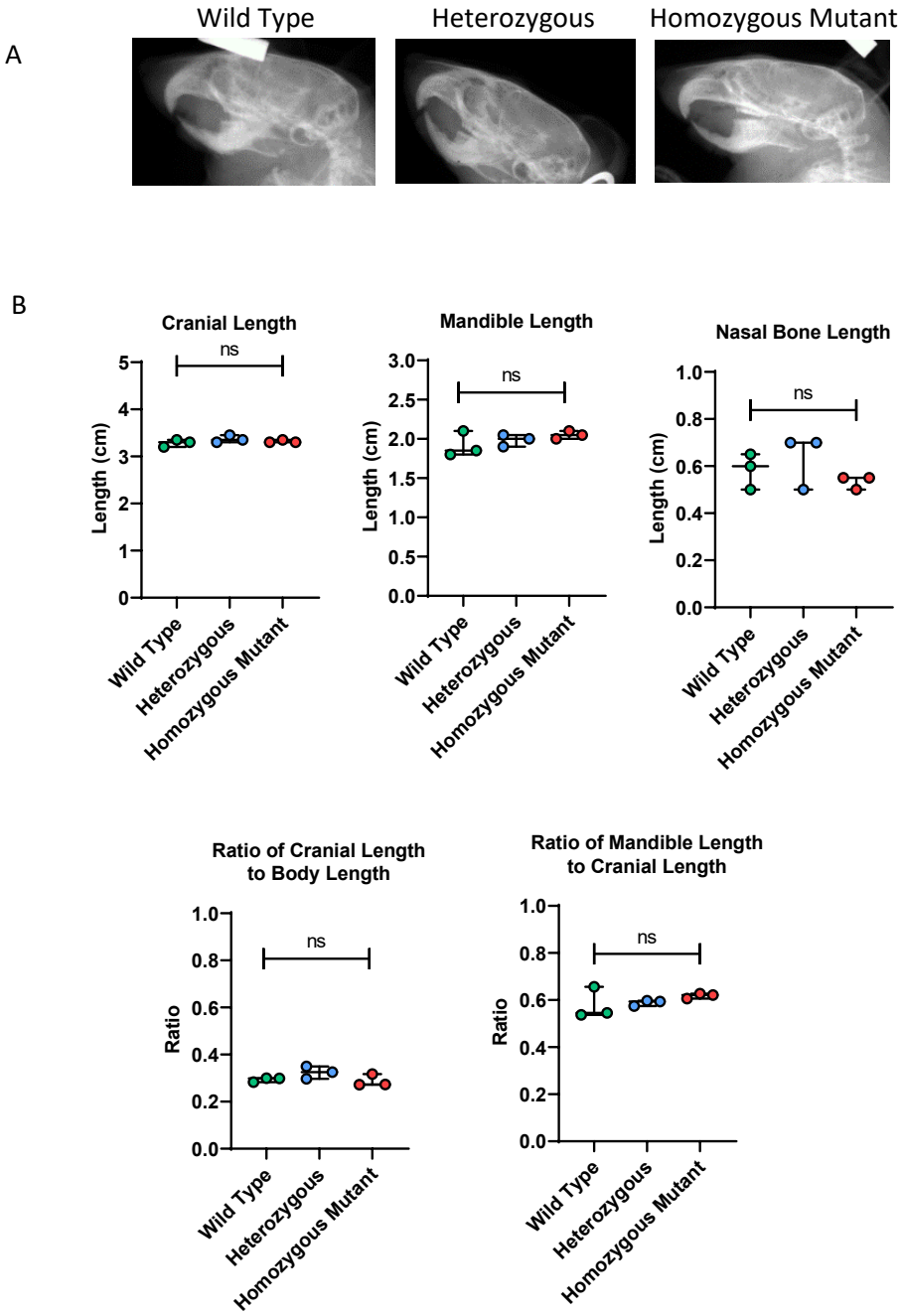
A
Wild Type
Heterozygous
Homozygous Mutant
B
Cranial Length
Mandible Length
Nasal Bone Length
Length (cm)
ns
Wild Type
Heterozygous
Homozygous Mutant
Ratio of Cranial Length to Body Length
Ratio of Mandible Length to Cranial Length
Ratio

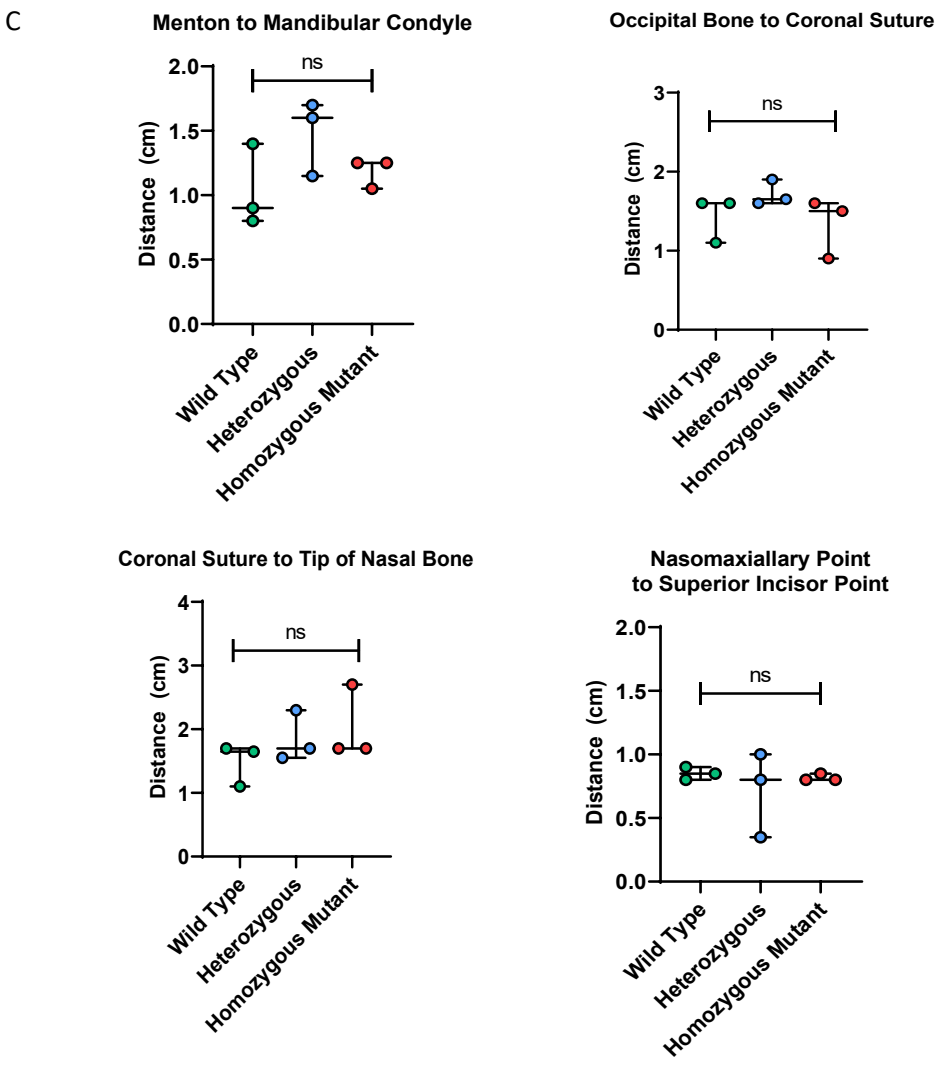

Figure 4-8. Radiographic Analysis of the Head. X-ray analysis was performed on the heads using cranial landmarks. (A) Close up images from the full body x-rays seen in figure 5. (B) The ratio of cranial length normalized to body length was not significantly different between wild type and mutant mice, nor were the lengths of the mandible, nasal bone or the ratio of the mandible to the cranial length. (C) No differences were observed in any of the cranial structures and distances including the distance between the sutures and other cranial landmarks.

Histologic Analysis of BANF A12T/A12T Mice

Histologic analysis of LMNA G609G/G609G mice reveals a loss of subcutaneous adipose tissue, reduced hair follicle distribution and thinning of the dermal layer (S. H. Yang et al., 2006; Zaghini et al., 2020). Tissues derived from mesenchymal origin are preferentially affected by both HGPS and NGPS; therefore, we recovered tissue from the same mice on which radiographic analysis was performed. Tissue samples from skin, long bone, and joints were sectioned and stained with H&E as described in Chapter 2. Histologic analysis of skin sections from A12T/A12T mice were assessed by measuring the subcutaneous fat thickness and the dermal thickness. There were no measurable differences in the distribution of the layers of the skin. Further, while there were no gross skeletal abnormalities between wild type and A12T/A12T mice, we looked at the structures of the bone and cartilage at the microscopic level. The thickness of the epiphyseal line was also measured alongside other bone parameters including overall organization of trabeculae, compact bone, and cartilage distribution. There were no differences in the overall histology of the long bones between wild type and A12T/A12T mice.

The overall histologic analysis of tissues derived from A12T mice revealed no abnormalities compared with wild type mice (Figure 4-9 A). This was not wholly surprising based on the normal skeletal architecture, normal growth rate and lifespan, and the absence of any gross visible anomalies between the groups of mice. From the study of HGPS mouse models, we know that a dominant mutation in the context of the human syndrome requires homozygous expression system to be recapitulated in a mouse model. Furthermore, in the case of WRN null mice, mice do not exhibit a premature aging phenotype that mimics WS until the mice are bred with Terc -/- mice. This implies that

generating a mouse model that mirrors human NGPS has not been as precise as modeling the effect of A12T on cellular function.

Figure 4-9

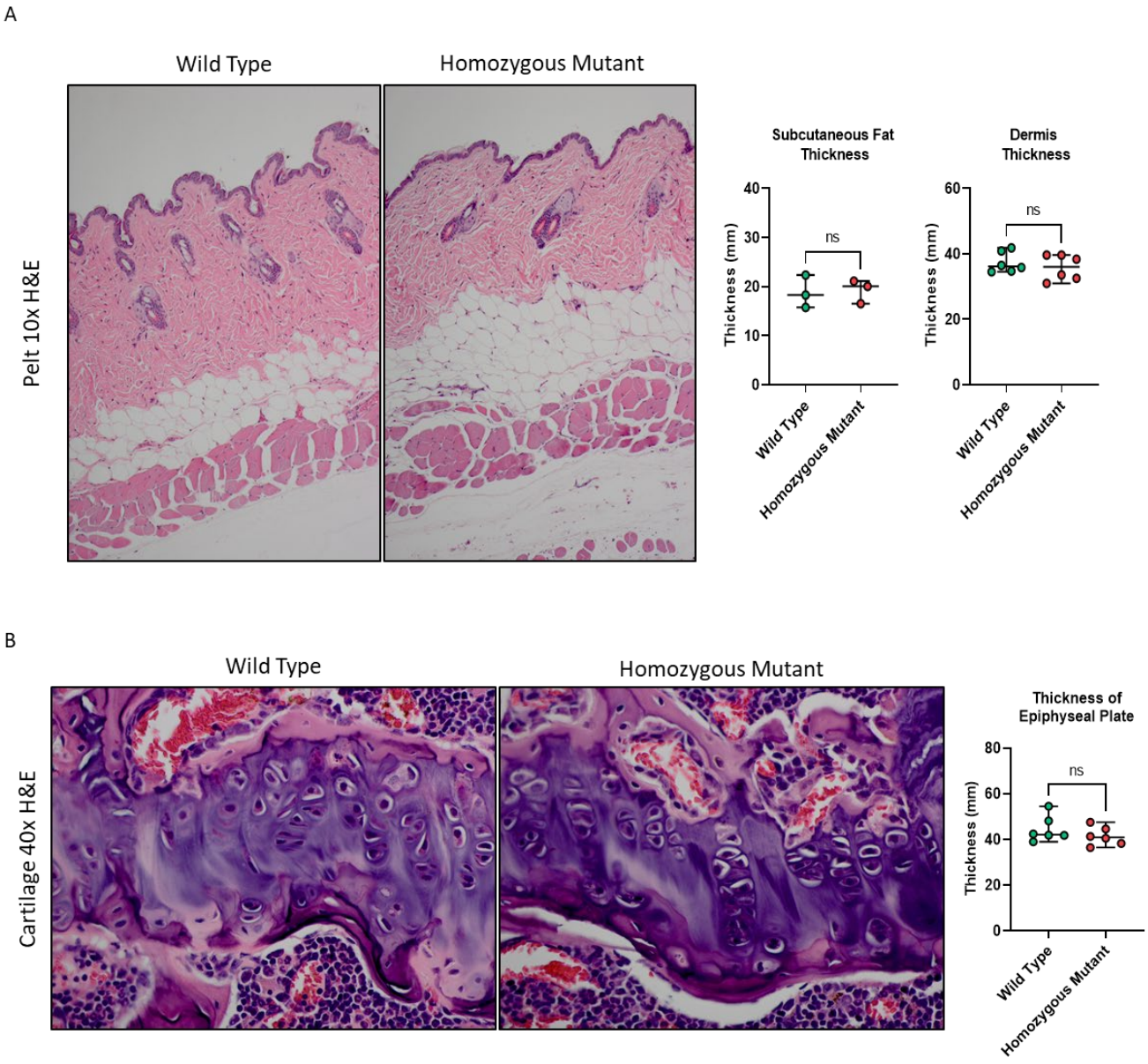
A
Wild Type
Homozygous Mutant
Pelt 10x H&E
Subcutaneous Fat Thickness
Thickness (mm)
40
30
20
10
0
ns
Wild Type
Homozygous Mutant
Dermis Thickness
Thickness (mm)
60
40
20
0
ns
Wild Type
Homozygous Mutant
B
Wild Type
Homozygous Mutant
Cartilage 40x H&E
Thickness of Epiphyseal Plate
Thickness (mm)
80
60
40
20
0
ns
Wild Type
Homozygous Mutant

Figure 4-9 Histologic Analysis of select BAF A12T/A12T Tissue. (A) Skin section stained with H&E at 10x magnification in wild type and BAF A12T/A12T mice; the subcutaneous fat and dermal thicknesses were measured. 3-5 fields were analyzed, and statistical significance was determined by students T-test. (B) Section of epiphyseal line of the tibia stained with H&E at 40x magnification in wild type and A12T/A12T mice; the epiphyseal thickness was measured. 5 fields were analyzed, and statistical significance was determined by Student's T-test.

Analysis of Primary Dermal Fibroblasts from BAF A12T/A12T Mice

As mentioned in the introduction to this chapter, the use of primary cells derived from mouse models of premature aging have been informative in dissecting some of the molecular mechanisms underlying disease etiology and progression. In order to generate a primary fibroblast cell line from WT and A12T/A12T mice, 1mm ear biopsies were harvested, and explant cultures were established from the outgrowth of the dermal fibroblasts. Our hope was that the study of these cells would reveal important pathways affected by homozygous inheritance of the BAF A12T mutation. The first parameter that we aimed to study was the proliferation of these primary dermal fibroblasts once they were in culture. The apparent doubling time of WT cells was approximately 25.5h, whereas the doubling time of mutant cells was approximately 24.3h, a negligible difference in doubling times between the two conditions. Furthermore, the growth curves were analyzed by plating cells at equal densities and counting live cells for three days after (Trypan blue staining). The growth curves were very similar between all the cell lines and we can conclude from these data that there are no differences in the proliferation of A12T/A12T fibroblasts compared to wild type.

Furthermore, since the expression of A12T results in a nuclear envelopathy (Figure 3-3), we analyzed the nuclear morphology of primary dermal fibroblasts. Cells were analyzed by immunofluorescent staining of Lamin A and scored based on the scoring schema described above. Greater than 50% of the A12T/A12T cells had an aberrant nuclear morphology with a score of 2 or greater. To complement this analysis, we used automated imaging software analysis to assess the nuclear circularity of both wild type cells and A12T/A12T cells. The departure from circularity in A12T/A12T expressing cells was significantly greater than wild type cells, as expected. This was an excellent proof of

concept and solidified the data that the inheritance of homozygous A12T results in dysmorphic nuclear envelopes.

However, as discussed in Chapter 3, nuclear envelopathy is strongly associated with a premature cellular aging phenotype. Our next analyses were therefore focused on whether A12T/A12T dermal fibroblasts accumulate the hallmarks of premature aging. While there were no differences in the rates of proliferation between wild type or A12T/A12T fibroblasts, we still aimed to analyze whether there was a fraction of senescent cells that might contribute to a premature cellular aging phenotype. We performed SA-β-galactosidase staining on primary dermal fibroblasts and quantified the proportion of positively stained cells. Less than 10% of the primary dermal fibroblasts exhibited SA-β-galactosidase positive staining, indicating that neither wild type nor A12T/A12T expressing cells undergo replicative senescence. Furthermore, as discussed in Chapter 3, cells that exhibit premature aging phenotypes usually contain an elevated of the histone variant H3K9me3, which marks areas of SAHF (Romero-Bueno et al., 2019). We measured H3K9me3 intensity by immunofluorescence to analyze its distribution and steady state levels, in order to ask whether SAHF are being formed in these cells. The levels and distribution of H3K9me3 were unaltered in the dermal fibroblasts derived from A12T/A12T mice.

To measure the induction of the DNA damage response pathway, cells were treated with Etoposide at a concentration of 100μM for one hour and the induction of gamma-H2AX was monitored. Wild type and A12T/A12T fibroblasts both appropriately induced the DNA damage response in the presence of etoposide and neither displayed any basal DNA damage. Lastly, we assayed the accumulation of ROS in primary dermal fibroblasts by treating cells with DCFDA. As a positive control, cells were treated with

hydrogen peroxide for one hour prior to the assay. There was no noticeable difference between wild type and A12T/A12T dermal fibroblasts in the basal level of ROS, but H_2O_2 treatment led to a marked increase in ROS levels in all cells.

Figure 4-10

A

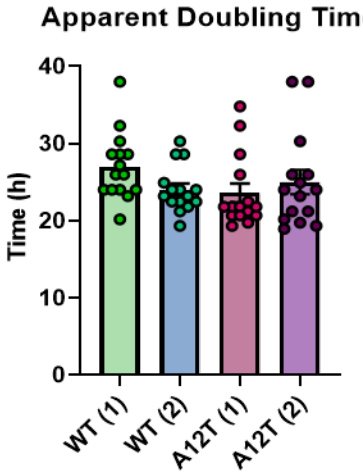

B

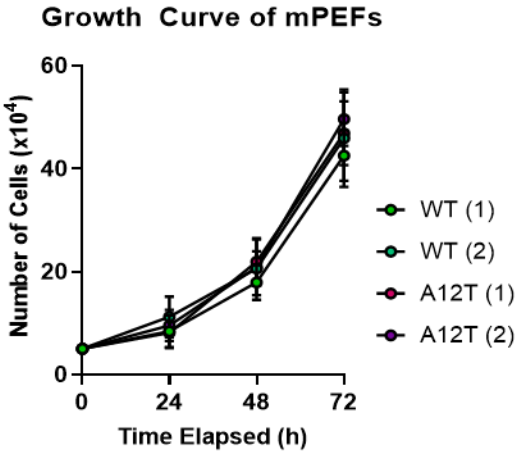

C

	WT (1)	WT (2)	A12T (1)	A12T (2)
Mean	26.99	24.03	23.58	24.99

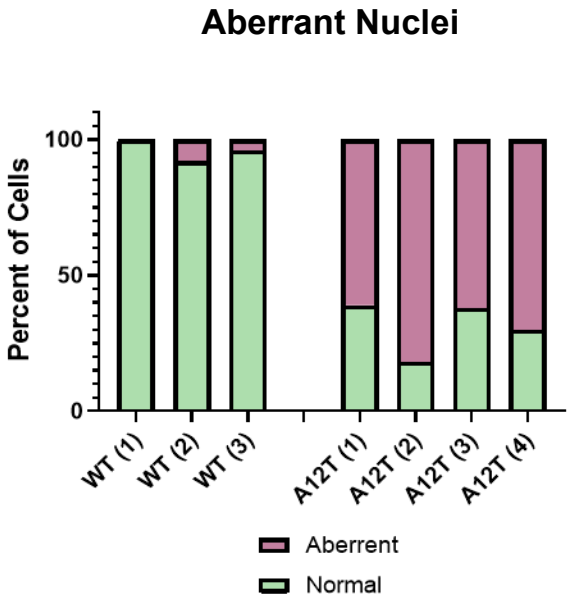

D

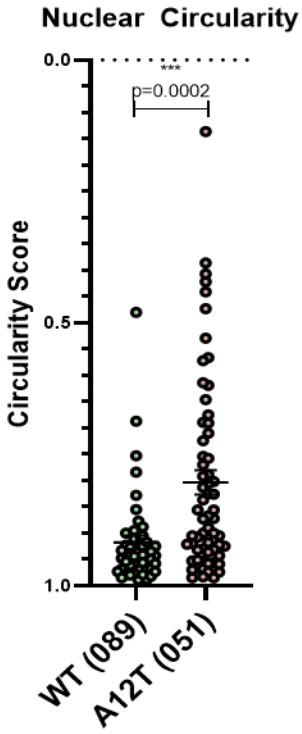

E

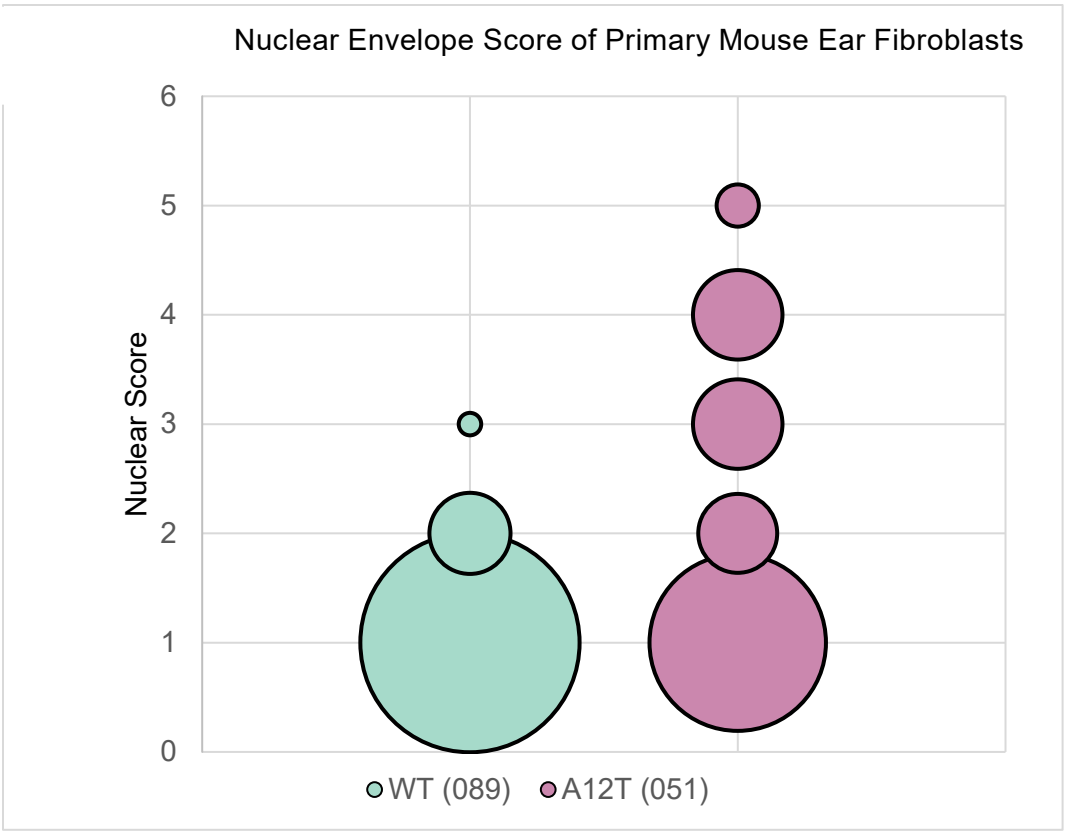
Nuclear Envelope Score of Primary Mouse Ear Fibroblasts
Nuclear Score
6
5
4
3
2
1
0
WT (089)
A12T (051)

Figure 4-10. Analysis of Growth and Nuclear Envelopathy in Primary Dermal Fibroblasts. (A) Apparent doubling of primary fibroblasts established from the outgrowth of dermal biopsies from two wild type mice and two A12T/A12T mice. N=15, significance determined by students T-tests. (2) Cells were seeded at equal densities and counted every day for 3 days by staining with Trypan Blue and counting live cells. This was repeated in 5 independent experiments and cell number was plotted against time to generate a growth curve. (C) Cells were analyzed by immunofluorescence of Lamin A for nuclear morphology abnormalities. Normal nuclei were defined by a score of 1 based on the scale defined in Molitor & Traktman 2013, and aberrant nuclei were defined by a score >1. 50-60% of the cells expressing A12T/A12T exhibited dysmorphic nuclei compared to wild type. Cells from four different mice WT mice and four A12T/A12T mice were analyzed. (D) Nuclear circularity was assessed by immunofluorescence of Lamin A, and then an automated software program assessed the nearness of the nucleus to a perfect circle, defined as 1, and the departure from a circle defined as 0>x<1. Approximately 250 cells were analyzed from fibroblasts cultures derived from one wild type mouse and one A12T/A12T mouse in 2 independent experiments. Statistical significance was determined by students T-test. (E) Using the scoring scheme defined in Molitor and Traktman 2013, cell nuclei were assigned a score of 1-6, with 1 defined as smooth round nuclei, and 6 as multinucleated and blebbed. WT primary dermal fibroblasts exhibited 87% normal nuclei, whereas only 56% of A12T/A12T dermal fibroblasts had normal nuclei, and 30% had nuclei with a score of 3 or greater.

Figure 4-11

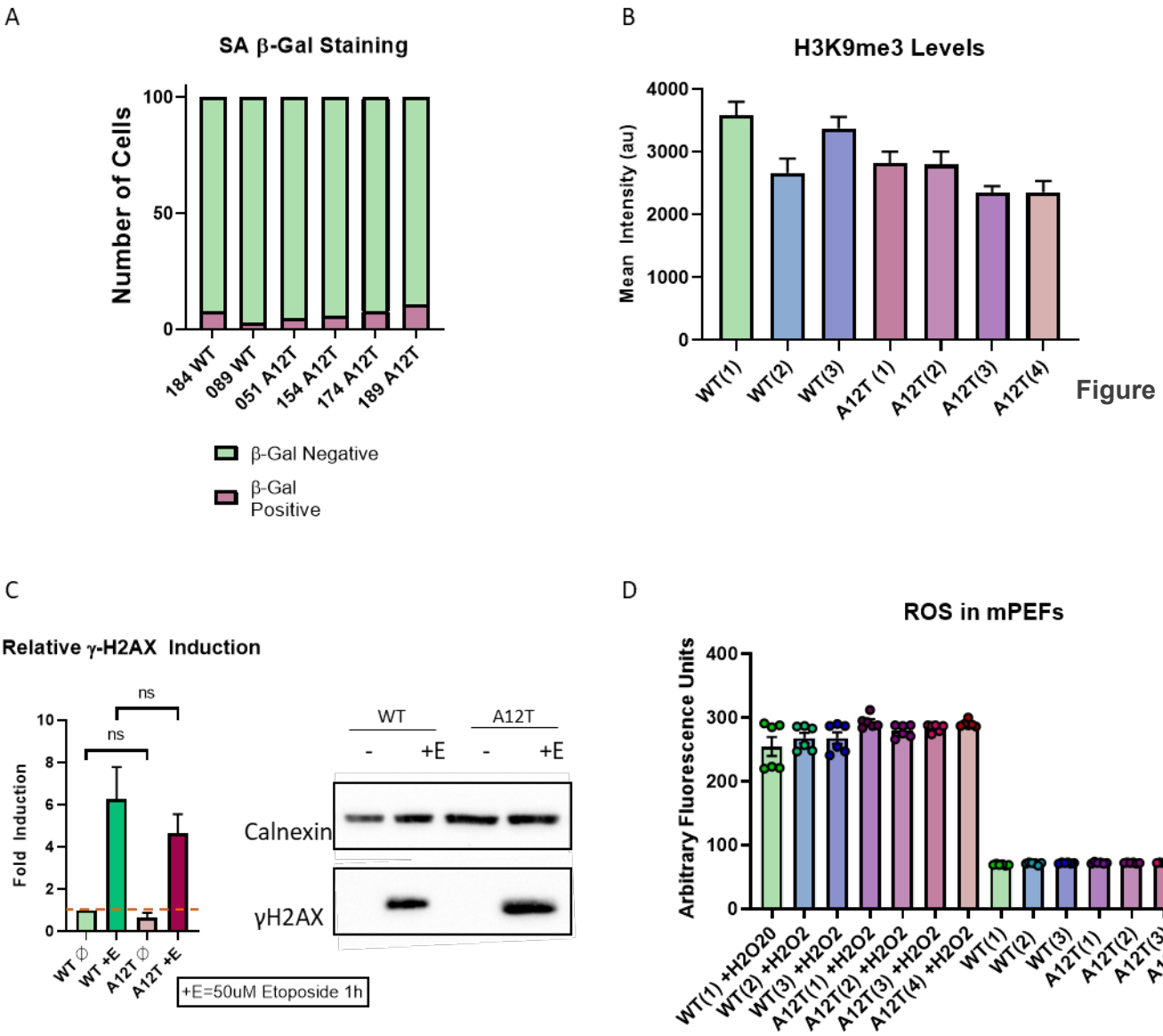
A
SA β-Gal Staining
Number of Cells
100
50
0
184 WT
089 WT
051 A12T
154 A12T
174 A12T
189 A12T
β-Gal Negative
β-Gal Positive
B
H3K9me3 Levels
Mean Intensity (au)
4000
3000
2000
1000
0
WT(1)
WT(2)
WT(3)
A12T (1)
A12T(2)
A12T(3)
A12T(4)
C
Relative γ-H2AX Induction
Fold Induction
ns
ns
10
8
6
4
2
0
WT ϕ
WT +E
A12T ϕ
A12T +E
WT
A12T
-
+E
-
+E
Calnexin
γH2AX
+E=50uM Etoposide 1h
D
ROS in mPEFs
Arbitrary Fluorescence Units
400
300
200
100
0
WT(1) +H2O20
WT(2) +H2O2
WT(3) +H2O2
A12T(1) +H2O2
A12T(2) +H2O2
A12T(3) +H2O2
A12T(4) +H2O2
WT(1)
WT(2)
WT(3)
A12T(1)
A12T(2)
A12T(3)
A12T(4)

4-11. Assessment of Premature Aging Hallmarks in Primary Dermal Fibroblasts. (A) SA β-galactosidase staining of primary dermal fibroblasts were imaged by phase microscopy and then quantified. N=3 independent experiments from cultures derived from 3 wild type mice and 3 A12T/A12T mice. (B) H3K9me3 levels in primary fibroblast nuclei were analyzed by immunofluorescence intensity. Cultures derived from 3 WT mice and 4 A12T mice were analyzed in 3 independent experiments. (C) Cells were treated with 100uM Etoposide for 1h and then subjected to immunoblotting for γH2AX as a marker of the induction of the DNA damage response pathway. This is representative of 3 independent experiments using cultures derived from 1 wild type mouse and 1 A12T/A12T mouse. (D) Cells were treated with DCFDA in order to measure the accumulation of reactive oxygen species in the cells. All cells were treated with H_2O_2 as a positive control prior to DCFDA treatment. H_2O_2 treated cells had a fluorescence intensity of greater than between 250-300 A.U., a massive increase compared to the untreated cells which have a fluorescence intensity of less than 100 A.U. with no variations between wild type and A12T/A12T mice.

Discussion

In generating a CRISPR/Cas9 A12T/A12T mouse, we were aiming to recapitulate some of the clinical manifestations of NGPS in mice. Taking the previous data from murine models of HGPS and other premature aging syndromes, we hypothesized that a novel NGPS mouse model would be a valuable tool used to elucidate the fundamental mechanisms of disease progression in a tissue-specific, systems-based approach.

Mouse models of premature aging have been able to recapitulate some of the clinical manifestations of the disease including skeletal abnormalities, failure to thrive, alopecia and other severe phenotypes. NGPS patients suffer from progressive and dramatic skeletal degeneration, scoliosis, adipolysis and alopecia. The A12T/A12T mice that we developed do not present a premature aging syndrome. Their lifespan is comparable to wild type C57/B6 mice, they grow and thrive appropriately, they do not have skeletal defects or abnormalities, and at the histologic level, A12T/A12T derived tissue is healthy and free of the hallmarks of NGPS. However, primary dermal fibroblasts derived from A12T/A12T mice do exhibit nuclear morphology defects, and in fact almost 60% of these cells display some amount of nuclear dysmorphia. This envelopathy, though, is not accompanied by the induction of stress responses or the onset of replicative senescence.

Similarly to the, WRN null mouse model, the BAF A12T/A12T mice may need to be stressed by “second hit”. Crossing A12T/A12T mice with mice that are deficient in another gene that contributes to premature aging or that is involved in mesenchymal stem cell maintenance or bone remodeling may begin to elucidate mechanisms of organismal aging involving A12T/A12T expression. In the case of HGPS, a dominant disease, mice expressing LMNA G609G/+ do not exhibit a severe phenotype compared to LMNA G609G/G609G mice. NGPS arises from the homozygous expression of BAF A12T,

therefore it in not possible to increase the severity of the inheritance. These complexities between the clinical manifestation of human progeria syndromes and the parallel mouse models aiming to recapitulate these diseases highlight the challenges of developing a mouse model to study a disease state at the organismal level.

In Chapter 3, we hypothesized that the homozygous expression of BAF A12T would result in an overall loss of heterochromatin, which in turn would alter gene expression profiles through alterations in gene accessibility. We next asked whether we could recapitulate the disease phenotype with the development of an NGPS mouse model to assess the impact of the A12T mutation on aging at the organismal level, while also establishing a primary cell line to assess the cellular phenotype too. The data shown in both Chapters 3 and 4 clearly indicate that the primary effect of the BAF A12T mutation is unlikely to be at the level of chromatin organization and architecture, and that epithelial cells in the context of MCF-10a cells, and primary fibroblasts derived from an A12T/A12T both do not exhibit the effects of premature aging despite exhibiting a severe nuclear envelopathy.

In continuing to ask how BAF A12T contributes to premature aging, we shifted our focus from epigenetic modulation to other ways that BAF A12T may be affecting the nuclear envelope and why the clinical manifestations preferentially impact tissue of mesenchymal origin. As we were completing our analysis of the work described in this chapter, a publication from the Zinn-Justin lab (Samson et al., 2018) revealed a key finding that shifted our paradigm of BAF function. Samson et al. presented the first ternary structure of Emerin, BAF and the IgG fold of Lamin A. Residue ala^{12} of BAF is found on the surface of BAF that binds to Lamin A, and indeed is buried in the interface. This indicated to us that our assessment of BAF function would not be complete if we did not

integrate binding to Lamin A in our future analyses. Therefore, to continue to assess how BAF A12T affects the structure and function of the nucleus, our subsequent studies were performed using iPSCs that carried +/+ or A12T/A12T alleles at the endogenous BANF1 locus. These isogenic, pluripotent cells can be further differentiated to different cell types to assess the impact of the mutation.

Chapter 5: The Assessment of BAF A12T Expression in Mesenchymal Stem Cell Maintenance

Introduction

The use of patient-derived cells as a method to study premature aging syndromes has been a historically powerful method to study the molecular mechanisms behind the disease state. The ability to reprogram patient cells in to pluripotent cells provides the opportunity to model disease development and progression through the differentiation program. As reviewed in Carrero et al in 2016, several studies have been able to demonstrate upon reprogramming somatic cells taken from progeria patients, there was a reversal in age-related phenotypes reversal in age-related phenotypes including increased telomere length, loss of senescence and a restoration of mitochondrial fitness (Carrero, Soria-Valles, & López-Otín, 2016). The modeling done by previous labs in the study of HGPS have helped frame and inform subsequent studies of premature aging syndromes at the cellular level.

Human iPSCs resemble human embryonic stem cells in that they have the ability to differentiate into all somatic cells of the body (Bellin, Marchetto, Gage, & Mummery, 2012). Studying iPSCs is particularly important in the case of premature aging, where cells are difficult to culture and study as a result of their replicative senescence. The limitation arising from the use of reprogrammed patient cells is the unavailability of matched control cells with identical genetic background; therefore, the study of patient cells compared to control cells is not a direct comparison. While this is an accepted methodology, the use of CRISPR/Cas9 technology to generate iPSCs with a homozygous BAF A12T mutation and a matched isogenic control is a more direct method of studying the contribution A12T to cellular aging.

Patients with NGPS do not begin to exhibit symptoms until approximately two years of age, highlighting that this is not a developmental disorder but rather a degenerative one. Patients suffer from severe osteolysis, adipolysis and craniofacial defects indicating that tissue arising from mesenchymal origin are preferentially affected (R. Cabanillas et al., 2011; Puente et al., 2011).

At the onset of our study of BAF and A12T's roles at the nuclear periphery, we initially hypothesized that the contribution of A12T to premature cellular aging would result from alterations in chromatin organization and changes in overall gene accessibility and gene expression. The data indicated that the impact of A12T was not on the level of chromatin architecture. However, data from the Zinn-Justin lab indicate that Alanine 12 is found on the surface of BAF that binds to the Ig Fold of Lamin A, and that the A12T mutation is buried in this binding surface (Samson et al., 2018). Furthermore, since the BAF A12T-associated progeria primarily affects tissues of mesenchymal origin, we shifted from the use of mammary epithelial cells to performing our studies using iPSCs that carried +/+ or A12T/A12T alleles at the endogenous BANF1 locus. These isogenic, pluripotent cells can be further differentiated to different cell types to assess the impact of the mutation.

Rationale

Progerias offer a pathologic model that mirrors accelerated physiologic aging. The study of these models has been instrumental in identifying and characterizing genetic mutations that perturb NE structure and function. The tissue-specificity of NGPS is poorly understood, but the impact on tissues of mesenchymal origin has led to the **hypothesis that survival, proliferation or differentiation of mesenchymal stem cells (MSCs) is perturbed**. Patient fibroblasts exhibit dysmorphic nuclei, however the molecular

mechanisms behind premature cellular aging in A12T -expressing cells is still unclear.

The homozygous expression of A12T causes dysmorphic nuclei in all cells, but the impact of the envelopathy varies between cell types. Using isogenic WT and A12T/A12T iPSCs, we aimed to differentiate them to induced MSCs (iMSCs). Using this model and the data from Samson et al. 2018, we **hypothesize that defective BAF-Lamin A interactions compromise the structural network of the nuclear lamina and weaken the nuclear envelope.**

Results

Generating iMSCs and hepatocytes from iPSCs

HGPS also preferentially affects cells of mesenchymal origin, and through the study of reprogrammed patient derived cells and genetically manipulated stem cells that express Progerin, the cell-type specific pathologies have been attributed to stem cell exhaustion and differentiation defects (Halaschek-Wiener & Brooks-Wilson, 2007; Scaffidi & Misteli, 2008). NGPS preferentially affects tissues arising from mesenchymal origin (R. Cabanillas et al., 2011). In order to ask whether the mesenchymal stem cell defects observed in HGPS are mirrored in the case of NGPS, we sought to generate a mesenchymal stem cell line derived from iPSCs expressing A12T. Applied Stem Cell generated two BAF A12T/A12T cell lines (derived from ASE-9203 iPSCs) using CRISPR/Cas9 technology to change the codon sequence encoding Alanine 12 in Exon 2 of the endogenous BANF1 gene locus. iPSCs must be cultured and passaged on Matrigel coated dishes and do not express Lamin A, and as such, do not exhibit nuclear envelope dysmorphia (Dan Constantinescu, Heather L Gray, Paul J Sammak, Gerald P Schatten, & Antonei B Csoka, 2006). In order to address the tissue specificity behind NGPS, we

differentiated iPSCs to induced mesenchymal stem cells, and to a cell type that is unaffected by NGPS such as hepatocytes.

To generate iMSCs, iPSCs were plated on Matrigel coated dishes and cultured in FBS-containing media for 21 days in a protocol developed from Zhang et al. who generated iMSCs and vascular smooth muscle cells from iPSCs to study the contribution of Progerin expression in these models (Zhang et al., 2011). After the 21st day, cells were passaged onto dishes coated with 0.1% gelatin, and after three passages, cells were plated on uncoated tissue culture dishes. The success of this protocol is measured by the ability of the cells to continue to proliferate on uncoated culture dishes. When iPSCs are cultured on Matrigel, they appear circular and grow in colonies, with no observable differences between WT and A12T cells. When the cells transition into FBS-containing media, they begin to grow in a tightly packed monolayer and develop a lenticular shape until they are passaged on gelatin, where they elongate and become spindle-shaped and maintain tight packing between the cells. Once on plastic, wild type cells maintain a similar phenotype as when they are cultured on gelatin. However, when A12T expressing cells are cultured on plastic, they lose the spindle shape and the cytoplasm spreads to form a circular shaped cell. This is the first key difference that we observed between wild type cells and A12T expressing cells (Figure 5-1 A-B).

Pluripotent stem cells do not express Lamin A, whereas differentiated cells do. Lamin A/C is thought to play a role in the maintenance of differentiated cells. It is also acts as an important factor in stem cell differentiation and plays a role in the differentiation of MSCs into osteoblasts and adipocytes (Bermeo, Vidal, Zhou, & Duque, 2015; Dan Constantinescu et al., 2006). Lamin B, is present in all cell types, and Lamin B expression is highest in pluripotent stem cells (D. Constantinescu, H. L. Gray, P. J. Sammak, G. P.

Schatten, & A. B. Csoka, 2006). The expression of Lamin B is required for proper organogenesis and cells that are deficient in Lamin B have misshapen nuclei and undergo premature cellular senescence (Y. Kim et al., 2011; Vergnes, Péterfy, Bergo, Young, & Reue, 2004). WT and A12T iPSCs express Emerin at equal steady state levels across differentiation. As expected, iPSCs do not express do not express Lamin A, and express Lamin B1. Once iPSCs are differentiated into iMSCs, Lamin A steady state levels increase and Lamin B1 levels decrease; however there is no significant difference between the levels of Lamin A or Lamin B steady state levels between WT iMSCs and A12T iMSCs (Figure 5-1 C).

The further characterization of the iMSCs will be discussed in upcoming sections, however we first wanted to demonstrate that any differences we observed in A12T expressing iMSCs were a direct result of the cell type specificity. Therefore, in order to ask whether the phenotypes observed in A12T iMSCs are cell type specific, examined the effect of A12T expression in a cell type that is not affecting in NGPS patients. Hepatocytes are terminally differentiated epithelial cells of the liver which express Lamin A (Barboro, D'Arrigo, Repaci, Patrone, & Balbi, 2010). Using a well-defined differentiation protocol established by our MUSC colleague Stephen Duncan's lab, WT or A12T iMSCs were differentiated into hepatocytes (Si-Tayeb et al., 2010). Of note, when iPSCs are differentiated into hepatocytes, they remain on a Matrigel substrate throughout differentiation. Furthermore, induced Hepatocytes are quiescent and unable to be further cultured once they are terminally differentiated.

When iPSCs were differentiated into hepatocytes (kindly performed by our collaborator Ray Liu), the overall cellular morphology between wild type and A12T expressing cells was indistinguishable. Moreover, the ability of A12T iPSCs to differentiate

into hepatocytes and express hepatocyte specific markers was just as efficient at wild type (Figure 4-2 A). WT iHepatocytes and A12T iHepatocytes exhibited similar steady state levels of Apolipoprotein B (Apo B) and HNF4α, two functional markers of hepatocytes. iHepatocytes were then subjected to SA-β-Gal staining. The great majority of WT and A12T-expressing hepatocytes were overwhelmingly negative for SA-β-Gal staining, with only ~10% of the population staining partially positive or positive with Blue-Gal (Figure 5-2 B). Lastly, we examined whether A12T-expressing hepatocytes exhibited a nuclear envelopathy. Nuclear dysmorphia was scored as described previously. A12T expressing hepatocytes exhibited a mild nuclear envelopathy, reinforcing the fact that A12T expression in any cell type results in aberrant nuclear envelope architecture.

Figure 5-1

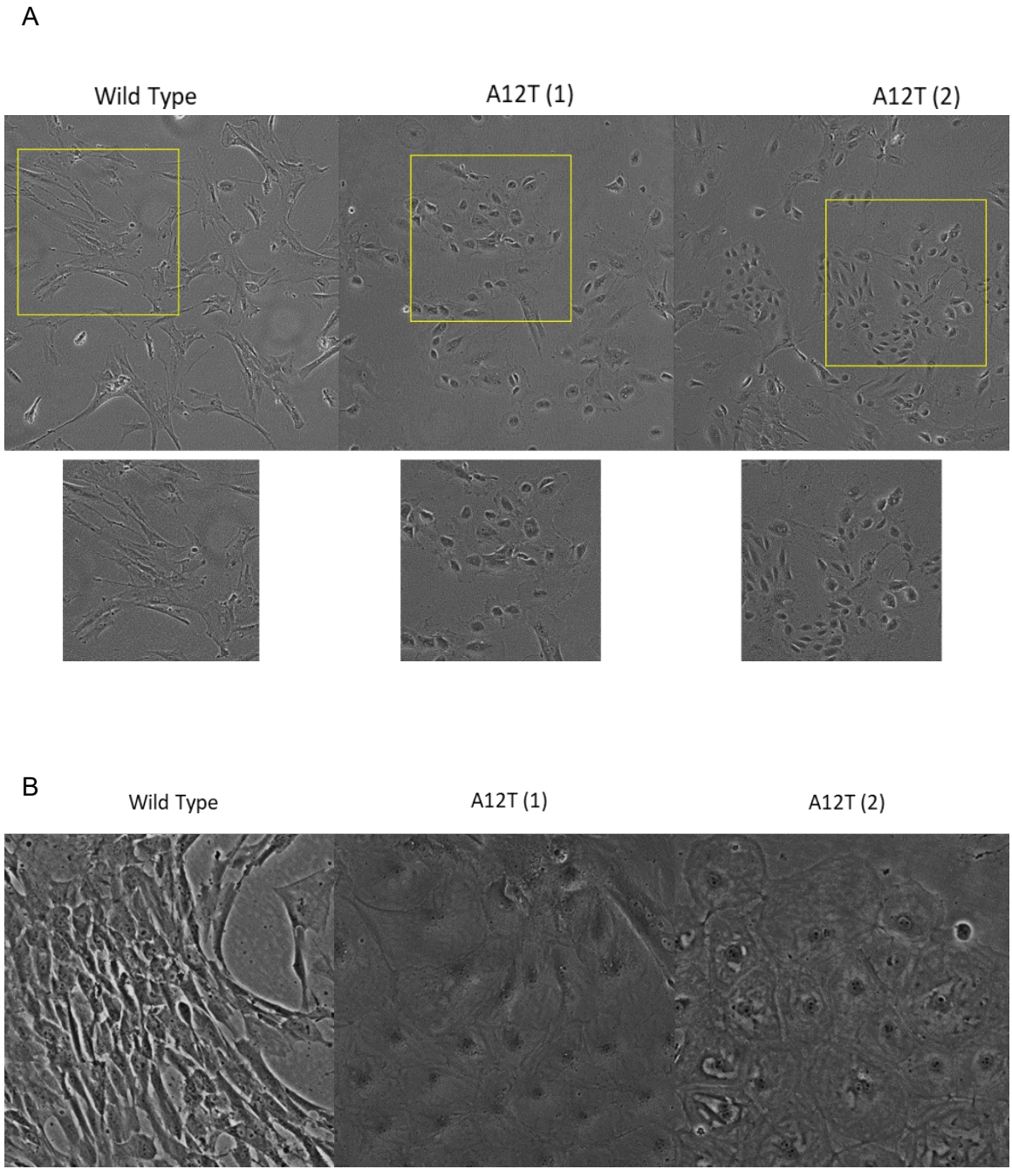

C

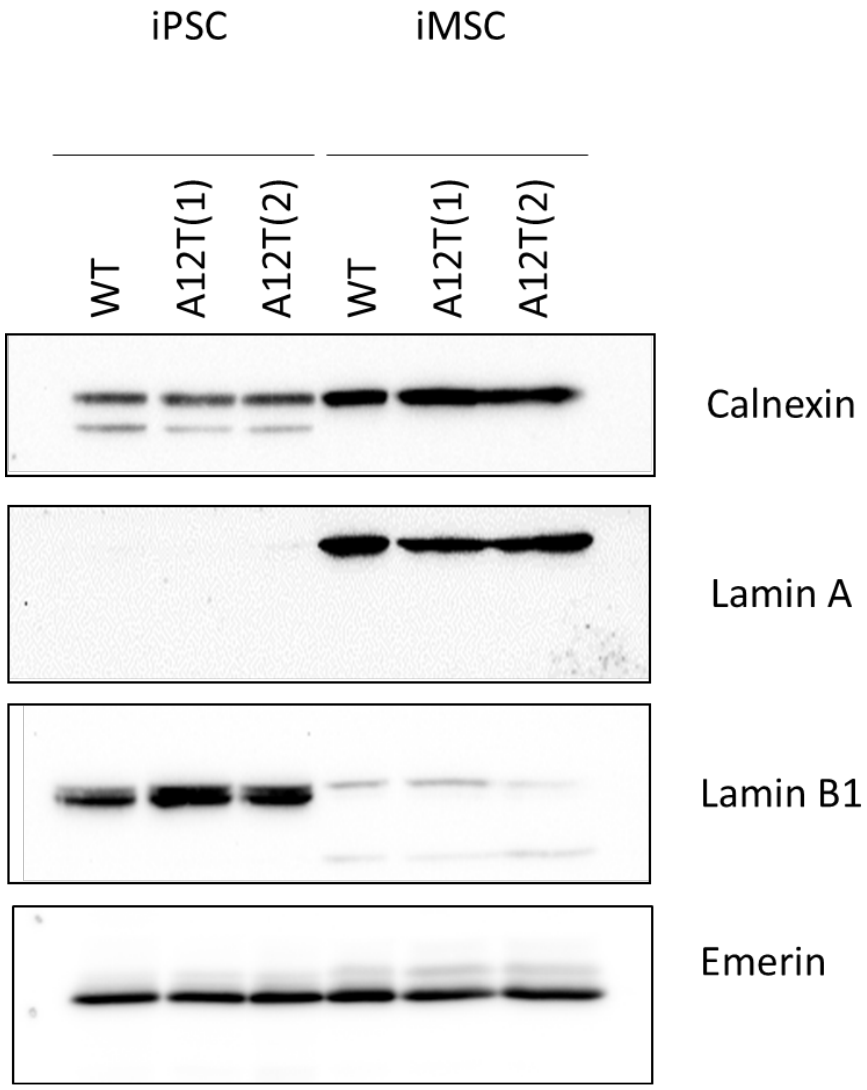
iPSC
iMSC
WT
A12T(1)
A12T(2)
WT
A12T(1)
A12T(2)
Calnexin
Lamin A
Lamin B1
Emerin

Figure 5-1. Principal Characterization of iMSCs. (A) Phase microscopy images at 20x magnification of WT and A12T iMSCs in their first passage on plastic. As evidenced by the inlaid images, WT iMSCs exhibit elongated, spindle shaped morphology, whereas A12T expressing iMSCs exhibit lenticular shaped nuclei and a more rounded cell body. (B) Phase microscopy images at 40x magnification p.3 on plastic. The shape of the cells is divergent between WT iMSCs and A12T iMSCs. Where WT iMSCs are elongated and spindle-shaped and pack in a tight monolater, A12T expressing cells are circular and the cytoplasm is spread out. Furthermore, A12T iMSCs form clusters on the culture plastic rather than a cohesive monolayer. (C). The steady state levels of Lamin A, Lamin B1 and Emerin were analyzed by immunoblotting. The steady state levels of Emerin do not change between WT and A12T expressing cells, nor did they differ between iPSC and iMSCs. Lamin A is not expressed in iPSCs, and is expressed in high levels in MSCs, however there is no difference in the steady state levels of Lamin A between WT and A12T expressing iMSCs. Lamin B1 is highly expressed in pluripotent cells and diminishes in differentiated cells. WT and A12T iPSCs express Lamin B at similar steady state levels and Lamin B1 levels diminish after differentiation to iMSCs in both A12T and WT expressing cells

Figure 5-2

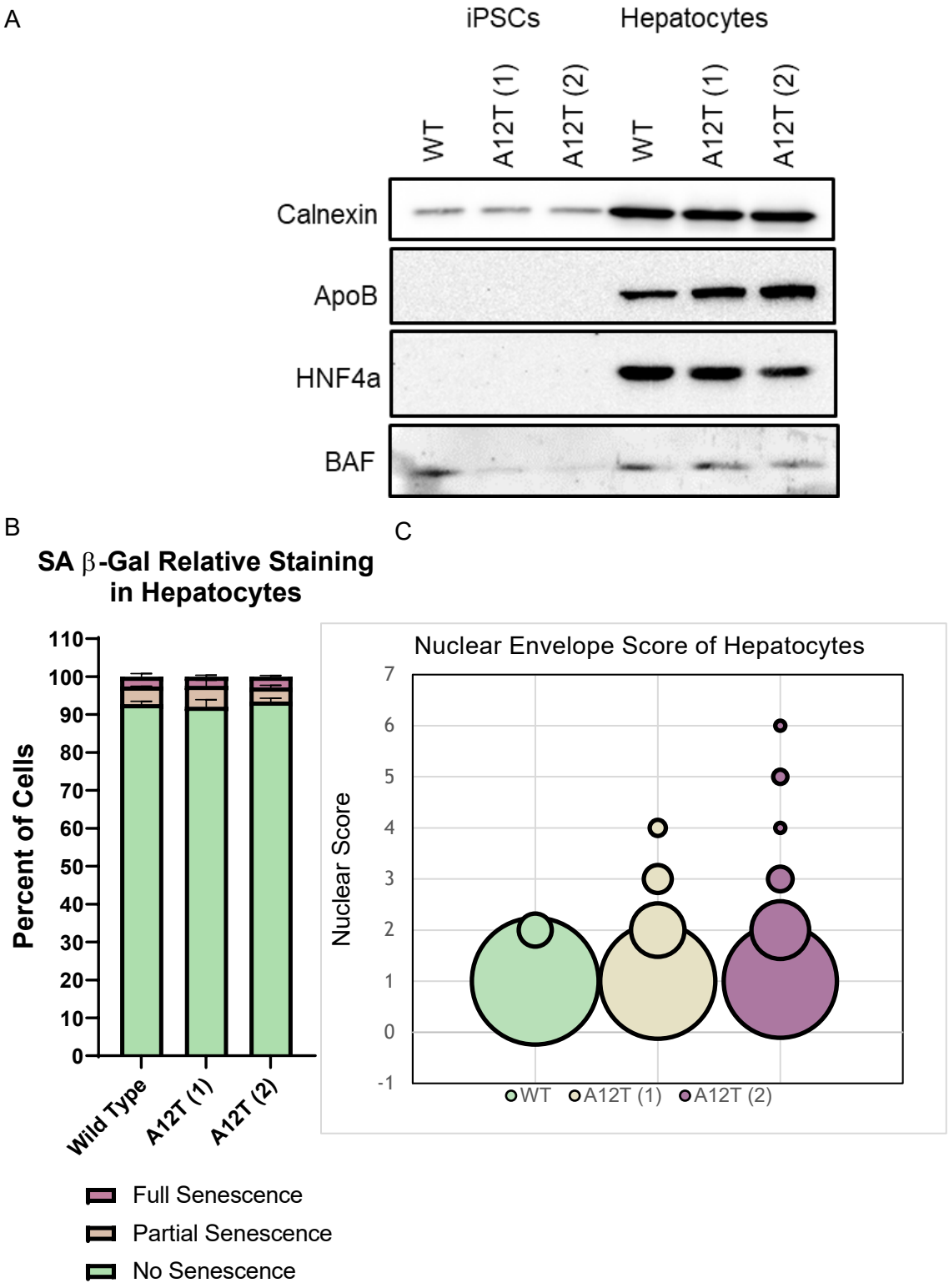
A
iPSCs
Hepatocytes
WT
A12T (1)
A12T (2)
WT
A12T (1)
A12T (2)
Calnexin
ApoB
HNF4a
BAF
B
SA β-Gal Relative Staining in Hepatocytes
Percent of Cells
110
100
90
80
70
60
50
40
30
20
10
0
Wild Type
A12T (1)
A12T (2)
Full Senescence
Partial Senescence
No Senescence
C
Nuclear Envelope Score of Hepatocytes
Nuclear Score
7
6
5
4
3
2
1
0
-1
WT
A12T (1)
A12T (2)

Figure 5-2. Assessment of A12T Expressing Hepatocytes. WT and A12T expressing iPSCs were differentiated into hepatocytes. (A) Immunoblot analysis of two hepatocyte markers, Apolipoprotein B (ApoB) and HNF4α, reveals that there is no significant difference in the steady state levels of these proteins n=4. (B) SA-β-Gal treatment of hepatocytes was performed n=3 and cells were designated “negative”, “partial” or “full” for Blue-Gal staining as described above. 90% of these cells exhibited no Blue-Gal staining, indicating that BAF A12T-expressing hepatocytes do not become senescent. (C) Nuclear envelope score was determined by using the scoring scheme from Molitor & Traktman 2014. A12T expressing hepatocytes exhibited a nuclear envelopathy compared to WT hepatocytes as expected n=4.

Characterizing A12T expressing iMSCs by Flow Cytometry and Differentiation Potential

Mesenchymal Stem Cells (MSCs) are multipotent stromal-like cells that are derived from the mesoderm (Pittenger et al., 1999). They are found in a variety of tissue including bone marrow, adipose tissue, bone, cartilage and the umbilical cord and are able to differentiate into the associated cell types to repair damaged tissue (C. Chen & Hou, 2016; Divya et al., 2012). In 2006, the International Cellular Therapy Society established the minimal criteria to define mesenchymal stem cells: 1) They must adhere to and proliferate on tissue culture plastic 2) They must express CD73/CD90 and CD105 and must not contain CD45, CD45, CD20 or CD14 and 3) they must maintain their ability to differentiate into adipocytes, osteoblasts and chondrocytes (Dominici et al., 2006). While MSCs are derived from the mesoderm and are defined by their ability to differentiate into adipocytes, osteoblasts and chondrocytes, studies have also shown that they exhibit plasticity in their potency and are able to differentiate into cells of the ectodermal layer such as neurons, and cells of the endodermal layer such as myocytes (C. Chen & Hou, 2016; Divya et al., 2012). Importantly, mesenchymal stem cells exhibit a homing capacity, in which they migrate to damaged tissue where they mitigate the immune response at the site of damage, and contribute to the healing process through tissue regeneration and the inhibition of fibrosis (Klopp, Gupta, Spaeth, Andreeff, & Marini III, 2011).

To continue our analysis of the iMSCs we generated, we sought to examine the functional characteristics of the cells. Building on the minimal requirements of defining an MSC, we characterized iMSCs as cells that are able to adhere to, and proliferate on, tissue culture plastic. By extrapolation from the literature regarding bone marrow-derived mesenchymal stem cells, we postulated that our iMSCs should express the surface markers CD90, CD73 and CD105, and should be negative for CD34, CD45, CD20 and

CD14 (Dominici et al., 2006). Finally, and importantly, our iMSCs should be able to differentiate into cells of mesenchymal lineage such as osteoblasts and pre-adipocytes. We used commercially available mesenchymal stem cells as a positive control, this presented a caveat because these cells are derived from the adipose tissue of patients undergoing liposuction, and therefore, these commercial MSCs are considered hASCs, human adipose-derived MSCs. It is important to highlight this difference, because human mesenchymal stem cells arise from within the niche of the bone marrow or resident tissue and are exposed to a variety of signaling molecules that inform the surface markers of human-derived primary cells. Furthermore, conventionally MSCs are derived from the bone marrow (BMMSCs), a site of residence of hematopoietic stem cells (HSCs), therefore the importance of the surface markers is a method to distinguish HSCs from BMMSCs.

We first performed flow cytometry on commercial MSCs and wild type iMSCs by staining cells with surface marker-specific antibodies conjugated to different fluorophores: CD90-FITC, CD73-APC and CD105-PE, while the negative surface markers were all conjugated with –PerCP. We gated on live, individual cells to conduct our analyses and asked whether there were variations in the staining of any of these surface markers. As expected, neither the commercial MSCs nor our iMSCs expressed CD34/CD45/CD20/CD14. Both commercial MSCs and wild type iMSCs stained positive for both CD90 and CD73; however, our wild type iMSCs did not express CD105. (Figure 5-3 D). While Domincini et al. defined the three positive surface markers that *must* be present in mesenchymal stem cells, other studies have shown that a subpopulation of $CD105^-$ mesenchymal stem cells are refractory to TGF-β signaling and that have an increased capacity for osteogenic differentiation (Levi et al., 2011).

Building on these data, we performed lineage differentiations in which commercial MSCs and iMSCs were cultured in adipogenic-defined or osteogenic-defined media to generate pre-adipocytes and osteoblasts respectively. Commercial MSCs and wild type iMSCs both effectively differentiate into pre-adipocytes and osteoblasts as assessed by Oil-Red-O staining for adipocytes or Alizarin Red for osteoblasts (Figure 5-3 B). In fact, wild type iMSCs differentiated into osteoblasts at a greater efficiency than commercial MSCs, confirming the finding from Levi et al. that CD105 negative mesenchymal stem cells function effectively as mesenchymal stem cells. Cumulatively, these data gave us the confidence that our mesenchymal stem cell differentiation protocol was effective and resulted in functional MSCs (Figure 5-3 B).

We therefore moved next to the differentiation and characterization of A12T-expressing iPSCs into iMSCs in order to assess the impact of A12T on mesenchymal stem cells. We performed flow cytometry on wild type and A12T iPSCs and iMSCs in order to observe the shift from iPSC-associated surface marker expression to iMSC-associated surface marker expression (Figure 5-4). We found that WT and A12T iPSCs all expressed CD90 (expected, as CD90 is a marker of stem cells) to similar levels, and they were all negative for the expression of CD73/CD105 and CD34/CD45/CD20/CD14. When differentiated into mesenchymal stem cells, and assessed at their first three passages on plastic, A12T expressing iMSCs expressed CD90 to a similar level as WT iMSCs. Whereas WT iMSCs expressed CD73, A12T iMSCs did not. Additionally, and as expected from the data shown below (Figure 5-4), neither WT iMSCs nor A12T iMSCs expressed CD105, or CD34/CD45/CD20/CD14. Over time, A12T iPSCs begin to express one of the negative CD34/CD45/CD20/C14 markers (although we are unable to distinguish which one since they are all conjugated with the same fluorophore).

These data indicate that A12T iMSCs are have a reduced capacity to differentiate into mesenchymal stem cells compared to WT iMSCs. This was further confirmed during a differentiation assay in which WT iMSCs and A12T iMSCs were cultured in adipogenic-defined or osteogenic-defined media on plastic tissue culture dishes. While WT iMSCs differentiated into pre-adipocytes and osteoblasts, A12T iMSCs all detached from the culture surface and died (data not shown). These data suggested that A12T expressing cells exhibited defects in differentiating into functional mesenchymal stem cells however, we noticed that the defect occurred over time, during passaging on plastic culture dishes. This lead us to believe that: either A12T iMSCs might functionally arrive at iMSCs but are unable to withstand culture conditions, or are unable to differentiate into iMSCs at all. We aimed to investigate this question further and sought to understand the etiology of the A12T iMSC phenotype.

Figure 5-3

A

FITC-CD90+

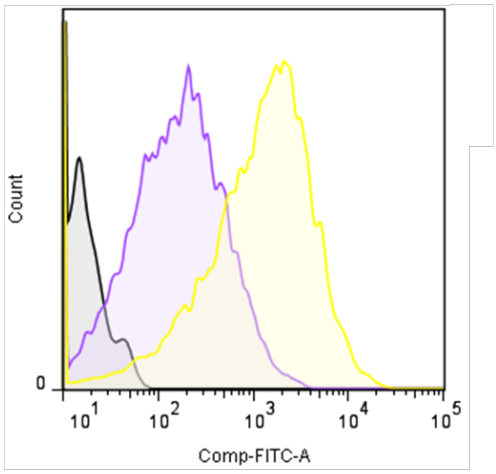

Population Name
Specimen_001_LaCells_015.fcs
Specimen_001_Px+_014.fcs
Specimen_001_B's_013.fcs

APC-CD73+

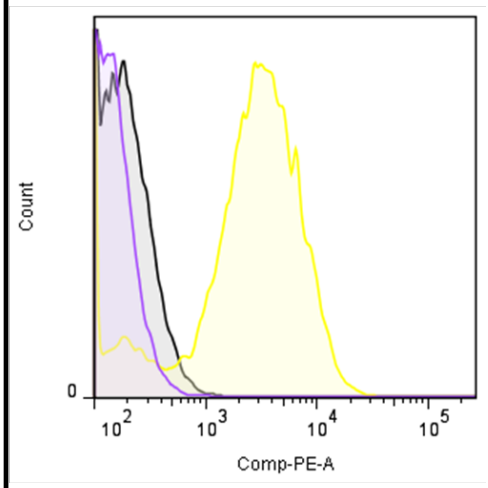

Population Name
Specimen_001_LaCells_015.fcs
Specimen_001_Px+_014.fcs
Specimen_001_B's_013.fcs

PE-CD105+

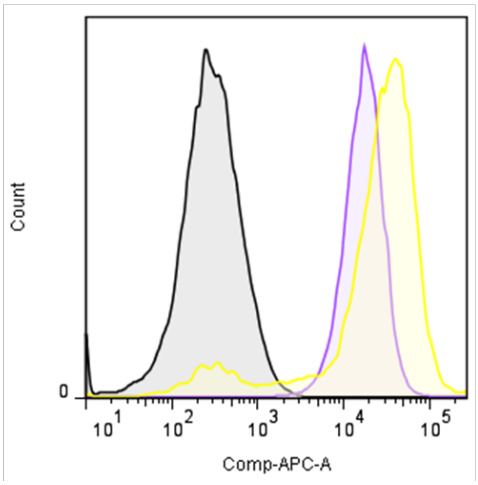

Population Name
Specimen_001_LaCells_015.fcs
Specimen_001_Px+_014.fcs
Specimen_001_B's_013.fcs

PerCP-CD34-/CD45-/CD20-/CD14-

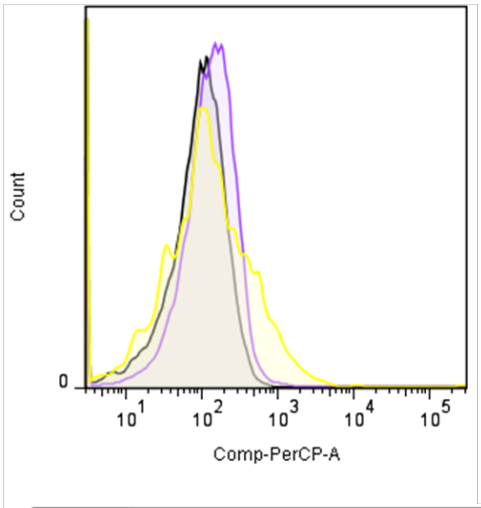

Population Name
Specimen_001_LaCells_015.fcs
Specimen_001_Px+_014.fcs
Specimen_001_B's_013.fcs

B

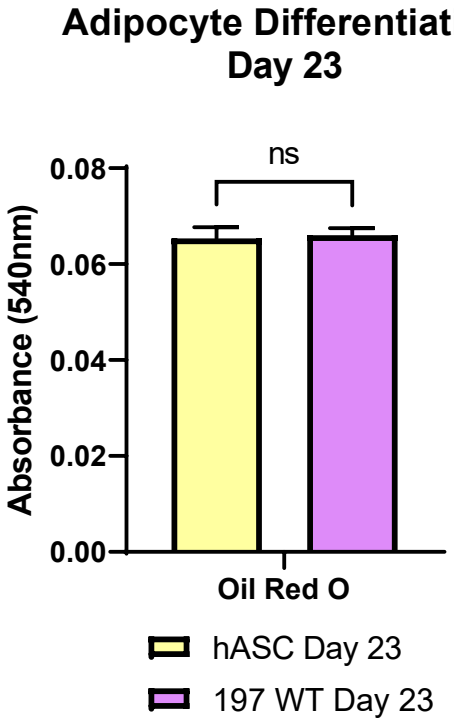
Adipocyte Differentiation
Day 23
ns
0.08
0.06
0.04
0.02
0.00
Absorbance (540nm)
Oil Red O
hASC Day 23
197 WT Day 23

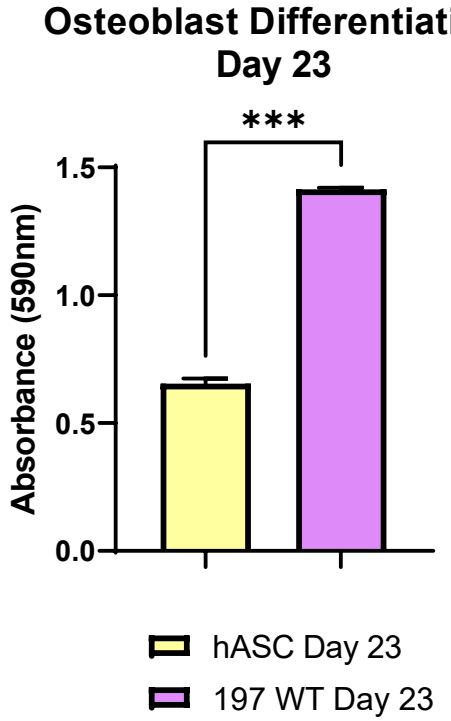
Osteoblast Differentiation
Day 23
***
1.5
1.0
0.5
0.0
Absorbance (590nm)
hASC Day 23
197 WT Day 23

Figure 5-3. Characterization of iMSC Phenotype (A) 10,000 cells were analyzed by flow cytometry. Live, individual cells were gated on and the histograms of expression of CD90, CD73, CD105 and CD34/CD45/CD20/CD14 were plotted. Monkey kidney epithelial cells, BSC40s, (Bs-Black) were used as a negative control for MSCs Commercial MSCs (LaCells-yellow) highly express CD90/CD73/CD105 and do not express CD/34/CD/45/CD20/CD14 as expected. Normal, human derived bone marrow stem cells were analyzed (Px-Purple) as well; however their expression profiles indicate that they are CD73 negative subpopulation but they were not used for further experimentation. (B) Absorbance of Oil Red O staining for Pre-Adipocyte staining and of Alizarin Red for Osteoblast staining. Samples were stained on day 23 of differentiation and then stain was solubilized and quantified by spectrophotometer at the appropriate wavelengths for the stain. Crystal Violet staining was used to normalize for cell number, and the absorbance was graphed. N=2 independent experiments, each performed in triplicate. Statistical significance was determined by Student's T-Test

Figure 5-4

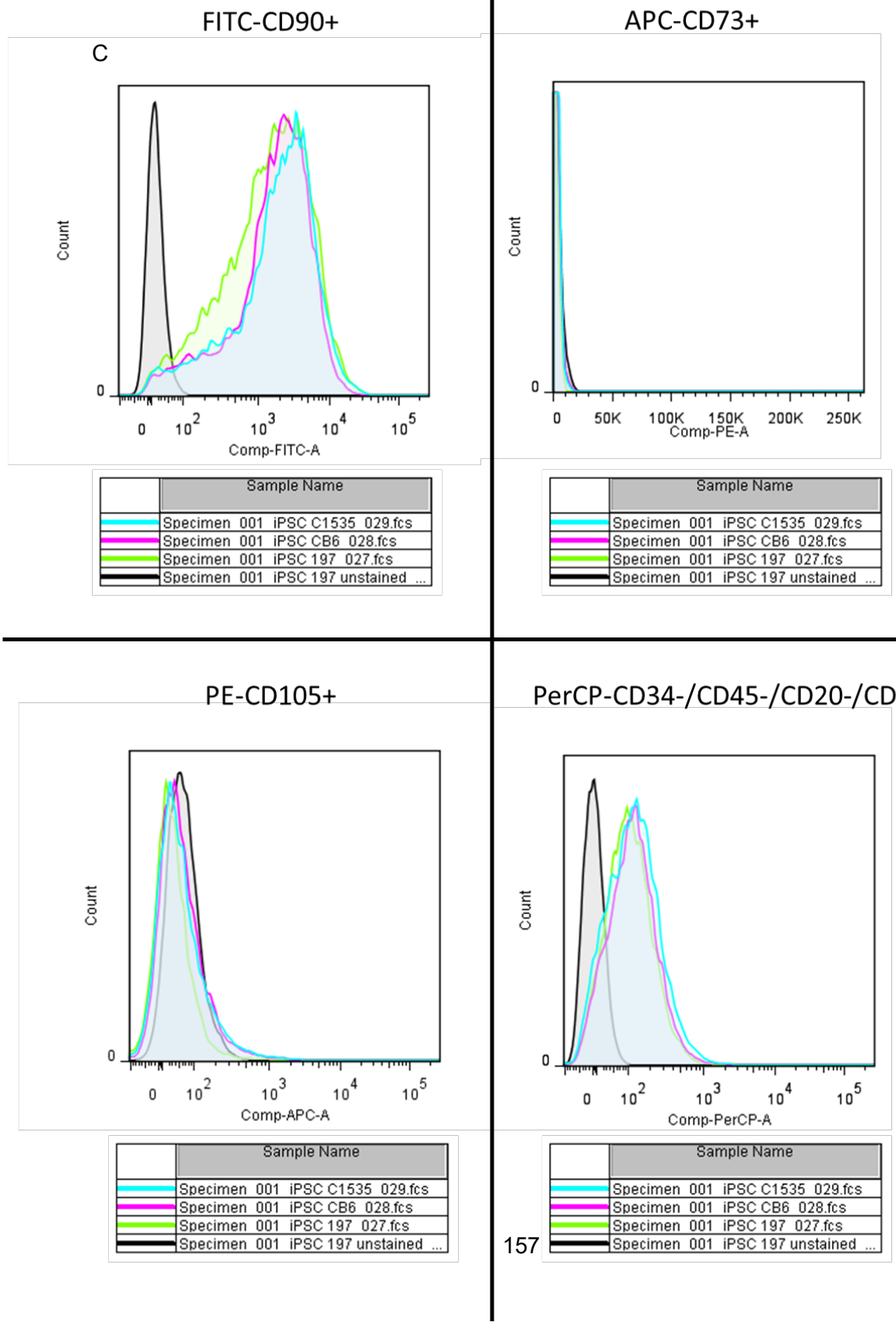
FITC-CD90+
C
Count
0
0
10^2
10^3
10^4
10^5
Comp-FITC-A
Sample Name
Specimen_001_iPSC C1535_029.fcs
Specimen_001_iPSC CB6_028.fcs
Specimen_001_iPSC 197_027.fcs
Specimen_001_iPSC 197 unstained ...
APC-CD73+
Count
0
0
50K
100K
150K
200K
250K
Comp-PE-A
Sample Name
Specimen_001_iPSC C1535_029.fcs
Specimen_001_iPSC CB6_028.fcs
Specimen_001_iPSC 197_027.fcs
Specimen_001_iPSC 197 unstained ...
PE-CD105+
Count
0
0
10^2
10^3
10^4
10^5
Comp-APC-A
Sample Name
Specimen_001_iPSC C1535_029.fcs
Specimen_001_iPSC CB6_028.fcs
Specimen_001_iPSC 197_027.fcs
Specimen_001_iPSC 197 unstained ...
PerCP-CD34-/CD45-/CD20-/CD14-
Count
0
0
10^2
10^3
10^4
10^5
Comp-PerCP-A
Sample Name
Specimen_001_iPSC C1535_029.fcs
Specimen_001_iPSC CB6_028.fcs
Specimen_001_iPSC 197_027.fcs
Specimen_001_iPSC 197 unstained ...

D

FITC-CD90+

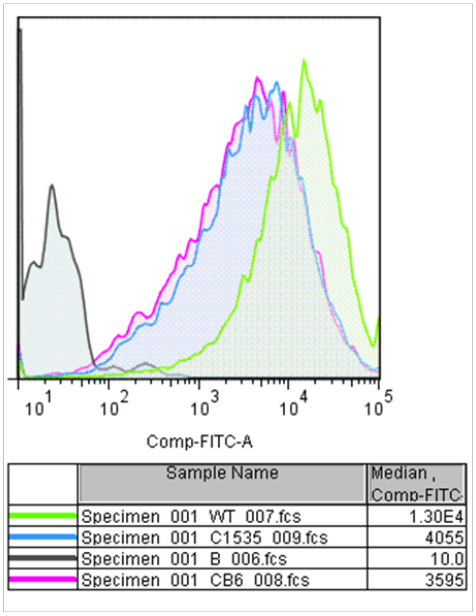

Sample Name	Median , Comp-FITC
Specimen_001_WT_007.fcs	1.30E4
Specimen_001_C1535_009.fcs	4055
Specimen_001_B_006.fcs	10.0
Specimen_001_CB6_008.fcs	3595

APC-CD73+

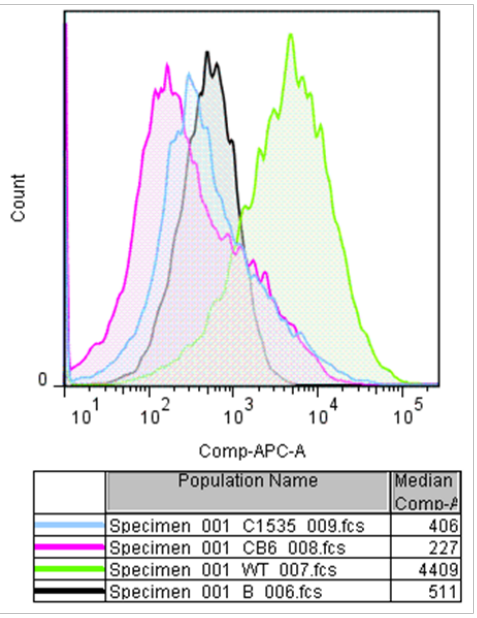

Population Name	Median Comp-A
Specimen_001_C1535_009.fcs	406
Specimen_001_CB6_008.fcs	227
Specimen_001_WT_007.fcs	4409
Specimen_001_B_006.fcs	511

PE-CD105+

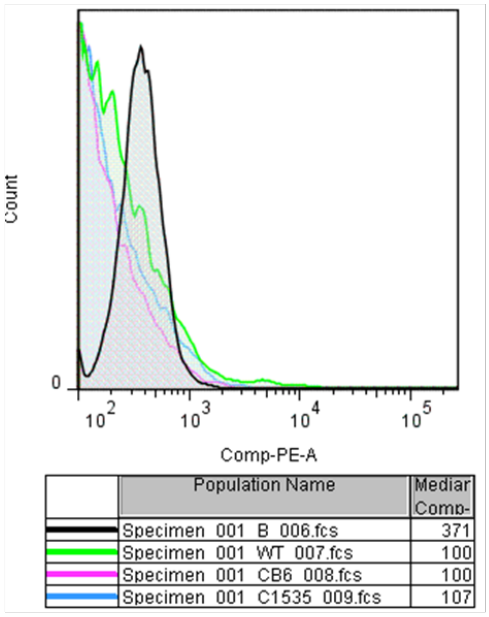

Population Name	Median Comp-
Specimen_001_B_006.fcs	371
Specimen_001_WT_007.fcs	100
Specimen_001_CB6_008.fcs	100
Specimen_001_C1535_009.fcs	107

PerCP-CD34-/CD45-/CD20-/CD14-

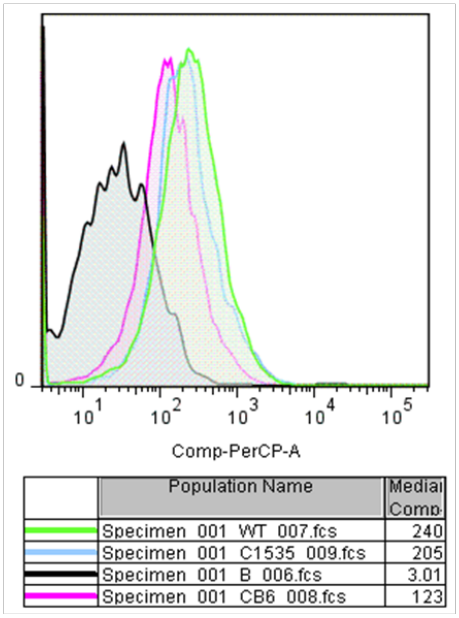

Population Name	Median Comp-
Specimen_001_WT_007.fcs	240
Specimen_001_C1535_009.fcs	205
Specimen_001_B_006.fcs	3.01
Specimen_001_CB6_008.fcs	123

Figure 5-4. Flow Cytometry Analysis of iPSC and iMSC Surface Markers. 10,000 cells were analyzed by flow cytometry. Live, individual cells were gated on and the histograms of expression of CD90, CD73, CD105 and CD34/CD45/CD20/CD14 were plotted. Monkey kidney epithelial cells, BSC40s, (Bs-Black) were used as a negative control for MSCs (A) iPSCs were analyzed for their surface marker expression prior to differentiation. WT iPSCs (iPSC 197-green) and A12T iPSCs (iPSC CB6-pink & iPSC C1535-blue) both express CD90 but do not express CD73, CD105 or CD34/CD45/CD20/CD14. (B) iMSCs were analyzed by flow cytometry at passages 1, 2 and 3 (representative image of p.2 iMSCs). WT iMSCs (WT-green) express CD90 and CD73. They do not express CD105, nor do they express CD34/CD45/CD20/CD14. A12T iPSCs (CB6-pink & C1535-blue) express CD90, but do not express CD73 or CD105, nor do they express CD34/CD45/CD20/CD14.

BAF A12T iMSCs Have Dysmorphic Nuclei

The homozygous expression of A12T in all cell types results in a dysmorphic nuclear envelope. To begin to address the impact of A12T expression on iMSC function, we examined nuclear envelope morphology. Cells were stained using a Vimentin antibody as a positive marker for mesenchymal stem cells or stromal cells, and a Lamin A antibody to delineate the nuclear envelope and were assessed by fluorescence microscopy as described above (Figure 5-5 A).

Approximately 60% of the A12T-expressing iMSCs display some amount of nuclear envelopathy (Figure 5-5 B). Using the scoring scheme described in Molitor & Traktman 2014(T. P. Molitor & Traktman, 2014), the distribution of the severity of the nuclear dysmorphia was analyzed. Wild type iMSCs displayed uniformly normal nuclei (90%), whereas only 40% of A12T-expressing iMSCs exhibited normal nuclei. Highly dysmorphic nuclei with scores of 3 and above were seen at a frequency of approximately 20-25% (Figure 5-5 C). The nuclear envelopathy is more severe in iMSCs than what we observed in the MCF-10a model. Furthermore, A12T iMSCs exhibited a greater frequency of micronuclei compared to WT iMSCs (Figure 4-6). Micronuclei are a post- mitotic phenomenon in which whole or fragmented chromosomes that were not incorporated during nuclear envelope reassembly are packaged into micronuclei (Luzhna, Kathiria, & Kovalchuk, 2013). Nuclear envelopathies are thought to arise in two ways, either through interphase tension within the nucleus or as a result of inappropriate nuclear envelope reassembly. Therefore, the presence of a severe envelopathy in A12T iMSCs could be an interphase phenomenon or a post mitotic phenomenon (or both), whereas the presence of micronuclei is a result of a post mitotic defect.

Figure 5-5

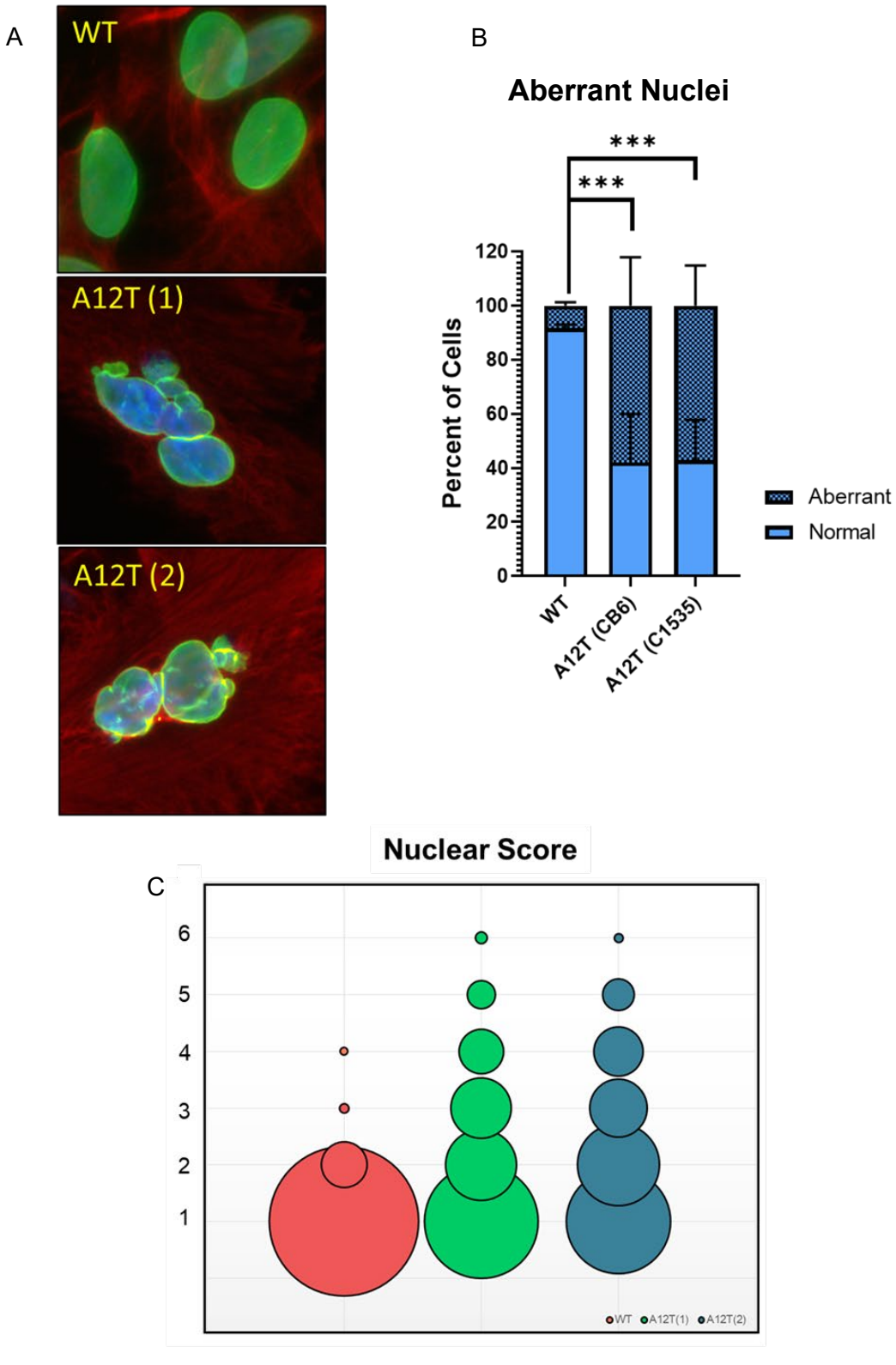
A
WT
A12T (1)
A12T (2)
B
Aberrant Nuclei
***
***
Percent of Cells
120
100
80
60
40
20
0
WT
A12T (CB6)
A12T (C1535)
Aberrant
Normal
C
Nuclear Score
6
5
4
3
2
1
WT
A12T(1)
A12T(2)

Figure 5-5. Analysis of Dysmorphic Nuclei in A12T iMSCs. (A) WT iMSCs have rounded, smooth nuclei when analyzed by immunofluorescence of Lamin A; in contrast, A12T iMSCs exhibit dysmorphic nuclei that contain severe invaginations, blebs and multinucleation (B) Cells were analyzed by immunofluorescence of Lamin A to for nuclear morphology abnormalities. Normal nuclei were defined by a score of 1 based on the scale defined in Molitor & Traktman 2014, and aberrant nuclei were defined by a score >1. 60% of the iMSCs expressing A12T exhibited dysmorphic nuclei. (C) Using the scoring scheme defined in Molitor and Traktman 2014, cell nuclei were assigned a score of 1-6, with 1 defined as smooth round nuclei, and 6 as multinucleated and blebbed. WT I MSCs exhibited 90% normal nuclei, whereas 20-25% of A12T iMSCs had nuclei with a score of 3 or greater. These experiments were repeated in biological triplicate and statistical significance of (B) was determined by Student's T-test.

Figure-5-6

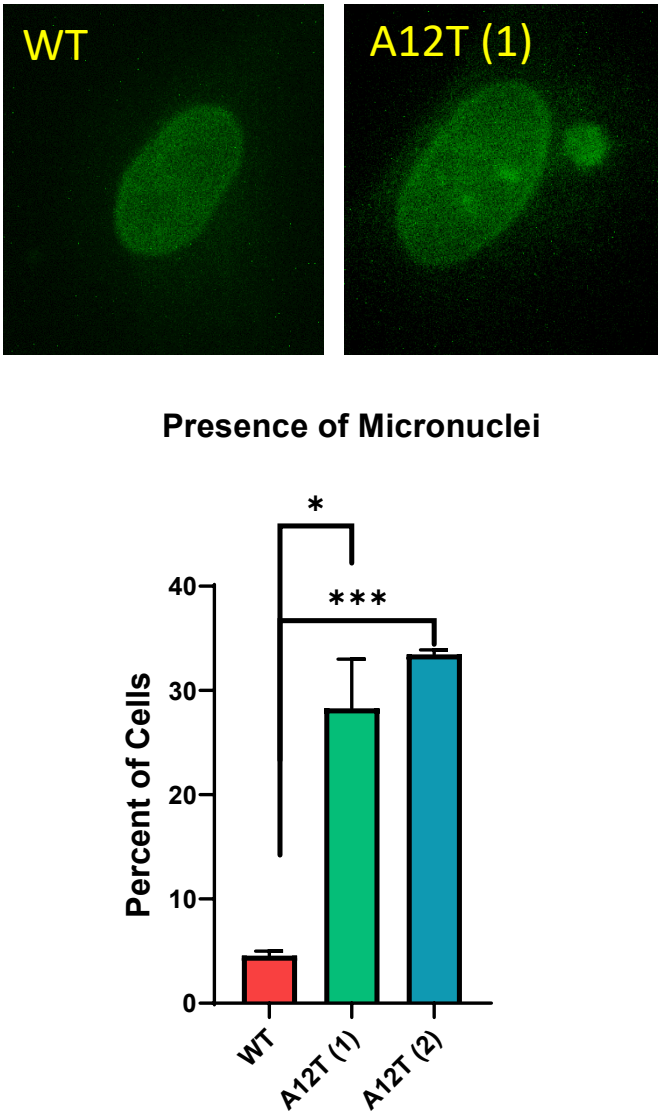

Figure 5-6. Analysis of Micronuclei. WT and A12T iMSC cells were analyzed by immunofluorescence of Lamin A to assess for the presence of micronuclei. WT iMSCs only had an incidence of micronuclei at a rate of approximately 5%, whereas A12T iMSCs exhibited a frequency of micronuclei of 25-35%. Data shown represent 3 independent experiments and statistical significance was determined by Student's T-test.

BAF A12T Expressing iMSCs Exhibit Altered Actin Distribution and Nuclear Herniation and Rupture

The inner nuclear envelope contains transmembrane proteins such as the LEM domain proteins, but also SUN proteins that interact with Nesprins which, together form the LINC complex that bridges the cytoskeleton to the inner nuclear skeleton by interacting with Lamin A as described in Chapter 1 (Crisp et al., 2005). The connection between the cytoskeleton and the nucleoskeleton influences many aspects of cellular structure and function, including nuclear positioning and mechanotransduction (Tapley & Starr, 2013). MSCs are mechanosensitive cells and their mechanotransduction and actin cytoskeleton arrangement are regulated by shear stress (Kuo et al., 2015). Based on the morphological differences we observed in the cells under phase microscopy (Figure 5-1 A&B), we sought to examine the actin cytoskeleton organization in WT and A12T iMSCs. Assessment of the actin cytoskeleton was achieved by staining cells with a Lamin A antibody and with Phalloidin conjugated to rhodamine to visualize the nuclear lamina and the actin cytoskeleton. We then quantified the actin fiber length (Figure 5-7 B), the classification of actin distribution (cortical actin vs stress fibers) and whether there were changes in the amount of actin over the nucleus. Actin fiber length corresponds to the morphological differences we observed under phase microscopy: WT iMSCs had elongated, spindle-like cell bodies, and as such had long, parallel actin fibers running the length of the cell. A12T iMSCs on the other hand, exhibited shorter actin fibers that crisscrossed throughout the cell rather than being organizing into parallel bundles. WT iMSC actin cytoskeleton was predominantly arranged into stress fibers, with cortical actin bundles present in the cell edges. A12T expressing iMSCs exhibited an increase in the distribution of cortical actin as opposed to stress fibers (Figure 5-7 D). Any disruptions in cell polarity may cause alterations in the distribution of focal adhesions and may result in the organization of the

actin network into radial arcs that contain a dense meshwork of peripheral actin filaments and few stress fibers (McHardy, Warabi, Andersen, Roskelley, & Roberge, 2005). We hypothesized that the radial distribution of actin in A12T iMSCs may have altered the proportion of actin that passes over the nucleus. The distribution of actin “on” the nucleus, termed actin caps, play an important role in protecting it from external forces. Actin caps are longitudinal actin fibers that run parallel with the stress fibers and terminate at focal adhesions (Davidson & Cadot, 2021; J.-K. Kim et al., 2017). Conversely, nuclear confinement as a result of contractile rings surrounding the nucleus and interacting with the LINC complex, are responsible for insults to the nuclear envelope and are a direct cause of nuclear rupture and chromatin herniation in mechanosensitive cells or cells with compromised nuclear envelope integrity (Hatch & Hetzer, 2016). We quantified the actin caps on the nucleus and found that there was a decrease in the distribution of actin over the nucleus in A12T iMSCs compared to WT iMSCs (Figure 5-7 C). Taken together, the transition of parallel stress fibers to short, radial cortical fibers and the loss of actin caps on the nucleus in A12T expressing iMSCs, indicate that the actin network within the iMSCs is caging the nucleus and could in turn be causing mechanical stress on the nuclear envelope.

Next, we asked whether there were gross changes in the arrangement of the actin cytoskeleton based on the hardness of the culture substrate. Since the diversion of the cellular morphology between WT and A12T expressing iMSCs was dependent on whether they were being cultured on Matrigel, gelatin or plastic, we cultured WT iMSCs on these three substrates. We then stained these cells with rhodamine-phalloidin and measured actin fiber length (Figure 5-7 D). Actin fiber length significantly decreased with increasing hardness of the substrate on which the cells were cultured. This led us to postulate that

mechanosensitive iMSCs begin to exhibit the deleterious effects of the A12T mutation once they are subcultured on plastic and the actin cytoskeleton is shortened. Actin fiber shortening may result in the loss of actin caps, imparting mechanical stress on the already aberrant nuclear envelope.

Using immunofluorescence analysis of Lamin A distribution within iMSCs, we asked whether the radial conformation of the actin cytoskeleton was causing nuclear herniation and rupture as reported by Hatch in 2016 (Hatch & Hetzer, 2016). Cells were defined as having undergone a rupture or chromatin herniation if the DAPI staining of the DNA extruded beyond the Lamin A border of the nucleus. We found that 15-20% of A12T iMSCs exhibited instances of nuclear rupture, see Figure 5-8. This was a striking finding, because the leaking of nuclear material into the cytoplasm can trigger stress responses in the cell, including the induction of the senescence associated secretory phenotype (SASP) and eventual replicative senescence (Dou et al., 2017; Glück & Ablasser, 2019). The implication that there may be an induction of replicative senescence as a consequence of the expression of A12T in iMSCs points at a potential molecular etiology for the preferential decay of MSCs in the context of NGPS. It also highlights a newly described role for BAF in the context of cytoskeletal arrangement, the effects on the nuclear Lamin meshwork, and the downstream sequelae that result from insults to this interconnected network.

Figure 5-7

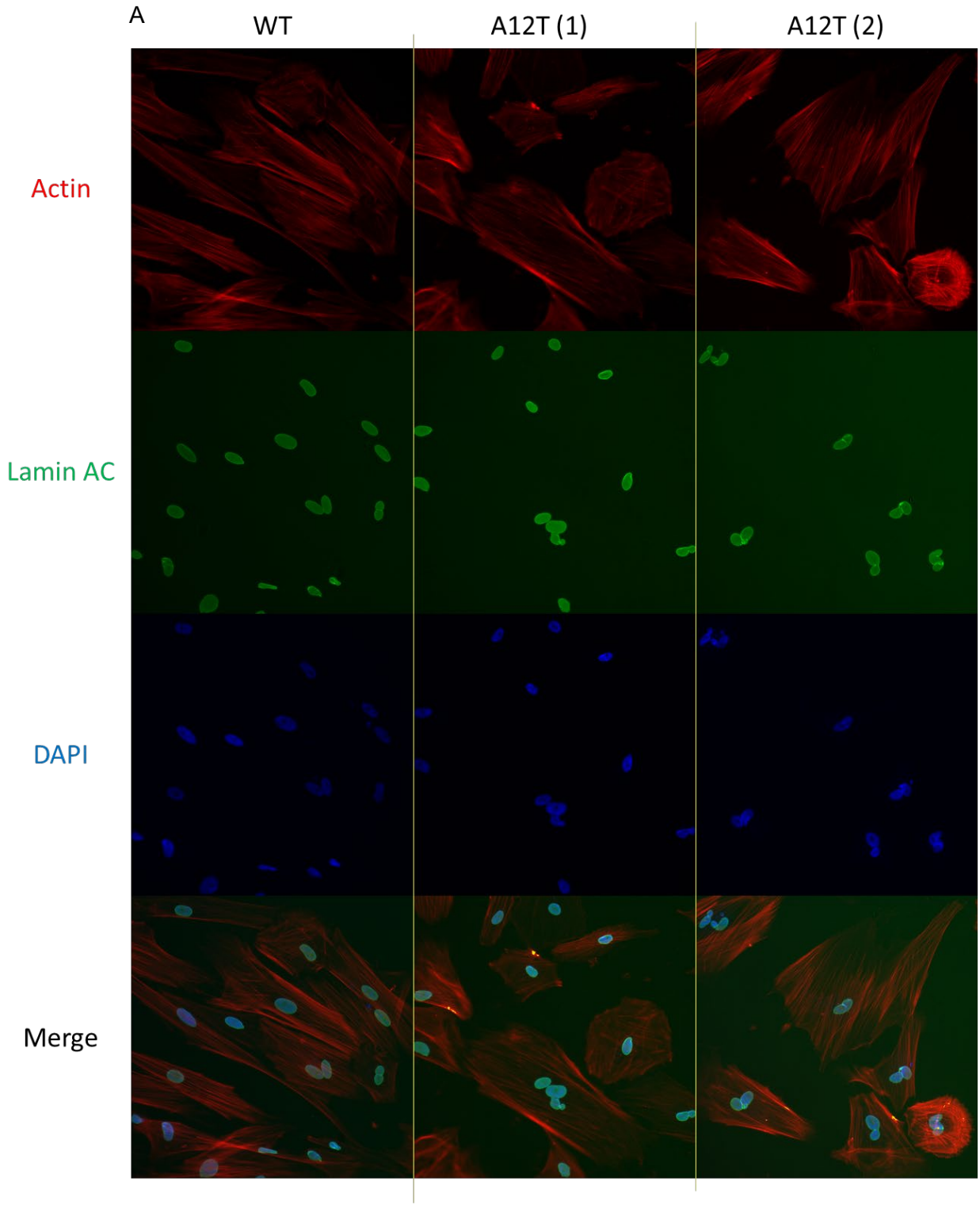

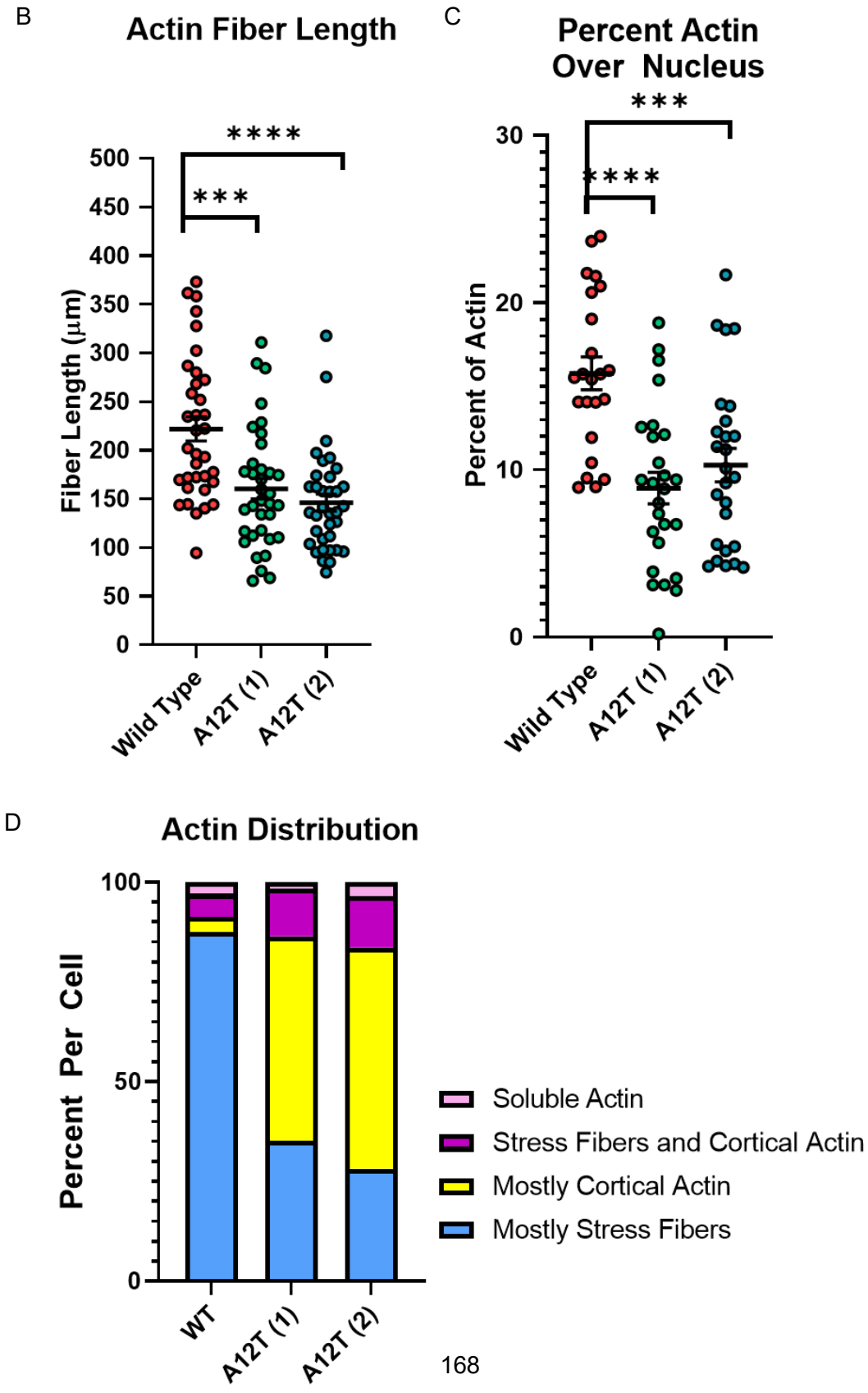
B
Actin Fiber Length
****
***
Fiber Length (μm)
500
450
400
350
300
250
200
150
100
50
0
Wild Type
A12T (1)
A12T (2)
C
Percent Actin Over Nucleus
***
****
Percent of Actin
30
20
10
0
Wild Type
A12T (1)
A12T (2)
D
Actin Distribution
Percent Per Cell
100
50
0
WT
A12T (1)
A12T (2)
Soluble Actin
Stress Fibers and Cortical Actin
Mostly Cortical Actin
Mostly Stress Fibers

E

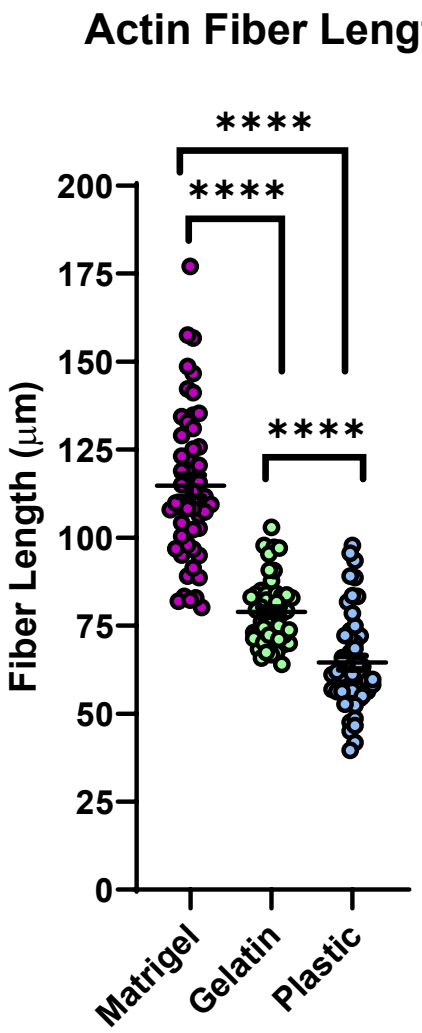
Actin Fiber Length
****
****
****
Fiber Length (μm)
200
175
150
125
100
75
50
25
0
Matrigel
Gelatin
Plastic

Figure 5-7. Actin Distribution in A12T Expressing iMSCs. (A) Immunofluorescence analysis of WT and A12T iMSCs to assess actin distribution after staining with rhodamine-phalloidin and anti-Lamin A to evaluate the nuclear envelope. WT iMSC cells had long, parallel actin fibers running the length of the cell. A12T iMSCs on the other hand, exhibited shorter actin fibers that crisscrossed throughout the cell rather than organizing in parallel bundles. (B) Actin fiber length was quantified and the average actin fiber length per cell of approximately 50 cells from 3 independent experiments was plotted. Significance was determined by Student's T-Test. (C) We quantified the actin caps on the nucleus and found that there was a significant decrease in the distribution of actin over the nucleus in A12T iMSCs compared to WT iMSCs. N=3 independent experiments, statistical significance was determined by Student's T-Test. (D) 75% of the actin in WT iMSCs was organized into stress fibers. Whereas only 30% of the actin in A12T iMSCs was distributed into stress fibers, and about 50% organized into cortical actin. (E) Actin fiber length was measured and quantified and the average actin fiber length per cell of approximately 100 cells and 2 independent experiments was plotted. Significance was determined by Student's T-Test.

Figure 5-8

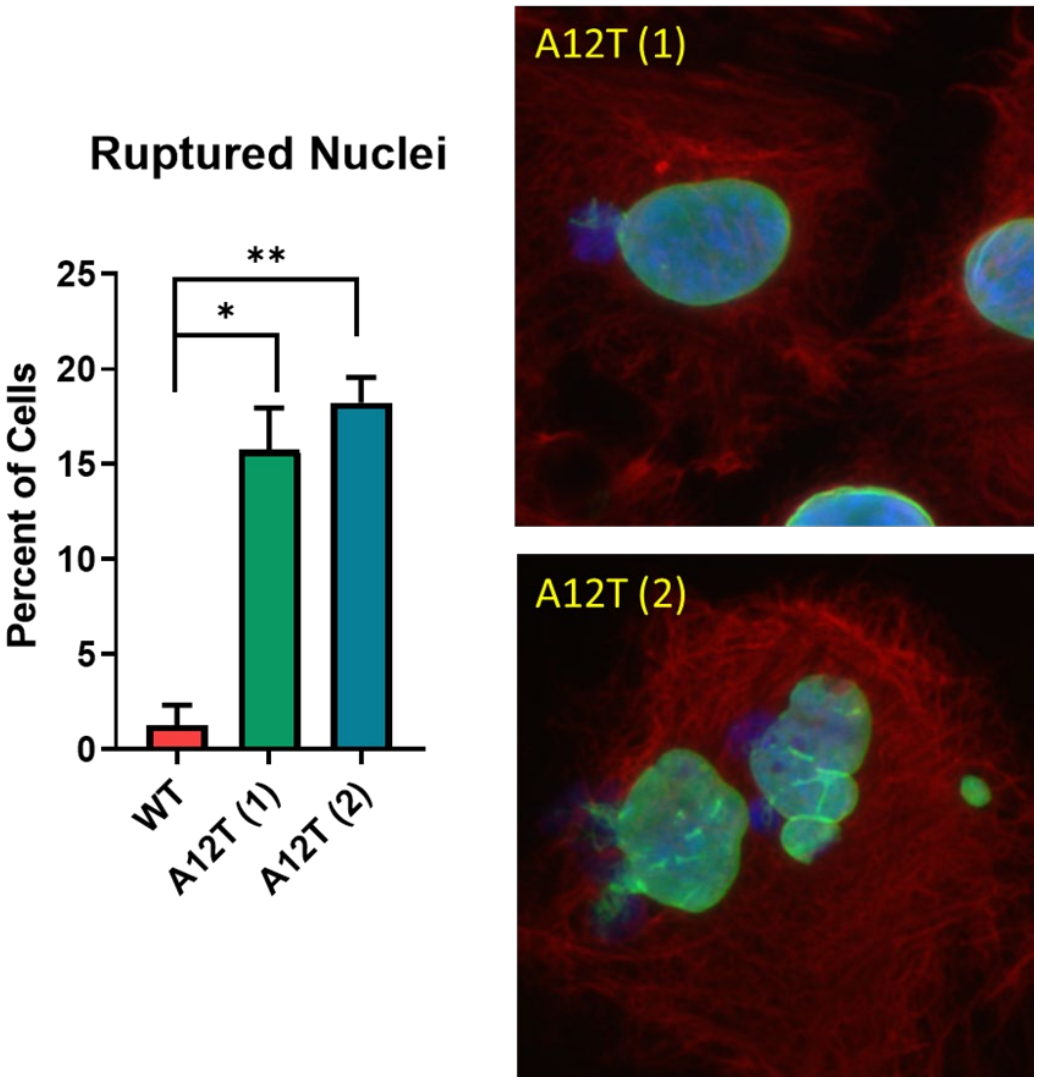
Ruptured Nuclei
Percent of Cells
25
20
15
10
5
0
**
*
WT
A12T (1)
A12T (2)
A12T (1)
A12T (2)

Figure 5-8. Assessment of Nuclear Rupture and Chromatin Herniation. Immunofluorescence of Vimentin (red), Lamin A (green) of iMSCs and DNA staining using DAPI (blue). Rupture was defined as DAPI staining that extends beyond the Lamin A border of the nucleus. 15-20% of A12T iMSCs exhibited nuclear rupture compared to approximately 2.5% of WT iMSCs. n= 150 cells from 3 independent experiments and statistical significance was determined by multiple Student's T-Test.

Premature Cellular Aging is a Result of Stress Signal Accumulation and Senescence

As previously mentioned, the leakage of DNA into the cytoplasm elicits a cellular stress response that may lead to the induction of the SASP pathway and in turn increase the incidence of replicative senescence (Campisi, 2013). Cellular senescence is defined as a cellular effector program that can be triggered in response to various stressors including genotoxic stress, oxidative stress, and mitochondrial dysfunction through the induction of the p53/p21 pathway or the p16/RB pathway (Glück & Ablasser, 2019). The activation of the SASP and the induction of replicative senescence is accompanied by the increase in senescence-associated β-galactosidase activity (a key marker used to identify senescent cells), as well as the hallmarks of aging described in Chapter 1 (Lopez-Otin et al., 2013).

To ask whether the incidence of nuclear ruptures result in the induction of replicative senescence and other cellular stress responses, we first asked whether there was an accumulation of ROS, measured by the intensity of DCFDA as described previously. A12T iMSCs cultured for just 1 passage on plastic exhibited the accumulation of ROS to a greater extent than wild type iMSCs treated with H_2O_2. This indicates that A12T iMSCs undergo oxidative stress, a hallmark of prematurely aged cells (Figure 5-9 A). Next, we analyzed the steady state levels of p53, to measure whether A12T iMSCs had an increase in the induction of this stress response pathway. A12T iMSCs have a 4-fold increase in the steady state levels of p53 as compared to WT controls, indicating that iMSCs not only accumulate ROS but also p53 in response to cellular stress (Figure 5-9 B).

Lastly, we measured the presence of senescence-associated β-galactosidase in WT and A12T iMSCs over a period of multiple passages. This was accomplished by

treating cells with X-gal and measuring the amount of X-gal cleavage by β-galactosidase to produce Blue-Gal: a blue colored insoluble compound visible in the cell. Cells were classified as “negative” if they contained no blue color in the cytoplasm, “partial” if the area of cytoplasm was less than 50% Blue-Gal, and “positive” if the area of cytoplasm was greater than 50% Blue-Gal staining. As a positive control, wild type iMSCs were treated with 10μM H2O2 for one week leading up to the assay. During their first passage on plastic, only approximately 20% of A12T iMSCs exhibited any evidence of senescence. After just one additional passage on plastic, approximately 80% of the cells exhibited either partial or complete senescence. Of the 80%, only about half of these cells exhibited complete senescence, and with subsequent passages both the proportion of cells exhibiting senescence, and the ration of complete: partial senescence, increased. In contrast, WT iMSCs maintained a proportion of non-senescent cells of greater than 80% across the span of passages assessed. On the other hand, by passage 5, approximately 70% of the A12T expressing cells and the cells treated with H_2O2 exhibited complete senescence, and the remainder exhibited partial senescence. By this point, the iMSCs were no longer able to be passaged. Meanwhile, WT iMSCs were able to be passaged continually without a loss of proliferation capacity for at least 40 passages. These data supported our hypothesis that the survival and proliferation of mesenchymal stem cells expressing A12T is greatly diminished.

Figure 5-9

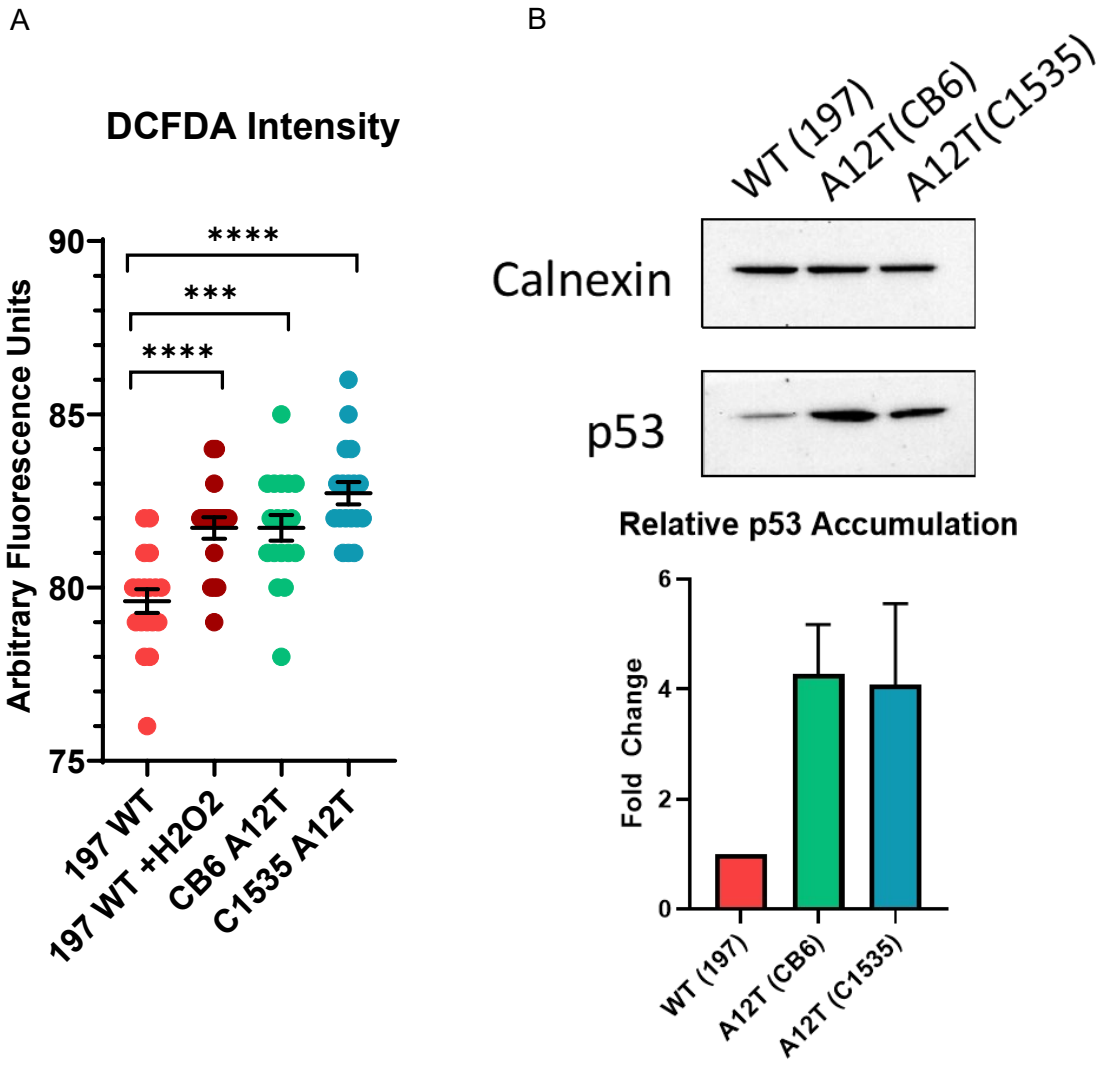
A
DCFDA Intensity
Arbitrary Fluorescence Units
90
85
80
75
****
***
****
197 WT
197 WT +H2O2
CB6 A12T
C1535 A12T
B
WT (197)
A12T(CB6)
A12T(C1535)
Calnexin
p53
Relative p53 Accumulation
Fold Change
6
4
2
0
WT (197)
A12T (CB6)
A12T (C1535)

C

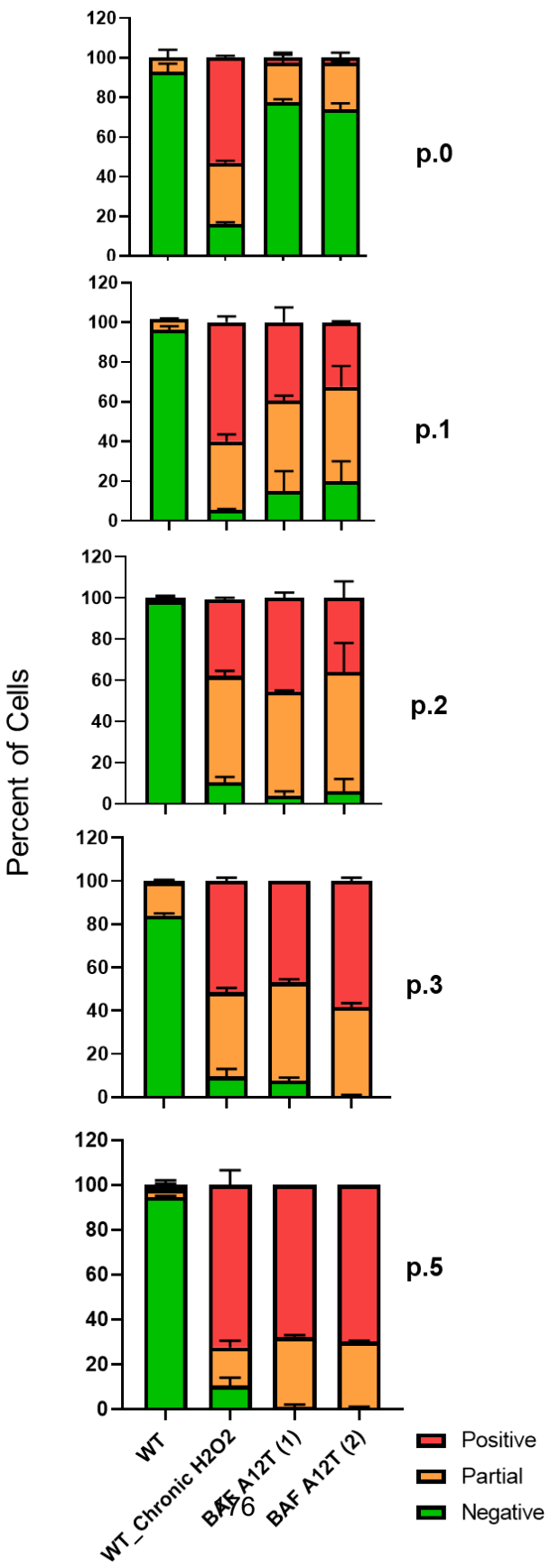
SA-β-Galactosidase Staining
Percent of Cells
120
100
80
60
40
20
0
p.0
p.1
p.2
p.3
p.5
WT
WT_Chronic H2O2
BAF A12T (1)
BAF A12T (2)
Positive
Partial
Negative

Figure 5-9. Assessment of the Accumulation of Cellular Stress Responses and Senescence. (A) Cells were treated with DCFDA in order to measure the accumulation of reactive oxygen species in the cells. WT iMSCs cells were treated with H_2O_2 as a positive control prior to DCFDA treatment. A12T iMSCs exhibited a DCFDA intensity level equal to or greater than the positive control cells, indicating that A12T iMSCs were accumulating ROS. N=3 independent experiments, statistical significance was determined by Student's T-Test. (B) Immunoblot analysis of p53 steady state levels between WT and A12T iMSCs exhibited that p53 steady state levels are 4-fold greater in A12T iMSCs compared to WT iMSCs. N=3 independent experiments. (C) SA-β-Gal staining of WT iMSCs, WT iMSCs treated with H2O2 and A12T iMSCs across 5 passages. Cells were classified as "negative" if they contained no blue color in the cytoplasm, "partial" if the area of cytoplasm was less than 50% Blue-Gal, and "positive" if the area of cytoplasm was greater than 50% Blue-Gal staining.

A12T BAF Exhibits Defective Binding to Lamin A

Data from the Zinn-Justin lab indicate that Alanine 12 of BAF is found on the surface of BAF that binds to the Ig Fold of Lamin A, and that the A12T mutation is buried in this binding surface (Samson et al., 2018). By revealing the interface between the BAF dimer and the Lamin A Ig Fold domain, Samson et al mapped several residues found on the Lamin A Ig Fold that are frequently mutated in atypical progerias (Figure 5-10 A). Their preliminary data indicated that there was diminished binding between Lamin A and BAF A12T, suggesting that the complex between BAF and Lamin A/C is destabilized in the context of NGPS and other progeroid syndromes. We posited that this data could be the puzzle piece that tied together the phenotypes seen in the mechanosensitive iMSCs and the etiology of the loss of the structural integrity of the nucleus. Furthermore, taking what was shown in Chapter 1 about the biochemical analysis of BAF A12T, the previously known functions of BAF were unaffected by the mutation. With LEM-domain binding, DNA binding, phosphorylation by VRK1 and intracellular half-life all appearing to behave similar to WT BAF, we were perplexed by how the mutation was affecting BAF function. The surface on which A12T appears on the BAF dimer originally piqued our interest as a binding surface. Previous reports had mapped that surface as being involved in histone binding and chromatin compaction- which helped inform the hypothesis we established in Chapter 3 (R. Montes de Oca et al., 2005). Given our data (Chapter 3) indicating that A12T's effect on the cell is not at the level of chromatin organization, and using this data from Samson et al. 2018 study, we hypothesized that the loss of the BAF-Lamin A interaction in the presence of A12T destabilizes the Lamin A meshwork within the nucleus, causing mass cytoskeletal rearrangements which in turn cause nuclear rupture, chromatin herniation and ultimately replicative senescence.

To test the BAF: Lamin A interactions directly, we performed *in vitro* co-immunoprecipitation assays. Lysates prepared from bacteria programmed to express recombinant GST-Lamin A Ig fold (WT, R453C or R527H) were applied to Glutathione-sepharose beads, and then purified BAF WT or BAF A12T were added to the beads containing the immobilized GST-Lamin A-IgF. After binding was allowed to occur, beads were washed carefully and both inputs and eluates were resolved electrophoretically and subjected to immunoblot analysis to visualize both GST-Ig Fold Lamin A and BAF.

WT BAF readily bound to GST-Lamin A WT, and as demonstrated by the Zinn-Justin lab, did not bind to Lamin A R435C or R527H. These two mutant alleles are implicated in atypical progerias that are buried in the BAF: Lamin A interface. While Samson et al. observed diminished binding of A12T to Lamin A, in our hands we saw a total abrogation of binding between A12T and Lamin A WT (Figure 5-10 B).

Figure 5-10

A

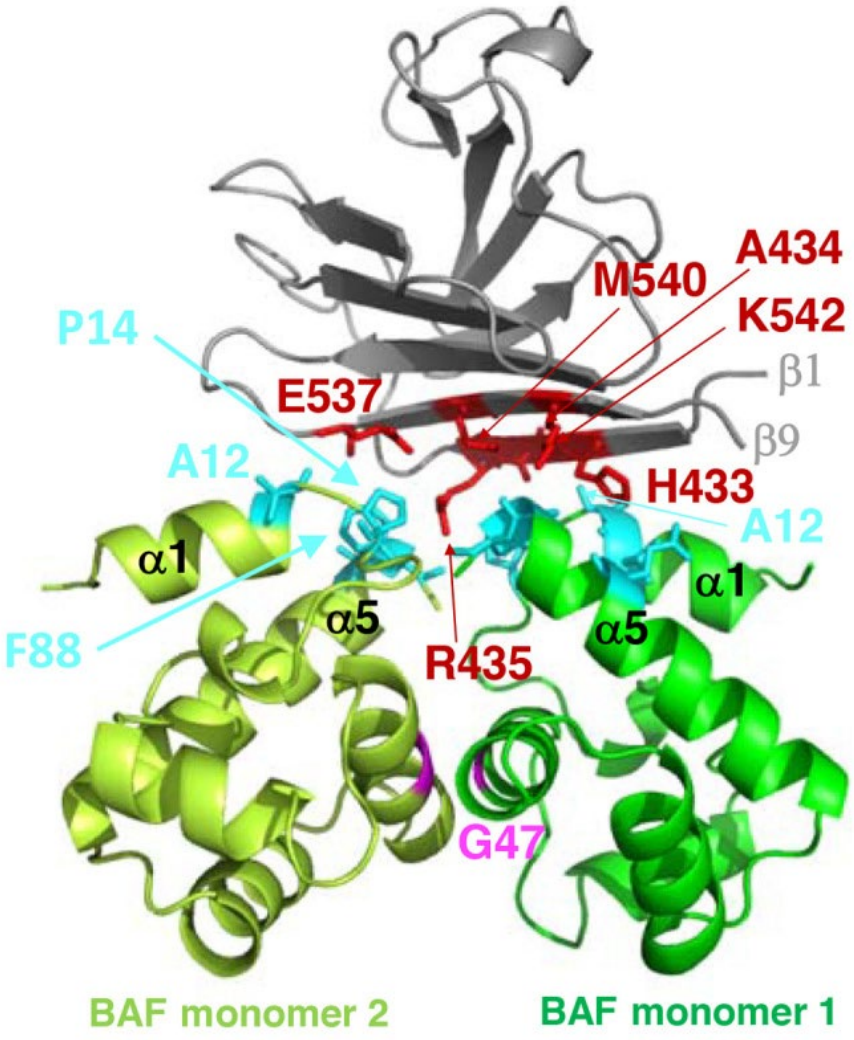
A434
M540
K542
P14
β1
E537
β9
A12
H433
A12
α1
α1
α5
α5
F88
R435
G47
BAF monomer 2
BAF monomer 1

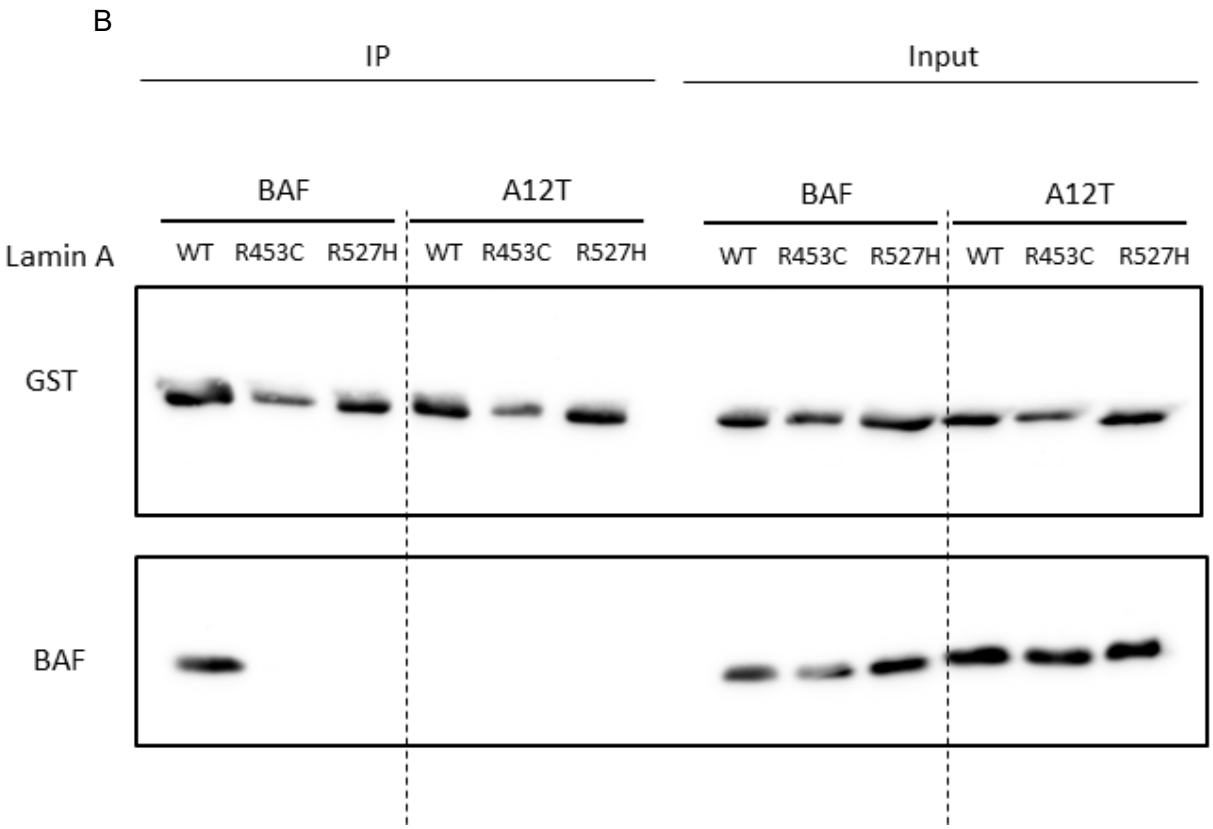

Figure 5-10. In Vitro Binding Assay of Lamin A with BAF. (A) Binding surface between Lamin A Ig fold (gray) and BAF dimer (green) taken from (Samson et al., 2018). Highlighted in red are the residues that cause atypical progeria when mutated. Highlighted in blue are the residues on BAF that are involved in the BAF:Lamin binding interface. G47 between the BAF dimers (purple) is required for dimerization. (B) GST-tagged Ig fold of Lamin A (either WT, R435C or R527H) was immobilized on glutathione sepharose beads and then incubated with purified recombinant WT or A12T BAF. WT BAF readily bound the Ig fold of Lamin A, but did not bind to the two LA-IgF mutants shown to abrogate binding, R435C and R527H. On the other hand, A12T was unable to bind WT Lamin or any of the mutant Lamins at all. N=4 independent experiments. (Purified BAF proteins were prepared by Dr. Aye Mon.)

Discussion

The study of progerias offers a pathologic model that provides insight into accelerated physiologic aging and has been a valuable tool for characterizing the molecular mechanisms of premature aging, specifically in the context of perturbations to the nuclear envelope.

Patients that are affected by premature aging syndromes exhibit degeneration of tissue derived from mesenchymal origin. Studies examining the tissue specificity in the context of HGPS led to the hypothesis mesenchymal stem cell survival and proliferation, and it is thought that patient MSC reservoirs are depleted as a result. We sought to identify the molecular mechanisms behind NGPS's tissue specificity and to understand whether the homozygous expression of A12T preferentially impacted mesenchymal stem cells.

A12T expressing iMSC cellular morphology diverges greatly from WT iMSCs and instead of elongated cell bodies with spindle-like morphology, they are circular with spread out cytoplasms and lenticular nuclei. In order to understand these functional and morphological differences, we assessed the actin cytoskeleton of these cells and found that iMSCs exhibit changes in actin arrangement. WT iMSC actin is organized into elongated, parallel stress fibers running the length of cell, whereas A12T iMSCs exhibit shorter fiber length, organized in radial arcs around the nucleus. The confinement of the nucleus by these radial bundles and loss of actin caps causes an increase in the mechanical stress on the nucleus, and in turn results in an increased incidence of nuclear rupture.

The downstream effects of these morphological differences and nuclear rupture includes the leakage of DNA into the cytoplasm results the accumulation of reactive oxygen species, increased p53 signaling and eventual complete replicative senescence.

Knowing that these cells do not exhibit these phenotypes when cultured on Matrigel or gelatin, we posit that the mechanosensitive nature of mesenchymal stem cells, coupled with A12T's effect on the nuclear envelope leads to nuclear rupture in A12T expressing cells, where WT expressing iMSCs are able to withstand the mechanical forces. Furthermore, BAF's interaction with the Lamin A meshwork of the nucleoskeleton may be a stabilizing force within the nucleus. A12T is unable to bind the Ig fold of Lamin A and in turn destabilizes the nucleoskeletal meshwork. Since the nucleoskeleton is bridged to the cytoskeleton through the LINC complex's direct interaction with Lamin A, the destabilization of the Lamin A:BAF interaction results in an inability to withstand mechanical forces arising from the mechanotransduction of mechanical forces along the actin network. See Figure 5-11.

Through the understanding that the mechanosensitive nature of iMSCs predisposes these cells to nuclear deformation when cultured on hard substrates, and that the expression of A12T in these cells exacerbates nuclear deformity and induces nuclear rupture and DNA leakage, it became clearer why A12T iMSCs exhibit stem cell dysfunction. While the pre-iMSCs are cultured on softer substrates such as Matrigel and gelatin, the actin cytoskeleton exerts less force on the nuclei. Once moved to a harder substrate, A12T nuclei are prone to catastrophic mechanical stress and as such are unable to proliferate efficiently on plastic. Flow cytometry and differentiation assays were performed on iMSCs that had already been subcultured on plastic, undergone nuclear deformation by the actin cytoskeleton and may have already begun to undergo replicative senescence. While it's easy to dismiss these cells as not falling under the classification of functional MSCs, it was important for us to elucidate the mechanisms underlying this observation.

Importantly, these data are specific to iMSCs and none of these effects are observed in hepatocytes derived from A12T expressing iPSCs. This leads us to believe that the effects seen are a result of the mechanosensitive nature of MSCs and that the deleterious effects of the A12T mutation on tissue derived from mesenchymal origin in patients are a result of the direct effect the A12T mutation has on mesenchymal stem cells.

By elucidating the contribution of BAF to the stabilization of the Lamin A meshwork and its novel role in mechanotransduction, we have gotten closer to understanding the molecular mechanisms of A12T's contribution of premature cellular aging in mesenchymal stem cells. However, in order to strengthen these findings, we must establish whether the loss of Lamin A binding to BAF through other mutations on the BAF binding interface results in nuclear envelopathy and premature cellular senescence as well. Furthermore, we would benefit from examining whether we are able to reverse these effects by moving A12T iMSCs from a hard surface, like plastic, onto a softer substrate such as Matrigel; or by relieving the stress imparted by the actin cytoskeleton through treatment with either a pharmacologic agent such as Blebbistatin, or through the genetic manipulation of the LINC complex such as depleting SUN proteins.

Figure 5-11

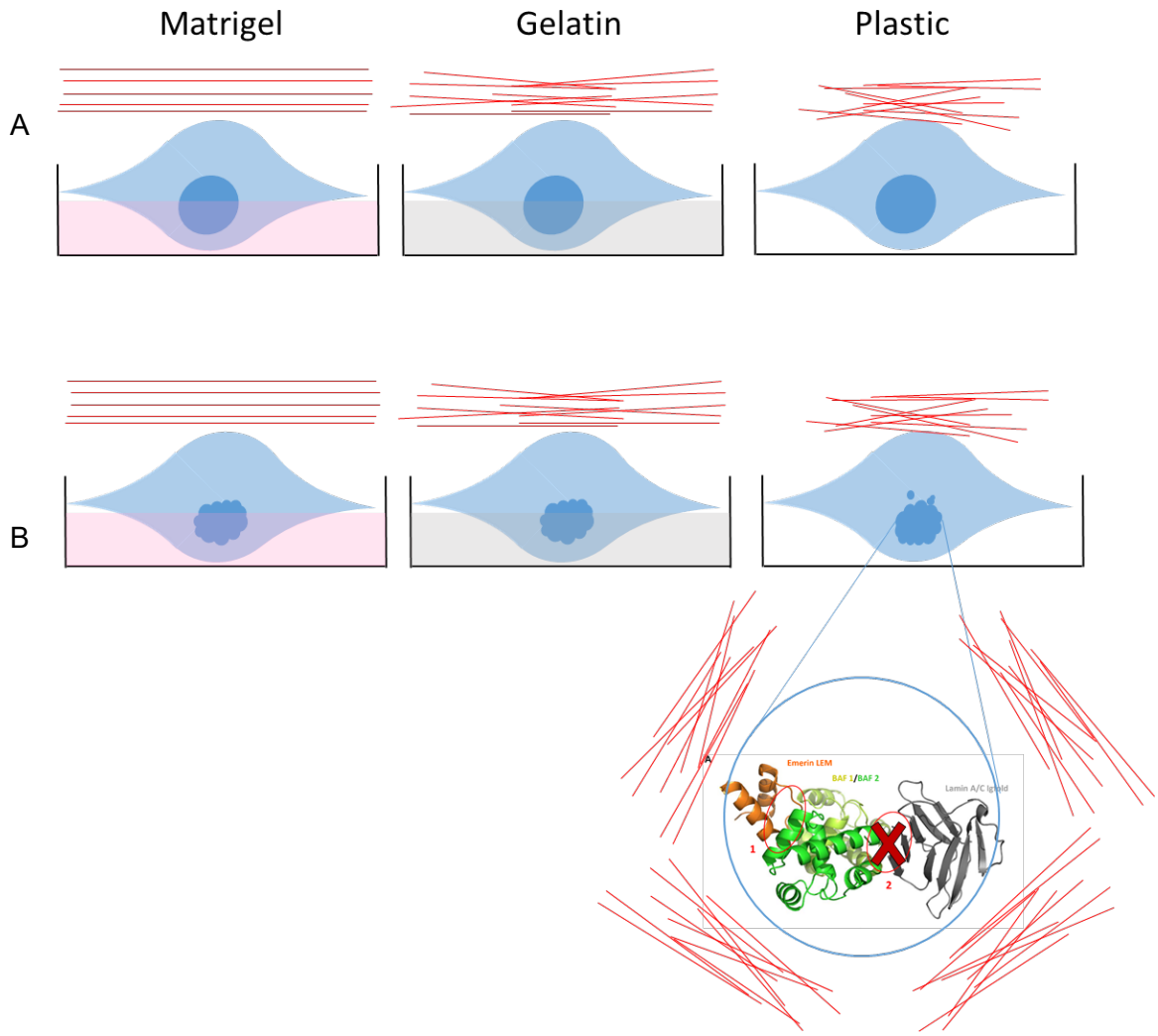
Matrigel
Gelatin
Plastic
A
B
Emerin LEM
BAF 1/BAF 2
Lamin A/C Ig fold
1
2

Figure 5-11. Model of A12T Contribution to iMSC Dysfunction. Pink= Matrigel, gray=gelatin, red= actin cytoskeleton dark blue= nucleus inlay= Lamin A and BAF binding interface (A) When WT iMSCs are cultured on varying substrates, their in-tact nuclear envelope is able to withstand the actin rearrangement that occurs on harder substrates and the cells do not exhibit any functional differences. (B) A12T iMSCs exhibit nuclear envelope defects regardless of the substrate on which they are cultured, however when they are cultured on a hard substrate such as plastic, the actin rearrangement results in radial actin bundles caging the nucleus and including nuclear rupture and chromatin herniation. The reason the nuclear envelope is unable to withstand these forces falls back on to the loss of BAF-Lamin A binding in A12T expressing cells. The destabilization of this interaction in turn destabilizes the Lamin A meshwork within the nucleus and the cells are unable to withstand mechanical forces transduced along the actin network on a hard substrate such as plastic. As a result, DNA leaks into the cytoplasm causing the accumulation of cellular stress responses and ultimately replicative senescence.

Chapter 6: Discussion

The studies emerging about the complexity and dynamic nature of the nuclear envelope have been garnering the attention of more and more research groups in recent years. The categorization of a subset of diseases associated with components of the nuclear lamina, laminopathies, has elucidated the contribution of the nuclear lamina to the maintenance of cell homeostasis, nuclear structure and function and cellular aging.

BAF is an essential protein that bridges the nuclear lamina and chromatin and regulates nuclear structure. Phosphorylation of BAF by VKR1 regulates its interactions with dsDNA, and LEM-D proteins and alters its subcellular localization (R.J. Nichols et al., 2006). Molitor and Traktman demonstrated in 2014 that the depletion of VRK1 resulted in nuclear dysmorphia in MCF-10a cells and decreased the fraction of mobile BAF (T. P. Molitor & Traktman, 2014). Molitor and Traktman also published that the depletion of VRK1 slowed the doubling time of breast cancer cells and reduced the instances of distal metastases in a breast cancer model (T.P. Molitor & Traktman, 2013). Moreover, the homozygous inheritance of a missense mutation in BAF from Alanine 12 to Threonine results in a premature aging syndrome termed NGPS; patient-derived cells exhibit aberrant nuclear envelope structure, thereby designating it as a laminopathy (Puente et al., 2011). We hypothesized that the hypophosphorylation of BAF contributed to the nuclear envelope defect observed in VRK1-depleted cells and that the discovery of the A12T mutation could further inform the model generated by Molitor and Traktman and help elucidate the molecular mechanisms underlying these observations.

At the onset of this study, we hypothesized that the surface on which the A12T mutation occurred was important in chromatin condensation and histone binding (R. Montes de Oca et al., 2005; Samson et al., 2018; Segura-Totten et al., 2002). We posited

that the mutation had implications in chromatin structure and organization. To examine the contribution of BAF A12T on the spatial organization within the nucleus, we generated a model in MCF-10a cells wherein we modestly overexpress shRNA resistant 3XF-BAF or 3XF-A12T while depleting endogenous BAF in order to approach near homozygous expression.

We demonstrated that the expression of A12T causes a nuclear envelopathy in MCF10a cells and sought to examine the different aspects of cellular aging such as genomic instability, epigenetic alterations, alterations in protein synthesis, cellular senescence, and the accumulation of reactive oxygen species (Lopez-Otin et al., 2013). We determined there were no significant changes in the steady state levels of the nuclear periphery proteins, histone modifications, or the substructures of the nucleus; nor were there alterations in *de novo* protein synthesis. A12T expressing cells did not exhibit accumulation of cellular stress responses, nor did we observe and variation in cell proliferation. Furthermore, we asked whether premature aging in this model might manifest with gross alterations at the level of euchromatin and heterochromatin organization. Using electron microscopy and ATAC-Seq, we were unable to distinguish changes in overall nuclear organization. The data show that there were no gross alterations in chromatin compaction, indicating that alterations in gene accessibility and severely altered gene expression are unlikely to be responsible for the defects seen at the nuclear envelope and eventual premature cellular aging phenotype.

The data generated from addressing questions of premature aging in MCF-10a cells indicates that this model does not mirror the hallmarks of premature cellular aging. However, we learned from these analyses that while BAF A12T causes a nuclear envelopathy, nuclear envelopathies are not sufficient to result in cellular aging and

dysfunction. This finding presents a unique opportunity to address the contributions of BAF to the architecture of the nuclear envelope without the cell suffering the deleterious effects of premature aging and eventual replicative senescence.

Murine models of HGPS and other premature aging syndromes have been able to recapitulate some of the clinical manifestations of the disease. We theorized that generating a novel NGPS mouse model would be a valuable tool used to elucidate the fundamental mechanisms of disease progression in a tissue-specific, systems-based approach. To achieve this, we contracted with Applied Stem cell to generate A12T/+ mice using CRISPR/Cas9 technology, with the aim of mirroring the clinical manifestations of NGPS.

While the A12T/A12T mice do not present a premature aging syndrome, primary dermal fibroblasts derived from A12T/A12T mice exhibit nuclear morphology defects. At the cellular level, this envelopathy, was not accompanied by cellular stress responses or replicative senescence. The complexities between the clinical manifestation of human progeria syndromes and the parallel mouse models aiming to recapitulate these diseases highlight the challenges of developing a mouse model to study a disease state at the organismal level. The reasons why some murine models are unable to recapitulate the disease model or require more severe patterns of inheritance is unclear. While there are most certainly differences between human and mouse physiology, it remains unknown why the inheritance of A12T/A12T in mice does not cause a premature aging syndrome. Unknown redundancy mechanisms in the mice may be masking the contributions of the A12T to protect the cell and organism from its deleterious effects. Crossing A12T/A12T mice with other mouse models of premature aging, or mice with defects in the tissues of mesenchymal origin may aid in revealing the ways in which A12T contributes to the

process of organismal aging and mesenchymal stem cell maintenance. Mesenchymal stem cells are found in many tissue types and behave as the reservoir for tissue regeneration after injury. They also exhibit homing capabilities and immuno-modulatory functions (Pittenger et al., 1999). Therefore, while A12T expressing mice do not exhibit defects in premature aging, we have not examined whether the expression of A12T results in defective wound healing or tissue regeneration after injury such as bone breaks. Additionally, harvesting bone marrow from these mice to ask whether the proportion of BMMSCs is different over time as the mice age, or characterizing whether they exhibit premature cellular aging similar to the iMSCs generated from iPSCs would answer the question of cell type specificity vs species specificity as well.

Dermal fibroblasts derived from A12T/A12T mice exhibited nuclear envelope dysmorphia but did not exhibit markers of premature cellular aging. In the same way that stressing the mouse model with a “second hit” through genetic or injury, future studies of the primary dermal fibroblasts with additional stress might reveal differences between WT and A12T expressing cells that would have remained undetected in an “unstressed” model. BAF has been shown to play an important role in the recognition and repair of nuclear ruptures by binding to herniated chromatin and recruiting INM proteins and their associated membranes with the help of ESCRT-III machinery (Halfmann et al., 2019; Young et al., 2020). Using microfluidics chambers as a model for confined migration BAF and A12T expressing dermal fibroblasts could be examined for differences in the ability to withstand confinement and mechanical stress (how quickly it ruptures in confined spaces) and assess the repair efficacy in A12T expressing cells.

Our initial hypothesis relied on the idea that surface of BAF on which the A12T mutation occurs was a result of altered interactions with chromatin and histones.

Furthermore, we posited that generating a model system for the analysis of A12T's impact on organismal aging, and cellular aging through an expression system that introduced A12T in the endogenous locus would provide us with clearer insight on the disease etiology. Moreover, the causes for the tissue-specificity of NGPS are unclear, but the impact on tissues of mesenchymal origin led us to the hypothesis that survival, proliferation or differentiation of mesenchymal stem cells is perturbed.

Therefore, to examine the effect of A12T expression on MSCs we transitioned from the use of MCF-10a cells to isogenic iPSCs that carried +/+ or A12T/A12T alleles at the BANF1 locus. W differentiated the iPSCs into induced mesenchymal stem cells (iMSCs), or a cell type unaffected by NGPS. We were able to establish that there were no functional defects in A12T iPSCs differentiated into hepatocytes. While A12T hepatocytes exhibit a mild nuclear envelopathy, they express hepatocyte markers at similar levels to WT hepatocytes, and do not exhibit cellular senescence.

We established a differentiation protocol from iPSCs to iMSCs and were able to show that WT iMSCs were functional as stem cells and efficiently differentiated into osteoblasts and pre-adipocytes. The first distinction we observed between WT and A12T iMSCs was a notable morphological difference. To examine this further, we analyzed the actin cytoskeleton using immunofluorescence. We observed that the actin cytoskeleton of WT iMSC is organized into elongated, parallel stress fibers running the length of cell, whereas A12T iMSCs exhibit shorter fiber length, organized in radial arcs around the nucleus. The radial distribution of actin and confinement of that imparts mechanical stress on the nucleus, resulting in an increased incidence of nuclear rupture and the leakage of the components of the nucleus into the cytoplasm. The downstream effects of the leakage

of DNA into the cytoplasm results the accumulation of reactive oxygen species, increased p53 signaling and eventual complete replicative senescence.

The dependence of these phenotypes on substrate hardness was intriguing to us. Knowing that these cells do not exhibit these phenotypes when cultured on Matrigel or gelatin, we proposed that A12T's effect on the nuclear envelope leads to nuclear rupture in A12T-expressing, mechanosensitive iMSCs on hard substrates, whereas WT expressing iMSCs are able to withstand the mechanical forces. Furthermore, the publication of the ternary structure of a LEM-D protein, BAF and the IgG fold of Lamin A revealed that Alanine 12 is buried in the of BAF-Lamin A interface (Samson et al., 2018). Using the data from Samson et al. 2018, we pursued the hypothesis that the A12T mutation diminishes the interaction with Lamin A, and the loss of the interaction compromises the structural network of the nuclear lamina and weakens the nuclear envelope.

BAF's interaction with the Lamin A meshwork of the nucleoskeleton is a stabilizing force within the nucleus. While WT BAF is able to bind the Ig Fold of Lamin A, A12T is unable to bind the Ig fold of Lamin A and in turn destabilizes the nucleoskeletal meshwork. Through the interaction of the cytoskeleton with the nucleoskeleton and in turn, Lamin A, the destabilization of the Lamin A: BAF interaction results in an inability to withstand mechanical forces arising from the mechanotransduction of mechanical forces along the actin network. We were able to reveal a novel role for BAF in mechanotransduction and the stabilization of the Lamin A meshwork within the nucleus. This observation is relevant to one the molecular mechanisms by which the BAF A12T allele contributes to premature cellular aging in mesenchymal stem cells.

The elastic modulus of Matrigel is ~0.3kPa, gelatin is ~40-50kPa and tissue culture plastic is >1MPa. The increase in substrate hardness from Matrigel to tissue culture plastic is greater than 3,000 fold and is not physiologically relevant. While MSCs are exposed to different niches in vivo such as bone marrow, fat and bone, the range of mechanical stress does not begin to approach the order of MPa. For example, bone's elastic modulus is approximately 50 kPa, similar to the elastic modulus of gelatin; and bone marrow's elastic modulus is ~0.2kPa, similar to the elastic modulus of Matrigel. A12T expressing iMSCs clearly have a lower threshold for withstanding mechanical forces applied when cultured on plastic, however it would be interesting to examine whether these effects are rescued when iMSCs that have been cultured on plastic are moved to softer substrates. By moving cells onto substrates 500 fold softer (gelatin) and relieving the stress from the actin cytoskeleton, do A12T expressing cells recover from the accumulation of stress responses and return to a healthy state? Furthermore, since the mechanical forces are transduced along the actin cytoskeleton, would relieving the strain of the actin cytoskeleton on the nucleus decrease the frequency of nuclear rupture and in turn reduce the fraction of senescent iMSCs? Inhibiting actin dynamics by treatment with Blebbistatin has been shown to relieve the stress on the nuclear envelope and in turn improve aberrant nuclear envelope morphology (Hatch & Hetzer, 2016). Furthermore, several studies have shown that by depleting components of the LINC complex, relieves the tension from the actin cytoskeleton on the nucleus. In both these ways we can ask whether the replicative senescence observed in the iMSCs are 1) reversible 2) truly a result of the mechanical strain imparted by the cytoskeleton.

The transduction of mechanical forces from the cell periphery to along the actin cytoskeleton initiates a signaling cascade to modify gene expression in an effort to

respond to the extracellular environment appropriately. Therefore, understanding the pathways involved, such as the YAP/TAZ pathway and whether signaling is altered in the presence of the A12T mutation would open a series of potential downstream studies of the potential gene expression alterations in WT BAF iMSCs or A12T iMSCs in response to mechanical stress.

Moreover, our observation that A12T does not bind Lamin A implicates the BAF: Lamin A as a critical interaction for the structural integrity of the nucleus. To strengthen these findings, further examination of the Lamin A-binding interface must be performed to determine whether other mutations on the BAF binding interface results in nuclear envelopathy and premature cellular senescence as well. Samson et al. mapped residues on Lamin A that are buried in the BAF binding interface that are mutated in atypical progerias. By identifying previously unknown residues on the surface of BAF that are involved in the interaction with Lamin A, we can examine whether their mutation and leads to the loss of the BAF: Lamin interaction, and whether, when expressed in iMSCs, results in a nuclear envelopathy and premature cellular aging. If, however the envelopathy and premature aging syndrome are a result of the loss of the BAF: Lamin A interaction, then we must also assess this interaction in the primary dermal fibroblasts. Do A12T dimers overcome the binding deficit observed in the iMSCs due to species-related differences in the Ig Fold of murine Lamin A? While R435 and R527 are conserved in murine Lamin A (the two residues in which mutations to Alanine are unable to bind WT BAF), other residues in this region are not conserved. Therefore, to ask whether there is a species-driven difference in the BAF: Lamin A interaction, or whether the loss of binding is still observed, we would perform binding assays between murine BAF and murine Lamin A.

In conclusion, BAF carries out its function through its binding partners, and the BAF dimer ties together LEM-D proteins, Lamin A and dsDNA and acts as an organizing hub at the nuclear periphery. BAF plays extensive roles in the maintenance of the structure and function in interphase and mitosis and this study indicates that the interaction of BAF and Lamin at the nuclear periphery plays a central role in stabilizing the entire meshwork of the nucleoskeleton Figure (6-1). In summary, the work done in this study has revealed the contributions of the BAF A12T mutation to the integrity of the nuclear envelope and has elucidated a novel role for BAF in the context of mechanosensitivity, mechanotransduction, and the network of the nucleoskeleton and cytoskeleton. We have also begun to understand the tissue specificity of NGPS through the study of MSCs and have learned that A12T has deleterious effects on mechanosensitive cells but that other cell types are more resilient in overcoming insult to the nuclear membrane morphology (Figure 6-1). Through the study of three separate models of A12T inheritance, we have highlighted the nuances of this mutation's effect both at the cellular and organismal level. Furthermore, this study has generated valuable tools for the study of BAF and A12T outside the context of premature cellular aging. The generation of a dermal fibroblast cell line from an A12T/A12T mouse offers a toolkit for the analysis of the roles of BAF and A12T without suffering the consequences of premature cellular aging such as replicative senescence.

Figure 6-1

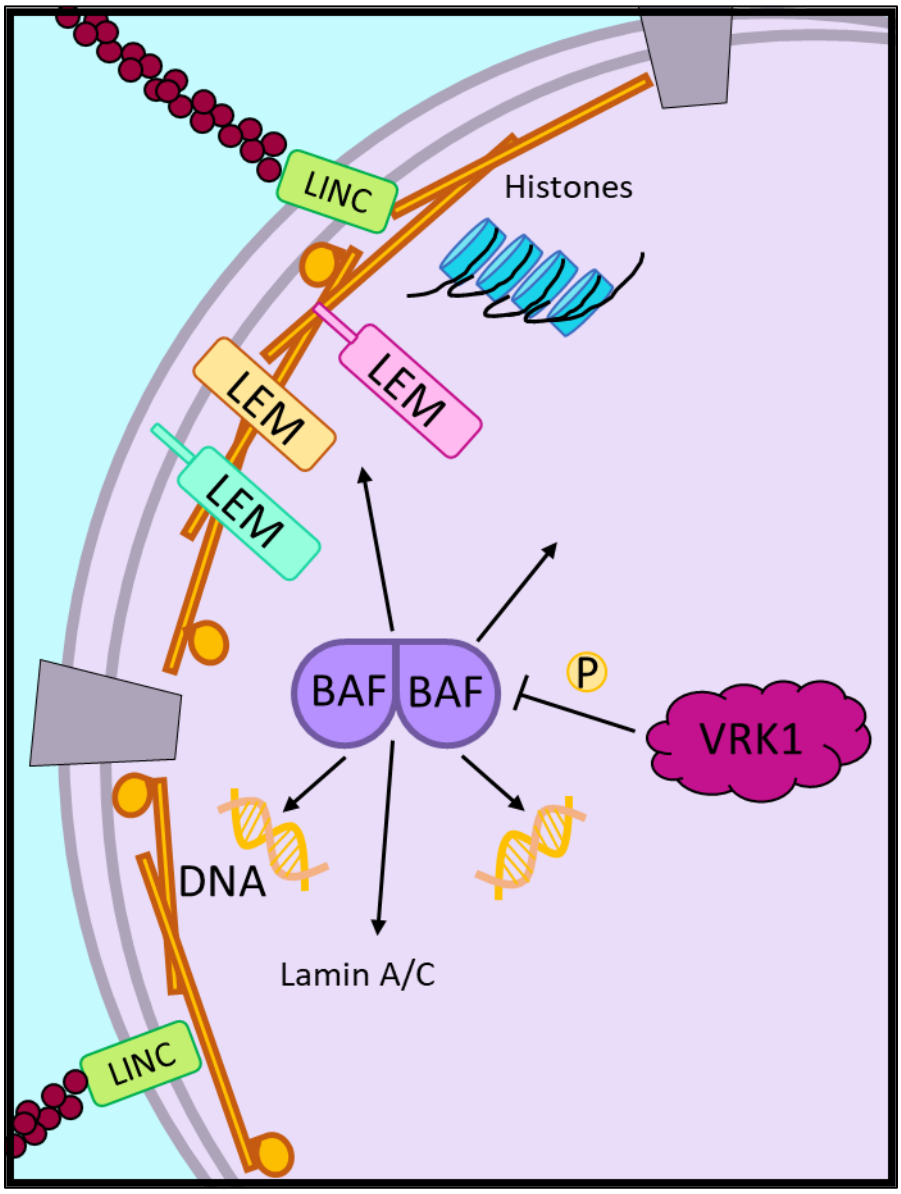

Figure 6-1. Summary of BAF Binding Partners. The BAF dimer creates a nuclear organizing hub. The BAF dimer creates two binding surfaces at either pole, one that creates a LEM-D binding saddle, and the other that binds the Ig fold of Lamin A. On either side of the dimer BAF binds dsDNA in a sequence independent manner. BAF is phosphorylated by VRK1 which regulates its affinity to its binding partners.

Figure 6-2

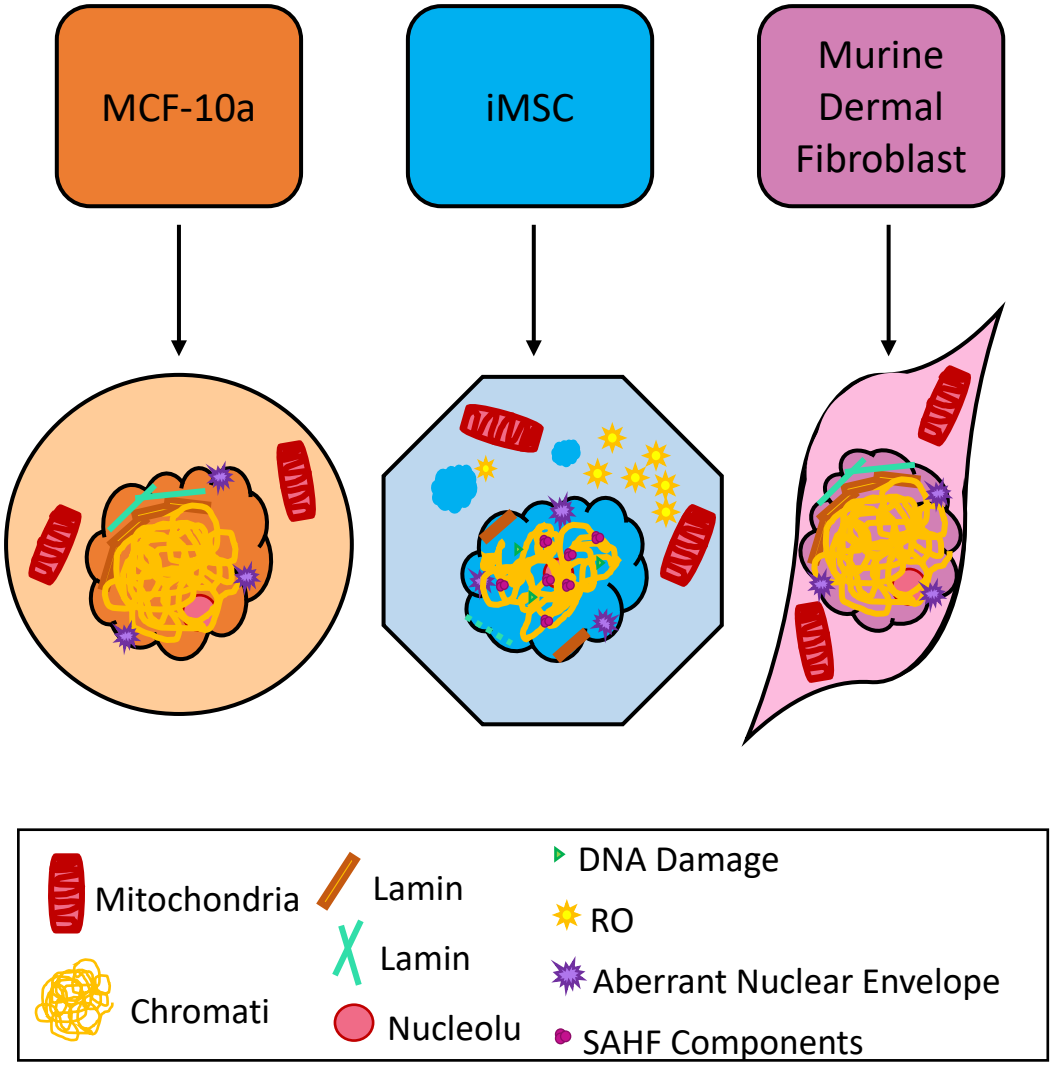

Figure 6-2. Summary of Models. MCF-10a cells and dermal fibroblasts from A12T/A12T mice both exhibit nuclear envelope morphology defects without suffering deleterious downstream consequences of premature aging. When iMSCs express A12T, they exhibit nuclear envelope dysmorphia but also present with premature cellular aging culminating from the accumulation of ROS and DNA damage as a result of chromatin herniation due to nuclear rupture.

Works Cited

Adams, C. C., & Workman, J. L. (1993). Nucleosome displacement in transcription. *Cell, 72*(3), 305-308.

Alexiadis, V., Varga-Weisz, P. D., Bonte, E., Becker, P. B., & Gruss, C. (1998). In vitro chromatin remodelling by chromatin accessibility complex (CHRAC) at the SV40 origin of DNA replication. *The EMBO Journal, 17*(12), 3428-3438.

Anderson, D. J., & Hetzer, M. W. (2008a). The life cycle of the metazoan nuclear envelope. *Curr. Opin. Cell Biol, 20*(4), 386-392. Retrieved from http://www.ncbi.nlm.nih.gov/pubmed/18495454

http://ac.els-cdn.com/S0955067408000574/1-s2.0-S0955067408000574-main.pdf?_tid=842d1364-4c30-11e5-aec9-00000aab0f6c&acdnat=1440620876_1c1be8deefb778d28a05cd8e94473c88

Anderson, D. J., & Hetzer, M. W. (2008b). Shaping the endoplasmic reticulum into the nuclear envelope. *J. Cell Sci, 121*(Pt 2), 137-142. Retrieved from http://www.ncbi.nlm.nih.gov/pubmed/18187447

http://jcs.biologists.org/content/121/2/137.full.pdf

Armanios, M., Alder, J. K., Parry, E. M., Karim, B., Strong, M. A., & Greider, C. W. (2009). Short telomeres are sufficient to cause the degenerative defects associated with aging. *Am J Hum Genet, 85*(6), 823-832. doi:10.1016/j.ajhg.2009.10.028

Asencio, C., Davidson, I. F., Santarella-Mellwig, R., Ly-Hartig, T. B., Mall, M., Wallenfang, M. R., . . . Gorjanacz, M. (2012). Coordination of kinase and phosphatase activities by Lem4 enables nuclear envelope reassembly during mitosis. *Cell, 150*(1), 122-135. doi:S0092-8674(12)00644-7 [pii];10.1016/j.cell.2012.04.043 [doi]

Baker, D. J., Wijshake, T., Tchkonia, T., LeBrasseur, N. K., Childs, B. G., van de Sluis, B., . . . van Deursen, J. M. (2011). Clearance of p16Ink4a-positive senescent cells delays ageing-associated disorders. *Nature, 479*(7372), 232-236. doi:10.1038/nature10600

Barboro, P., D'Arrigo, C., Repaci, E., Patrone, E., & Balbi, C. (2010). Organization of the lamin scaffold in the internal nuclear matrix of normal and transformed hepatocytes. *Experimental Cell Research, 316*(6), 992-1001. doi:https://doi.org/10.1016/j.yexcr.2009.12.010

Barton, L. J., Soshnev, A. A., & Geyer, P. K. (2015). Networking in the nucleus: a spotlight on LEM-domain proteins. *Curr Opin Cell Biol, 34*, 1-8. doi:10.1016/j.ceb.2015.03.005

Beato, M., & Eisfeld, K. (1997). Transcription factor access to chromatin. *Nucleic acids research, 25*(18), 3559-3563.

Beck, L. A., Hosick, T. J., & Sinensky, M. (1990). Isoprenylation is required for the processing of the lamin A precursor. *The Journal of cell biology, 110*(5), 1489-1499. doi:10.1083/jcb.110.5.1489

Bellin, M., Marchetto, M. C., Gage, F. H., & Mummery, C. L. (2012). Induced pluripotent stem cells: the new patient? *Nature Reviews Molecular Cell Biology, 13*(11), 713-726. doi:10.1038/nrm3448

Bengtsson, L., & Wilson, K. L. (2006). Barrier-to-autointegration factor phosphorylation on Ser-4 regulates emerin binding to lamin A in vitro and emerin localization in vivo. *Mol. Biol. Cell, 17*(3), 1154-1163. Retrieved from http://www.ncbi.nlm.nih.gov/pubmed/16371512

http://www.ncbi.nlm.nih.gov/pmc/articles/PMC1382305/pdf/1154.pdf

Bergo, M. O., Gavino, B., Ross, J., Schmidt, W. K., Hong, C., Kendall, L. V., . . . Young, S. G. (2002). Zmpste24 deficiency in mice causes spontaneous bone fractures, muscle weakness, and a prelamin A processing defect. *Proceedings of the National Academy of Sciences of the United States of America, 99*(20), 13049-13054. doi:10.1073/pnas.192460799

Bermeo, S., Vidal, C., Zhou, H., & Duque, G. (2015). Lamin A/C Acts as an Essential Factor in Mesenchymal Stem Cell Differentiation Through the Regulation of the Dynamics of the Wnt/β-Catenin Pathway. *J Cell Biochem, 116*(10), 2344-2353. doi:10.1002/jcb.25185

Bernardes de Jesus, B., Vera, E., Schneeberger, K., Tejera, A. M., Ayuso, E., Bosch, F., & Blasco, M. A. (2012). Telomerase gene therapy in adult and old mice delays aging and increases longevity without increasing cancer. *EMBO Mol Med, 4*(8), 691-704. doi:10.1002/emmm.201200245

Blackburn, E. H., Greider, C. W., & Szostak, J. W. (2006). Telomeres and telomerase: the path from maize, Tetrahymena and yeast to human cancer and aging. *Nat Med, 12*(10), 1133-1138. doi:10.1038/nm1006-1133

Blair, K. A. (1990). Aging: Physiological Aspects and Clinical Implications. *The Nurse Practitioner, 15*(2), 14-30. Retrieved from https://journals.lww.com/tnpj/Fulltext/1990/02000/Aging__Physiological_Aspects_and_Clinical.8.aspx

Bodnar, A. G., Ouellette, M., Frolkis, M., Holt, S. E., Chiu, C. P., Morin, G. B., . . . Wright, W. E. (1998). Extension of life-span by introduction of telomerase into normal human cells. *Science, 279*(5349), 349-352. doi:10.1126/science.279.5349.349

Boulon, S., Westman, B. J., Hutten, S., Boisvert, F.-M., & Lamond, A. I. (2010). The nucleolus under stress. *Molecular cell, 40*(2), 216-227.

Bouzid, T., Kim, E., Riehl, B. D., Esfahani, A. M., Rosenbohm, J., Yang, R., . . . Lim, J. Y. (2019). The LINC complex, mechanotransduction, and mesenchymal stem cell function and fate. *Journal of Biological Engineering, 13*(1), 68. doi:10.1186/s13036-019-0197-9

Brachner, A., & Foisner, R. (2014). Lamina-associated polypeptide (LAP)2α and other LEM proteins in cancer biology. *Adv Exp Med Biol, 773*, 143-163. doi:10.1007/978-1-4899-8032-8_7

Bridger, J. M., & Kill, I. R. (2004). Aging of Hutchinson–Gilford progeria syndrome fibroblasts is characterised by hyperproliferation and increased apoptosis. *Experimental Gerontology, 39*(5), 717-724. doi:https://doi.org/10.1016/j.exger.2004.02.002

Broers, J. L., Kuijpers, H. J., Ostlund, C., Worman, H. J., Endert, J., & Ramaekers, F. C. (2005). Both lamin A and lamin C mutations cause lamina instability as well as loss of internal nuclear lamin organization. *Exp Cell Res, 304*(2), 582-592. doi:10.1016/j.yexcr.2004.11.020

Brown, R. (1833). Observations on the Organs and Mode of Fecudnation in Orchideae and Asclepiadeae. *Trans Linn Soc Lon, 16*, 685-746.

Buchwalter, A., & Hetzer, M. W. (2017). Nucleolar expansion and elevated protein translation in premature aging. *Nat Commun, 8*(1), 328. doi:10.1038/s41467-017-00322-z

Buendia, B., Courvalin, J. C., & Collas, P. (2001). Dynamics of the nuclear envelope at mitosis and during apoptosis. *Cell Mol Life Sci, 58*(12-13), 1781-1789. doi:10.1007/pl00000818

Buenrostro, J. D., Wu, B., Chang, H. Y., & Greenleaf, W. J. (2015). ATAC-seq: A Method for Assaying Chromatin Accessibility Genome-Wide. *Current Protocols in*

Molecular Biology, 109(1), 21.29.21-21.29.29. doi:https://doi.org/10.1002/0471142727.mb2129s109

Burke, B., & Stewart, C. L. (2006). The laminopathies: the functional architecture of the nucleus and its contribution to disease. *Annu Rev Genomics Hum Genet, 7*, 369-405. doi:10.1146/annurev.genom.7.080505.115732

Burke, B., & Stewart, C. L. (2013). The nuclear lamins: flexibility in function. *Nature Reviews Molecular Cell Biology, 14*(1), 13-24. doi:10.1038/nrm3488

Cabanillas, R., Cadinanos, J., Villameytide, J. A., Perez, M., Longo, J., Richard, J. M., . . . Lopez-Otin, C. (2011). Nestor-Guillermo progeria syndrome: a novel premature aging condition with early onset and chronic development caused by BANF1 mutations. *Am. J. Med. Genet. A, 155A*(11), 2617-2625. doi:10.1002/ajmg.a.34249 [doi]

Cabanillas, R., Cadiñanos, J., Villameytide, J. A. F., Pérez, M., Longo, J., Richard, J. M., . . . López-Otín, C. (2011). Néstor–Guillermo progeria syndrome: A novel premature aging condition with early onset and chronic development caused by BANF1 mutations. *American Journal of Medical Genetics Part A, 155*(11), 2617-2625. doi:https://doi.org/10.1002/ajmg.a.34249

Cai, M., Huang, Y., Zheng, R., Wei, S. Q., Ghirlando, R., Lee, M. S., . . . Clore, G. M. (1998). Solution structure of the cellular factor BAF responsible for protecting retroviral DNA from autointegration. *Nat. Struct. Biol, 5*(10), 903-909. Retrieved from http://www.ncbi.nlm.nih.gov/pubmed/9783751

Caille, N., Thoumine, O., Tardy, Y., & Meister, J. J. (2002). Contribution of the nucleus to the mechanical properties of endothelial cells. *J Biomech, 35*(2), 177-187. doi:10.1016/s0021-9290(01)00201-9

Campisi, J. (1998). The Role of Cellular Senescence in Skin Aging. *Journal of Investigative Dermatology Symposium Proceedings, 3*(1), 1-5. doi:https://doi.org/10.1038/jidsymp.1998.2

Campisi, J. (2013). Aging, cellular senescence, and cancer. *Annual review of physiology, 75*, 685-705.

Cao, K., Capell, B. C., Erdos, M. R., Djabali, K., & Collins, F. S. (2007). A lamin A protein isoform overexpressed in Hutchinson–Gilford progeria syndrome interferes with mitosis in progeria and normal cells. *Proceedings of the National Academy of Sciences, 104*(12), 4949-4954. doi:10.1073/pnas.0611640104

Cao, K., Graziotto, J. J., Blair, C. D., Mazzulli, J. R., Erdos, M. R., Krainc, D., & Collins, F. S. (2011). Rapamycin reverses cellular phenotypes and enhances mutant protein clearance in Hutchinson-Gilford progeria syndrome cells. *Science Translational Medicine, 3*(89), 89ra58-89ra58.

Carrero, D., Soria-Valles, C., & López-Otín, C. (2016). Hallmarks of progeroid syndromes: lessons from mice and reprogrammed cells. *Disease Models & Mechanisms, 9*(7), 719-735. doi:10.1242/dmm.024711

Cau, P., Navarro, C., Harhouri, K., Roll, P., Sigaudy, S., Kaspi, E., . . . Lévy, N. (2014). *Nuclear matrix, nuclear envelope and premature aging syndromes in a translational research perspective.* Paper presented at the Seminars in cell & developmental biology.

Chandra, T., Ewels, P. A., Schoenfelder, S., Furlan-Magaril, M., Wingett, S. W., Kirschner, K., . . . Reik, W. (2015). Global reorganization of the nuclear landscape in senescent cells. *Cell Rep, 10*(4), 471-483. doi:10.1016/j.celrep.2014.12.055

Chandra, T., & Narita, M. (2013). High-order chromatin structure and the epigenome in SAHFs. *Nucleus, 4*(1), 23-28. doi:10.4161/nucl.23189

Chang, S., Multani, A. S., Cabrera, N. G., Naylor, M. L., Laud, P., Lombard, D., . . . DePinho, R. A. (2004). Essential role of limiting telomeres in the pathogenesis of Werner syndrome. *Nat Genet, 36*(8), 877-882. doi:10.1038/ng1389

Chen, C., & Hou, J. (2016). Mesenchymal stem cell-based therapy in kidney transplantation. *Stem cell research & therapy, 7*(1), 1-7.

Chen, N. Y., Kim, P., Weston, T. A., Edillo, L., Tu, Y., Fong, L. G., & Young, S. G. (2018). Fibroblasts lacking nuclear lamins do not have nuclear blebs or protrusions but nevertheless have frequent nuclear membrane ruptures. *Proceedings of the National Academy of Sciences, 115*(40), 10100-10105.

Cheung, H.-H., Liu, X., Canterel-Thouennon, L., Li, L., Edmonson, C., & Rennert, Owen M. (2014). Telomerase Protects Werner Syndrome Lineage-Specific Stem Cells from Premature Aging. *Stem Cell Reports, 2*(4), 534-546. doi:https://doi.org/10.1016/j.stemcr.2014.02.006

Chubb, J. R., Boyle, S., Perry, P., & Bickmore, W. A. (2002). Chromatin motion is constrained by association with nuclear compartments in human cells. *Current Biology, 12*(6), 439-445.

Constantinescu, D., Gray, H. L., Sammak, P. J., Schatten, G. P., & Csoka, A. B. (2006). Lamin A/C expression is a marker of mouse and human embryonic stem cell differentiation. *Stem cells, 24*(1), 177-185.

Constantinescu, D., Gray, H. L., Sammak, P. J., Schatten, G. P., & Csoka, A. B. (2006). Lamin A/C expression is a marker of mouse and human embryonic stem cell differentiation. *Stem cells, 24*(1), 177-185. doi:10.1634/stemcells.2004-0159

Cremer, T., & Cremer, C. (2001). Chromosome territories, nuclear architecture and gene regulation in mammalian cells. *Nature reviews genetics, 2*(4), 292-301.

Crisp , M., Liu , Q., Roux , K., Rattner , J. B., Shanahan , C., Burke , B., . . . Hodzic , D. (2005). Coupling of the nucleus and cytoplasm: Role of the LINC complex. *Journal of Cell Biology, 172*(1), 41-53. doi:10.1083/jcb.200509124

Dahl, K. N., Engler, A. J., Pajerowski, J. D., & Discher, D. E. (2005). Power-law rheology of isolated nuclei with deformation mapping of nuclear substructures. *Biophys J, 89*(4), 2855-2864. doi:10.1529/biophysj.105.062554

Dalton, J., Goldman, J. S., & Sampson, J. B. (2015). The muscular dystrophies. In *Genetic Counseling for Adult Neurogenetic Disease* (pp. 251-262): Springer.

Davidson, P. M., & Cadot, B. (2021). Actin on and around the Nucleus. *Trends in Cell Biology, 31*(3), 211-223. doi:https://doi.org/10.1016/j.tcb.2020.11.009

Davie, J. R., & Chadee, D. N. (1998). Regulation and regulatory parameters of histone modifications. *Journal of cellular biochemistry, 72*(S30–31), 203-213.

De Oca, R. M., Lee, K. K., & Wilson, K. L. (2005). Binding of barrier to autointegration factor (BAF) to histone H3 and selected linker histones including H1. 1. *Journal of Biological Chemistry, 280*(51), 42252-42262.

De Sandre-Giovannoli, A., Bernard, R., Cau, P., Navarro, C., Amiel, J., Boccaccio, I., . . . Lévy, N. (2003). Lamin A Truncation in Hutchinson-Gilford Progeria. *Science, 300*(5628), 2055-2055. doi:10.1126/science.1084125

De Sandre-Giovannoli, A., Bernard, R., Cau, P., Navarro, C., Amiel, J., Boccaccio, I., . . . Lévy, N. (2003). Lamin a truncation in Hutchinson-Gilford progeria. *Science, 300*(5628), 2055. doi:10.1126/science.1084125

De Vos, W. H., Houben, F., Kamps, M., Malhas, A., Verheyen, F., Cox, J., . . . Marcelis, C. L. (2011). Repetitive disruptions of the nuclear envelope invoke temporary loss of cellular compartmentalization in laminopathies. *Human molecular genetics, 20*(21), 4175-4186.

Dechat, T., Gajewski, A., Korbei, B., Gerlich, D., Daigle, N., Haraguchi, T., . . . Foisner, R. (2004). LAP2alpha and BAF transiently localize to telomeres and specific regions on chromatin during nuclear assembly. *J Cell Sci, 117*(Pt 25), 6117-6128. doi:10.1242/jcs.01529

Dechat, T., Pfleghaar, K., Sengupta, K., Shimi, T., Shumaker, D. K., Solimando, L., & Goldman, R. D. (2008). Nuclear lamins: major factors in the structural organization and function of the nucleus and chromatin. *Genes & development, 22*(7), 832-853. doi:10.1101/gad.1652708

Dekker, J., Rippe, K., Dekker, M., & Kleckner, N. (2002). Capturing chromosome conformation. *Science, 295*(5558), 1306-1311.

Dekker, J., & van Steensel, B. (2013). Chapter 7 - The Spatial Architecture of Chromosomes. In A. J. M. Walhout, M. Vidal, & J. Dekker (Eds.), *Handbook of Systems Biology* (pp. 137-151). San Diego: Academic Press.

Demontiero, O., Vidal, C., & Duque, G. (2012). Aging and bone loss: New insights for the clinician. *Therapeutic Advances in Musculoskeletal Disease, 4*(2), 61-76. doi:10.1177/1759720X11430858

Denais, C. M., Gilbert, R. M., Isermann, P., McGregor, A. L., Te Lindert, M., Weigelin, B., . . . Lammerding, J. (2016). Nuclear envelope rupture and repair during cancer cell migration. *Science, 352*(6283), 353-358.

Dephoure, N., Zhou, C., Villen, J., Beausoleil, S. A., Bakalarski, C. E., Elledge, S. J., & Gygi, S. P. (2008). A quantitative atlas of mitotic phosphorylation. *Proceedings of the National Academy of Sciences of the United States of America, 105*(31), 10762-10767. doi:10.1073/pnas.0805139105

Divya, M. S., Roshin, G. E., Divya, T. S., Rasheed, V. A., Santhoshkumar, T. R., Elizabeth, K. E., . . . Pillai, R. M. (2012). Umbilical cord blood-derived mesenchymal stem

cells consist of a unique population of progenitors co-expressing mesenchymal stem cell and neuronal markers capable of instantaneous neuronal differentiation. *Stem cell research & therapy, 3*(6), 1-16.

Dixon, J. R., Selvaraj, S., Yue, F., Kim, A., Li, Y., Shen, Y., . . . Ren, B. (2012). Topological domains in mammalian genomes identified by analysis of chromatin interactions. *Nature, 485*(7398), 376-380.

Dominici, M., Le Blanc, K., Mueller, I., Slaper-Cortenbach, I., Marini, F., Krause, D., . . . Horwitz, E. (2006). Minimal criteria for defining multipotent mesenchymal stromal cells. The International Society for Cellular Therapy position statement. *Cytotherapy, 8*(4), 315-317. doi:10.1080/14653240600855905

Dorner, D., Vlcek, S., Foeger, N., Gajewski, A., Makolm, C., Gotzmann, J., . . . Foisner, R. (2006). Lamina-associated polypeptide 2alpha regulates cell cycle progression and differentiation via the retinoblastoma-E2F pathway. *The Journal of cell biology, 173*(1), 83-93. doi:10.1083/jcb.200511149

Dou, Z., Ghosh, K., Vizioli, M. G., Zhu, J., Sen, P., Wangensteen, K. J., . . . Berger, S. L. (2017). Cytoplasmic chromatin triggers inflammation in senescence and cancer. *Nature, 550*(7676), 402-406. doi:10.1038/nature24050

Efeyan, A., & Serrano, M. (2007). P53: Guardian of the Genome and Policeman of the Oncogenes. *Cell cycle (Georgetown, Tex.), 6*(9), 1006-1010.

Emery, A. E., & Dreifuss, F. E. (1966). Unusual type of benign x-linked muscular dystrophy. *J Neurol Neurosurg Psychiatry, 29*(4), 338-342. doi:10.1136/jnnp.29.4.338

Eriksson, M., Brown, W. T., Gordon, L. B., Glynn, M. W., Singer, J., Scott, L., . . . Collins, F. S. (2003). Recurrent de novo point mutations in lamin A cause Hutchinson-Gilford progeria syndrome. *Nature, 423*(6937), 293-298. doi:10.1038/nature01629

Espejel, S., Klatt, P., Murcia, J. M. n.-d., Martín-Caballero, J., Flores, J. M., Taccioli, G., . . . Blasco, M. A. (2004). Impact of telomerase ablation on organismal viability, aging, and tumorigenesis in mice lacking the DNA repair proteins PARP-1, Ku86, or DNA-PKcs. *The Journal of cell biology, 167*(4), 627-638.

Felsenfeld, G., & McGhee, J. D. (1986). Structure of the 30 nm chromatin fiber. *Cell, 44*(3), 375-377.

Fisher, H. G., Patni, N., & Scheuerle, A. E. (2020). An additional case of Nestor-Guillermo progeria syndrome diagnosed in early childhood. *Am J Med Genet A*. doi:10.1002/ajmg.a.61777

Fisher, H. G., Patni, N., & Scheuerle, A. E. (2020). An additional case of Néstor-Guillermo progeria syndrome diagnosed in early childhood. *American Journal of Medical Genetics Part A, 182*(10), 2399-2402. doi:https://doi.org/10.1002/ajmg.a.61777

Flurkey, Currer, & Harrison. (2007). Lifespan as a Biomarker. In J. G. Fox (Ed.), *American College of Laboratory Medicine Series*. Amsterdam; Boston: Elsevier.

Furukawa, K. (1999). LAP2 binding protein 1 (L2BP1/BAF) is a candidate mediator of LAP2-chromatin interaction. *J. Cell Sci, 112 (Pt 15)*, 2485-2492. Retrieved from http://www.ncbi.nlm.nih.gov/pubmed/10393804

Furukawa, K., Sugiyama, S., Osouda, S., Goto, H., Inagaki, M., Horigome, T., . . . Nishida, Y. (2003). Barrier-to-autointegration factor plays crucial roles in cell cycle progression and nuclear organization in Drosophila. *J. Cell Sci, 116*(Pt 18), 3811-3823. Retrieved from http://www.ncbi.nlm.nih.gov/pubmed/12902403

http://jcs.biologists.org/content/116/18/3811.full.pdf

Gabriel, D., Roedl, D., Gordon, L. B., & Djabali, K. (2015). Sulforaphane enhances progerin clearance in H utchinson–G ilford progeria fibroblasts. *Aging Cell, 14*(1), 78-91.

Gagné, J. P., Pic, E., Isabelle, M., Krietsch, J., Ethier, C., Paquet, E., . . . Poirier, G. G. (2012). Quantitative proteomics profiling of the poly(ADP-ribose)-related response to genotoxic stress. *Nucleic Acids Res, 40*(16), 7788-7805. doi:10.1093/nar/gks486

Gall, J. G. (1964). Electron Microscopy of the Nuclear Envelope. In *The Nuclear Membrane and Nucleocytoplasmic Interchange* (pp. 4-25). Vienna: Springer Vienna.

Gesson, K., Vidak, S., & Foisner, R. (2014). Lamina-associated polypeptide (LAP)2α and nucleoplasmic lamins in adult stem cell regulation and disease. *Semin Cell Dev Biol, 29*(100), 116-124. doi:10.1016/j.semcdb.2013.12.009

Gilbert, N., Gilchrist, S., & Bickmore, W. A. (2004). Chromatin Organization in the Mammalian Nucleus. In *International Review of Cytology* (Vol. 242, pp. 283-336): Academic Press.

Glück, S., & Ablasser, A. (2019). Innate immunosensing of DNA in cellular senescence. *Current Opinion in Immunology, 56*, 31-36. doi:https://doi.org/10.1016/j.coi.2018.09.013

Goldman, R. D., Shumaker, D. K., Erdos, M. R., Eriksson, M., Goldman, A. E., Gordon, L. B., . . . Collins, F. S. (2004). Accumulation of mutant lamin A causes progressive changes in nuclear architecture in Hutchinson-Gilford progeria syndrome. *Proc. Natl. Acad. Sci. U. S. A, 101*(24), 8963-8968. Retrieved from http://www.ncbi.nlm.nih.gov/pubmed/15184648

http://www.ncbi.nlm.nih.gov/pmc/articles/PMC428455/pdf/1018963.pdf

Gonzalez-Sandoval, A., & Gasser, S. M. (2016). On TADs and LADs: Spatial Control Over Gene Expression. *Trends Genet, 32*(8), 485-495. doi:10.1016/j.tig.2016.05.004

Gordon, L. B., Kleinman, M. E., Miller, D. T., Neuberg, D. S., Giobbie-Hurder, A., Gerhard-Herman, M., . . . Snyder, B. D. (2012). Clinical trial of a farnesyltransferase inhibitor in children with Hutchinson–Gilford progeria syndrome. *Proceedings of the National Academy of Sciences, 109*(41), 16666-16671.

Gorjanacz, M. (2012). LEM-4 promotes rapid dephosphorylation of BAF during mitotic exit. *Nucleus, 4*(1). doi:22961 [pii]

Gorjanacz, M., Klerkx, E. P., Galy, V., Santarella, R., Lopez-Iglesias, C., Askjaer, P., & Mattaj, I. W. (2007). Caenorhabditis elegans BAF-1 and its kinase VRK-1 participate directly in post-mitotic nuclear envelope assembly. *EMBO J, 26*(1), 132-143. Retrieved from http://www.ncbi.nlm.nih.gov/pubmed/17170708

http://emboj.embopress.org/content/embojnl/26/1/132.full.pdf

Gotzmann, J., & Foisner, R. (2006). A-type lamin complexes and regenerative potential: a step towards understanding laminopathic diseases? *Histochemistry and Cell Biology, 125*(1), 33-41.

Greer, E. L., Maures, T. J., Hauswirth, A. G., Green, E. M., Leeman, D. S., Maro, G. S., . . . Brunet, A. (2010). Members of the H3K4 trimethylation complex regulate lifespan in a germline-dependent manner in C. elegans. *Nature, 466*(7304), 383-387. doi:10.1038/nature09195

Guarente, L. (2011). Sirtuins, aging, and metabolism. *Cold Spring Harb Symp Quant Biol, 76*, 81-90. doi:10.1101/sqb.2011.76.010629

Guelen, L., Pagie, L., Brasset, E., Meuleman, W., Faza, M. B., Talhout, W., . . . de Laat, W. (2008). Domain organization of human chromosomes revealed by mapping of nuclear lamina interactions. *Nature, 453*(7197), 948-951.

Halaschek-Wiener, J., & Brooks-Wilson, A. (2007). Progeria of stem cells: stem cell exhaustion in Hutchinson-Gilford progeria syndrome. *The Journals of Gerontology Series A: Biological Sciences and Medical Sciences, 62*(1), 3-8.

Halfmann, C. T., Sears, R. M., Katiyar, A., Busselman, B. W., Aman, L. K., Zhang, Q., . . . Roux, K. J. (2019). Repair of nuclear ruptures requires barrier-to-autointegration factor. *Journal of Cell Biology, 218*(7), 2136-2149. doi:10.1083/jcb.201901116

Hambright, W. S., Niedernhofer, L. J., Huard, J., & Robbins, P. D. (2019). Murine models of accelerated aging and musculoskeletal disease. *Bone, 125*, 122-127. doi:https://doi.org/10.1016/j.bone.2019.03.002

Haraguchi, T., Kojidani, T., Koujin, T., Shimi, T., Osakada, H., Mori, C., . . . Hiraoka, Y. (2008). Live cell imaging and electron microscopy reveal dynamic processes of BAF-directed nuclear envelope assembly. *Journal of cell science, 121*(15), 2540-2554.

Haraguchi, T., Koujin, T., Osakada, H., Kojidani, T., Mori, C., Masuda, H., & Hiraoka, Y. (2007). Nuclear localization of barrier-to-autointegration factor is correlated with progression of S phase in human cells. *Journal of cell science, 120*(12), 1967-1977. doi:10.1242/jcs.03461

Haraguchi, T., Koujin, T., Segura-Totten, M., Lee, K. K., Matsuoka, Y., Yoneda, Y., . . . Hiraoka, Y. (2001). BAF is required for emerin assembly into the reforming nuclear envelope. *J. Cell Sci, 114*(Pt 24), 4575-4585. Retrieved from http://www.ncbi.nlm.nih.gov/pubmed/11792822

http://jcs.biologists.org/content/114/24/4575.full.pdf

Harman, D. (1965). THE FREE RADICAL THEORY OF AGING: EFFECT OF AGE ON SERUM COPPER LEVELS. *J Gerontol, 20*, 151-153. doi:10.1093/geronj/20.2.151

Harr, J. C., Gonzalez-Sandoval, A., & Gasser, S. M. (2016). Histones and histone modifications in perinuclear chromatin anchoring: from yeast to man. *EMBO Rep, 17*(2), 139-155. doi:10.15252/embr.201541809

Harris, D., & Engelman, A. (2000). Both the structure and DNA binding function of the barrier-to-autointegration factor contribute to reconstitution of HIV type 1 integration in vitro. *J. Biol. Chem, 275*(50), 39671-39677. Retrieved from http://www.ncbi.nlm.nih.gov/pubmed/11005805

http://www.jbc.org/content/275/50/39671.full.pdf

Hatch, E. M., & Hetzer, M. W. (2016). Nuclear envelope rupture is induced by actin-based nucleus confinement. *Journal of Cell Biology, 215*(1), 27-36.

Hayflick, L., & Moorhead, P. S. (1961). The serial cultivation of human diploid cell strains. *Exp Cell Res, 25*, 585-621. doi:10.1016/0014-4827(61)90192-6

Hebbes, T. R., Thorne, A. W., & Crane-Robinson, C. (1988). A direct link between core histone acetylation and transcriptionally active chromatin. *The EMBO Journal, 7*(5), 1395-1402.

Hetzer, M. W. (2010). The nuclear envelope. *Cold Spring Harb Perspect Biol, 2*(3), a000539. doi:10.1101/cshperspect.a000539

Hetzer, M. W., Walther, T. C., & Mattaj, I. W. (2005). Pushing the envelope: structure, function, and dynamics of the nuclear periphery. *Annu Rev Cell Dev Biol, 21*, 347-380. doi:10.1146/annurev.cellbio.21.090704.151152

Heun, P., Laroche, T., Shimada, K., Furrer, P., & Gasser, S. M. (2001). Chromosome dynamics in the yeast interphase nucleus. *Science, 294*(5549), 2181-2186.

Itahana, K., Dimri, G., & Campisi, J. (2001). Regulation of cellular senescence by p53. *European journal of biochemistry / FEBS; European journal of biochemistry / FEBS, 268*(10), 2784-2791. doi:ejb2228 [pii]

Jakob, B., Splinter, J., Conrad, S., Voss, K. O., Zink, D., Durante, M., . . . Taucher-Scholz, G. (2011). DNA double-strand breaks in heterochromatin elicit fast repair protein recruitment, histone H2AX phosphorylation and relocation to euchromatin. *Nucleic Acids Res, 39*(15), 6489-6499. doi:10.1093/nar/gkr230

Janzen, V., Forkert, R., Fleming, H. E., Saito, Y., Waring, M. T., Dombkowski, D. M., . . . Scadden, D. T. (2006). Stem-cell ageing modified by the cyclin-dependent kinase inhibitor p16INK4a. *Nature, 443*(7110), 421-426. doi:10.1038/nature05159

Jeyapalan, J. C., & Sedivy, J. M. (2008). Cellular senescence and organismal aging. *Mech Ageing Dev, 129*(7-8), 467-474. doi:10.1016/j.mad.2008.04.001

Johnson, S. C., Rabinovitch, P. S., & Kaeberlein, M. (2013). mTOR is a key modulator of ageing and age-related disease. *Nature, 493*(7432), 338-345. doi:10.1038/nature11861

Kill, I. R., Faragher, R. G., Lawrence, K., & Shall, S. (1994). The expression of proliferation-dependent antigens during the lifespan of normal and progeroid human fibroblasts in culture. *J Cell Sci, 107 (Pt 2)*, 571-579.

Kim, J.-K., Louhghalam, A., Lee, G., Schafer, B. W., Wirtz, D., & Kim, D.-H. (2017). Nuclear lamin A/C harnesses the perinuclear apical actin cables to protect nuclear morphology. *Nature Communications, 8*(1), 1-13.

Kim, Y., Sharov, A. A., McDole, K., Cheng, M., Hao, H., Fan, C.-M., . . . Zheng, Y. (2011). Mouse B-type lamins are required for proper organogenesis but not by embryonic stem cells. *Science, 334*(6063), 1706-1710.

Kind, J., & van Steensel, B. (2014). Stochastic genome-nuclear lamina interactions. *Nucleus, 5*(2), 124-130. doi:10.4161/nucl.28825

Kirkwood, T. B., & Holliday, R. (1979). The evolution of ageing and longevity. *Proceedings of the Royal Society of London. Series B. Biological Sciences, 205*(1161), 531-546.

Kitten, G. T., & Nigg, E. A. (1991). The CaaX motif is required for isoprenylation, carboxyl methylation, and nuclear membrane association of lamin B2. *The Journal of cell biology, 113*(1), 13-23. doi:10.1083/jcb.113.1.13

Klass, M. R. (1983). A method for the isolation of longevity mutants in the nematode Caenorhabditis elegans and initial results. *Mech Ageing Dev, 22*(3-4), 279-286. doi:10.1016/0047-6374(83)90082-9

Klopp, A. H., Gupta, A., Spaeth, E., Andreeff, M., & Marini III, F. (2011). Concise review: dissecting a discrepancy in the literature: do mesenchymal stem cells support or suppress tumor growth? *Stem cells, 29*(1), 11-19.

Kornberg, R. D., & Lorch, Y. (1991). Irresistible force meets immovable object: transcription and the nucleosome. *Cell, 67*(5), 833-836.

Kornberg, R. D., & Lorch, Y. (1999). Twenty-five years of the nucleosome, fundamental particle of the eukaryote chromosome. *Cell, 98*(3), 285-294.

Kubben, N., Brimacombe, K. R., Donegan, M., Li, Z., & Misteli, T. (2016). A high-content imaging-based screening pipeline for the systematic identification of anti-progeroid compounds. *Methods, 96*, 46-58.

Kuo, Y. C., Chang, T. H., Hsu, W. T., Zhou, J., Lee, H. H., Hui-Chun Ho, J., . . . Kuang-Sheng, O. (2015). Oscillatory shear stress mediates directional reorganization of actin cytoskeleton and alters differentiation propensity of mesenchymal stem cells. *Stem cells, 33*(2), 429-442.

Kuro-o, M., Matsumura, Y., Aizawa, H., Kawaguchi, H., Suga, T., Utsugi, T., . . . Nabeshima, Y. I. (1997). Mutation of the mouse klotho gene leads to a syndrome resembling ageing. *Nature, 390*(6655), 45-51. doi:10.1038/36285

Lachapelle, S., Gagné, J. P., Garand, C., Desbiens, M., Coulombe, Y., Bohr, V. A., . . . Lebel, M. (2011). Proteome-wide identification of WRN-interacting proteins in untreated and nuclease-treated samples. *J Proteome Res, 10*(3), 1216-1227. doi:10.1021/pr100990s

Lammerding, J., Fong, L. G., Ji, J. Y., Reue, K., Stewart, C. L., Young, S. G., & Lee, R. T. (2006). Lamins A and C but not lamin B1 regulate nuclear mechanics. *J Biol Chem, 281*(35), 25768-25780. doi:10.1074/jbc.M513511200

Lammerding, J., Hsiao, J., Schulze, P. C., Kozlov, S., Stewart, C. L., & Lee, R. T. (2005). Abnormal nuclear shape and impaired mechanotransduction in emerin-deficient cells. *J. Cell Biol, 170*(5), 781-791. Retrieved from http://www.ncbi.nlm.nih.gov/pubmed/16115958

http://www.ncbi.nlm.nih.gov/pmc/articles/PMC2171355/pdf/200502148.pdf

Lamond, A. I., & Sleeman, J. E. (2003). Nuclear substructure and dynamics. *Current Biology, 13*(21), R825-R828. doi:https://doi.org/10.1016/j.cub.2003.10.012

Längst, G., & Becker, P. B. (2001). Nucleosome mobilization and positioning by ISWI-containing chromatin-remodeling factors. *Journal of cell science, 114*(14), 2561-2568.

Lee, H.-W., Blasco, M. A., Gottlieb, G. J., Horner, J. W., Greider, C. W., & DePinho, R. A. (1998). Essential role of mouse telomerase in highly proliferative organs. *Nature, 392*(6676), 569-574.

Lee, M. S., & Craigie, R. (1994). Protection of retroviral DNA from autointegration: involvement of a cellular factor. *Proc. Natl. Acad. Sci. U. S. A, 91*(21), 9823-9827. Retrieved from http://www.ncbi.nlm.nih.gov/pubmed/7937898

https://www.pnas.org/content/pnas/91/21/9823.full.pdf

Leitch, A. R. (2000). Higher levels of organization in the interphase nucleus of cycling and differentiated cells. *Microbiology and Molecular Biology Reviews, 64*(1), 138-152.

Levi, B., Wan, D. C., Glotzbach, J. P., Hyun, J., Januszyk, M., Montoro, D., . . . Longaker, M. T. (2011). CD105 protein depletion enhances human adipose-derived stromal cell osteogenesis through reduction of transforming growth factor β1 (TGF-β1) signaling. *J Biol Chem, 286*(45), 39497-39509. doi:10.1074/jbc.M111.256529

Liao, C.-Y., & Kennedy, B. K. (2014). Chapter Five - Mouse Models and Aging: Longevity and Progeria. In C. L. Stewart (Ed.), *Current Topics in Developmental Biology* (Vol. 109, pp. 249-285): Academic Press.

Liu, B., Wang, J., Chan, K. M., Tjia, W. M., Deng, W., Guan, X., . . . Zhou, Z. (2005). Genomic instability in laminopathy-based premature aging. *Nat Med, 11*(7), 780-785. doi:10.1038/nm1266

Loi, M., Cenni, V., Duchi, S., Squarzoni, S., Lopez-Otin, C., Foisner, R., . . . Capanni, C. (2016). Barrier-to-autointegration factor (BAF) involvement in prelamin A-related chromatin organization changes. *Oncotarget, 7*(13), 15662-15677. doi:10.18632/oncotarget.6697

Lombard, D. B., Beard, C., Johnson, B., Marciniak, R. A., Dausman, J., Bronson, R., . . . Guarente, L. (2000). Mutations in the WRN Gene in Mice Accelerate Mortality in a p53-Null Background. *Molecular and Cellular Biology, 20*(9), 3286-3291. doi:10.1128/mcb.20.9.3286-3291.2000

Lombardi, M. L., & Lammerding, J. (2011). Keeping the LINC: the importance of nucleocytoskeletal coupling in intracellular force transmission and cellular function. *Biochem Soc Trans, 39*(6), 1729-1734. doi:10.1042/BST20110686

Lopez-Otin, C., Blasco, M. A., Partridge, L., Serrano, M., & Kroemer, G. (2013). The hallmarks of aging. *Cell, 153*(6), 1194-1217. doi:10.1016/j.cell.2013.05.039

Lovett, D. B., Shekhar, N., Nickerson, J. A., Roux, K. J., & Lele, T. P. (2013). Modulation of Nuclear Shape by Substrate Rigidity. *Cell Mol Bioeng, 6*(2), 230-238. doi:10.1007/s12195-013-0270-2

Luzhna, L., Kathiria, P., & Kovalchuk, O. (2013). Micronuclei in genotoxicity assessment: from genetics to epigenetics and beyond. *Frontiers in genetics, 4*, 131-131. doi:10.3389/fgene.2013.00131

Maegawa, S., Hinkal, G., Kim, H. S., Shen, L., Zhang, L., Zhang, J., . . . Issa, J. P. (2010). Widespread and tissue specific age-related DNA methylation changes in mice. *Genome Res, 20*(3), 332-340. doi:10.1101/gr.096826.109

Mallanna, S. K., Ormsbee, B. D., Iacovino, M., Gilmore, J. M., Cox, J. L., Kyba, M., . . . Rizzino, A. (2010). Proteomic analysis of Sox2-associated proteins during early stages of mouse embryonic stem cell differentiation identifies Sox21 as a novel regulator of stem cell fate. *Stem cells, 28*(10), 1715-1727.

Malone, C. J., Fixsen, W. D., Horvitz, H. R., & Han, M. (1999). UNC-84 localizes to the nuclear envelope and is required for nuclear migration and anchoring during C.

elegans development. *Development, 126*(14), 3171-3181. Retrieved from https://dev.biologists.org/content/develop/126/14/3171.full.pdf

Marcelot, A., Petitalot, A., Ropars, V., Le Du, M.-H., Samson, C., Dubois, S., . . . Zinn-Justin, S. (2021). Di-phosphorylated BAF shows altered structural dynamics and binding to DNA, but interacts with its nuclear envelope partners. *Nucleic acids research*. doi:10.1093/nar/gkab184

Martin, G. M., Sprague, C. A., & Epstein, C. J. (1970). Replicative life-span of cultivated human cells. Effects of donor's age, tissue, and genotype. *Lab Invest, 23*(1), 86-92.

McHardy, L. M., Warabi, K., Andersen, R. J., Roskelley, C. D., & Roberge, M. (2005). Strongylophorine-26, a Rho-dependent inhibitor of tumor cell invasion that reduces actin stress fibers and induces nonpolarized lamellipodial extensions. *Molecular Cancer Therapeutics, 4*(5), 772-778. doi:10.1158/1535-7163.Mct-04-0310

Méndez-López, I., & Worman, H. J. (2012). Inner nuclear membrane proteins: impact on human disease. *Chromosoma, 121*(2), 153-167. doi:10.1007/s00412-012-0360-2

Molitor, T. P., & Traktman, P. (2013). Molecular genetic analysis of VRK1 in mammary epithelial cells: depletion slows proliferation in vitro and tumor growth and metastasis in vivo. *Oncogenesis, 2*, e48. doi:oncsis201311 [pii];10.1038/oncsis.2013.11 [doi]

Molitor, T. P., & Traktman, P. (2014). Depletion of the protein kinase VRK1 disrupts nuclear envelope morphology and leads to BAF retention on mitotic chromosomes. *Mol Biol Cell, 25*(6), 891-903. doi:10.1091/mbc.E13-10-0603

Montes de Oca, R., Andreassen, P. R., & Wilson, K. L. (2011). Barrier-to-Autointegration Factor influences specific histone modifications. *Nucleus, 2*(6), 580-590. doi:10.4161/nucl.2.6.17960

Montes de Oca, R., Lee, K. K., & Wilson, K. L. (2005). Binding of barrier to autointegration factor (BAF) to histone H3 and selected linker histones including H1.1. *J Biol Chem, 280*(51), 42252-42262. doi:10.1074/jbc.M509917200

Montes de Oca, R., Shoemaker, C. J., Gucek, M., Cole, R. N., & Wilson, K. L. (2009). Barrier-to-autointegration factor proteome reveals chromatin-regulatory partners. *PLoS One, 4*(9), e7050. doi:10.1371/journal.pone.0007050

Moskalev, A. A., Shaposhnikov, M. V., Plyusnina, E. N., Zhavoronkov, A., Budovsky, A., Yanai, H., & Fraifeld, V. E. (2013). The role of DNA damage and repair in aging through the prism of Koch-like criteria. *Ageing Res Rev, 12*(2), 661-684. doi:10.1016/j.arr.2012.02.001

Navarro, C. L., De Sandre-Giovannoli, A., Bernard, R., Boccaccio, I., Boyer, A., Geneviève, D., . . . Lévy, N. (2004). Lamin A and ZMPSTE24 (FACE-1) defects cause nuclear disorganization and identify restrictive dermopathy as a lethal neonatal laminopathy. *Hum Mol Genet, 13*(20), 2493-2503. doi:10.1093/hmg/ddh265

Nelson, G., Wordsworth, J., Wang, C., Jurk, D., Lawless, C., Martin-Ruiz, C., & von Zglinicki, T. (2012). A senescent cell bystander effect: senescence-induced senescence. *Aging Cell, 11*(2), 345-349. doi:10.1111/j.1474-9726.2012.00795.x

Nichols, R. J., Wiebe, M. S., & Traktman, P. (2006). The vaccinia-related kinases phosphorylate the N' terminus of BAF, regulating its interaction with DNA and its retention in the nucleus. *Mol Biol Cell, 17*(5), 2451-2464. doi:10.1091/mbc.e05-12-1179

Nichols, R. J., Wiebe, M. S., & Traktman, P. (2006). The vaccinia-related kinases phosphorylate the N' terminus of BAF, regulating its interaction with DNA and its

retention in the nucleus. *Mol. Biol. Cell, 17*(5), 2451-2464. doi:E05-12-1179 [pii];10.1091/mbc.E05-12-1179 [doi]

Nogueiras, R., Habegger, K. M., Chaudhary, N., Finan, B., Banks, A. S., Dietrich, M. O., . . . Tschöp, M. H. (2012). Sirtuin 1 and sirtuin 3: physiological modulators of metabolism. *Physiol Rev, 92*(3), 1479-1514. doi:10.1152/physrev.00022.2011

Oshima, J., Martin, G. M., & Hisama, F. M. (1993). Werner Syndrome. In M. P. Adam, H. H. Ardinger, R. A. Pagon, S. E. Wallace, L. J. H. Bean, K. Stephens, & A. Amemiya (Eds.), *GeneReviews(®)*. Seattle (WA): University of Washington, Seattle

Osorio, F. G., Navarro, C. L., Cadinanos, J., Lopez-Mejia, I. C., Quiros, P. M., Bartoli, C., . . . Lopez-Otin, C. (2011). Splicing-directed therapy in a new mouse model of human accelerated aging. *Sci Transl Med, 3*(106), 106ra107. doi:10.1126/scitranslmed.3002847

Osorio, F. G., Navarro, C. L., Cadinanos, J., Lopez-Mejia, I. C., Quiros, P. M., Bartoli, C., . . . Lopez-Otin, C. (2011). Splicing-Directed Therapy in a New Mouse Model of Human Accelerated Aging. *Science Translational Medicine, 3*(106), 1-11.

Pajerowski, J. D., Dahl, K. N., Zhong, F. L., Sammak, P. J., & Discher, D. E. (2007). Physical plasticity of the nucleus in stem cell differentiation. *Proc Natl Acad Sci U S A, 104*(40), 15619-15624. doi:10.1073/pnas.0702576104

Paquet, N., Box, J. K., Ashton, N. W., Suraweera, A., Croft, L. V., Urquhart, A. J., . . . Richard, D. J. (2014). Nestor-Guillermo Progeria Syndrome: A Biochemical Insight Into Barrier-to-Autointegration Factor 1, Alanine 12 Threonine Mutation. *BMC Molecular Biology, 15*(27), 1471-2199.

Paquet, N., Box, J. K., Ashton, N. W., Suraweera, A., Croft, L. V., Urquhart, A. J., . . . Richard, D. J. (2014). Nestor-Guillermo Progeria Syndrome: a biochemical insight into Barrier-to-Autointegration Factor 1, alanine 12 threonine mutation. *BMC Mol Biol, 15*, 27. doi:10.1186/s12867-014-0027-z

Pegoraro, G., Kubben, N., Wickert, U., Göhler, H., Hoffmann, K., & Misteli, T. (2009). Ageing-related chromatin defects through loss of the NURD complex. *Nat Cell Biol, 11*(10), 1261-1267. doi:10.1038/ncb1971

Pendás, A. M., Zhou, Z., Cadiñanos, J., Freije, J. M. P., Wang, J., Hultenby, K., . . . López-Otín, C. (2002). Defective prelamin A processing and muscular and adipocyte alterations in Zmpste24 metalloproteinase–deficient mice. *Nature Genetics, 31*(1), 94-99. doi:10.1038/ng871

Pickersgill, H., Kalverda, B., De Wit, E., Talhout, W., Fornerod, M., & van Steensel, B. (2006). Characterization of the Drosophila melanogaster genome at the nuclear lamina. *Nature Genetics, 38*(9), 1005-1014.

Pittenger, M. F., Mackay, A. M., Beck, S. C., Jaiswal, R. K., Douglas, R., Mosca, J. D., . . . Marshak, D. R. (1999). Multilineage potential of adult human mesenchymal stem cells. *Science, 284*(5411), 143-147.

Pollina, E. A., & Brunet, A. (2011). Epigenetic regulation of aging stem cells. *Oncogene, 30*(28), 3105-3126. doi:10.1038/onc.2011.45

Powers, E. T., Morimoto, R. I., Dillin, A., Kelly, J. W., & Balch, W. E. (2009). Biological and chemical approaches to diseases of proteostasis deficiency. *Annu Rev Biochem, 78*, 959-991. doi:10.1146/annurev.biochem.052308.114844

Pruss, D., Hayes, J. J., & Wolffe, A. P. (1995). Nucleosomal anatomy–where are the histones? *Bioessays, 17*(2), 161-170.

Puente, X. S., Quesada, V., Osorio, F. G., Cabanillas, R., Cadinanos, J., Fraile, J. M., . . . Lopez-Otin, C. (2011). Exome sequencing and functional analysis identifies BANF1 mutation as the cause of a hereditary progeroid syndrome. *Am. J. Hum. Genet, 88*(5), 650-656. doi:S0002-9297(11)00151-0 [pii];10.1016/j.ajhg.2011.04.010 [doi]

Puhka, M., Vihinen, H., Joensuu, M., & Jokitalo, E. (2007). Endoplasmic reticulum remains continuous and undergoes sheet-to-tubule transformation during cell division in mammalian cells. *The Journal of cell biology, 179*(5), 895-909. doi:10.1083/jcb.200705112

Qiu, X., Brown, K., Hirschey, M. D., Verdin, E., & Chen, D. (2010). Calorie restriction reduces oxidative stress by SIRT3-mediated SOD2 activation. *Cell Metab, 12*(6), 662-667. doi:10.1016/j.cmet.2010.11.015

Romero-Bueno, R., de la Cruz Ruiz, P., Artal-Sanz, M., Askjaer, P., & Dobrzynska, A. (2019). Nuclear Organization in Stress and Aging. *Cells, 8*(7). doi:10.3390/cells8070664

Rossi, D. J., Bryder, D., Seita, J., Nussenzweig, A., Hoeijmakers, J., & Weissman, I. L. (2007). Deficiencies in DNA damage repair limit the function of haematopoietic stem cells with age. *Nature, 447*(7145), 725-729. doi:10.1038/nature05862

Rout, M. P., Aitchison, J. D., Suprapto, A., Hjertaas, K., Zhao, Y., & Chait, B. T. (2000). The yeast nuclear pore complex: composition, architecture, and transport mechanism. *The Journal of cell biology, 148*(4), 635-651. doi:10.1083/jcb.148.4.635

Salminen, A., Kaarniranta, K., & Kauppinen, A. (2012). Inflammaging: disturbed interplay between autophagy and inflammasomes. *Aging (Albany NY), 4*(3), 166-175. doi:10.18632/aging.100444

Samson, C., Petitalot, A., Celli, F., Herrada, I., Ropars, V., Le Du, M. H., . . . Zinn-Justin, S. (2018). Structural analysis of the ternary complex between lamin A/C, BAF and emerin identifies an interface disrupted in autosomal recessive progeroid diseases. *Nucleic Acids Res*. doi:10.1093/nar/gky736

Samwer, M., Schneider, M. W. G., Hoefler, R., Schmalhorst, P. S., Jude, J. G., Zuber, J., & Gerlich, D. W. (2017). DNA Cross-Bridging Shapes a Single Nucleus from a Set of Mitotic Chromosomes. *Cell, 170*(5), 956-972 e923. doi:10.1016/j.cell.2017.07.038

Santiago-Fernández, O., Osorio, F. G., Quesada, V., Rodríguez, F., Basso, S., Maeso, D., . . . López-Otín, C. (2019). Development of a CRISPR/Cas9-based therapy for Hutchinson–Gilford progeria syndrome. *Nature Medicine, 25*(3), 423-426. doi:10.1038/s41591-018-0338-6

Scaffidi, P., & Misteli, T. (2005). Reversal of the cellular phenotype in the premature aging disease Hutchinson-Gilford progeria syndrome. *Nature Medicine, 11*(4), 440-445.

Scaffidi, P., & Misteli, T. (2006). Lamin A-Dependent Nuclear Defects in Human Aging. *Science, 312*(5776), 1059-1063. doi:10.1126/science.1127168

Scaffidi, P., & Misteli, T. (2008). Lamin A-dependent misregulation of adult stem cells associated with accelerated ageing. *Nature cell biology, 10*(4), 452-459.

Schirmer, E. C., Florens, L., Guan, T., Yates, J. R., III, & Gerace, L. (2003). Nuclear membrane proteins with potential disease links found by subtractive proteomics. *Science, 301*(5638), 1380-1382. Retrieved from http://www.ncbi.nlm.nih.gov/pubmed/12958361

http://www.sciencemag.org/content/301/5638/1380.full.pdf

Schirmer, E. C., & Gerace, L. (2005). The nuclear membrane proteome: extending the envelope. *Trends Biochem. Sci, 30*(10), 551-558. Retrieved from http://www.ncbi.nlm.nih.gov/pubmed/16125387

http://ac.els-cdn.com/S0968000405002380/1-s2.0-S0968000405002380-main.pdf?_tid=b7f1f00a-4ceb-11e5-bfd9-00000aacb360&acdnat=1440701279_702e527c522fe05b79c2bd1cf37f7d2f

Segura-Totten, M., Kowalski, A. K., Craigie, R., & Wilson, K. L. (2002). Barrier-to-autointegration factor: major roles in chromatin decondensation and nuclear assembly. *The Journal of cell biology, 158*(3), 475-485. doi:10.1083/jcb.200202019

Shaklai, S., Somech, R., Gal-Yam, E. N., Deshet-Unger, N., Moshitch-Moshkovitz, S., Hirschberg, K., . . . Rechavi, G. (2008). LAP2ζ binds BAF and suppresses LAP2β-mediated transcriptional repression. *European journal of cell biology, 87*(5), 267-278.

Shazeeb, M. S., Cox, M. K., Gupta, A., Tang, W., Singh, K., Pryce, C. T., . . . Sabbagh, Y. (2018). Skeletal Characterization of the Fgfr3 Mouse Model of Achondroplasia Using Micro-CT and MRI Volumetric Imaging. *Scientific Reports, 8*(1), 469. doi:10.1038/s41598-017-18801-0

Shimamoto, A., Kagawa, H., Zensho, K., Sera, Y., Kazuki, Y., Osaki, M., . . . Tahara, H. (2014). Reprogramming suppresses premature senescence phenotypes of Werner syndrome cells and maintains chromosomal stability over long-term culture. *PLoS One, 9*(11), e112900. doi:10.1371/journal.pone.0112900

Si-Tayeb, K., Noto, F. K., Nagaoka, M., Li, J., Battle, M. A., Duris, C., . . . Duncan, S. A. (2010). Highly efficient generation of human hepatocyte–like cells from induced

pluripotent stem cells. *Hepatology, 51*(1), 297-305. doi:https://doi.org/10.1002/hep.23354

Simpson, R. T. (1991). Nucleosome positioning: occurrence, mechanisms, and functional consequences. *Progress in nucleic acid research and molecular biology, 40*, 143-184.

Swift, J., Ivanovska, I. L., Buxboim, A., Harada, T., Dingal, P. C. D. P., Pinter, J., . . . Discher, D. E. (2013). Nuclear Lamin-A Scales with Tissue Stiffness and Enhances Matrix-Directed Differentiation. *Science, 341*(6149), 1240104. doi:10.1126/science.1240104

Tapley, E. C., & Starr, D. A. (2013). Connecting the nucleus to the cytoskeleton by SUN–KASH bridges across the nuclear envelope. *Current Opinion in Cell Biology, 25*(1), 57-62. doi:https://doi.org/10.1016/j.ceb.2012.10.014

Thoma, F., & Koller, T. (1977). Influence of histone H1 on chromatin structure. *Cell, 12*(1), 101-107.

Thompson, L. H., & Schild, D. (2002). Recombinational DNA repair and human disease. *Mutat Res, 509*(1-2), 49-78. doi:10.1016/s0027-5107(02)00224-5

Tiku, V., Jain, C., Raz, Y., Nakamura, S., Heestand, B., Liu, W., . . . Antebi, A. (2017). Small nucleoli are a cellular hallmark of longevity. *Nature Communications, 8*(1), 16083. doi:10.1038/ncomms16083

Tsiligiri, M., Fekos, C., Theodoridou, E., & Lavdaniti, M. (2014). An Overview of Hutchinson Gilford Progeria Syndrome (HGPS). *British Journal of Medicine and Medical Research, 5*(12), 1527-1533. doi:10.9734/BJMMR/2015/13452

Umland, T. C., Wei, S. Q., Craigie, R., & Davies, D. R. (2000). Structural basis of DNA bridging by barrier-to-autointegration factor. *Biochemistry, 39*(31), 9130-9138. Retrieved from http://www.ncbi.nlm.nih.gov/pubmed/10924106

http://pubs.acs.org/doi/pdfplus/10.1021/bi000572w

Ungricht, R., & Kutay, U. (2017). Mechanisms and functions of nuclear envelope remodelling. *Nature Reviews Molecular Cell Biology, 18*(4), 229-245. doi:10.1038/nrm.2016.153

Varela, I., Cadiñanos, J., Pendás, A. M., Gutiérrez-Fernández, A., Folgueras, A. R., Sánchez, L. M., . . . López-Otín, C. (2005). Accelerated ageing in mice deficient in Zmpste24 protease is linked to p53 signalling activation. *Nature, 437*(7058), 564-568. doi:10.1038/nature04019

Vergnes, L., Péterfy, M., Bergo, M. O., Young, S. G., & Reue, K. (2004). Lamin B1 is required for mouse development and nuclear integrity. *Proceedings of the National Academy of Sciences, 101*(28), 10428-10433.

Vidak, S., & Foisner, R. (2016). Molecular insights into the premature aging disease progeria. *Histochemistry and Cell Biology, 145*(4), 401-417. doi:10.1007/s00418-016-1411-1

Villa-Bellosta, R., Rivera-Torres, J., Osorio, F. G., Acín-Pérez, R., Enriquez, J. A., López-Otín, C., & Andrés, V. (2013). Defective extracellular pyrophosphate metabolism promotes vascular calcification in a mouse model of Hutchinson-Gilford progeria syndrome that is ameliorated on pyrophosphate treatment. *Circulation, 127*(24), 2442-2451. doi:10.1161/circulationaha.112.000571

Wang, K., & Klionsky, D. J. (2011). Mitochondria removal by autophagy. *Autophagy, 7*(3), 297-300. doi:10.4161/auto.7.3.14502

Wang, X., Xu, S., Rivolta, C., Li, L. Y., Peng, G.-H., Swain, P. K., . . . Dryja, T. P. (2002). Barrier to autointegration factor interacts with the cone-rod homeobox and represses its transactivation function. *Journal of Biological Chemistry, 277*(45), 43288-43300.

Wenzel, V., Roedl, D., Gabriel, D., Gordon, L. B., Herlyn, M., Schneider, R., . . . Djabali, K. (2012). Naïve adult stem cells from patients with Hutchinson-Gilford progeria syndrome express low levels of progerin in vivo. *Biol Open, 1*(6), 516-526. doi:10.1242/bio.20121149

Wiebe, M. S., Nichols, R. J., Molitor, T. P., Lindgren, J. K., & Traktman, P. (2010). Mice deficient in the serine/threonine protein kinase VRK1 are infertile due to a progressive loss of spermatogonia. *Biology of reproduction, 82*(1), 182-193. doi:10.1095/biolreprod.109.079095

Wilson, E. B. (1900). *The Cell in Development and Inheritence* (H. F. Osbron Ed. Second ed.). New York: The Macmillan Company.

Wolffe, A. (1998). *Chromatin: structure and function*: Academic press.

Wu, R. S., Panusz, H. T., Hatch, C. L., & Bonner, W. M. (1986). Histones and their modification. *Critical Reviews in Biochemistry, 20*(2), 201-263.

Yamaza, H., Komatsu, T., Wakita, S., Kijogi, C., Park, S., Hayashi, H., . . . Shimokawa, I. (2010). FoxO1 is involved in the antineoplastic effect of calorie restriction. *Aging Cell, 9*(3), 372-382. doi:10.1111/j.1474-9726.2010.00563.x

Yang, L., Guan, T., & Gerace, L. (1997). Integral membrane proteins of the nuclear envelope are dispersed throughout the endoplasmic reticulum during mitosis. *J. Cell Biol, 137*(6), 1199-1210. Retrieved from http://www.ncbi.nlm.nih.gov/pubmed/9182656

http://www.ncbi.nlm.nih.gov/pmc/articles/PMC2132536/pdf/14511.pdf

Yang, S. H., Meta, M., Qiao, X., Frost, D., Bauch, J., Coffinier, C., . . . Fong, L. G. (2006). A farnesyltransferase inhibitor improves disease phenotypes in mice with a

Hutchinson-Gilford progeria syndrome mutation. *The Journal of Clinical Investigation, 116*(8), 2115-2121. doi:10.1172/JCI28968

Young, A. M., Gunn, A. L., & Hatch, E. M. (2020). BAF facilitates interphase nuclear membrane repair through recruitment of nuclear transmembrane proteins. *Molecular biology of the cell, 31*(15), 1551-1560. doi:10.1091/mbc.E20-01-0009

Zaghini, A., Sarli, G., Barboni, C., Sanapo, M., Pellegrino, V., Diana, A., . . . Squarzoni, S. (2020). Long term breeding of the Lmna G609G progeric mouse: Characterization of homozygous and heterozygous models. *Experimental Gerontology, 130*, 110784. doi:https://doi.org/10.1016/j.exger.2019.110784

Zhang, J., Lian, Q., Zhu, G., Zhou, F., Sui, L., Tan, C., . . . Colman, A. (2011). A Human iPSC Model of Hutchinson Gilford Progeria Reveals Vascular Smooth Muscle and Mesenchymal Stem Cell Defects. *Cell Stem Cell, 8*(1), 31-45. doi:https://doi.org/10.1016/j.stem.2010.12.002

Zheng, R., Ghirlando, R., Lee, M. S., Mizuuchi, K., Krause, M., & Craigie, R. (2000). Barrier-to-autointegration factor (BAF) bridges DNA in a discrete, higher-order nucleoprotein complex. *Proc. Natl. Acad. Sci. U. S. A, 97*(16), 8997-9002. Retrieved from http://www.ncbi.nlm.nih.gov/pubmed/10908652

http://www.ncbi.nlm.nih.gov/pmc/articles/PMC16810/pdf/pq008997.pdf

Zheng, R., Ghirlando, R., Lee, M. S., Mizuuchi, K., Krause, M., & Craigle, R. (2000). Barrier-to-Autointegration Factor (BAF) Bridges DNA in a Discrete, Higher-Order Nucleoprotein Complex. *PNAS, 97*(16), 8997-9002.